

University of Southampton Research Repository ePrints Soton

Copyright © and Moral Rights for this thesis are retained by the author and/or other copyright owners. A copy can be downloaded for personal non-commercial research or study, without prior permission or charge. This thesis cannot be reproduced or quoted extensively from without first obtaining permission in writing from the copyright holder/s. The content must not be changed in any way or sold commercially in any format or medium without the formal permission of the copyright holders.

When referring to this work, full bibliographic details including the author, title, awarding institution and date of the thesis must be given e.g.

AUTHOR (year of submission) "Full thesis title", University of Southampton, name of the University School or Department, PhD Thesis, pagination

UNIVERSITY OF SOUTHAMPTON

FACULTY OF PHYSICAL SCIENCES

AND ENGINEERING

OPTOELECTRONICS RESEARCH CENTRE

**Modelling of Multimode Erbium-doped
Fibre Amplifiers for Mode-division
Multiplexed Transmission Systems**

✓By

Qiongyue Kang

Thesis for the degree of Doctor of Philosophy

September 2015

[UNIVERSITY OF SOUTHAMPTON](#)

FACULTY OF PHYSICAL SCIENCES AND ENGINEERING

[OPTOELECTRONICS RESEARCH CENTRE](#)

Doctor of Philosophy

**Modelling of Multimode Erbium-doped Fibre Amplifiers for Mode-division
Multiplexed Transmission Systems**

By [Qiongyue Kang](#)

Abstract

This PhD thesis, undertaken within the framework of MODEGAP, covers the design and optimization of high-performance in-line Multimode Erbium-Doped Fiber Amplifiers (MM-EDFAs) or Few-mode (FM) EDFA for next-generation SDM transmission systems based on Mode-Division Multiplexing (MDM). In the MM-EDFAs, minimizing the differential modal gain (DMG) is of paramount importance to prevent system outage.

By using an experimentally validated commercial amplifier simulator, I proposed a 2-mode-group EDF design incorporating ring doping that allows accurate modal gain control amongst the two-mode groups using a simple and much more practical LP₀₁ pump mode. Subsequently a 2-mode-group ring-doped EDF according to my design was fabricated in-house and a portable 2-mode-group EDFA with low DMG built and tested, confirming my predictions. My 2-mode-group EDFA design lay at the heart of several successful 2-mode-group fiber based transmission experiments, as listed in this thesis.

To investigate the vector modes effects in FM-EDFAs, we developed our own MM-EDFA simulator capable of modelling both the Linear Polarized (LP) modes and the full vector solutions. We have concluded that, in practice, the LP amplifier model is valid and sufficient enough to predict the FM-EDFA performance. I proposed a 4-mode-group EDFA design that offered DMG < 1dB across four-mode groups using a customized pump profile. As the number of guided modes increases, the required pump power also increases which means expensive single-mode pump diodes are needed in the core-pumping approach. Cladding pumping is an alternative way to provide pump radiation with the advantages of reducing the costs. Consequently, I upgraded our in-house

amplifier simulator to a cladding-pump-able MM-EDFA design tool incorporating an optimization algorithm (i.e. Genetic Algorithm) that accepts customized criteria and allows a large number of free parameters to be optimized simultaneously. Using this tool, I proposed the designs and optimizations of cladding-pumped 4 and 6-mode-group EDFAs.

Apart from the standard step-index MM-EDFAs, I also investigated novel fiber amplifiers with ring-index profiles for SDM applications. The first type of ring-index fiber discussed in this thesis is of solid core and weakly guiding. The solid-core ring core fiber has an advantage of reducing digital signal processing complexity in MDM transmission. I proposed a 6-mode-group ring core multimode erbium doped fiber amplifier (RC-MM-EDFA) capable of providing almost identical gain among the six mode groups within the C band using either core- or cladding-pumped implementations. The second type of ring-index fiber is an air-core fiber that enables the stable transmission of Orbital Angular Momentum (OAM) modes, which can be used as another degree of freedom for information multiplexing. I have created a new variant of my amplifier model targeting OAM modes and have achieved DMG lower than 0.5 dB for 12 OAM modes in an air-core EDF.

Table of contents

Abstract	I
Table of contents.....	III
List of tables.....	VI
List of figures.....	VII
Declaration of authorship	XII
Acknowledgements.....	XIII
Definitions and Abbreviations.....	XIV
Chapter 1. Introduction	1
1.1 Thesis motivation	1
1.2 Research aims	5
1.3 Outline of the thesis.....	6
Chapter 2. Background	9
2.1 Modes in cylindrical optical fibers.....	9
2.1.1 Vector solutions for step-index fibers.....	9
2.1.2 Linearly polarized modes for weakly guiding step-index fibers	14
2.1.3 Mode solver using COMSOL Multiphysics 4.3®	17
2.2 Erbium-doped fiber amplifier	18
2.2.1 Atomic-rate equations for three-level laser system	18
2.2.2 Gain coefficient and amplified spontaneous emission in single-mode erbium-doped fiber amplifiers	20
2.2.3 Modelling of multimode erbium-doped fiber amplifier	28
2.2.4 Noise figure	32
2.3 General modelling results of a 2-mode-group EDFA	34
2.4 Conclusion.....	40
Chapter 3. Modelling of 2-mode-group EDFA with linearly polarized approximation	41
3.1 Experimental validation of the LP modes based 2-mode-group EDFA model	42
3.2 Modal gain control in 2-mode-group EDFAs	46
3.2.1 Design of 2-mode-group EDFs with raised-edge index profile	46
3.2.2 Design of 2-mode-group EDFs incorporate ring doping.....	49
3.3 Amplifier modelling based on fabricated 2-mode-group ring doped EDF52	
3.4 Conclusion.....	64

Chapter 4. Development of the in-house MM-EDFA simulator.....	65
4.1 The validation of the in-house MM-EDFA simulator.....	66
4.2 Vector modes based MM-EDFA model	69
4.2.1 Transverse mode intensity evolution in passive fibers	70
4.2.2 Vector modes based MM-EDFA model.....	72
4.3 Impact of mode beating effects in 2-mode-group EDFA.....	75
4.3.1 LP _{11b} pump	75
4.3.2 LP ₁₁ pump	79
4.3.3 LP ₀₁ pump	81
4.3.4 Conclusion.....	82
4.4 Birefringence effects in 2-mode-group EDFAs.....	83
4.4.1 The birefringence model	83
4.4.2 Modes in fibers with slight core ellipticity	85
4.4.3 The modal gain in two-mode erbium-doped fiber amplifiers with an elliptical core	86
4.4.4 Discussion of modal coherency in few-mode EDFAs.....	88
4.5 Conclusion.....	90
Chapter 5. Design optimization of FM-EDFAs supporting four mode groups and beyond.....	92
5.1 Design of core-pumped 4-mode-group EDFA.....	92
5.1.1 Simulation results	93
5.2 Amplifier modeling based on fabricated four-mode-group EDF	97
5.3 Cladding-pumped MM-EDFA model.....	103
5.3 Modeling of cladding-pumped 4-mode-group EDFA using in-house erbium-doped preforms.....	107
5.5 Design of cladding-pumped EDFA supporting four-mode-group and beyond.....	110
5.5.1 Genetic algorithm	111
5.5.2 Design of a cladding-pumped four-mode-group and a six-mode-group EDFA.	114
5.6 Conclusion.....	122
Chapter 6: Modeling of active fibers with ring-index profile.....	124
6.1 Modeling of erbium-doped ring-core fibers.....	125
6.1.1 Modeling of bent ring-core multimode erbium-doped fiber amplifier	126

Table of contents

6.1.2 Modeling of core-pumped ring-core multimode erbium-doped fiber amplifier	127
6.1.3 Modeling of cladding-pumped ring-core multimode erbium-doped fiber amplifier	129
6.1.4 Conclusion	131
6.2 Amplification of twelve orbital-angular-momentum modes in an air-core erbium-doped fiber	131
6.2.1 Orbital angular-momentum modes in fibers	132
6.2.2 Core-pumped orbital angular-momentum erbium-doped fiber amplifiers.....	135
6.2.3 Cladding-pumped orbital angular-momentum erbium-doped fiber amplifiers.....	139
6.3 Conclusions	143
Chapter 7: Conclusion and Future work.....	144
7.1 Conclusion.....	144
7.2 Future work	146
7.2.1 Erbium doped fiber amplifiers for SDM applications	146
7.2.2 Design of special rare-earth-doped fibers	148
References	149
Appendix: List of publications	159
Journal Publications	159
Conference Publications	160

List of tables

Table 2.1. The mathematical relationship between the LP modes and the vector modes for the LP_{01} and LP_{11} mode groups [37]. Here “a” and “b” are used to represent the orientation of the intensity pattern of the LP_{11} mode.	16
Table 3.1. Signal coupling efficiencies associated with the modification of ND in F1.	48
Table 3.2. The effective indices of the vector modes from the LP_{11} and LP_{21} mode groups at 1550nm for three different core diameters from the ring doped preform	54
Table 4.1. Intensity profile of the signal and pump modes used in the LP model and vector model respectively.	76
Table 4.2. Intensity profile of the signal and pump modes used in the LP model and vector model respectively.	79
Table 4.3. Intensity profile of the signal and pump modes used in the LP model and vector model respectively.	82
Table 5.1. The coupling coefficients of LP_{01} , LP_{11} , LP_{21} and LP_{02} modes from the passive 4-mode-group fiber to the 4-mode-group ring-doped EDF.....	100
Table 5.2. Simulation parameters used in the modeling of cladding-pumped 4-mode-group “batman” EDF and 4-mode-group ring-doped EDF.	107
Table 6.1. Modal properties of the RC EDFA.	127

List of figures

Figure 1.1. The evolution of the data-carry capacity of optical fibres, documented by key experimental demonstrations. Image after Ref. [4].	2
Figure 2.1. A step index fiber with cylindrical symmetry; the central shaded region indicates the fiber core with a radius of “a”	10
Figure 2.2. x and y polarizations of the electric fields for the first two modes of the series $l = 0, 1, 2$. The outer circles represent the core-cladding interface of the optical fiber with a radius of a. The inner circles indicate the zero of the functions. The lines crossing the center of the fiber core represent the zeros of $\cos(l\phi)$ or $\sin(l\phi)$ [37].	15
Figure 2.3. Energy level diagram corresponding to a basic three-level laser system, where the laser transition occurs between levels 1 (i.e. ground) and 2 (i.e. metastable). The symbols R, W, and A correspond to pumping rates, stimulated emission rates and spontaneous decay rates between related levels. Superscripts R and NR refer to radiative and non-radiative decays respectively.	19
Figure 2.4. Three-level energy diagram of erbium ions in silica glass.	21
Figure 2.5. Absorption and emission cross-sections of erbium-doped $\text{Al}_2\text{O}_3\text{-SiO}_2$ glass.	23
Figure 2.6. Signal-gain coefficient as a function of wavelength for different population inversion based on cross-section data [46].	23
Figure 2.7. Schematic diagram of an MM EDFA. DM: Dichroic mirror ($R = 980 \text{ nm}$, $T = 1535\text{-}1565 \text{ nm}$).	28
Figure 2.8. A sample diagram of the user interface of the Optisystem 11.0 MM-EDFA module.	35
Figure 2.9. (a) The refractive-index profile of a 2-mode-group EDFA at $1.55 \mu\text{m}$ with a uniform erbium doping profile indicated by the blue shaded area. (b) The signal and pump intensity distributions.	35
Figure 2.10. The modal gain evolutions against fiber position for different pump modes (a) LP_{01} pump; (b) LP_{11b} pump; (c) LP_{21b} pump and (d) LP_{02} pump.	37
Figure 2.11. (a) The power evolution of the total forward and backward ASE along the fiber length. (b) The forward ASE spectrum at the output end of the amplifier.	39
Figure 2.12. The population inversion distribution along the fiber length.	40
Figure 3.1. (a) The FRIP and dopant profiles (i.e. shaded blue region) of F1, and the supported signal modes. (b) DMG vs. input signal power pumped by LP_{01p} and LP_{21p} for both F1 and step-index (SI) EDF.	42
Figure 3.2. The experimental setup of the in-house 2-mode-group EDFA from [25].	44
Figure 3.3. Gain for LP_{01} and LP_{11a} modes vs. input signal power under the central-pump launch condition. The dots denote experimental data, while the lines are simulation fittings.	44
Figure 3.4. Gain for LP_{01} and LP_{11a} modes vs. input signal power under the offset-pump launch condition. The dots represent experimental data, while the lines show theoretical predictions.	45
Figure 3.5. (a) The FRIP of F1, (b) the evolution of LP_{01s} , and (c) LP_{11s} mode intensity distribution in F1 and modified FRIPs with ND varying from 0.3 to 1.0. The dashed lines in (b) and (c) indicate a radial position of $\pm 9 \mu\text{m}$, which is the fiber radius.	46
Figure 3.6. Contour map for the differential gain between LP_{01s} and LP_{11s} (i.e. in dB scale) with X-axis of normalized depth for tuning FRIP based on F1 (i.e. see Figure 3.5(a)) and Y-axis of pump	

List of figures

power ratio between LP_{21p} and LP_{01p}). The vertical dashed lines represent the signal coupling efficiency for LP_{01} in accordance with the ND.....	48
Figure 3.7. F2 with ring-doped profile (i.e. shaded blue region) and supported signal modes. Labels: a is the core radius, and t is the thickness of the doped region.....	50
Figure 3.8. (a) Differential gain between LP_{01s} and LP_{11s} at 1530 nm versus input signal power for different t/a ratios. (b) Modal gains against LP_{01} pump power for F2 with a value of $t/a = 0.52$	50
Figure 3.9. (a) Modal gain evolution of LP_{01s} and LP_{11s} along the fiber position for wavelengths of 1530 nm and 1550 nm, based on $t/a = 0.52$. (b) Modal gain dependence on the wavelength.	51
Figure 3.10. The RI profile and Er doping distribution of the Er ring-doped preform.	53
Figure 3.11. The RI profile of the 2-mode-group erbium ring-doped fiber.	55
Figure 3.12. The measured absorption spectrum of the 2-mode-group ring-doped EDF, provided by Dr. Y. Jung.	55
Figure 3.13. The measurement setup for modal gain analysis of the two-mode-group Er^{3+} ring-doped fiber: mode multiplexer (MUX), two-mode-group erbium-doped fiber amplifier (2-mode-group EDFA) and mode de-multiplexer (DEMUX).....	56
Figure 3.14. The measured modal gains as a function of input pump powers for several of EDF lengths. Data was provided by Dr Y. Jung.	57
Figure 3.15. (a) Modal gain as a function of input pump powers. Black curves: experimental measurements, red curves: simulation fittings using erbium-doping profile (i.e. assuming no diffusion from outer core to inner core) shown in (b).....	59
Figure 3.16. (a) Modal gain as a function of input pump powers. Black curves: experimental measurements, red curves: simulation fittings using assumed erbium-doping profile (i.e. $\lambda = 6$) shown in (b).	59
Figure 3.17. (a) The modal gain as a function of input pump powers. Black curves: experimental measurements, red curves: simulation fittings using assumed erbium-doping profile (i.e. $\lambda = 4$) shown in (b).	59
Figure 3.18. (a) Modal gain as a function of input pump powers. Black curves: experimental measurements, red curves: simulation fittings using assumed erbium-doping profile (i.e. $\lambda = 2$) shown in (b).	60
Figure 3.19. (a) The modal gain as a function of input pump powers; black curves: experimental data; red curves: simulation fittings using the measured erbium-doping profile shown in (b)...	60
Figure 3.20. The mode-dependent gain evolution against pump powers for a 2-mode-group EDF of 6 m with the offset pump launch condition (i.e. LP_{11} pump).....	62
Figure 3.21. Experimental setup. 1: 256-Gb/s DP-16QAM constellations back-to-back single-mode. 2: Spectrum at the transmitter side (96 channels). 3: Spectrum after DEMUX. [27]	63
Figure 3.22. Field trial and few-mode link setup[70].....	63
Figure 3.23. Re-circulating loop experimental setup with in-line 2-mode-group EDFAs over a total distance of over 1000 km[71].....	64
Figure 4.1. The total backward ASE power evolution against the fiber length. The solid black line represents the result obtained from Optisystem 11.0®. The red dots represent the results obtained from the in-house amplifier simulator after 1 iteration. The green dots represent the results obtained from the in-house amplifier simulator after 10 iterations.	68
Figure 4.2. The total forward ASE power evolution against the fiber length. The solid black line represents the result obtained from Optisystem 11.0®. The red dots represent the results	

List of figures

obtained from the in-house amplifier simulator after 1 iteration. The green dots represent the results obtained from the in-house amplifier simulator after 10 iterations.	68
Figure 4.3. (a) The LP_{01} signal power evolution and (b) the LP_{11b} signal power evolution against the fiber length. The solid black line represents the result obtained from Optisystem 11.0®. The red dots represent the results obtained from the in-house amplifier simulator after 1 iteration. The green dots represent the results obtained from the in-house amplifier simulator after 10 iterations.	69
Figure 4.4. The LP_{01} pump signal power evolutions against the fiber length. The solid black line represents the result obtained from Optisystem 11.0®. The red dots represent the results obtained from the in-house amplifier simulator after 1 iteration. The green dots represent the results obtained from the in-house amplifier simulator after 10 iterations.	69
Figure 4.5. Mode intensity profile of (a) TE_{01} , and (b) $HE_{21(odd)}$. The arrows indicate the electric field distribution. Location A ($0\ \mu\text{m}$, $5\ \mu\text{m}$), location B ($0\ \mu\text{m}$, $0\ \mu\text{m}$), and location C ($5\ \mu\text{m}$, $0\ \mu\text{m}$) are used in Figure 4.6.	71
Figure 4.6. (a) Mode-power evolution of the HE_{11} signal mode (i.e. solid blue), the sum of HE_{21} and TE_{01} signal modes (i.e. dashed blue), LP_{01} signal mode (i.e. solid red) and LP_{11} signal mode (i.e. dashed red). (b) Modal pump depletion of the sum of HE_{21} and TE_{01} pump modes (i.e. solid blue) and LP_{11} pump mode (i.e. solid red) (c) The normalized population inversion along the fiber positions at 3 transverse spatial locations. Green: location A ($0\ \mu\text{m}$, $5\ \mu\text{m}$), red: location B ($0\ \mu\text{m}$, $0\ \mu\text{m}$), and blue: location C ($5\ \mu\text{m}$, $0\ \mu\text{m}$), as shown in Figure 4.7 on page 69. The dashed lines are the simulated normalized population inversions based on the scalar LP model. (d) The integrated normalized population inversion against the fiber length for both the VM and the LP models.	76
Figure 4.7. (a) Modal gain power evolution of the LP_{01}/HE_{11} signal mode (i.e. solid line) and the LP_{11} /"equivalent LP_{11} signal mode" (i.e. dashed line) pumped by LP_{11} /"equivalent LP_{11} " pump mode simulated under LP/vector 2-mode-group EDFA models. (b) The corresponding pump power evolution under 2 different models. (c) The integrated normalized population inversion against the fiber length for both the VM and LP models.	80
Figure 4.8(a) Modal signal power evolution of the LP_{01}/HE_{11} signal mode (i.e. solid line) and the LP_{11} /"equivalent LP_{11} signal mode" (i.e. dashed line) pumped by the LP_{01}/HE_{11} pump mode simulated under LP/vector FM-EDFA models. (b) The pump power evolution under 2 different models.	82
Figure 4.9. A schematic diagram to illustrate the dimensions of an elliptical core with $D = 0.5\%$	85
Figure 4.10 The coupling coefficient of the $LP_{11,ref,s}$ into the two vector modes at different deviations (D). The insets show the mode intensity profiles (MIPs) of the vector modes at various values of D and of the $LP_{11,ref,s}$. The white circles outline 8 mm radius circles.	86
Figure 4.11. Comparison of the modal gain evolutions based on the VM model at various values of D with coherent modes, as shown by the black and red lines. The green lines represent the modal gain evolutions based on the LP model.	87
Figure 4.12. Comparison of modal gain evolutions along the fiber position for the 2-mode-group EDFA simulated using LP modes and LP VMs for $D=0.5\%$ without mode beating.	89
Figure 5.1. Dopant cross-sections for the four-mode-group EDF. (b) RI and doping profiles (i.e. shaded region) of the four-mode-group EDF. Mode intensity profiles of the (c) signal and (d) pump modes, where the shaded regions indicate erbium-doped regions. (e) Intensity pattern of the guided modes.	94
Figure 5.2. Contour plot of the maximum modal gain difference against the variation of R_o and R_i with pump arrangement of (a) $P_{LP01p}:P_{LP41p} = 1:1$, (b) $P_{LP01p}:P_{LP41p} = 6:4$, and (c) $P_{LP01p}:P_{LP41p} = 4:6$. The total pump power was set to 350 mw throughout.	95

List of figures

Figure 5.3. (a) The modal gain and RMS value of the gain difference across the four modes against the variation of total pump power. Signal at 1530 nm power per mode was set to -10 dBm. (b) Modal gain dependence on signal power per mode.	96
Figure 5.4. Modal gains against input pump power for the proposed ring doped 4-mode-group EDFA.	97
Figure 5.5. Experimental setup of the in-house 4-mode-group EDFA.	98
Figure 5.6. The measured RI profiles and simulated mode intensity profiles of (a) the 4-mode-group passive fiber, and (b) the 4-mode-group ring-doped EDF.	100
Figure 5.7. Measured mode-dependent gain as a function of launched pump power for different pump spatial modes (a) LP_{01p} , and (b) LP_{21p} with backward pumping configuration.	101
Figure 5.8. Simulation fitting of the 4-mode-group EDFA using experimental parameters for (a) LP_{01p} dominated case, and (b) the LP_{21p} dominated case.	102
Figure 5.9. A typical cross-section of a DCF with a D-shaped inner cladding. The black solid line indicates the FRIP of the DCF.	105
Figure 5.10. Brightness conversion in a cladding-pumped fiber [97].	106
Figure 5.11. Simulated modal gain as a function of the pump power for (a) cladding-pumped 4-mode-group “batman” EDF, and (b) cladding-pumped 4-mode-group ring-doped EDF.	108
Figure 5.12. Experimental setup of the in-house cladding-pumped 4-mode-group “batman” EDF [100].	109
Figure 5.13. Experimental arrangement of the heterogeneous space-division multiplexing network, where a six parallel single-mode fiber span, a six-core coupled multi-core fiber span, and a six-spatial-mode fiber span (i.e. equivalent to four-mode-group fiber) are connected and integrated. The cladding-pumped 4-mode-group “batman” EDF developed at the ORC was successfully applied in the 59 km few-mode fiber span in this work [101].	110
Figure 5.14. Basic process of a GA, after [106].	112
Figure 5.15. Application of a GA to minimize the DMG in a cladding-pumped 4-mode-group EDFA. (a) Evolution of the fitness value for the best individual for 5 runs of the same GA application. (b) Evolution of the best individual and the average fitness of the total population.	113
Figure 5.16. The fiber RI profile, the signal mode intensity distributions, and the doping profile of (a) 4-mode-group EDFA, denoted as “F1”, and (b) 6-mode-group EDFA, denoted as “F2”, to be optimized through the GA. ρ_i (m^{-3}) is the doping concentration of the i^{th} core layer.	116
Figure 5.17. Modal gain (i.e. solid line), noise figure (i.e. dashed line) and DMG (i.e. red dotted line) characteristics of the best (a) four-mode-group EDFA, and (b) six-mode-group EDFA calculated by the GA.	116
Figure 5.18. Variation of the DMG vs. signal wavelength as the doping concentration of (a) the 1 st , (b) the 2 nd , and (c) the 3 rd core layer is changed for fiber F1. Solid lines represent “+” variations, while dashed lines represent “-” variations.	118
Figure 5.19. Variation of the DMG vs. signal wavelength as the doping concentration of (a) the 1 st , (b) the 2 nd , (c) the 3 rd and (d) the 4 th core layer is changed for the fiber F2. Solid lines represent “+” variations, while dashed lines represent “-” variations.	119
Figure 5.20. Variation of the DMG against signal wavelength as the structural parameter (a) x_1 , and (b) x_2 is changed for the fiber F1. Solid lines represent “+” variations, while dashed lines represent “-” variations.	120
Figure 5.21. Variation of the DMG vs. signal wavelength as the structural parameter (a) a_1 , (b) a_2 , and (c) a_3 is changed for the fiber F2. Solid lines represent a “+” variations, while dashed lines represent “-” variations.	121

List of figures

Figure 6.1. RI of the RC EDFA when it is straight (i.e. black line) and with a bend radius of 5 cm.	126
Figure 6.2. Modal gain evolution against fiber position for LP ₀₁ pump and LP ₄₁ pump in a (a) straight, and (b) bent fiber.	128
Figure 6.3. Modal gain evolution against fiber position for cladding pumping in straight, and bent RC EDFA.	129
Figure 6.4. WDM signal gain spectrum of the cladding-pumped RC EDFA.	130
Figure 6.5. Modes of a SI fiber under the (a) scalar approximation, and (b) full-vector solutions. (c) Large modal effective RI splitting between the vectors modes in an OAM fiber.	133
Figure 6.6. (a) RIP of the air-core fiber overlaid with the normalized signal intensity profile of the OAM states $ L =5, 6, 7$. (b) The effective RI difference (Δn_{eff}) between the vector modes within the same $ L $ family as a function of wavelength, for a radial order of $m=1$	134
Figure 6.7. (a) RIP of the air-core fiber overlaid with the normalized signal intensity profile of the OAM states with $ L =5, 6, 7$. The green shaded areas indicate fully doped cores. (b) WDM performance of the air-core fiber pumped by the fundamental mode LP ₀₁ (i.e. or OAM _(0,1)). ...	136
Figure 6.8. The distribution of DMGs and their corresponding pump OAM _(L, m) , plotted in order of decreasing mode effective index that of the same “m” group, where “m” denotes the radial mode order. The blue numbers (e.g. “1”, “2”) under the mode labels corresponds to the mode number shown in Figure 6.9.	137
Figure 6.9. The waterfall plots of the DMGs (ΔG) against to the 29 pump OAM _(L, m) families (correspond to the pump modes listed in Figure 6.8) and the variation of a_1 . The insert on the upper left hand side corner shows the confined doping structure determined by parameter a_1 in the air core OAM amplifier.	138
Figure 6.10. Schematic diagram showing the RI profile of a double-clad OAM EDFA, and the overlap between the pump light and signal intensity distributions.	139
Figure 6.11. (a) RIP of the air-core fiber with labelled design parameter (a_1). (b) DMG as a function of a_1 for cladding-pumping operation.	140
Figure 6.12. WDM performance of the cladding-pumped OAM amplifier.	141
Figure 6.13. Forward and backward ASEs of the cladding-pumped OAM amplifier.	142
Figure 6.14. Normalized population inversion of the cladding-pumped OAM amplifier.	142
Figure 7.1. Two types of uncoupled Multicore EDFs.	145

Declaration of authorship

I, *Qiongyue Kang*, declare that the thesis entitled *Modelling of Multimode Erbium-doped Fibre Amplifiers for Mode-division Multiplexed Transmission Systems* and the work presented in it are my own. I confirm that:

- this work was done wholly or mainly while in candidature for a research degree at this University;
- where any part of this thesis has previously been submitted for a degree or any other qualification at this University or any other institution, this has been clearly stated;
- where I have consulted the published work of others, it is always clearly attributed;
- where I have quoted from the work of others, the source is always given. With the exception of such quotations, this thesis is entirely my own work;
- I have acknowledged all main sources of help;
- where the thesis is based on work done by myself jointly with others, I have made clear exactly what was done by others and what I have contributed myself;
- parts of this work have been published as Appendix: List of publications.

Signed:

Date: 28/09/2015

Acknowledgements

I am indebted to many members of the Optoelectronics Research Centre for their support. First and foremost I offer my sincerest gratitude to my supervisor, Prof. David Richardson for welcoming me to his group and giving me the opportunity to work in this exciting field, and for his unwavering support. I am grateful to Dr Shaif-ul Alam and Dr Francesco Poletti for their guidance, encouragement and time to discuss my progress and ideas. I greatly appreciate all the valuable advices and numerous discussions received from Dr Eeleong Lim and Dr Yongmin Jung. I am also indebted to Prof Jayanta Sahu for supporting my simulations with state-of-the-art fiber drawing facilities. A warm thanks also goes to Dr Catherine Baskiotis for introducing me the powerful simulation software COMSOL and showing me how to do mode analysis using COMSOL step by step with great patience. I would like to thank Dr Zhihong Li, Dr Simon Teh, Dr Lin Xu, Mr Di Lin and all the group members, for their support and help. I am also thankful for the funding provided by the Engineering and Physical Sciences Research Council (EPSRC).

Finally, I want to thank my dearest son Phillip (born during the 2nd year of my PhD), my husband George and my parents Mrs Zhijun He, Mr Yong Kang for their companion and encouragement all the way through this journey.

Definitions and Abbreviations

ASE	Amplified spontaneous emission
EDFA	Erbium doped fiber amplifier
ESA	Excited state absorption
EPSRC	Engineering and Physical Sciences Research Council
DCF	Double-clad fiber
DMG	Differential modal gain
FL	Fiber length
FMF	Few-mode fiber
FRIP	Fiber refractive index profile
GA	Genetic Algorithm
LP	Linear polarised
LP VM	Linearly polarized vector mode
MCF	Multi-core fibers
MCVD	Modified chemical vapor deposition
MIMO	Multiple-input multiple-output
MFD	Mode field diameter
MMF	Multi-mode fiber

Definitions and Abbreviations

MODEGAP	Multi-mode capacity enhancement with photonic bandgap fibres
ND	Normalized depth
NF	Noise figure
ORC	Optoelectronics research centre
OAM	Orbital angular momentum
RCF	Ring core fiber
RI	Refractive index
RMS	Root mean square
SDM	Space division multiplexing
SI	Step index
SIMS	Secondary ion mass spectrometry
SNR	Signal to noise ratio
TMIE	Transverse-mode intensity evolution
VM	Vector mode
WDM	Wavelength division multiplexing

Chapter 1: Introduction

Most people take the high-speed fiber-optic internet for granted, not knowing the challenges and innovations behind it. Retracing the roots of fiber-optic communications back to 1854, John Tyndall demonstrated to the Royal Society that light could be guided along a curved stream of water [1], proving that light signals can be bent by total internal reflection. In the mid-1960s, the very best bulk optical glasses at the time exhibited an attenuation of $\sim 10^3$ dB/km. The problem was, an attenuation of ~ 20 dB/km or lower is required for practical communications [2]. The task seemed daunting, but by 1970 the scientists at Corning overcame this challenge and created an optical fiber with an attenuation of 17 dB/km [3]. Since then fiber-optic communication systems went on to revolutionize the telecommunications industry and have played a major role in the birth of the information age. Owing to their inherent advantages of higher data-carrying capacity and lower loss over electrical transmission, optical fibers have mostly replaced copper wire networks in the developed world.

1.1 Thesis motivation

The hundreds of millions of kilometres of optical fiber that transport data from one part of our planet to another in the form of light pulses provide the bedrock of the information era in which we live in. Throughout the past three decades, the developments of low-loss transmission fibers, optical amplifiers, wavelength-division multiplexing (WDM) and high-efficiency coding have enabled the capacity per fiber to be increased by one order of magnitude every four years, as shown in Figure 1.1 [4]. One of those breakthroughs was the invention of the single-mode EDFA in 1987 [5], [6]. EDFAs are the by far the most important fiber amplifiers for the purpose of long-range fiber-optic communications centred at $1.55\text{ }\mu\text{m}$ (i.e. the optical communication C- band). These amplifiers can be integrated directly into an optical network, avoiding the need to convert optical signals to electrical signals for amplification and re-launch. In addition, fiber amplifiers based on stimulated Raman scattering [7]–[9] is another key

technology to compensate the transmission loss experienced in long-distance fibers. Raman amplification can be obtained by pumping a nonlinear fiber with a high-power laser that exhibits a frequency about 13.2 THz higher from the signal that needs to be amplified. Due to the tunability of the amplification band by simply changing the pump wavelength, a 100-nm flat spectrum using Raman amplification has been demonstrated [10]. Raman scattering is a non-linear process, and generally provides much lower gain coefficient (e.g. distributed Raman amplification through the standard germanium doped transmission fiber [9]) compared with what rare earth doped amplifier can offer. In this thesis, the linear amplifiers based on EDFs are investigated as an approach to compensate transmission losses, and thus enable long haul communication (>1000km).

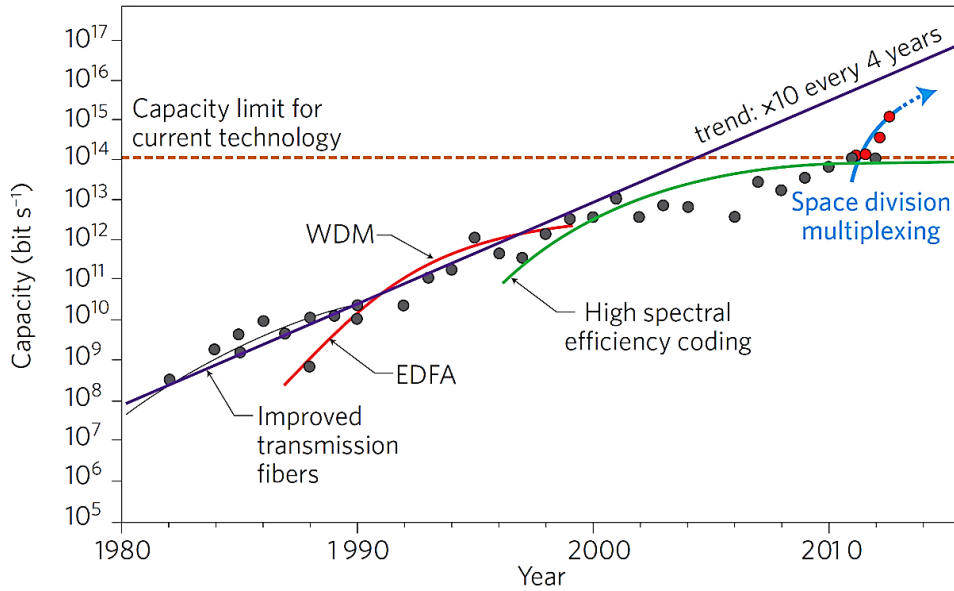


Figure 1.1. The evolution of the data-carry capacity of optical fibres, documented by key experimental demonstrations. Image after Ref. [4].

On one hand, the data traffic in the world's networks today is growing at around 40% year-on-year [11], primarily driven by the bandwidth-hungry applications such as social networking, cloud computing and video streaming. On the other hand, there is a fundamental upper limit of the data-carrying capacity of the single-mode fiber. This limit is imposed by, on one side, the received optical signal-to-noise ratio established by Claude Shannon in 1948 [4], [11]–[13], and

on the other side, the non-linear transmission impairments [14] that makes it impossible to continue increasing spectral efficiency indefinitely by increasing the launched power. The data-carrying capacity limit of a standard single-mode fiber is estimated to be ~ 100 Tbit/s, which corresponds to the spectral bandwidth of the single-mode EDFA (i.e. 11 THz including the C and L amplification bands). Given that we are now within a factor of 2 in the lab and 10 in the field of this theoretical maximum data-carrying capacity of single-mode fiber (i.e. exploiting full usage of amplitude, phase, polarisation and wavelength dimensions), fears are growing of a looming capacity crunch sometime beyond 2020. Radically new fiber technologies are therefore required to avoid such a problem and to allow continued growth of the internet into the future. The only signaling dimension not used in current systems is “space” and most approaches to capacity scaling are focussed on exploiting this fact. Such approaches are generally referred to as space-division multiplexing (SDM) [4]. SDM can be realized through the use of multiple parallel systems based on the existing single-mode, single-core fiber technology or by exploiting the more radical alternatives such as multi-core fibers (MCFs) [15], multi-mode fibers (MMFs) [16] and hybrid SDM fibers (e.g. few-mode multi-core fibers) [17].

Back in late 2010, the ORC succeeded to launch a large-scale research project, MODEGAP (i.e. Multi-mode capacity enhancement with photonic bandgap fibres). It was sponsored by the EU FP7 programme to address the need of overcoming the “capacity crunch” through SDM. This PhD thesis, undertaken within the framework of the MODEGAP project, covers the design and optimization of high-performance in-line multimode erbium-doped fiber amplifiers (MM-EDFAs) for next-generation SDM transmission systems based on mode-division multiplexing (MDM). In such MDM systems, the N orthogonal modes of the multimode are used to define N parallel signalling channels, which provide approximately an N -fold increase in capacity compared with conventional single-mode single-core fiber technology. The MM-EDFA is critical to the commercial viability of MDM, providing the key capability of amplifying all signal modes simultaneously, and thereby providing a higher efficiency and

lower cost per bit compared with the use of N parallel single-mode EDFAs. The differential modal gain (DMG) is a key characteristic of the MM-EDFA. Careful engineering of the MDG in an MM-EDFA is of paramount importance to obtain reliable system operation and to prevent system outages.

The first demonstration of MDM for fiber communication was reported in 1982 [18]. However, soon after the focus shifted to single-mode fiber communication technologies, and the topic of MDM was left alone for nearly 30 years. The very first demonstration of a MM-EDFA was reported as far back as 1991 [19], in which the multiple guided modes were treated as one signal path. Later in 2000, a two-stage MM-EDFA was reported as an optically pre-amplified receiver [20]. In 2007, a theoretical analysis of modal competition in rare-earth doped lasers and amplifiers was reported. In particular, the impact of tailoring the doping profile on the modal gain performance was discussed [21]. Yet only recently, serious attention has been given to building a complete network platform to exploit the MDM approach, owing to the tremendous development of digital signal processing (DSP). In the MMF-based system, although the N guided signal modes are orthogonal to each other, mode coupling is usually unavoidable during propagation due to random perturbations such as fiber non-uniformity, bends and twists. This means the energy of any data symbol within a particular mode will spread out into other modes. Eventually, after long-distance transmission, the signal detected in one particular spatial mode at the receiver may contain information of all the other spatial modes. This is usually mathematically described by a $2N$ by $2N$ coupling matrix, where N is the number of spatial modes, and 2 represents the polarization degeneracy. This crosstalk must be undone in order to recover the independent data streams. The method to do so is called multi-input multi-output (MIMO) digital signal processing [22]. In March 2011, the first MDM transmission experiment (i.e. over 137 km) based on two-mode-group fibers without in-line amplifiers using coherent 6×6 MIMO processing was reported as a post-deadline paper in the conference OFC 2011 by Bell Labs, Alcatel Lucent, US [23]. In the following month of the same year, the first theoretical modelling of a MM-EDFA dedicated to MDM systems with the aim of

gain equalization over two signal mode-groups by tailoring the pump modal profile, was reported by CREOL, University of Central Florida [24]. In September 2011, in the post-deadline session of ECOC 2011, the world's first experimental demonstration of a 2-mode-group EDFA was reported by the ORC under the MODEGAP project [25]. Around the same time, the first 2-mode-group fiber transmission experiment (i.e. over 50 km) with an inline 2-mode-group EDFA was demonstrated by NEC labs, US [26]. Since then, MDM has attracted immense attention from top telecommunication labs both in industry and academia from all over the world. A competitive global race to develop MDM technology effectively began, which was timely since the author started her PhD in the design and modeling of MM-EDFAs for MDM systems. Around the same time, the MCF technology that forms the basis of SDM systems, was being developed around the world as well. Significant progress has been made in this area in pushing up the number of distinguishable spatial channels in a single fiber with a maximum cladding diameter of 230 μm from mechanical considerations [15]. Since MCFs are not covered in this thesis, only a brief review of the MCFs is presented here. For single-mode MFCs, the highest core count reported so far is a 30-core MCF with a heterogeneous core arrangement [27]. For few-mode MCFs, the state-of-the-art is a MCF with 108 spatial channels, realized by 36 cores and 3 mode for each core [28]. The state-of-the-art multicore-EDFA reported to date is a single-mode 19-core EDFA that has been used as an in-line amplifier in a transmission link with a length of over 1200 km [29].

1.2 Research aims

Undertaken within the framework of MODEGAP, this thesis sought to

- (1) Understand the fundamentals of optical modes (i.e. vector and scalar) in fibers.
- (2) Develop a flexible and powerful MM-EDFA simulation tool that is capable of accurate MM-EDFA modeling and fiber design optimization. My own MM-EDFA simulator has been verified by commercial software and experimental measurements. My research work has generated new fiber

amplifier designs that are crucial to MODEGAP and has led to a number of high profile publications (such as ECOC and OFC conference postdeadline papers) and the commercialization of our two and four-mode-group EDFAs.

- (3) Investigate MM-EDFAs of ring-index profile for MDM systems. Unlike conventional step-index fibers, such ring fibers guide ring shaped modes whose intensity profiles can be quite similar to each other and thus potentially it is easier to equalize the modal gains.

Accomplishing these objectives has required interaction and collaboration with the amplifier characterization team and the ORC fiber fabrication team. Their contribution to the work presented in this thesis is explicitly acknowledged where appropriate.

1.3 Outline of the thesis

The outline of this thesis is laid out as follows:

Firstly, Chapter 2 presents the background knowledge of modes in cylindrical optical fibers. The full vectorial solutions, scalar approximations in weakly guiding fibers and the relationship between the vector modes and the so-called LP modes in the weakly guided regime are reviewed accordingly. The 2nd part of chapter 2 reviews the fundamentals of the erbium-doped fiber amplifier. The modeling of MM-EDFAs is covered and a discussion of the numerical resolution of the multimode ASE is included. The typical modelling results of a standard step-index 2-mode-group EDFA using commercial software (Optisystem 11.0®) is presented. Chapter 2 lays the foundation for all the modeling work in the rest of the thesis.

In Chapter 3, the simulation results supported by experimental verification using our existing 2-mode-group EDF are presented and confirm this reliable MM-EDFA amplifier model can be used for further modeling and design work. Next, a systematic design of a 2-mode-group EDFA with the goal of finding a design providing modal gain equalization is presented. Based on the author's findings, a

2-mode-group ring-doped EDFA was made in-house, which has led to the success of several high-profile long-haul 2-mode-group fiber based transmission experiments. In the conclusion of this chapter, the main limitations of this commercial code are discussed.

In Chapter 4, firstly a basic in-house MM-EDFA simulator based on LP modes is presented and verified using the commercial code. Subsequently, a MM-EDFA based on vector modes is developed. Next, a systematic study of the impact of mode beating on the modal gain properties of a 2-mode-group EDFA is given using different signal and pump combinations. Since birefringence tends to exist in fabricated fibers, its theory and impact on 2-mode-group EDFAs is also investigated. Our conclusion from this chapter is that, the LP-mode-based MM-EDFA simulator is valid and reasonably accurate to predict the modal gain properties of weakly guiding MM-EDFAs in a real transmission system, given the full spatial degeneracies of the LP modes are used.

Chapter 5 presents the designs of MM-EDFAs that support four-mode and six-mode groups. Firstly, a core-pumped 4-mode-group EDFA is designed and simulated using a multiple ring doping approach. Then, the modeling of the fabricated 4-mode-group EDFA undertaken using experimental parameters is presented. The discrepancies between the modeling results and measured gains are carefully analysed and addressed after taking into account the fact that the mode mismatch resulting mode crosstalk and mode dependent splice losses between the 4-mode-group passive fiber and 4-mode-group EDF used in the experiment. Next, the simulation of cladding pumping is given representing a cost-effective alternative to core pumping. A double-clad 4-mode-group EDFA made in-house according to the cladding-pumped 4-mode-group EDFA simulations using in-house erbium-doped preforms is shown. Again, the cladding-pumped MM-EDFA simulation model is verified from the feedback of experimental data. In order to inverse design a cladding-pumped EDFA supporting more than four modes, a powerful genetic algorithm is introduced and merged into our MM-EDFA simulator.

Unlike the previous chapters, Chapter 6 presents the modeling results based on special fibers that exhibit a ring-index profile. The first type is a ring-core fiber (RCF) that support LP modes, which can be used for MDM systems with the benefits of reducing MIMO complexity due to their unique modal properties. The second type is a ring-index fiber with an air hole in the center that supports orbital angular momentum (OAM) modes. The OAM modes are also eigenmodes of the fiber and uses different basis sets compared with the vector modes discussed in section 2.1.1 of chapter 2. OAM modes offer another degree of freedom for information multiplexing and due to the large vector-splitting nature of the OAM modes, MIMO-free transmission can be potentially achieved [30], [31]. Section 6.2 presents the modeling of the amplification of such OAM modes and the design optimization of the OAM EDFA.

Finally, the summary and discussion about future research directions are included in Chapter 7.

Chapter 2: Background

In MDM transmission systems, the distinct spatial paths in MMFs are used as independent signal-carrying channels. This chapter briefly reviews the fundamentals of optical modes in fiber. It starts by considering the homogeneous vector wave equations and establishes the exact vector-mode solutions of a step-index fiber. Then, the theory of scalar approximation in weakly guiding fibers with scalar solutions is discussed, with a mention of some vector modes that are nearly degenerate with certain LP mode-groups. Mathematical equations are then established to show how the LP modes can be represented as linear combinations of certain vector modes, as well to review their accuracy in describing real modes. The second part of this chapter reviews the atomic-rate equations used for modelling light amplification in a three-level laser system, followed by an introduction to the gain coefficient and generation of ASE in single-mode EDFA systems. Then, the concept and rate/ propagation equations of MM EDFAs are introduced. The numerical methods used to resolve the rate and propagation equations of the MM EDFA are discussed. Finally, the basic characteristics of a step-index 2-mode-group EDFA are discussed.

2.1 Modes in cylindrical optical fibers

2.1.1 Vector solutions for step-index fibers

An optical fiber is generally a transparent medium made primarily of silica (i.e. pure glass). It is capable of confining light within its core which usually has a higher refractive index (RI) than its cladding, in order to transmit optical information along the waveguide by the mechanism of total internal reflection. The guided light propagates in distinct spatial paths or modes according to the physical characteristics of the optical fiber. This section reviews the fundamental concepts of guided modes in step-index fibers, as shown in Figure 2.1.

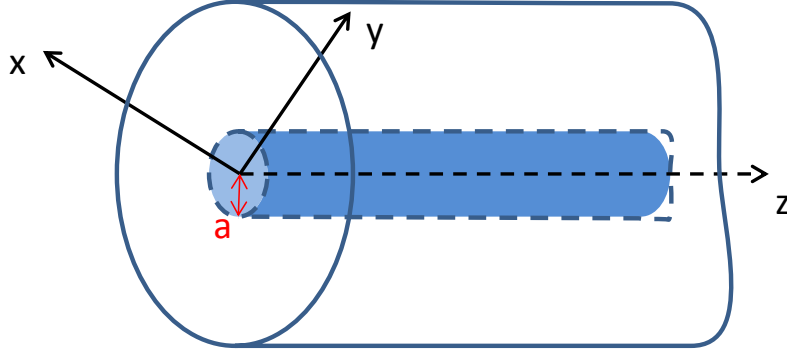


Figure 2.1. A step index fiber with cylindrical symmetry; the central shaded region indicates the fiber core with a radius of “a”.

From the general Maxwell equation, one can obtain the homogeneous vector wave equations in the absence of current (i.e. the current density J is zero) as below:

$$\begin{cases} (\nabla^2 + k^2 n^2)E = -\nabla(E \cdot \nabla \ln n^2) \\ (\nabla^2 + k^2 n^2)H = (\nabla \times H) \times \nabla \ln n^2 \end{cases} \quad 2.1$$

where ∇^2 is the vector Laplacian operator, $k = 2\pi/\lambda$ is the wave vector and n is the RI. For a waveguide that is translation invariant (i.e. n is z -independent), the electric field E and magnetic field H can be expressed in Cartesian form:

$$\begin{aligned} E(x, y, z) &= e(x, y)e^{i\beta z} = (e_t + e_z)e^{i\beta z}, \\ H(x, y, z) &= h(x, y)e^{i\beta z} = (h_t + h_z)e^{i\beta z}, \end{aligned} \quad 2.2$$

The fields e_t are solutions of the reduced wave equation [1]:

$$\nabla_t^2 e_t + (k^2 n^2 - \beta^2)e_t = -\nabla_t(e_t \cdot \nabla_t \ln n^2) \quad 2.3$$

In a step index fiber, where the RI in each layer (i.e. core and cladding) is constant, the fields e_z and h_z within each layer are the solutions of Equation 2.3 [32]:

$$\begin{aligned} \nabla_t^2 e_z + (n^2 k^2 - \beta^2)e_z &= 0 \\ \nabla_t^2 h_z + (n^2 k^2 - \beta^2)h_z &= 0 \end{aligned} \quad 2.4$$

where β is the propagation constant, and

$$\nabla_t = \nabla - \hat{z}(\partial/\partial z) \text{ is the transverse gradient operator} \quad 2.5$$

The remaining field components are determined from e_t using Maxwell's equations. The solutions of Equation 2.3 determines the values of β , which are bound to the range [33]:

$$k^2 n_{cl}^2 \leq \beta^2 \leq k^2 n_{co}^2 \quad 2.6$$

where n_{co} is the RI of the core, and n_{cl} is the RI of the cladding. The effects of any discontinuities in $n(x,y)$ are fully contained in the term $\nabla_t \ln n^2$ from Equation 2.3. Owing to this term's appearance in the vector wave equation, the mode fields are generally hybrid, possessing longitudinal components e_z and h_z , as a result of wave-guiding. The solutions for e_z and h_z must satisfy Equation 2.4 both in the core and the cladding. Due to the circular symmetry of optical fibers, the field e_z and h_z can be expressed in the form:

$$e_z \text{ or } h_z = \psi_l(r) \begin{Bmatrix} \cos l\phi \\ \sin l\phi \end{Bmatrix} \quad 2.7$$

where $l (\geq 0)$ is an integer. By substituting into Equation 2.4 and using $\partial^2 \psi / \partial^2 \phi = -\nu^2 \psi$:

$$\begin{aligned} \frac{d^2 \psi_\ell(r)}{dr^2} + \frac{1}{r} \frac{d\psi_\ell(r)}{dr} + (k^2 n_{co}^2 - \beta^2 - \frac{\nu^2}{r^2}) \psi_\ell(r) &= 0, \\ \frac{d^2 \psi_\ell(r)}{dr^2} + \frac{1}{r} \frac{d\psi_\ell(r)}{dr} - (\beta^2 - k^2 n_{cl}^2 + \frac{\nu^2}{r^2}) \psi_\ell(r) &= 0, \end{aligned} \quad 2.8$$

The solution of the first equation of Equation 2.8 is a linear combination of the first and second kind of Bessel functions $J_l(Ur/a)$ and $Y_l(Ur/a)$, whereas the solution of the second equation of Equation 2.8 is a linear combination of the first and second kind of modified Bessel functions $I_l(Ur/a)$ and $K_l(Ur/a)$ with the following modal parameters:

$$\begin{cases} U = \sqrt{a^2 k^2 (n_{co}^2 - n_{eff}^2)} & \text{in the core,} \\ W = \sqrt{a^2 k^2 (n_{eff}^2 - n_{cl}^2)} & \text{in the cladding,} \\ V = \sqrt{a^2 k^2 (n_{co}^2 - n_{cl}^2)} & \text{normalized frequency,} \end{cases} \quad 2.9$$

where $n_{eff} = \beta/k$ is the effective RI of the guided mode. The eigenvalue equation can be established for a two-layer step-index fiber shown in Figure 2.1 by ensuring the continuity of four field components (i.e. e_z , h_z , e_ϕ and h_ϕ) at $r = a$ [4]:

$$(ln_{eff})^2 \left(\frac{V}{UW} \right)^4 = \left\{ \frac{n_{co}^2 J'_l(U)}{U J_l(U)} + \frac{n_{cl}^2 K'_l(W)}{W K_l(W)} \right\} \times \left\{ \frac{J'_l(U)}{U J_l(U)} + \frac{K'_l(W)}{W K_l(W)} \right\} \quad 2.10$$

Depending on whether $l = 0$ or not, there exists three types of modes, namely TE, TM and Hybrid modes.

For TE and TM modes ($l = 0$), Equation 2.10 reduces to:

$$\left\{ \frac{n_{co}^2 J_1(U)}{U J_0(U)} + \frac{n_{cl}^2 K_1(W)}{W K_0(W)} \right\} \times \left\{ \frac{J_1(U)}{U J_0(U)} + \frac{K_1(W)}{W K_0(W)} \right\} = 0 \quad 2.11$$

Each of the parentheses of Equation 2.11 can be zero. As detailed in the literature [4], the first of the parentheses of Equation 2.11 yields the eigenvalue equation of the Transverse Magnetic (TM) modes:

$$\frac{n_{co}^2 J_1(U)}{U J_0(U)} + \frac{n_{cl}^2 K_1(W)}{W K_0(W)} = 0 \quad 2.12$$

And the second of the parentheses of Equation 2.11 yields the eigenvalue equation of the Transverse Electric (TE) modes:

$$\frac{J_1(U)}{U J_0(U)} + \frac{K_1(W)}{W K_0(W)} = 0 \quad 2.13$$

For given values of V , either Equation 2.12 or Equation 2.13 gives a sequence of increasing eigenvalues (i.g. $U_{01} < U_{02} < \dots < U_{0m}$) that are associated with the

modes $TM_{01}, TM_{02}, \dots TM_{0m}$ in the case of Equation 2.12, and $TE_{01}, TE_{02}, \dots TE_{0m}$ in the case of Equation 2.13.

This type of mode can only exist in a very specific class of waveguides, which is y- and z- invariant planar waveguides and optical fibers with circular symmetry. These are the only two cases where $e_z = h_z = 0$ can occur, otherwise it is generally hybrid modes that are guided.

For hybrid modes, HE and EH ($l \neq 0$), Equation 2.10 can be written in a quadratic form that leads to two families of solutions.

Assuming $x = \frac{J'_l(U)}{U J_l(U)}$, $c = (l n_{eff})^2 \left(\frac{V}{UW}\right)^4$, and $b = \frac{K'_l(W)}{W K_l(W)}$, Equation 2.10 can be expressed as:

$$n_{co}^2 x^2 + x b (n_{co}^2 + n_{cl}^2) + (n_{cl}^2 b^2 - c) = 0 \quad 2.14$$

The solutions of Equation 2.14 can be written in the form of:

$$x = -b \left(1 - \frac{1}{2} \left(1 - \frac{n_{cl}^2}{n_{co}^2}\right)\right) \pm \sqrt{\frac{1}{4} b^2 \left(1 - \frac{n_{cl}^2}{n_{co}^2}\right)^2 + \frac{c}{n_{co}^2}} \quad 2.15$$

where each sign (\pm) corresponds to a different solution, leading to two different families of modes. According to literature [3], the sign “-” is associated with HE modes and the sign “+” is associated with EH modes. For given values of V and l , Equation 2.15 gives a sequence of increasing eigenvalues $U_{l1} < U_{l2} < \dots < U_{lm}$ that are associated to the modes $HE_{l1}, HE_{l2}, \dots HE_{lm}$ in the case of sign “-”, and to the modes $EH_{l1}, EH_{l2}, \dots EH_{lm}$ in the case of sign “+”.

The vector modes are eigen-solutions of the optical fiber/waveguide. The vector modes from the same optical fiber/waveguide should satisfy the orthogonality relation:

$$\int_{A^\infty} e_j \times h_k^* \cdot \vec{z} dA = \int_{A^\infty} e_k^* \times h_j \cdot \vec{z} dA = 0 \quad \text{with } j \neq k. \quad 2.16$$

where e_j and h_k are the electrical field and magnetic field of the j^{th} and k^{th} modes

respectively. These relations imply that the modes propagating in an ideal optical fiber (i.e. translation invariant) do not exchange energy. However, in practice, in step-index fibers, mode coupling is unlikely to be avoided during propagations due to fiber imperfections and perturbations like bends.

2.1.2 Linearly polarized modes for weakly guiding step-index fibers

The weakly guided approximation considerably simplifies the problem, and in most cases it is sufficiently accurate to describe the fields in optical fibers for telecommunication applications. “Weak guidance” is obtained when the RI contrast between the core and cladding is adequately small (i.e. $\Delta = \frac{n_{co} - n_{cl}}{n_{cl}} \ll 1$), which allows the term $\nabla_t \ln n^2$ to be neglected in Equation 2.3. This leads to a scalar wave equation, and gives rise to the theory of linearly polarized (LP) modes [34]–[36]. In this case, the LP mode becomes a quasi-transverse electromagnetic (TEM) wave with negligible longitudinal components (i.e. $e_z \approx 0$, $e_z \approx 0$). Due to the circular symmetry of the optical fibers, the transverse field components have the following separate form:

$$e_x \text{ or } e_y = \psi(r) \begin{cases} \cos \ell \phi \\ \sin \ell \phi \end{cases}, \quad 2.17$$

where l is an integer that represents the modal azimuthal number. The cosine and sine solutions refer to the even and odd modes respectively. With the term $\nabla_t \ln n^2$ being ignored, the scalar wave equation can be expressed as [2]:

$$\frac{d^2 \psi_\ell(r)}{dr^2} + \frac{1}{r} \frac{d\psi_\ell(r)}{dr} + (k^2 n^2 - \beta^2 - \frac{\ell^2}{r^2}) \psi_\ell(r) = 0, \quad 2.18$$

where the solutions of Equation 2.17 determine the propagation constant β of the scalar LP_{lm} family of modes. In Equation 2.17, the fields must satisfy the condition that $\psi(r)$ and its derivative are continuous at each interface. Based on that, the scalar wave Equation 2.17 is the differential equation of Bessel functions J_l and Y_l or modified Bessel functions I_l and K_l , depending on the sign of the term $k^2 n^2 - \beta^2$.

The eigenvalue equation can be established for a two-layer step-index fiber shown in Figure 2. by ensuring the continuity of $\psi_l(r)$ and $d\psi_l(r)/dr$ at $r = a$:

$$U \frac{J_{\ell+1}(U)}{J_{\ell}(U)} = W \frac{K_{\ell+1}(W)}{K_{\ell}(W)} \quad 2.19$$

where the modal parameters are defined in Equation 2.9. For given values of V and l , Equation 2.18 gives a series of discrete roots labelled U_{lm} , where m is the number (i.e. 1, 2, 3 ... m) of the roots, which represents the radial mode order. A summary of the lowest order members of the LP mode family is shown in Figure 2.2 below:

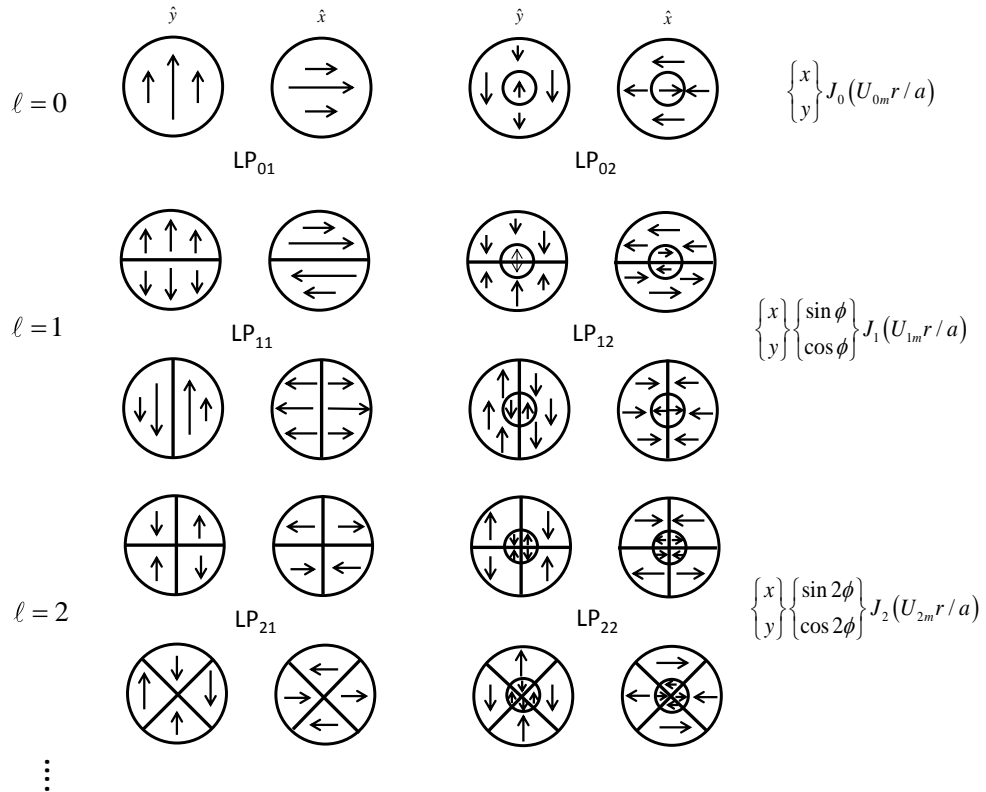
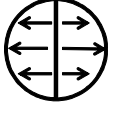
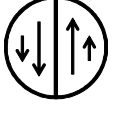

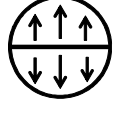


Figure 2.2. x and y polarizations of the electric fields for the first two modes of the series $l = 0, 1, 2$. The outer circles represent the core-cladding interface of the optical fiber with a radius of a . The inner circles indicate the zero of the functions. The lines crossing the center of the fiber core represent the zeros of $\cos(l\phi)$ or $\sin(l\phi)$ [37].

In the weakly guided regime, a group of vector modes has similar propagation constants that approach β of the corresponding LP mode-group. Under this

scenario, the vector modes become nearly degenerate, and are referred to as degenerate vector modes. In this case, the LP modes can be described as linear combinations of degenerate vector modes. The simplified mathematical relationship between the two lowest LP mode groups and the corresponding vector modes are listed below:

Table 2.1. The mathematical relationship between the LP modes and the vector modes for the LP_{01} and LP_{11} mode groups [38]. Here “a” and “b” are used to represent the orientation of the intensity pattern of the LP_{11} mode.

Mode group	Vector modes	LP modes
$l = 0, m = 1$	HE_{11}	LP_{01}
$l = 1, m = 1$	$HE_{21,even} + TM_{01}$	 $LP_{11a,x}$
	$HE_{21,even} - TM_{01}$	 $LP_{11a,y}$
	$HE_{21,odd} + TE_{01}$	 $LP_{11b,x}$
	$HE_{21,odd} - TE_{01}$	 $LP_{11b,y}$

In the weakly guided regime, when a linearly polarized electric field is incident on an optical fiber, only combinations of the LP modes that have the same polarization are excited. It is true that the scalar LP modes of an optical fiber are not real. These are merely mathematical solutions to the scalar wave equation.

However, since the linear combinations of vector modes are generally excited, the equivalent LP modes are a convenient shorthand that accurately describes the fields at the output of the fiber.

The concept of MDM transmission systems considers that each distinct mode is treated as an independent signal-carrying channel. Therefore, in principle the data capacity that a single fiber can support scales with the number of modes propagating in the fiber. To date, in the majority of reported cases [16-24, 26], the MDM transmission fibers and MM EDFA are all weakly guiding, and thus the LP modes approximation has been adopted in these papers.

2.1.3 Mode solver using COMSOL Multiphysics 4.3®

In this thesis, the electric and magnetic field components of the optical modes in fiber are obtained through the built-in mode solver of the commercial package COMSOL Multiphysics 4.3® [39], which is a general finite-element modeling tool. COMSOL Multiphysics 4.3® can be linked with the general computing software MATLAB [39] through the use of a scripting language. Consequently, the user can program in the MATLAB environment, and then call COMSOL to solve the physical modeling problems. Finally, the numerical solutions given by COMSOL are extracted and processed in MATLAB. In this way, simulation is flexible and powerful. The COMSOL mode-solver program that the author used to generate results in this thesis was originally developed and verified by Dr Catherine Baskiotis, a former research member in the Optoelectronics Research Centre. The eigen-solutions (i.e. modal effective indices and electric/magnetic fields) of the user-defined optical fiber/waveguide obtained from COMSOL are vector solutions. For weakly guiding fibers, the vector modes obtained from COMSOL are then processed in MATLAB to produce intensity modes (i.e. LP modes), according to the formulas in Table 2.1 [37], for the scalar-model EDFA simulations. In addition, as modal effective indices and modal profiles can be attained from COMSOL directly, other basic modal properties such as high-order mode cut-off wavelength, modal dispersion and modal effective-area [40] can be acquired through simple post-processing in MATLAB.

2.2 Erbium-doped fiber amplifier

For long-haul transmission systems, mainly the C (i.e. 1530–1565 nm) and L (i.e. 1565–1625 nm) bands are used because of the low loss of silica fibers (i.e. ~ 0.2 dB/km) in those wavelength bands [41]. Although the loss is small, for a 100 km span, the accumulated attenuation of the optical signal is 20 dB. Without amplification, only 1% of the transmitted signal would be detected at the receiver side. For 200 km, this would be 0.01% and so on. Therefore, the development of loss compensation techniques is essential to enable long-haul transmission. Until the late 80's, the only known method to overcome such loss was optoelectronic regeneration of the transmitted signal. This requires the optical signal carried at each wavelength to be detected and processed separately in the electrical domain, and subsequently converted back into optical domain. Clearly, this optoelectronic regeneration process is expensive and inefficient at overcoming fiber attenuation.

The invention of the single-mode EDFA in 1987 [42] brought about the capability of amplifying the attenuated signals of all wavelengths simultaneously in the optical domain. This provided new life to the optical-communications transmission window centred at 1.55 μm . Technologies that allow high bit-rate transmission over long distances also emerged. Similarly, to enable MDM in MMFs over long haul systems, inline EDFAs based on MMFs are required. This section reviews the fundamentals of modeling light amplification in single-mode EDFs [43], followed by the introduction into the multimode EDFA, which is the main topic of my thesis.

2.2.1 Atomic-rate equations for three-level laser system

Firstly, let's look at a three-level laser system with the energy levels shown in Figure 2.3. By definition, level 1 is the ground level, level 2 is the metastable level characterized by a relatively long fluorescence lifetime (τ), and level 3 is the pump level. The pumping rate from level 1 to 3 is R_{13} and the stimulated emission rate from level 3 to 1 is R_{31} . The spontaneous emission produces radiative decay

(i.e. $A_{32}^R + A_{31}^R$) and non-radiative decay (i.e. A_{32}^{NR}), with the latter assumed to be dominant. The stimulated absorption and emission rates between levels 1 and 2 are W_{12} and W_{21} respectively. The spontaneous emission from level 2 produces radiative (i.e. $A_{21}^R = 1/\tau$) and non-radiative decay (i.e. A_{21}^{NR}). For erbium-doped silica fibers, the former dominates.

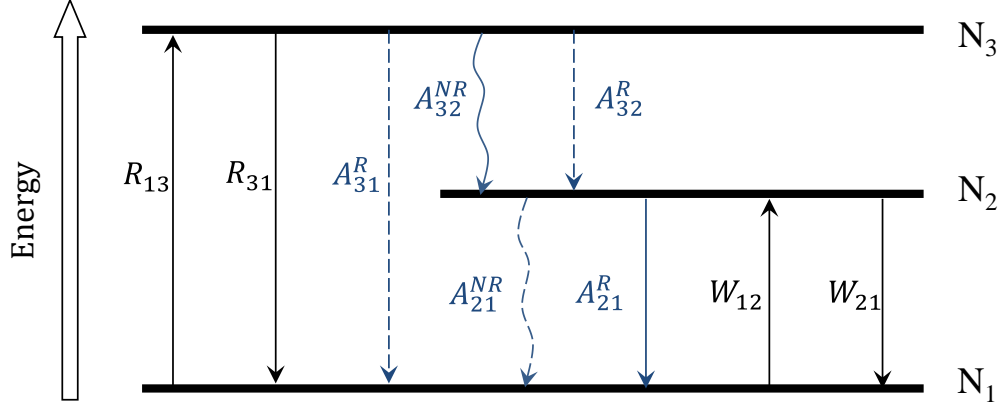


Figure 2.3. Energy level diagram corresponding to a basic three-level laser system, where the laser transition occurs between levels 1 (i.e. ground) and 2 (i.e. metastable). The symbols R , W , and A correspond to pumping rates, stimulated emission rates and spontaneous decay rates between related levels. Superscripts R and NR refer to radiative and non-radiative decays respectively.

The atomic rate equations based on the three-level laser system are:

$$\frac{dN_1}{dt} = -R_{13}N_1 + R_{31}N_3 - W_{12}N_1 + W_{21}N_2 + A_{21}N_2 \quad 2.20$$

$$\frac{dN_2}{dt} = W_{12}N_1 - W_{21}N_2 - A_{21}N_2 + A_{32}N_3 \quad 2.21$$

$$\frac{dN_3}{dt} = R_{13}N_1 - R_{31}N_3 - A_{32}N_3 \quad 2.22$$

where N_1 , N_2 and N_3 are the population densities of energy levels 1, 2 and 3 respectively. The erbium-doping concentration N_t satisfies the equation $N_t = N_1 + N_2 + N_3$. In the steady state, where the populations are time invariant, $dN_i/dt = 0$ ($i = 1, 2, 3$). Equations 2.20, 2.21 and 2.22 can be grouped by:

$$N_1 = N_t \frac{(1 + W_{21}\tau)(1 + \frac{R_{13}}{A_{32}})}{(1 + W_{21}\tau)(1 + \frac{R_{13} + R_{31}}{A_{32}}) + R_{13}\tau + W_{12}\tau(1 + \frac{R_{31}}{A_{32}})} \quad 2.23$$

$$N_2 = N_t \frac{R_{13}\tau + W_{12}\tau(1 + \frac{R_{13}}{A_{32}})}{(1 + W_{21}\tau)(1 + \frac{R_{13} + R_{31}}{A_{32}}) + R_{13}\tau + W_{12}\tau(1 + \frac{R_{31}}{A_{32}})} \quad 2.24$$

Now, we assume that the non-radiative decay rate of A_{32} dominates over the pumping rates $R_{13,31}$, and thus Equations 2.23 and 2.24 yield:

$$N_1 = N_t \frac{1 + W_{21}\tau}{1 + R\tau + W_{12}\tau + W_{21}\tau} \quad 2.25$$

$$N_2 = N_t \frac{R\tau + W_{12}\tau}{1 + R\tau + W_{12}\tau + W_{21}\tau} \quad 2.26$$

where $R = R_{13}$. With the above results, it is easy to find that N_3 is negligible due to the dominant non-radiative decay (A_{32}) towards the metastable level 2. The steady-state populations given by Equations 2.25 and 2.26 are central to the calculation of the gain coefficient in erbium-doped fibers, as all assumptions made for the three-level laser system described in section 2.2.1 fully apply to the cases involving erbium ions in silica glass.

2.2.2 Gain coefficient and amplified spontaneous emission in single-mode erbium-doped fiber amplifiers

The three-level energy system described in section 2.2.1 is a simplified representation of the erbium-glass system. In reality, the charge distribution in the glass host generates a permanent electric field, called a crystal or ligand field. A ligand field induces a Stark Effect, which results in the splitting of the energy levels. The Stark Effect makes the energy levels 1, 2 and 3 shown in Figure 2.4 become manifolds that consist of many sublevels. Figure 2.4 shows the three-level energy diagram of the erbium ions in silica glass that consists of the ground state (i.e. $^4I_{15/2}$) and two upper states (i.e. $^4I_{13/2}$ and $^4I_{11/2}$). Pumping at 980 nm

and 1480 nm is widely favoured as it avoids the excited state absorption (ESA) of the pump energy, where the erbium ions are excited to a fourth energy level by absorption of a pump or a signal photon from the metastable level 2 (i.e. $^4I_{13/2}$). Most of the time, ESA is an unwanted feature, as it can reduce the population density N_2 thus bring down the amplification efficiency. ESA is not strong in state of the art EDF and a detailed the analysis of ESA is beyond the scope of this thesis. In addition, the concentration related Er transitions (e.g. up conversion) is also ignored in the modelling of EDFAs in this thesis.

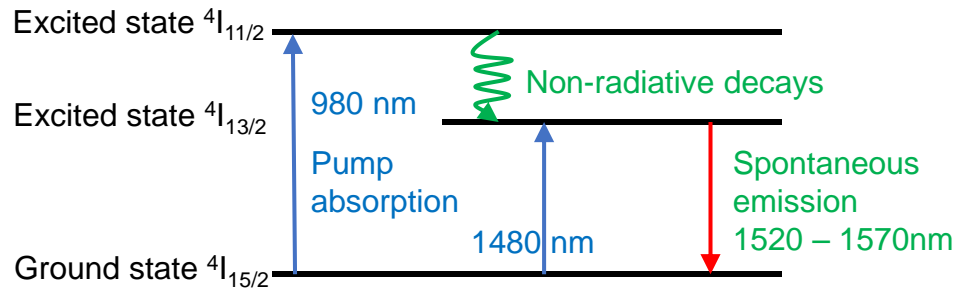


Figure 2.4. Three-level energy diagram of erbium ions in silica glass.

The steady-state population expressions for the three-level Stark split amplifier system which correspond to erbium silica glass are identical to Equations 2.24 and 2.25 shown in section 2.2.1, regardless of whether it is pumped at 980 nm or 1480 nm. But N_1 and N_2 are now called the total population densities of each manifold corresponding to ground state (i.e. $^4I_{15/2}$) and the metastable state (i.e. $^4I_{13/2}$). The coefficients of R and $W_{12, 21}$ are the overall pumping and stimulated emission rates. When pumping at 1480 nm, erbium ions are directly excited to the upper sub-levels of the $^4I_{13/2}$ metastable manifold. When pumped at 980 nm, erbium ions are excited to the upper energy level $^4I_{11/2}$ first, before quickly relaxing down non-radiatively to the metastable level, due to the short lifetime (i.e. 5-10 μ s) of the $^4I_{11/2}$ level. The lifetime of the metastable level $^4I_{13/2}$ is about 10 ms. As mentioned in section 2.2.1, the N_3 of level $^4I_{9/2}$ is negligible with regard to its effect on the average gain [44]. Therefore, the energy transition scheme can be simplified to a two-level system.

When a light signal with an intensity of I_s (i.e. power per area) at a wavelength of λ_s traverses an active medium by a distance of dz and population densities of N_1 (i.e. ground state) and N_2 (i.e. metastable state), the intensity change is given by [45]:

$$dI_s = (\sigma_e(\lambda_s)N_2 - \sigma_a(\lambda_s)N_1)I_s dz \quad 2.27$$

where $\sigma_a(\lambda_s)$ and $\sigma_e(\lambda_s)$ are the absorption and emission cross-sections respectively of the laser transition wavelength of λ_s . Figure 2.5 shows the absorption and emission cross-section profile of erbium ions in $\text{Al}_2\text{O}_3\text{-SiO}_2$ glass [46]. Equation 2.27 can be rewritten as:

$$\frac{dI_s}{dz} = \sigma_a(\lambda_s)(\eta(\lambda_s)N_2 - N_1)I_s \quad 2.28$$

where $\eta(\lambda_s) = \sigma_e(\lambda_s)/\sigma_a(\lambda_s)$ is the cross-section ratio. This parameter is of central importance in the modelling of erbium-doped fiber amplifiers. In Equation 2.28, the term $g = \sigma_a(\lambda_s)(\eta(\lambda_s)(N_2 - N_1))$ represents the signal-gain coefficient, which reflects the dependence of the gain coefficient on wavelength and relative medium inversion. Figure 2.6 plots the gain coefficient around the 1.5 μm laser transition of an erbium-doped fiber (i.e. assuming a concentration of $N_t = 1 \times 10^{25} \text{ m}^{-3}$) for different values of the population inversion N_2 . When $N_2 = 0\%$, all erbium ions are in the ground state and the gain coefficient is negative. Therefore, the medium is absorbing at all signal wavelengths. As N_2 increases, the longer wavelength region (i.e. L-band of 1565-1625 nm) will start to see positive gain coefficients prior to the short wavelength region (i.e. C-band of 1530-1565 nm). The medium becomes transparent only when a threshold N_2 is achieved, depending on the operating wavelength. When N_2 reaches 100% that represents full population inversion, the whole spectral range shown in Figure 2.6 will show positive gain coefficients.

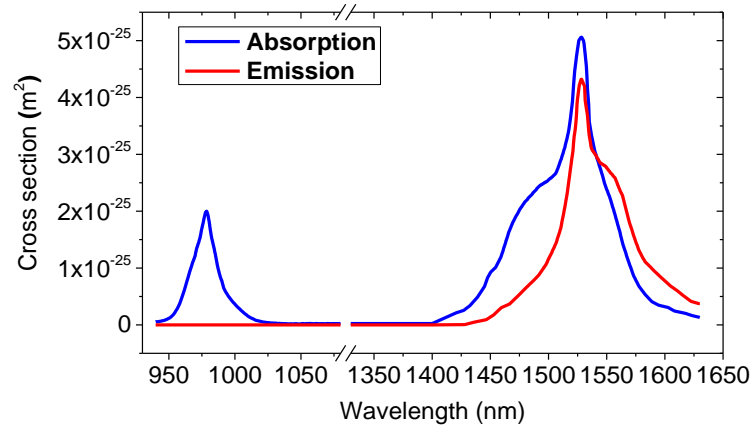


Figure 2.5. Absorption and emission cross-sections of erbium-doped $\text{Al}_2\text{O}_3\text{-SiO}_2$ glass.

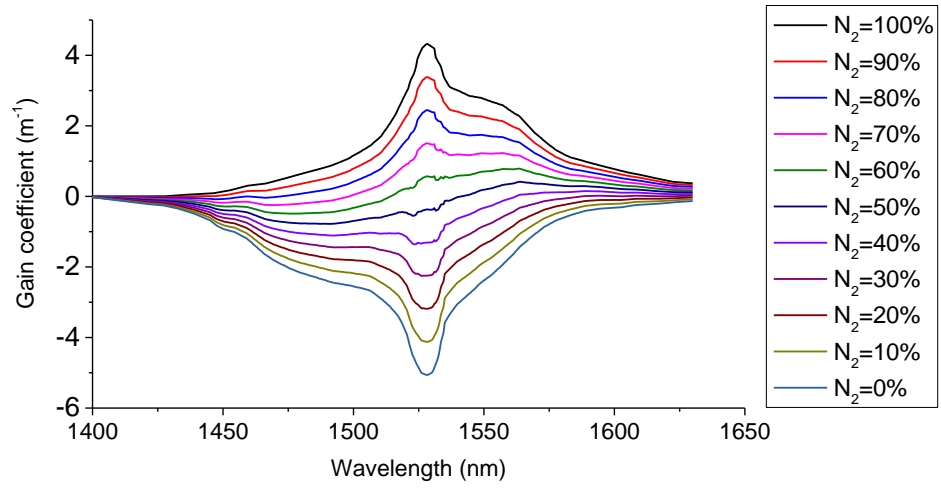


Figure 2.6. Signal-gain coefficient as a function of wavelength for different population inversion based on cross-section data [46].

The population inversion and gain coefficient also vary with the fiber longitudinal coordinate z , as the pump energy is absorbed along the optical fiber. The signal and pump power propagation equations must be expressed based on Equation 2.28, enabling the power evolution of the signal and pump along the amplifier length to be calculated. The single-mode EDFA is taken as an example. An optical signal travels in the fundamental mode of the fiber, with an intensity distribution of $I_s(r, \theta)$ in the fiber's transverse plane given by:

$$I_s(r, \theta) = P_s \cdot i_s(r, \theta) \quad 2.29$$

where $i_s(r, \theta)$ is the normalized intensity profile of the fundamental signal mode and P_s is the signal power residing in the mode. From Equation 2.29, we are able to rewrite Equation 2.28 as:

$$\frac{dP_s}{dz} = \sigma_a(\lambda_s)P_s \int_S \sigma_a(\lambda_s)(\eta(\lambda_s)N_2 - N_1)i_s(r, \theta)rdrd\theta \quad 2.30$$

where $i_s(r, \theta) = I_s(r, \theta)/(\iint I_s(r, \theta)rdrd\theta)$. Similarly, the pump power propagation equation can be written as:

$$\frac{dP_p}{dz} = -\sigma_a(\lambda_p)P_p 2\pi \int_S N_1 i_p(r, \theta)rdrd\theta \quad 2.31$$

where P_p is the power of the fundamental pump mode, and $i_p(r, \theta)$ is the normalized pump-mode profile. The emission cross-section of an EDF at 980 nm pump wavelength is nearly zero, so $\sigma_e(\lambda_p)$ can be neglected in deriving Equation 2.31. It is noteworthy that Equation 2.31 shows the case where the pump co-propagates with the signal. To include the case for a counter-propagation pump, Equation 2.31 must be modified to:

$$\frac{dP_p}{dz} = -u_k \sigma_a(\lambda_p)P_p 2\pi \int_S N_1 i_p(r, \theta)rdrd\theta \quad 2.32$$

where $u_k = 1$ or -1 denotes forward or backward pump direction.

From Equation 2.27 to 2.32, a major assumption was made for the pump and signal powers, which is homogeneous broadening. This means the spectral shape of the transition cross-section of all involved ions in the glass host are identical, which indicates that the energy level splitting (i.e. Stark Effect) for each erbium ion is identical. In reality, that is not the case as the crystal field associated with each site in the glass host is random. Also, the site coordination by neighboring atoms in the host (e.g. co-dopants) can randomly vary from one erbium ion to

another. These effects lead to inhomogeneous broadening [47], [48]. The detailed analysis of the gain coefficient under inhomogeneous broadening is beyond the scope of this thesis. Using the conclusion from chapter 1, book “Erbium doped fiber amplifiers: Principles and Applications” [43], after comparing a large number of experimental results and simulations, it can be assumed that the homogeneous approximation is accurate enough to model EDFAs in the saturation regime. Hence, the homogeneous broadening approximation is used for modeling of EDFA throughout this thesis.

The generation of noise in a linear optical amplifier comes from the spontaneous emission of the erbium ions in the excited energy state. In the case of EDFAs, the erbium ions in the metastable level have a finite lifetime (i.e. 10 ms). Some of the ions spontaneously return to the ground state, thus emitting a photon. The spontaneous decay process accompanies when the stimulated emission process. As opposed to stimulated emission, this photon has no coherent characteristics with respect to the incoming light signal. Furthermore, once generated, spontaneous emission can also be amplified as it propagates along the amplifier. Therefore, at the output end the collection of such spontaneously generated photons form a background noise adding to the light signal. This noise is known as amplified spontaneous emission (ASE). The first principles analysis of the generation of spontaneous emission in doped fibers can be found in [43]. The rate equation of spontaneous emission power within a noise bandwidth of $\Delta\nu$ is given by:

$$\frac{dP_{ASE}}{dz} = 2P_0\sigma_e(\nu) \int_S N_2(r, \theta) i_s(r, \theta) r dr d\theta \quad 2.33$$

where $P_0 = h\nu\Delta\nu$ is the power of one photon from spontaneous noise with bandwidth $\Delta\nu$, and $i_s(r, \theta)$ is the normalized noise mode profile, which is identical to the signal mode profile in the single-mode EDFA. The factor of 2 reflects the fact that spontaneous emission takes place in both polarization modes of the fiber. By combining Equation 2.30 and 2.33 we can obtain the evolution of the total signal power at a wavelength of λ_s and a bandwidth of $\Delta\nu$:

$$\frac{dP_s(\lambda_s)}{dz} = \sigma_a(\lambda_s) \int_S (\eta(\lambda_s) N_2 (P_s(\lambda_s) + 2P_0) - N_1 P_s(\lambda_s)) i_s r dr d\theta \quad 2.34$$

Equation 2.34 describes the phenomena of signal and as well as spontaneous noise amplification. In reality, ASE travels towards both ends of the fiber amplifier, namely forward ASE and backward ASE. The numerical solutions of both forward ASE and backward ASE will be discussed in section 2.2.3.

Equations 2.32 to 2.34 for pump, signal and ASE are functions of atomic populations (i.e. N_1 and N_2), which need to be written in terms of pump, signal intensity distributions and the associated saturation powers. The saturation power is the input signal power which in the steady state leads to a 3 dB gain reduction [43].

The emission rate of W_{21} in Equation 2.24 at a fiber position of z and transverse coordinates (r, θ) is proportional to the signal intensity of $I_s(r, \theta, z)$ and is given by:

$$W_{21}(r, \theta, z)\tau = \frac{\sigma_e(\nu_s)\tau}{h\nu_s} I_s(r, \theta, z) \quad 2.35$$

where $\sigma_e(\nu_s)$ is the emission cross-section at the signal wavelength. The absorption rate of W_{12} in Equation 2.24 is given by:

$$W_{12}(r, \theta, z)\tau = \frac{\sigma_a(\nu_s)\tau}{h\nu_s} I_s(r, \theta, z) \quad 2.36$$

Similarly, the pumping rate of R in Equation 2.24 is given by:

$$R(r, \theta, z)\tau = \frac{\sigma_a(\nu_p)\tau}{h\nu_s} I_p(r, \theta, z) \quad 2.37$$

where $\sigma_a(\nu_p)$ is the absorption cross-section at the pump wavelength, and $I_p(r, \theta, z)$ is the local pump intensity. The saturation intensity for a laser system can be written as [43]:

$$I_{sat}(v) = \frac{h\nu}{(\sigma_a(v) + \sigma_e(v))\tau} \quad 2.38$$

Therefore, the corresponding saturation power at a signal frequency of ν_s is:

$$P_{sat}(\nu_s) = \int_s \frac{h\nu}{(\sigma_a(v) + \sigma_e(v))\tau} dS \quad 2.39$$

With these definitions, the pumping, absorption and emission rates from Equations 2.35 to 2.3 can be written as:

$$W_{12}\tau = \frac{\sigma_a(\nu_s)}{\sigma_a(\nu_s) + \sigma_e(\nu_s)} \frac{I_s(z)}{I_{sat}(\nu_s)} \quad 2.40$$

$$W_{21}\tau = \frac{\sigma_e(\nu_s)}{\sigma_a(\nu_s) + \sigma_e(\nu_s)} \frac{I_s(z)}{I_{sat}(\nu_s)} \quad 2.41$$

$$R\tau = \frac{I_p(z)}{I_{sat}(\nu_p)} \quad 2.42$$

Using Equations 2.40 to 2.42, the steady-state populations of $N_{1,2}$ from Equations 2.23 and 2.24 can be expressed as:

$$N_1(r, \theta, z) = N_t \frac{1 + \frac{\sigma_e(\nu_s)}{\sigma_a(\nu_s) + \sigma_e(\nu_s)} \frac{I_s(z)}{I_{sat}(\nu_s)}}{1 + \frac{I_p(z)}{I_{sat}(\nu_p)} + \frac{I_s(z)}{I_{sat}(\nu_s)}} \quad 2.43$$

$$N_2(r, \theta, z) = N_t \frac{\frac{I_p(z)}{I_{sat}(\nu_p)} + \frac{\sigma_a(\nu_s)}{\sigma_a(\nu_s) + \sigma_e(\nu_s)} \frac{I_s(z)}{I_{sat}(\nu_s)}}{1 + \frac{I_p(z)}{I_{sat}(\nu_p)} + \frac{I_s(z)}{I_{sat}(\nu_s)}} \quad 2.44$$

Equations 2.43 and 2.44 only concern one pump mode and one signal mode, which is the most basic amplifier model. In “ M -wavelengths division multiplexed” and “ N -modes division multiplexed” systems, not only are multiple wavelength channels used, but also all the guided modes are used as independent signaling

channels at each signal wavelength. This implies $M \times N$ signals need to be amplified simultaneously in an N -mode EDFA. The derivation of the rate equations for a multimode EDFA is discussed in the following section.

2.2.3 Modelling of multimode erbium-doped fiber amplifier

The schematic diagram of the simulation model is shown in Figure 2.7. For the co-propagating pump scheme, N single-mode pump sources are converted into the required high-order modes and spatially combined with the signal, before being injected into the MM EDFA. The counter-propagating pump scheme is configured in a similar fashion, allowing both directions of pump propagation to be accounted for in the simulation. In the MM-EDFA model, the assumptions made are identical to the quasi-two level single-mode EDFA system described in the previous sections. The MMF discussed in this section is weakly guiding and the modes are well approximated by LP modes. For the remainder of this thesis, the notation LP_{ijs} and LP_{ijp} will be used to denote the LP_{ij} modes at the signal wavelength (i.e. within the C-band) and the pump wavelength (i.e. 980 nm) respectively.

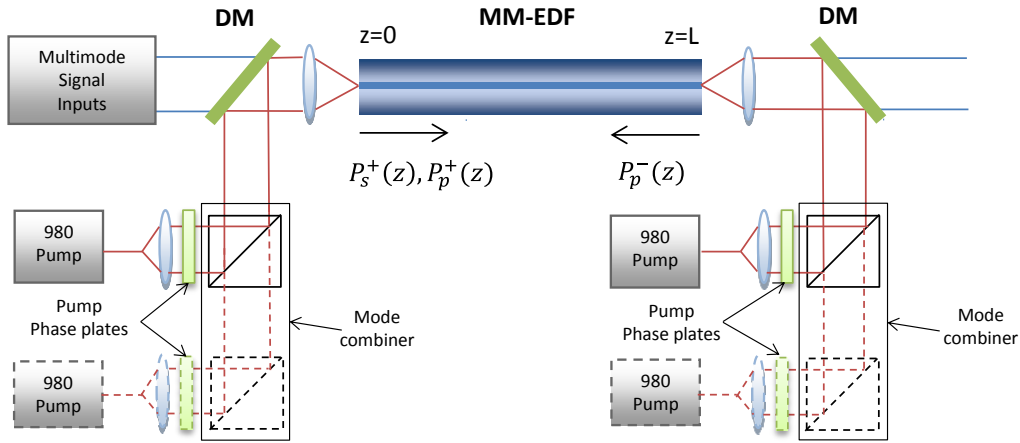


Figure 2.7. Schematic diagram of an MM EDFA. DM: Dichroic mirror ($R = 980$ nm, $T = 1535$ - 1565 nm).

In an “ M -wavelengths division multiplexed” and “ N -modes division multiplexed” system, the $M \times N$ signals and $M \times N$ noises all contribute to the steady-state population inversion. To include the effects of multiple signals and multiple pumps, Equations 2.43 and 2.44 need to be modified to:

$$N_1(r, \theta, z) = N_t \frac{1 + \sum_k \frac{\sigma_e(v_{s,k})}{\sigma_a(v_{s,k}) + \sigma_e(v_{s,k})} \frac{I_{s,k}(z)}{I_{sat}(v_{s,k})}}{1 + \sum_k \frac{I_{p,k}(z)}{I_{sat}(v_{p,k})} i_p(r, \theta) + \sum_k \frac{I_{s,k}(z)}{I_{sat}(v_{s,k})}} \quad 2.45$$

$$N_2(r, \theta, z) = N_t \frac{\sum_k \frac{I_{p,k}(z)}{I_{sat}(v_{p,k})} + \sum_k \frac{\sigma_a(v_{s,k})}{\sigma_a(v_{s,k}) + \sigma_e(v_{s,k})} \frac{I_{s,k}(z)}{I_{sat}(v_{s,k})}}{1 + \sum_k \frac{I_{p,k}(z)}{I_{sat}(v_{p,k})} + \sum_k \frac{I_{s,k}(z)}{I_{sat}(v_{s,k})}} \quad 2.46$$

where k denotes a combination of beam propagation direction (i.e. +, -), λ the wavelength of light, and (l, m) the transverse mode order and its orientation (i.e. even, odd). σ_{ak} and σ_{ek} are the absorption and emission cross-sections of the k^{th} beam. $P_k(z)$ is the power of the k^{th} beam, and it is equivalent to the integration of the light intensity $I_k(r, \phi, z)$ over the radial and azimuthal coordinates. In Equations 2.45 and 2.46, the term $I_{s,k}(z)$ represents the intensity profile of the k^{th} signal beam, and the term $I_{p,k}(z)$ represents the intensity profile of the k^{th} pump beam. $i_k(r, \phi) = I_k(r, \phi, z)/P_k(z)$ is the normalized optical intensity of the k^{th} beam, which can be obtained by using the scalar multi-layer approximation from the measured fiber RI profile [49]. In this thesis, the normalized modal intensity profile $i_k(r, \phi)$ is obtained from COMSOL through the following procedure:

- (1) Import the refractive index profile of the fiber to be studied into our ready-to-use COMSOL mode solver, as explained in section 2.1.3. Run COMSOL, and obtain the full electric (E_x , E_y and E_z) fields of the vector modes that are guided in the target fiber. The discretization steps of the mode-field matrix is user definable. In this thesis, for simulations of the 2-mode-group EDFA, the size of mode-field matrix was chosen to be “300 by 300” in polar coordinate. For larger cores of the EDFAs, the size of the mode-field matrixes should be increased accordingly to ensure the accuracy of the results.
- (2) Extract the vector mode fields from COMSOL and load them into the MATLAB. Synthesize the electric fields of the LP modes according to the LP and vector

modes relationship listed in Table 2.1 (or reference [38]). For example, the electric fields of $LP_{11a,x}$ can be synthesized using $HE_{21,even}$ and TM_{01} :

$$E_{LP11a,x} = E_{HE_{21,even}} + E_{TM_{01}} \quad 2.47$$

(3) The normalized modal intensity profile $i_k(r, \phi)$ can be obtained through the following normalization procedure:

$$i_k(r, \phi) = \frac{E_{x,LP}^2 + E_{y,LP}^2}{\iint (E_{x,LP}^2 + E_{y,LP}^2) r dr d\theta} \quad 2.48$$

The propagation equation of the k^{th} beam associated with multi-transverse-spatial modes is given by [50], [51].

$$\begin{aligned} \frac{dP_k(z)}{dz} = & u_k \sigma_{e,k} (P_k(z) + 2h\nu_k \Delta\nu) \iint_S i_k(r, \theta) N_2(r, \theta, z) r dr d\theta \\ & - u_k \sigma_{a,k} P_k(z) \iint_S i_k(r, \theta) N_1(r, \theta, z) r dr d\theta - u_k \alpha P_k(z) \end{aligned} \quad 2.49$$

where $u_k = 1$ and -1 denote mode propagation in the forward and backward directions respectively, $\Delta\nu$ is the noise bandwidth and α is the optical loss. $2h\nu_k \Delta\nu_k$ denotes the spontaneous emission contribution from the local metastable population (i.e. N_2). With specified boundary conditions at $z = 0$ and $z = L$ (e.g. input signal and pump power, backward and forward ASE power), Equations 2.45, 2.47 and 2.50 can be solved numerically by standard numerical integration techniques (i.e. shooting method and relaxation method [52]). The boundary conditions for forward and backward ASEs are “at $z = 0$, the forward ASE power spectrum should be zero”, and “at $z = L$, the backward ASE power spectrum should be zero”.

Numerical solutions of Equations 2.45, 2.46 and 2.49 have three general steps: (1) the integration of the transverse modal profiles to calculate the absorption and gain coefficients for pump and signal modes; (2) the integration over the fiber length; and (3) the evaluation of the boundary conditions for pump, signal

and noise. To discuss these three issues, we consider the case where the pump and signal co-propagate along the fiber amplifier. The first step is the simplest, as the boundary conditions of the signal and pump are known at $z = 0$. The second step is slightly complicated, but can be solved by using the Runge Kutta fourth-order algorithm. The longitudinal steps from $z=0$ to $z= L$ can be chosen to be 50 per meter for the LP model. When modal beating is considered, as illustrated in chapter 4, the longitudinal step size should be at least 10 times smaller than the smallest modal beating length involved in the simulation to ensure that the simulations are fully resolved. The evaluation of the boundary condition of noise in the third step is the most difficult one. In the absence of strong signal input, the two ASE power distributions along the fiber will mutually saturate the gain. While the forward ASE power spectrum is zero at $z = 0$, the backward ASE power spectrum is maximum at this point. Therefore, in order to perform the integration of the equations from $z = 0$ to $z = L$, assumptions must be made for the unknown backward ASE at $z = 0$. The two methods used to solve such forward and backward ASE problems are briefly explained.

The shooting method is a trial-and-error approach, in which the unknown boundary value at $z = 0$ is initially guessed. The system is then integrated from $z = 0$ to $z = L$, before the corresponding boundary value at $z = L$ is compared with the desired value (i.e. ideally the backward ASE power spectrum is zero at $z = L$), and the difference is used to correct the initial guess in the subsequent trials [52]. After many integration iterations, the backward ASE spectrum at $z = L$ would eventually vanish. This approach works well with single-mode EDFA or 2-mode-group EDFA, as the model normally converges within 100 iterations. However, for heavily multi-moded EDFA, the shooting method is not very efficient and is slow. In this thesis, the shooting method was applied to solve the two-mode-group EDFA problem in chapter 4. A more efficient algorithm, the relaxation method, was developed and applied for modeling of MM-EDFA supporting 4-mode-group and beyond in chapter 5 and 6. In general, relaxation method is recommended in modelling of MM-EDFA.

The relaxation method makes iterative adjustments to the solution. An initial set of boundary values is chosen for the first integration. The system is then integrated again in the reverse direction, using the corrected boundary values. To apply the relaxation method in solving the EDFA problem, in the first integration from $z = 0$ to $z = L$, it is assumed that there is no backward ASE in the model. Then, the whole set of equations including the backward ASE is then integrated from $z = L$ to $z = 0$. After the second integration, a set of quasi-solutions for both forward and backward ASE distributions are obtained. Of course, this set of quasi-solutions is not accurate. This is because in the first integration, the saturation effect at $z = 0$ caused by the backward ASE is neglected, which leads to an underestimated backward ASE in the second integration. To improve the accuracy, the system needs to be integrated back and forth (i.e. from $z = 0$ to $z = L$, then from $z = L$ to $z = 0$) using the quasi-solutions obtained from the previous trial. With the proposed algorithm, convergence towards the actual solutions can be achieved without exhausting the computer. The merit of this algorithm is that each integration roundtrip refines the mutual saturation effect and progressively improves the accuracy of the solutions. Iteration of this integration routine can be stopped when the difference between successive solutions is less than 0.1%.

2.2.4 Noise figure

In a linear optical amplifier (i.e. EDFA), amplifier noise is unavoidable. The fundamental reason behind this statement was illustrated in a fundamental paper by H. Heffner [53], which showed that “an ideal, noise-free amplifier violates Heisenberg’s uncertainty principle”. The ASE noise and the optical noise figure (NF) are important characteristics of EDFAs. The ASE power spectrum closely emulates the gain spectrum, so it provides useful information on the EDFA operating characteristics in various pump and signal power regimes. The $NF(\lambda)$ represents a measure of the signal-to-noise ratio (SNR) degradation from the input to the output of the amplifier. Of course, there are other sources of noise from the laser source (i.e. laser intensity and frequency noise), the photodetector (i.e. shot, thermal and amplifier noise) and the oscilloscope (i.e. thermal noise).

The noise-figure spectrum for an EDFA can be determined from the gain $G(\lambda)$ and spontaneous-emission factor spectra $n_{sp}(\lambda)$ [43]:

$$NF(\lambda) = \frac{1 + 2n_{sp}(\lambda)(G(\lambda) - 1)}{G(\lambda)} \quad 23.50$$

where

$$n_{sp}(\lambda) = \frac{1}{G(\lambda) - 1} \frac{P_{ASE}^{out}(forward, \lambda)}{2h\nu\Delta\nu} \quad 2.51$$

Substituting Equation 2.52 into Equation 2.51 gives:

$$NF(\lambda) = \frac{1}{G(\lambda)} + \frac{P_{ASE}^{out}(forward, \lambda)}{G(\lambda)h\nu\Delta\nu} \quad 2.52$$

where $1/G(\lambda)$ corresponds to the shot noise, $P_{ASE}^{out}(forward, \lambda)$ is the output noise power at the signal wavelength of λ , and $h\nu$ is the photon energy. In practice, there is ASE present at the input of the doped fiber, so P_{ASE}^{out} can be written as:

$$P_{ASE}^{out} = P_{amp} + P_{in} \times G \quad 2.53$$

where P_{amp} is the noise power generated by the EDFA. $P/\Delta\nu$ can be replaced by the noise spectral density of S. So Equation 2.52 becomes:

$$NF(\lambda) = \frac{1}{G(\lambda)} + \frac{S_{out}}{G(\lambda)h\nu} - \frac{S_{in}}{h\nu} \quad 2.54$$

In the limit where the gain becomes $G \gg 1$, the noise figure at the signal wavelength reduces to:

$$NF(\lambda) = 2n_{sp}(\lambda) \quad 2.55$$

where $n_{sp}(\lambda)$ can also be written as:

$$n_{sp}(\lambda) = \frac{\eta N_2}{\eta N_2 - N_1} \quad 2.56$$

In the high-gain region (i.e. $G \gg 1$), almost 100% population inversion is reached. This results in $\min(n_{sp}(\lambda)) = 1$, which means $NF(\lambda) \geq 2$. Hence, an EDFA has a minimum NF of 3 dB. In a MM-EDFA, the NF in a dB scale is:

$$NF(dB) = 10 \times \log_{10} \left(\frac{1}{G(\lambda_s, k)} + \frac{S_{out}(\lambda_s, k)}{G(\lambda_s, k)h\nu} - \frac{S_{in}(\lambda_s, k)}{h\nu} \right) \quad 2.57$$

where $S_{out}(\lambda_s, k)$ is the output ASE spectral density (i.e. units of W/Hz) of the k^{th} mode at the signal wavelength of λ_s , and $S_{in}(\lambda_s, k)$ is the input ASE spectral density. For the modeling of an MM EDFA, the input ASE power is usually set to zero, and thus $S_{in}(\lambda_s, k)/h\nu$ is neglected.

2.3 General modelling results of a 2-mode-group EDFA

I started the amplifier modeling work by using a commercial software commercial software Optisystem 11.0®. The underlying physics and mathematics of the commercial code is identical to those found in the MM-EDFA background review from section 2.2. An example of the MM EDFA module user interface is shown in Figure 2.8. The commercial amplifier solver was built under the assumption that the optical fibers are weakly guiding, and that the spatial modes can be well approximated as LP modes. The commercial code accepts a user-defined fiber refractive-index profile (FRIP) (i.e. the FRIP must be weakly guiding), and a user-defined erbium doping profile. The maximum number of LP mode-groups that can be calculated by this commercial software is seven. Users are able to define the power ratio among the multiple signal or pump modes. It can simulate forward, backward or bi-directional pumping cases as shown in Figure 2.8. The ASE is also calculated, and the user is able to define the bandwidth of individual noise bin as long as the total noise bandwidth is considered.

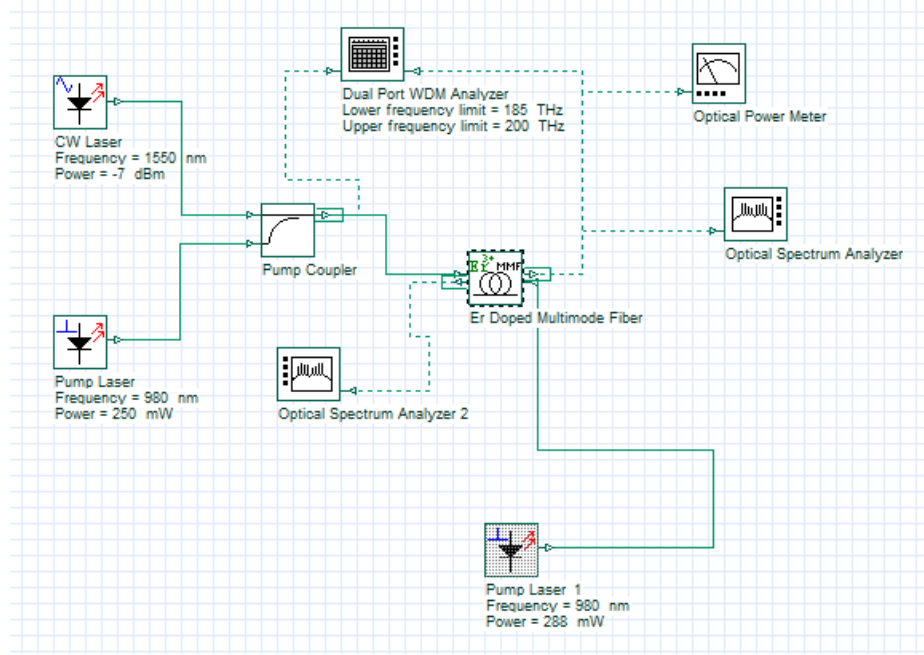


Figure 2.8. A sample diagram of the user interface of the Optisystem 11.0 MM-EDFA module.

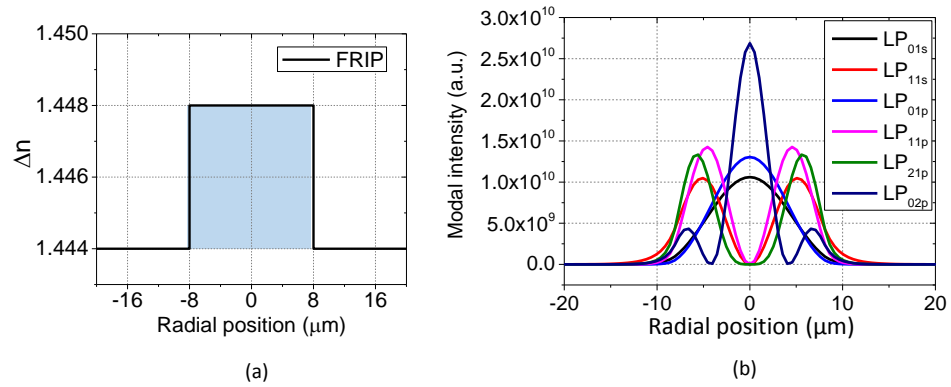


Figure 2.9. (a) The refractive-index profile of a 2-mode-group EDFA at 1.55 μm with a uniform erbium doping profile indicated by the blue shaded area. (b) The signal and pump intensity distributions.

Firstly, a two-mode-group EDFA in the 1.5 μm wavelength range is considered in this study. The RI profile of the 2-mode-group EDFA is shown in Figure 2.9(a), with an NA of 0.108 (similar to the NA of our in-house fabricated 2-mode-group EDFA shown in Figure 3.1 in the next chapter) and a core radius of 8 μm . The two-mode-group EDFA is fully doped with erbium ions with a concentration of $1.5 \times 10^{25} \text{ m}^{-3}$. This fiber amplifier guides LP_{01} and LP_{11} mode groups in the 1.5 μm wavelength range, and LP_{01} , LP_{11} , LP_{21} and LP_{02} mode groups at 980 nm, whose mode intensity profiles are shown in Figure 2.9(b). Throughout this thesis, the

fluorescence lifetime (i.e. 10 ms) as well as the emission and absorption cross-sections are derived from [46]. As discussed in section 2.1, the non- LP_{0m} mode-groups (e.g. LP_{11} and LP_{21}) have four degenerate modes. For example, the transverse intensity of the LP_{11} modes has two types of patterns or orientations, as illustrated in Table 2.2(a). Similarly, the intensity pattern of LP_{21a} and LP_{21b} are shown in Table 2.2(b). LP_{11a} exhibits two lobes that sit along the x-axis. LP_{11b} features two lobes that sit along the y-axis. Both LP_{11a} and LP_{11b} have two polarization degeneracies (i.e. x and y). These definitions are important because the modal gain is linked with the transverse intensity profiles of the signal and pump modes, and thus LP_{11a} and LP_{11b} may result in a different impact on the gain of the EDFA. It is assumed that the amplifier is polarization insensitive, which is generally valid for linear amplifiers such as EDFAs [43]. In this section, LP_{01} and LP_{11b} modes at 1550 nm are used as input signals, thus for simplicity the amplifier is referred to as a 2-mode-group EDFA. In order to study the gain dependency on different pump modes, the 2-mode-group EDFA was simulated under four pumping configurations, namely LP_{01} pump, LP_{11b} pump, LP_{21b} pump and LP_{02} pump, whose transverse intensity patterns are shown in Table 2.3. The length of the 2-mode-group EDFA was chosen to be 4 m. The input signal power was set to -10 dBm per mode and the input pump power was set to 250 mW. The total noise bandwidth considered in this simulation was 100 nm with 5 nm spacing between each noise component.

Table 2.2. (a) Signal mode intensity profiles of LP_{11a} and LP_{11b} ; (b) Pump mode intensity profiles of LP_{21a} and LP_{21b}

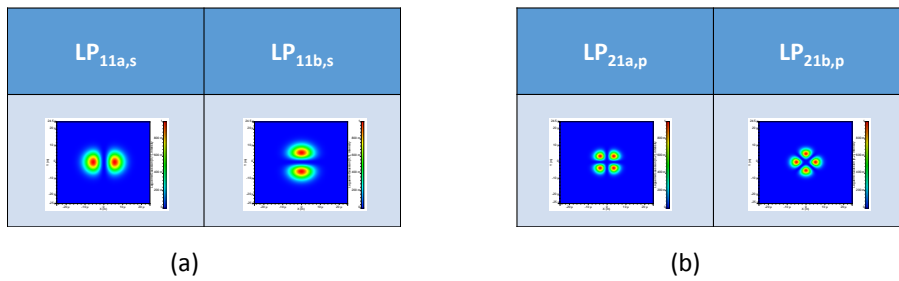
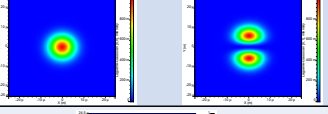
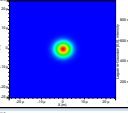
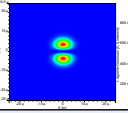
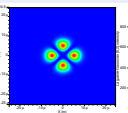
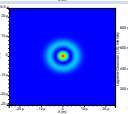


Table 2.3. The transverse mode intensity profiles of the signal modes and pump modes used for producing simulation results shown in Figure 2.10.

	Modal profile(s)
Signal modes: LP_{01} , LP_{11b}	
Pump mode: LP_{01}	
Pump mode: LP_{11b}	
Pump mode: LP_{21b}	
Pump mode: LP_{02}	

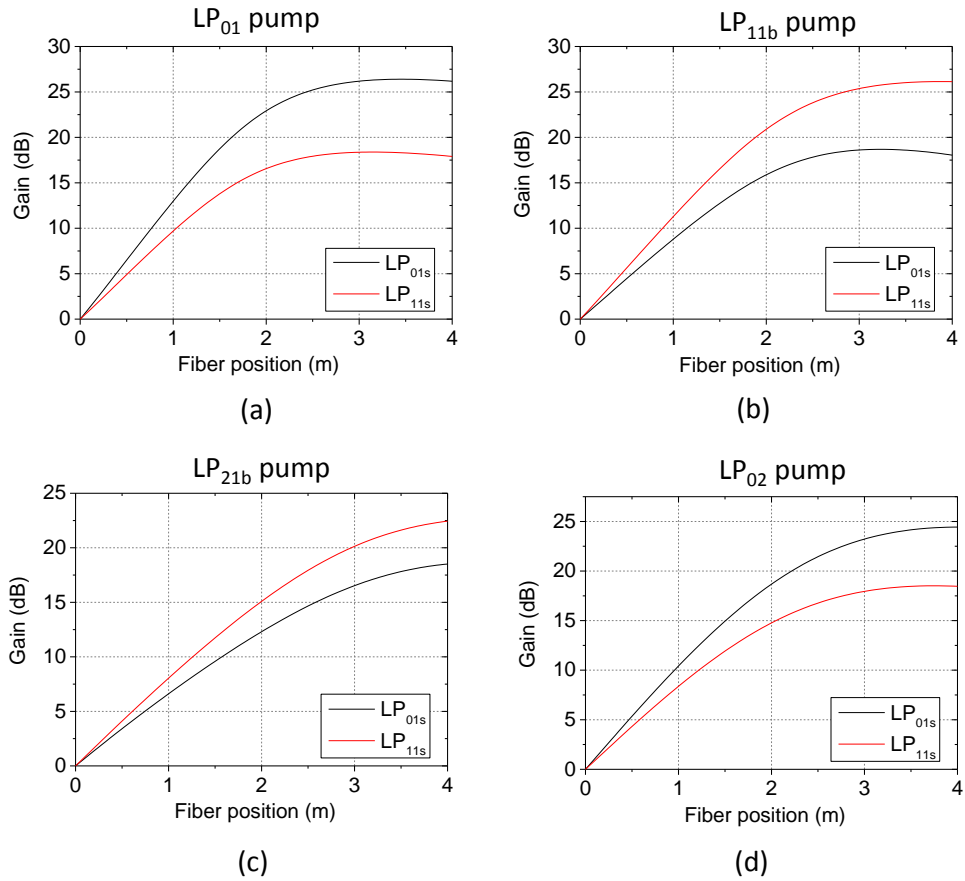


Figure 2.10. The modal gain evolutions against fiber position for different pump modes (a) LP_{01} pump; (b) LP_{11b} pump; (c) LP_{21b} pump and (d) LP_{02} pump.

Figure 2.10 shows the modal gain evolution along the fiber position for four pumping configurations. As the LP₀₁ pump mode has a larger overlap with the LP₀₁ signal mode, as shown by the intensity profiles in Figure 2.10(b), the gain for the LP₀₁ signal mode is significantly larger (i.e. 8 dB difference at $L = 4$ m) than that of the LP₁₁ signal mode in Figure 2.10(a). However, when pumped by the LP_{11b} pump mode whose intensity pattern matches with the LP_{11b} signal mode, the situation essentially reverses compared with the LP₀₁ pump case, as shown in Figure 2.10(b). The gain for the LP_{11b} signal mode is about 8 dB higher than that of the LP₀₁ signal mode at a fiber position of $L = 4$ m. In the third case, where the 2-mode-group EDFA is pumped by the LP_{21b} pump mode, apparently the gain still favours the high-order signal mode LP_{11b}. However, the gain difference between the LP₀₁ and LP_{11b} is reduced due to the LP_{21b} pump mode having two additional lobes along the x-axis compared with that of the LP_{11b} pump mode, which helped to increase the overlap between the LP₀₁ signal and the LP_{21b} pump. In the fourth case, the 2-mode-group EDFA is pumped by the LP₀₂ pump mode. Although the LP₀₁ signal mode sees a higher gain than that of the LP_{11b} signal mode, the gain difference is reduced compared with the case where the LP₀₁ pump was used. The additional ring in the intensity profile of the LP₀₂ pump mode helped to increase the overlap between the LP_{11b} signal and the LP₀₂ pump.

The noise properties of the 2-mode-group EDFA are similar to those of a single-mode EDFA. With a slight modification to the Equation 2.58, the mode-dependent $NF_{l,m}$ of mode LP _{l,m} is defined as:

$$NF_{l,m} \text{ (dB)} = 10 \log_{10} \left(\frac{1}{G_{l,m}(\lambda)} + \frac{S_{l,m}(\text{forward}, \lambda)}{G_{l,m}(\lambda) h \nu} \right) \quad 2.58$$

where the $S_{l,m}(\text{forward}, \lambda)$ is the forward noise power density (W/Hz) of the mode LP _{l,m} , $G_{l,m}(\lambda)$ is the modal gain of mode LP _{l,m} , and $\Delta \nu$ is the bandwidth of each noise component defined in the simulation (i.e. 5 nm). As an example, the noise properties of a 2-mode-group EDFA pumped by the LP₀₁ pump mode is presented. Figure 2.11(a) shows the total forward and total backward ASE power distribution along the fiber length. Aforementioned in section 2.2.3, at the position of $z = 0$ m, the forward ASE is zero while the backward ASE is the highest.

At a position of $z = 4$ m (i.e. the end of the amplifier), the forward ASE reaches a maximum while the backward ASE is zero. In this simulation, the maximum backward ASE is about 10 dBm, which noticeably suppresses the population inversion at the beginning of the fiber amplifier, as shown in Figure 2.12. The forward ASE power spectrum from 1500 nm to 1600 nm at a position of $z = 4$ m is plotted in Figure 2.11(b). Note that the results generated by the optical spectrum analyzer (i.e. an Optisystem 11.0® module used to collect light from single-mode fibers) can only give the information on the power percentage in the wavelength domain, and does not reflect the absolute power at each wavelength. The actual total noise power at 1550 nm, which is the signal wavelength, can be obtained from the total forward ASE power multiplied by the power percentage at 1550 nm worked out from the “optical spectrum analyzer”. In this case, the noise power percentage at 1550 nm (i.e. assuming the bandwidth is 1 nm) out of the 100 nm range is 2.5%. Therefore, the total noise power within the 1 nm window centered at 1550 nm is 0.0255 mW. From Optisystem 11.0, it is also known that 75% of the total noise power resides in the LP_{01} noise, while the rest of the power is split equally amongst the LP_{11a} and LP_{11b} noise. Consequently, the LP_{01} noise power (i.e. of 1 nm bandwidth centered at 1550 nm) is 0.019 mW and the LP_{11b} noise power (i.e. of 1 nm bandwidth centered at 1550 nm) is 0.0032 mW. Given the modal gains for the LP_{01} and LP_{11b} signals are 26.0 dB and 17.6 dB respectively, the noise figure for the LP_{01} and LP_{11b} signals can be deduced using Equation 2.58, which gives 4.8 dB and 5.2 dB respectively.

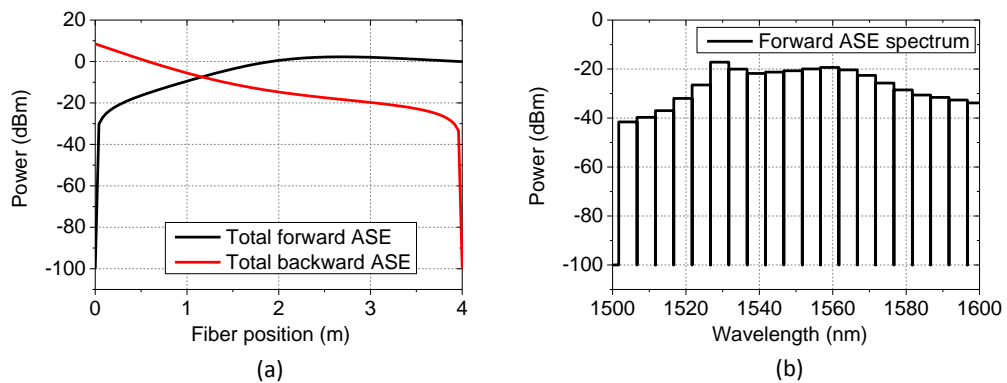


Figure 2.11. (a) The power evolution of the total forward and backward ASE along the fiber length. (b) The forward ASE spectrum at the output end of the amplifier.

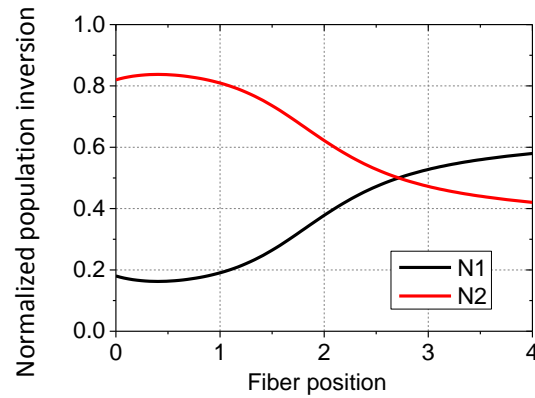


Figure 2.12. The population inversion distribution along the fiber length.

2.4 Conclusion

This chapter reviewed the derivation of the exact vector solutions (i.e. modes) of cylindrical step-index fibers. In weakly guiding fibers, where the core-to-cladding RI difference is adequately small, which is true for most of the telecommunication fibers, the vector solutions can be simplified to scalar solutions. Mathematical equations were established showing that LP modes can be represented as linear combinations of certain vector modes from the same LP mode group. Although the LP modes are not real modes in the weakly guiding region, they are accurate enough to describe the fields at the output of the optical fiber. We have established a COMSOL model to compute the vector solutions of the user-defined RI profile of the optical fiber. The second part of this chapter reviewed light amplification in single-mode EDFA and the rate/propagation equations for modelling MM-EDFA were established. After a discussion of numerical solutions (i.e. shooting method and relaxation method) of the MM-EDFA simulations, some general modelling results of a step-index 2-mode-group EDFA are presented. The experimental verification of the 2-mode-group EDFA simulation tool and the subsequent design and optimization of the 2-mode-group EDFA will be discussed in chapter 3.

Chapter 3: Modelling of 2-mode-group EDFA with linearly polarized approximation

After the introduction to modes in optical fibers and general modelling of MM-EDFA using LP modes, I proceed in this chapter to present the verification of the 2-mode-group EDFA modelling based on LP modes, new 2-mode-group EDFA designs generated, and finally fitting experimental data based on the real fabricated 2-mode-group EDFA. I used a commercial software, Optisystem 11.0®, to perform all the simulations in this chapter. To determine the accuracy of the software and to justify its use for future designs, an experimental verification was conducted using our “batman” 2-mode-group EDFA, of which the RI profile resembles “batman”. The “batman” 2-mode-group EDFA with a raised-edge refractive index profile is proven both experimentally and theoretically to be a better candidate than the conventional step-index 2-mode-group EDFA in terms of providing a low DMG. Thus, in section 3.2.1, I investigate whether modifying the central dip of the refractive index profile of the “batman” 2-mode-group EDFA would give even better performance. However, my findings show that, in order to deliver low DMG, the modified “batman” 2-mode-group EDFA would either require a complex pump modal profile or become unmatched to the conventional step-index/graded-index passive fiber. To address both problems, in section 3.2.2, I propose a new step-index 2-mode-group EDFA with a ring doping profile that is able to deliver low DMG using a simple LP_{01} pump mode. Based on my modelling results, a ring-doped 2-mode-group EDFA was fabricated in-house. From our preliminary experimental results, we suspect that the erbium ions had diffused from the outer layer towards the center of the core during the fabrication. My subsequent modelling predicts that there are considerable amount of erbium ions in the centre of the core, which later was confirmed by direct experimental measurement of the erbium distribution in the core. This in return, further confirmed that my simulation model is reliable. Although the erbium doping profile is not an idea ring, our ring-doped 2-mode-group EDFA is still able to give nearly equal gain for LP_{01} and LP_{11} modes in the C-band when

high-order pump modes are used (i.e. pump beam is offset-launched experimentally). Our ring-doped 2-mode-goup EDFA has been applied in several major transmission experiments with MODEGAP project collaborators, and resulted in a number of high impact publications.

3.1 Experimental validation of the LP modes based 2-mode-group EDFA model

Before I started my PhD at the ORC, a step-index 2-mode-goup EDFA and a “batman” 2-mode-goup EDFA, denoted as Fiber 1 (F1) shown in Figure 3.(a) were fabricated in-house. At that time, there was no 2-mode-goup EDFA modelling to systematically optimize the performance of the 2-mode-goup EDFA. The “batman” 2-mode-goup EDFA was made based on the physical intuition that the raised-edge index profile would increase the overlap between the erbium ions and the LP_{11} signal modes, thus promote the gain for the LP_{11} mode. The experimental results based on these two 2-mode-goup EDFAs were presented at the ECOC 2011 postdeadline session, showing that the “batman” 2-mode-goup EDFA offer lower DMG than that of the step-index 2-mode-goup EDFA under both central- and offset-pump launch conditions [25]. My PhD was concerned with providing numerical support to these early experimental results and thus to develop new optimal designs based on the theory I developed.

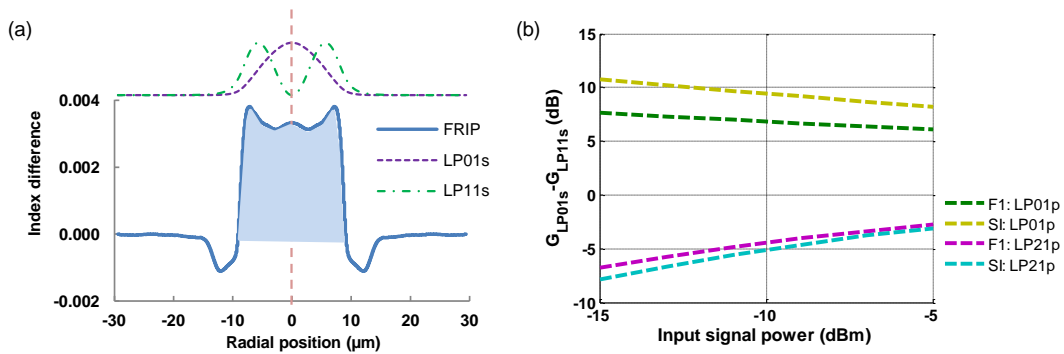


Figure 3.1. (a) The FRIP and dopant profiles (i.e. shaded blue region) of F1, and the supported signal modes. (b) DMG vs. input signal power pumped by LP_{01p} and LP_{21p} for both F1 and step-index (SI) EDF.

In this section, the simulations based on the “batman” 2-mode-group EDFA (i.e. F1) using the commercial software Optisystem 11.0® are discussed. As shown in Figure 3.1(a), F1 has a core diameter of 18 μm and a NA of 0.12. It guides 3 spatial modes, namely LP_{01} , LP_{11a} and LP_{11b} , within the C-band, up to LP_{02p} at 980 nm. The Er^{3+} doping concentration of F1 is set to be $15 \times 10^{24} \text{ m}^{-3}$ as estimated from the measured absorption of 10.1 dB/m at a pump wavelength of 980 nm. The background loss was neglected due to the short length of fibers required (e.g. 3-5 m). Firstly, to illustrate the importance of the model, general results from the modelling of F1 are presented in Figure 3.1(b).

In the simulations, LP_{11a} is used to represent the LP_{11s} mode-group of the signal, and LP_{21a} is used to represent the LP_{21p} mode-group of the pump. In Figure 3.1(b), the simulated DMG ($G_{\text{LP}01s} - G_{\text{LP}11s}$) is shown as a function of the input signal power per mode for both F1 and a conventional step-index (SI) 2-mode-group EDF (as shown in Figure 2.9(a)) when pumped by pure LP_{01p} and LP_{21p} modes with a fixed power of 250 mW. The EDFAs were considered to be forward pumped and a fiber length of 3.5 m was used in each case. As shown in Figure 3.1(b), the DMG exhibits a significant dependence on the pump modal configurations. The gain differences between the two signal modes of F1 are significantly less than those of the SI 2-mode-group EDF, which indicates that the EDF with a “batman” profile improves the amplifier performance in terms of reducing DMG. However, the simulations also indicate that a complex pump-field distribution (i.e. a combination of LP_{01p} and LP_{21p} modes) is required to minimize the DMG for both fiber designs.

To validate the numerical model, detailed gain measurements of an EDF with a “Batman” RI profile supporting 2 mode-groups was undertaken using the experimental setup reported in [54] (done by Dr Yongmin Jung), as shown in Figure 3.2. The EDF length was set to 3.5 m and the counter-propagating pump arrangement was employed. The wavelengths of both signal modes (i.e. LP_{01} and LP_{11}) were set to 1550 nm while the average input signal power per mode was varied from -10 dBm to 0 dBm. Both central- and offset-pump launch conditions of the pump that are explained in [25], [54] were considered in the modeling. For

the central-pump launch condition, where the pump beam was physically aligned to the center of the EDF, most of the pump power is expected to convert into circularly symmetric modes (i.e. LP_{01p} , LP_{02p}). However, a small amount of pump power might go into the asymmetric modes (i.e. LP_{11p} , LP_{21p}) due to any non-ideal alignment. In contrast, for offset-pump launch condition, asymmetric modes (i.e. LP_{11p} , LP_{21p}) are likely to be preferentially excited.

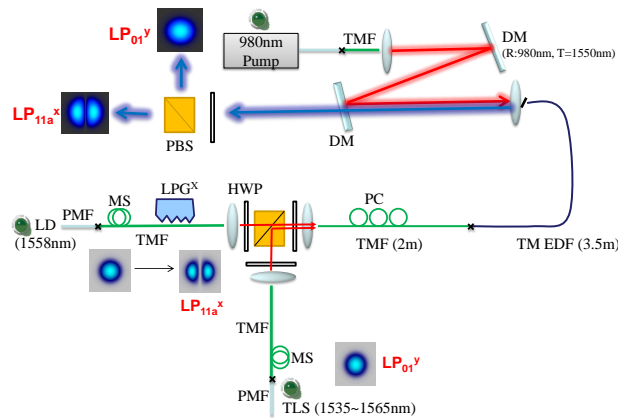


Figure 3.2. The experimental setup of the in-house 2-mode-group EDFA from [25].

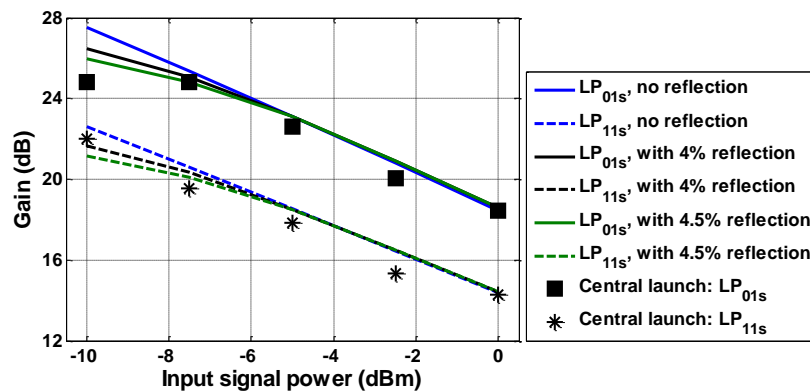


Figure 3.3. Gain for LP₀₁ and LP_{11a} modes vs. input signal power under the central-pump launch condition. The dots denote experimental data, while the lines are simulation fittings.

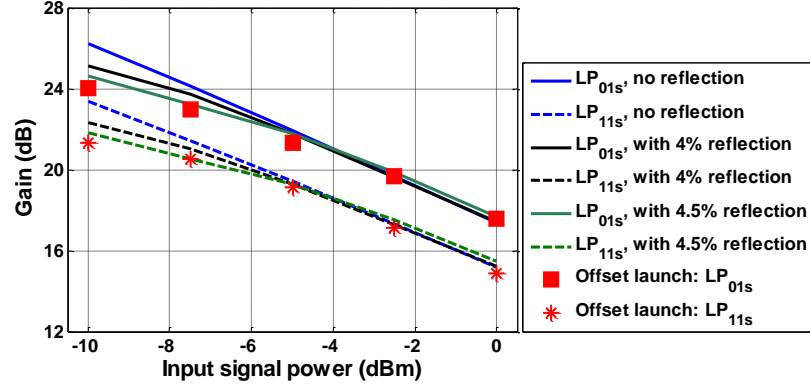


Figure 3.4. Gain for LP₀₁ and LP_{11a} modes vs. input signal power under the offset-pump launch condition. The dots represent experimental data, while the lines show theoretical predictions.

For the central-pump launch condition outlined in Figure 3.3, it was found that the best agreement between theory and experiment can be achieved by assuming that 65% of the total pump power (i.e. 280 mW) is in the LP_{01p} mode while the remaining 35% resides in the LP_{21p} mode. Here, it is to be noted that, in the simulation, the LP_{21p} was a combination of the two orientations of the LP_{21p} modes that the intensity of LP_{21p} has no azimuthal dependence. For the offset-pump launch condition illustrated in Figure 3.4, the best fit was achieved by assuming 40% of the pump power is in the LP_{01p} mode and the remaining 60% is in the LP_{21p} mode. Although the experimental data points show good agreement with those of simulation at high input-signal powers, a significant (i.e. 3 dB) discrepancy appears at low powers. In this experiment, the amplifier input end-face was flat cleaved, as to avoid significant mode mixing at the signal launch end. Consequently, we adjusted our simulation conditions with Fresnel reflection included at the input end of the 2-mode-group EDFA and the compared with experimental results again, as shown in Figure 3.3 and 3.4. With 4.5% reflection included, the apparent discrepancy at low powers is reduced from 3 dB to 0.8 dB and the general performance of the amplifier is well described over the full operating range. Hence, it can be concluded that the scalar-mode approximation and the various other assumptions listed hold well in modeling the 2-mode-group EDFA and can be reliably used to investigate and optimize new EDFA designs.

3.2 Modal gain control in 2-mode-group EDFAs

3.2.1 Design of 2-mode-group EDFs with raised-edge index profile

Modal gain control in few-mode EDFAs is of paramount importance for mode-division multiplexed transmission systems in order to minimize the loss of capacity and the chance of outages. Fundamentally, modal gain is associated with the overlap between signal and pump modal profiles and the rare-earth dopants. So the design freedom of few-mode EDFAs lies in fiber design (i.e. RI profile and dopant distribution) and pump modal configuration. As it shown from the previous section that a 2-mode-group EDF with a raised-edge index profile helps to reduce the DMG compared with the conventional SI-EDF. Consequently, this section initially examines the impact on DMG for a series of 2-mode-group EDFs with modified raised-edge profiles in conjunction with pump modal content control. Then I found that in order to achieve $\text{DMG} < 0.5 \text{ dB}$, either a complex pump modal profile is required or a ring shaped FRIP (i.e. the refractive index of the core centre is equal to cladding index). However, another problem is that the modes of a 2-mode-group EDFA with a ring-shaped FRIP do not match with the modes of standard step-index/graded-index passive fibers. Finally, a simple $\text{LP}_{01\text{p}}$ -pumped step-index 2-mode-group EDF with a ring-doped erbium distribution is proposed, which yields three advantages: (1) low pump-complexity; (2) low DMG; (3) and low mode-coupling losses when spliced to standard SI or graded-index passive fibers.

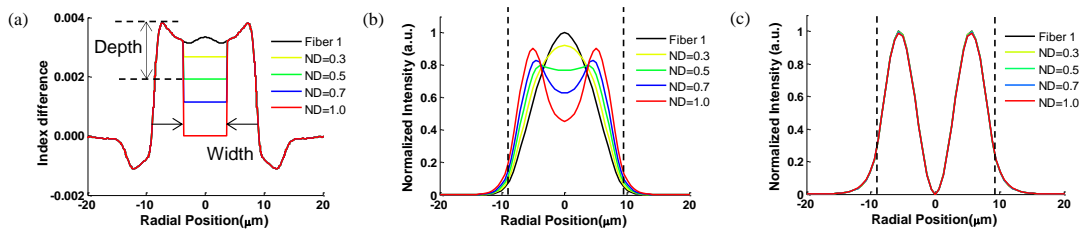


Figure 3.5. (a) The FRIP of F1, (b) the evolution of $\text{LP}_{01\text{s}}$, and (c) $\text{LP}_{11\text{s}}$ mode intensity distribution in F1 and modified FRIPs with ND varying from 0.3 to 1.0. The dashed lines in (b) and (c) indicate a radial position of $\pm 9 \mu\text{m}$, which is the fiber radius.

It has been experimentally validated for the 2-mode-group EDF F1 described in Figure 3.1(a), that the intentional central dip in its FRIP gives a lower differential gain between the LP₀₁ and LP₁₁ modes compared to the conventional SI design [55], [56]. In this section, I study to see whether equal modal gain or perhaps even higher gain for the LP₁₁ mode can be achieved by optimizing the depth of the central dip shown in Figure 3.1(a). Figure 3.5(a) shows the proposed RI profiles of F1 with its normalized depth (ND) varying from 0.3 to 1.0 while its width is fixed at 40% of the core diameter. The ND is defined as the ratio between the RI depth and the maximum difference between the core and cladding indices. The corresponding intensity distributions (i.e. normalized to the same power) of the LP_{01s} and LP_{11s} signal modes are plotted in Figure 3.5(b) and Figure 3.2(c) respectively. Again, it is assumed that the erbium-doping distribution closely follows the FRIP. This is generally expected from pioneer fabrication works. It can be seen from Figure 3.5(c) that the shape of the mode-field profile of LP_{11s} remains almost unchanged for the entire range of NDs. However, Figure 3.5(b) clearly shows that the LP_{01s} deforms significantly from its Gaussian shape when the normalized depth increases beyond 0.5. This level of modal distortion will have serious consequences in terms of coupling losses at the interface of 2-mode-group EDF and any passive transmission fiber spliced to it, due to the mode-field diameter (MFD) mismatch. To illustrate the impact of this, I considered splicing the 2-mode-group EDF with various values of ND to F1 (i.e. profile of a transmission fiber FRIP). The coupling efficiencies η_{LP01} and η_{LP11} for the LP_{01s} and LP_{11s} modes respectively, can be calculated by [57]:

$$\eta = \frac{\left| \int_0^{2\pi} \int_0^\infty \psi_{in}(r, \phi) \psi_i^*(r, \phi) r dr d\phi \right|^2}{\int_0^{2\pi} \int_0^\infty \psi_{in}(r, \phi) \psi_{in}^*(r, \phi) r dr d\phi \int_0^{2\pi} \int_0^\infty \psi_i(r, \phi) \psi_i^*(r, \phi) r dr d\phi} \quad 3.1$$

where Ψ_{in} is the mode supported in F1, and Ψ_i is the mode supported in the fiber with a modified FRIP. The results are listed in Table 3.1 below. Although the coupling efficiency for the LP_{11s} mode remain immune to changes in ND, that is

not the case for the LP_{01s} mode. The coupling efficiency drops down to 75% (i.e. ~ 1.25 dB loss) for extreme central dip depth under the ideal central-pump launch condition. I have also calculated the dependence of the differential modal-gain (i.e. $\Delta G = G_{LP_{01s}} - G_{LP_{11s}}$) on the NDs as well as the pump-field distribution and the result is illustrated by a contour map shown in Figure 3.6. Once again, backward pumping was used with a total pump power of 250 mW. The signal power of each mode is assumed to be -10 dBm at 1550 nm while the EDF length is set to 3.5 m.

Table 3.1. Signal coupling efficiencies associated with the modification of ND in F1.

ND	0.126	0.2	0.3	0.4	0.5	0.6	0.7	0.8	0.9	1.0
$\eta_{LP_{01}}$	1	0.999	0.994	0.977	0.952	0.920	0.881	0.838	0.792	0.745
$\eta_{LP_{11}}$	1	0.999	0.999	0.997	0.994	0.990	0.987	0.982	0.978	0.973

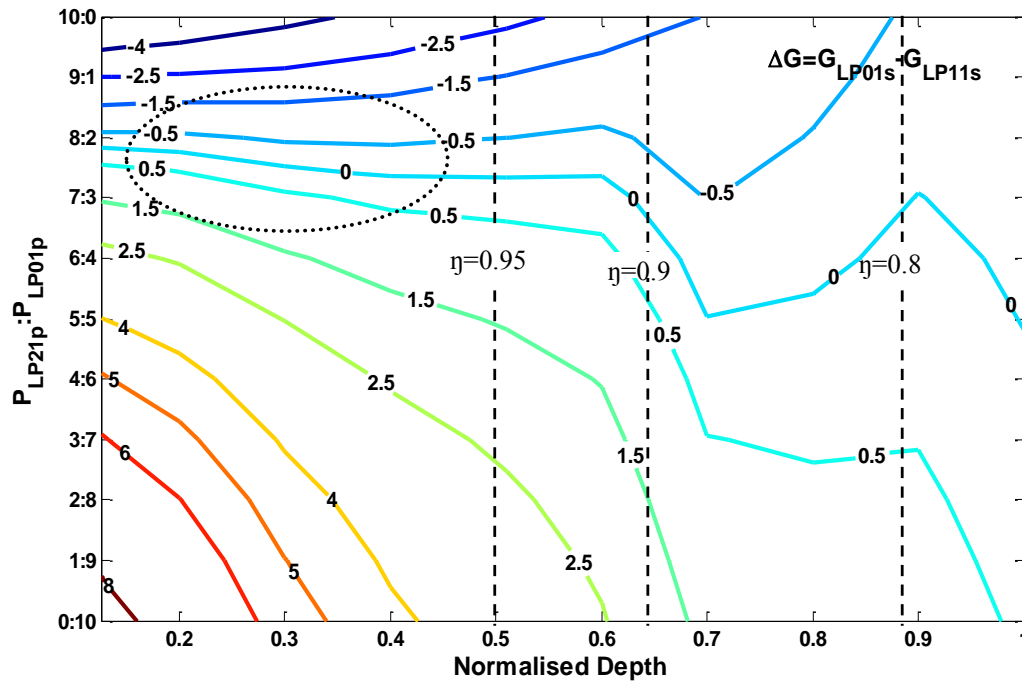


Figure 3.6. Contour map for the differential gain between LP_{01s} and LP_{11s} (i.e. in dB scale) with X-axis of normalized depth for tuning FRIP based on F1 (i.e. see Figure 3.5(a)) and Y-axis of pump power ratio between LP_{21p} and LP_{01p} . The vertical dashed lines represent the signal coupling efficiency for LP_{01} in accordance with the ND.

It can be seen from Figure 3.3 that $|\Delta G| < 1.5$ dB can be attained for a wide range of normalized depths. Smaller depths require a higher ratio of LP_{21p} to LP_{01p} , which is difficult to control in practice due to the excitation complexity of pure higher-order modes in the optical fiber. Although larger normalized depths require increasingly smaller LP_{21p} , the resulting intensity distribution of the LP_{01} signal mode is distorted significantly from the well-known Gaussian distribution and it is far from ideal in terms of coupling loss. Considering both the modal gain requirement as well as the tolerable coupling loss for the LP_{01s} mode, the most desirable region of operation lies in the upper left-hand corner of the contour map. This is indicated by the dotted ring in Figure 3.6, where the power ratio between LP_{21p} and LP_{01p} is around 8:2 and the ND is below 0.5 corresponding to an LP_{01s} coupling loss of less than 5%. Moreover, the modal gain of both the LP_{01s} and LP_{11s} modes in the region enclosed by the dotted ring is well above 20 dB.

3.2.2 Design of 2-mode-group EDFs incorporate ring doping

The physical origin of the DMG results from differences in the overlap of the pump mode, signal mode and the rare-earth dopants. As illustrated in Figure 3.6, the DMG can be changed substantially by tailoring the RI profile with fine tuning of the pump modal content. The condition that the dopant profile follows the FRIP comes from the specific fabrication process adopted for F1, rather than a fundamental mechanism. For example, it is possible to incorporate the dopant in an annular ring surrounding an undoped central-core region of a SI fiber. Previously ring-doping designs have been used in fiber laser applications, for example to increase slope efficiency at short emission waveband [58] of a 3-level system, or to selectively amplify certain modes in high-order-mode fiber [59]. From the ring doping structure in F2 shown in Figure 3.7, it is evident that there is great scope for engineering the relative overlap of the LP_{01} and LP_{11} signal modes with Er ions.

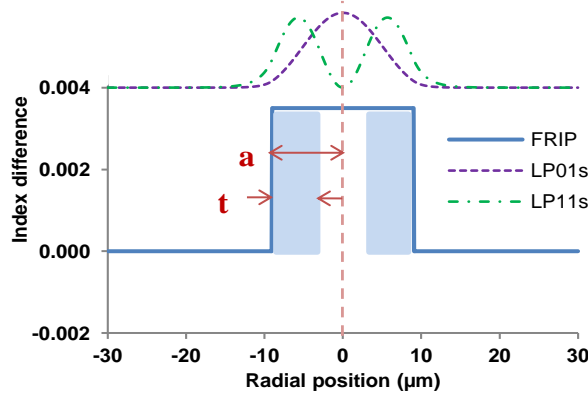


Figure 3.7. F2 with ring-doped profile (i.e. shaded blue region) and supported signal modes. Labels: a is the core radius, and t is the thickness of the doped region.

To illuminate the benefits to be derived from this design, Figure 3.8 shows the variation of DMG between LP_{01s} and LP_{11s} signal beams in a length of F2 forward pumped by a pure LP_{01p} of 980 nm pump beam for various values of the normalized ring thickness (i.e. defined by the ratio of t/a shown in Figure 3.7). The DMG values for a series of t/a values and the corresponding fiber length (FL) used are shown in Figure 3.8(a) below. The signal wavelength was chosen to be 1530 nm and pump power was fixed at 250 mW. It should be noted that the pump absorption per unit length increases with increasing t/a . For a fair comparison, the FL is adjusted to ensure that the total output signal power (i.e. sum of LP_{01s} and LP_{11s}) reaches the maximum for each t/a value.

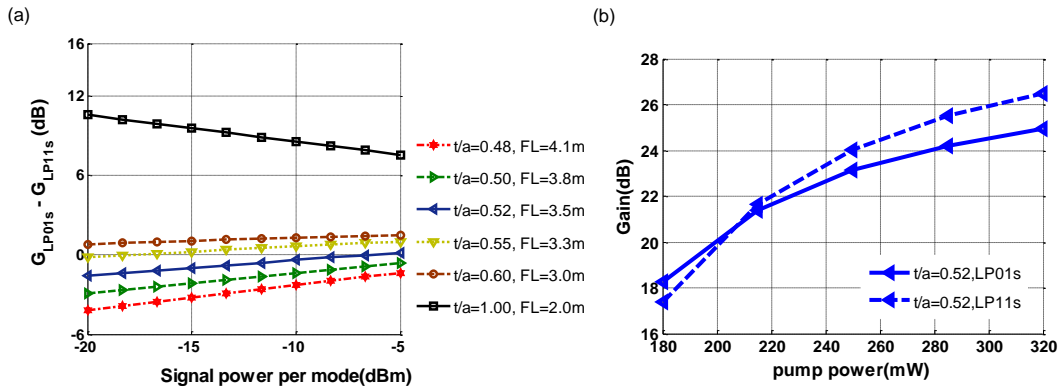


Figure 3.8. (a) Differential gain between LP_{01s} and LP_{11s} at 1530 nm versus input signal power for different t/a ratios. (b) Modal gains against LP_{01} pump power for F2 with a value of $t/a = 0.52$.

As can be seen, very-low levels of DMG can be obtained for a wide range of input powers for values of t/a around 0.52. Moreover, through fine tuning of t/a , both negative and positive values of DMG can be achieved. For comparison, we have plotted the DMG for the conventional uniformly doped SI-EDF (i.e. $t/a = 1$), which remains large and positive at all input powers. Figure 3.8(b) shows the modal gain properties against the LP₀₁ pump power for F2 with a value of $t/a = 0.52$ while fixing the input signal power at -10 dBm per mode. From both Figure 3.8(a) and (b), it can be seen that large gain differences could be resolved by tailoring the value of t/a , while fine tuning of the differential modal gain can be achieved by adjusting the pump power.

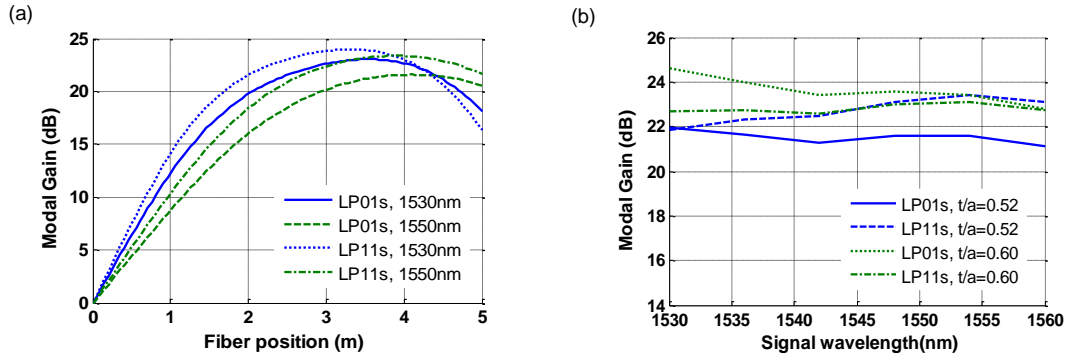


Figure 3.9. (a) Modal gain evolution of LP_{01s} and LP_{11s} along the fiber position for wavelengths of 1530 nm and 1550 nm, based on $t/a = 0.52$. (b) Modal gain dependence on the wavelength.

In practice, modal gain property for the entire C-band is also of paramount importance. To investigate this attribute, signal wavelengths at 1530 nm and 1550 nm were selected and a ratio of $t/a = 0.52$ were chosen so as to have a higher gain for the higher-order modes. The LP_{01p} pump power was set to 250 mW while an input power of -10 dBm was used for both LP_{01s} and LP_{11s}. The corresponding signal power evolution along the fiber is shown in Figure 3.9(a). At a fiber length of ~3.5 m, the gain for signals at 1530 nm is already saturated while those at 1550 nm are still increasing, which indicates that the fiber positions where the minimum absolute DMG value occur for signals at 1530 nm and 1550 nm are different. However, it is possible to minimize the gain excursion to within 1.5 dB across the full C-band for both LP_{01s} and LP_{11s} by choosing an EDF length of 4.3 m, as depicted by the blue lines shown in Figure 3.9(b).

Similarly, by adjusting the EDF length to 3.5 m with a ratio of $t/a = 0.6$, it is possible to obtain a higher gain for the LP_{01s} with minimal gain excursion (i.e. ~ 2 dB) across the C-band (i.e. green lines shown in Figure 3.9(b)). The bend sensitivity of the modes in F2 has also been considered, which is modeled through the simulation software COMSOL Multiphysics 4.3®. The COMSOL model that computes bend loss was developed by Dr Catherine Baskiotis based on analytical formulas from [60]. The impact of bending of F1 can be neglected for both pump and signal modes provided that the bend radius is kept larger than ~ 7.5 cm. This bend radius could be further reduced if required by adding additional features in the fiber cladding (e.g. RI trenches).

In conclusion, the ring-doping approach relaxes the condition where the dopant profile follows the FRIP, and it is capable of providing accurate control of the DMG in a 2-mode-group EDFA for a significantly simplified and much more practical LP₀₁-only based pumping configuration.

3.3 Amplifier modelling based on fabricated 2-mode-group ring doped EDF

Based on the author's findings, an erbium ring-doped preform was fabricated in-house, targeting a ratio of $t/a = 0.52$, core-to-cladding index difference = 0.0035 for the step-index ring-doped 2-mode-group EDF described in Figure 3.7 in the previous section. The preform was fabricated using the well-established modified chemical vapor deposition (MCVD) process coupled with solution doping [61], [62]. The erbium ring-doped preform has a two-layer core structure with different doping compositions between layers. The outer-core region is designed to be doped with active Er³⁺ ions with Al₂O₃ as a co-dopant, while the inner core is doped only with Al₂O₃ of a concentration designed to ensure that the RI of the two regions are well matched. Firstly, a porous SiO₂ core layer was deposited inside a silica tube and immersed in a methanol solution containing salts of erbium and aluminum co-dopants. Then, it is sintered into glass to obtain the erbium-doped region. Secondly, a pure Al₂O₃ silica layer (i.e. without Er³⁺

ions) was further deposited to produce a central RI-matched SI core. The resultant RI profile of the preform deviates slightly from that of an ideal SI profile and a small RI discontinuity between the inner and outer rings was observed in Figure 3.10. It is believed that the sintering process after the solution doping induces a loss of erbium and aluminum oxides from the core, causing a slight RI dip in the proximity of the interface between inner and outer core regions. The core-to-cladding RI difference of the fabricated preform is ~ 0.009 , which is much higher than intended. The t/a ratio in the fibers drawn from this preform will be discussed in the following sections.

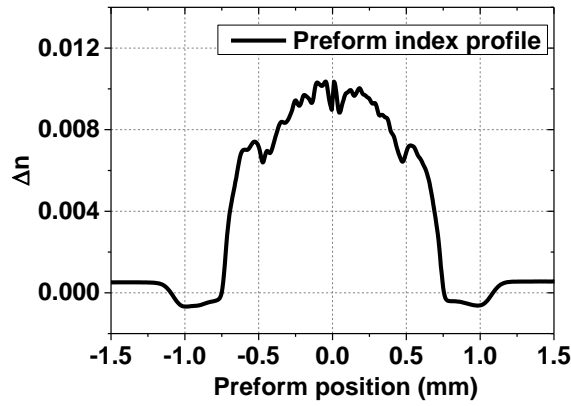


Figure 3.10. The RI profile and Er doping distribution of the Er ring-doped preform.

The experimental preform parameters were then fed back into our COMSOL mode-solver model to ascertain the final fiber core diameter that ensures the best guidance of the LP_{11} mode and the cut-off of LP_{21} mode in the $1.5 \mu\text{m}$ region. COMSOL gives full vector solutions, as explained in section 2.1.3. The effective indices of the vector modes from the LP_{11} and LP_{21} mode groups at 1550 nm for the three core diameters based on the ring doped preform are summarised in Table 3.2. At 1550 nm , the refractive index of the silica cladding is about 1.444025 according to the Sellmeier Formula [63], [64]. It is shown in the Table 3.2 that, when the core diameter is $14 \mu\text{m}$, the effective indices of the LP_{11} mode group are higher than those of the $13.5 \mu\text{m}$ diameter core. However, if I increase the core diameter to $14.5 \mu\text{m}$, the HE_{31} (i.e. belongs to the LP_{21} mode group) will be guided with its effective index just over the cladding index.

Table 3.2. The effective indices of the vector modes from the LP₁₁ and LP₂₁ mode groups at 1550nm for three different core diameters from the ring doped preform

		Core diameter (μm)		
		13.5	14	14.5
LP ₂₁	HE ₃₁	cut-off	cut-off	1.4440300
LP ₁₁	HE ₂₁	1.445772	1.446262	1.44668432
	TM ₀₁	1.445778	1.446267	1.44668833
	TE ₀₁	1.445781	1.446270	1.44669132

Based on the results of these numerical simulations, a fiber was drawn with an outer cladding diameter of 111 μm , a core diameter of 14 μm , with a FRIP shown in Figure 3.11. The estimated effective NA of the core is ~ 0.14 . The measured absorption at 980 nm is 5.56 dB/m, and the background loss is 21.4 dB/km at 1285 nm. The normalized ring thickness (t/a) is 0.48 as indicated by the RI dip shown in the measured FRIP in Figure 3.11. Before the fabricated 2-mode-group EDF was sent out to be analyzed for the exact erbium and aluminium ion distribution, some simple experiments and simulations were performed to establish a basic understanding of the modal gain properties of the in-house 2-mode-group ring-doped EDF. The absorption spectrum shown in Figure 3.12 reveals two high peaks around 978 nm and 1530 nm.

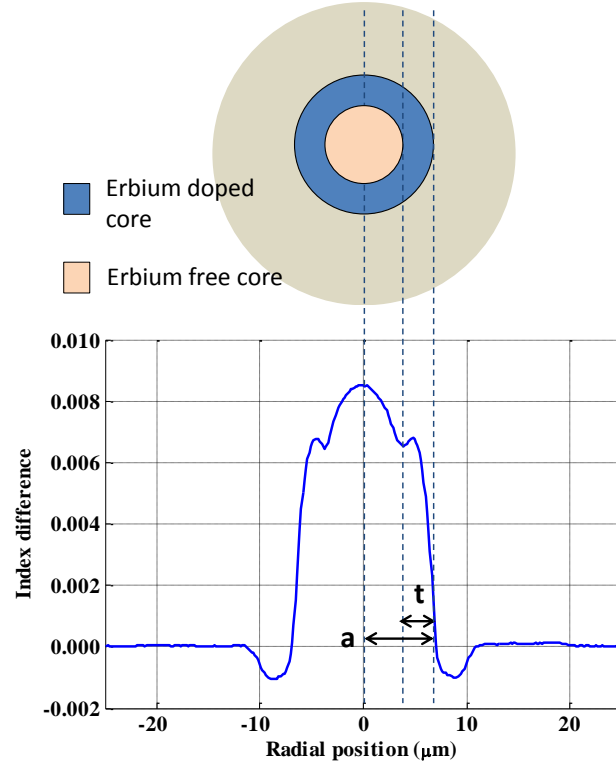


Figure 3.11. The RI profile of the 2-mode-group erbium ring-doped fiber.

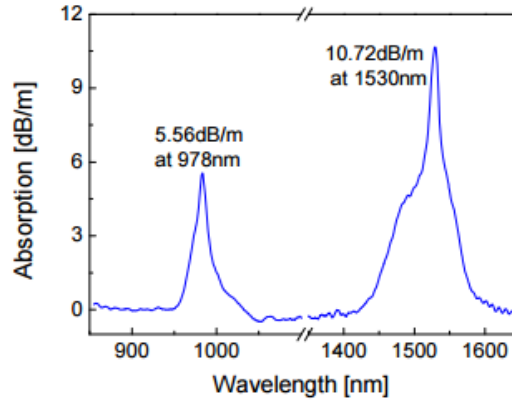


Figure 3.12. The measured absorption spectrum of the 2-mode-group ring-doped EDF, provided by Dr. Y. Jung.

The modal gain properties of the ring-doped 2-mode-group EDFA were measured by Dr. Y. Jung [65], with the experimental setup shown in Figure 3.13. The detailed description of the mode multiplexer, multimode amplifier and demultiplexer can be found in the group's paper [65]. Here, the essential features of this experiment as opposed to the experimental setup shown in Figure 3.2 are outlined below. In the mode multiplexer, the LP_{11} signal modes (i.e. LP_{11a} and

LP_{11b}) were converted from the LP_{01} beam through free-space phase plates. All three spatial modes were combined using two beam-splitters and coupled into a short length (~ 10 m) of passive two-mode-group fiber. An extinction ratio of >25 dB for three spatial modes was achieved. The 980 nm pump beam was free-space coupled into the other end of the 2-mode-group EDF, thus counter-propagating with respect to the signal beams.

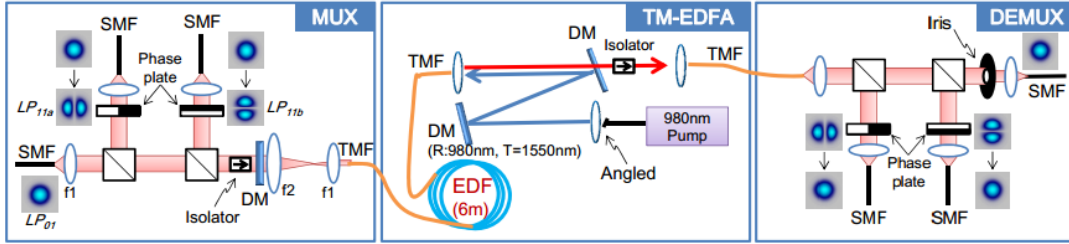


Figure 3.13. The measurement setup for modal gain analysis of the two-mode-group Er^{3+} ring-doped fiber: mode multiplexer (MUX), two-mode-group erbium-doped fiber amplifier (2-mode-group EDFA) and mode de-multiplexer (DEMUX).

First of all, for simple but effective modal gain measurement, different wavelengths were chosen for the seed signals of two different channels (i.e. 1550 nm for the LP_{01} and 1555 nm for the LP_{11}) and the combination of a tunable narrow bandpass filter (i.e. $\Delta\lambda = 2$ nm) and a power meter were used at the output of the amplifier to separate the individual channels. Figure 3.14 shows the mode-dependent gain for central-pump launch conditions measured as a function of the launched pump power for several different lengths of ring-doped EDF. The input signal power per channel was fixed at -2.5 dBm. For a 4 m length of EDF, the maximum achievable modal gain was 20 dB for the LP_{01} mode and 17 dB for the LP_{11} mode respectively. At a fixed pump power of 21 dBm, the gain for the LP_{01} mode increased monotonically from 14.8 dB to 16.6 dB as the length of EDF was increased from 4 m to 8 m. However, the gain of the LP_{11} mode increased from 10.6 dB to 11.2 dB for a 6 m length of fiber and then begins to decrease from 11.2 dB to 9.1 dB for further increases in EDF length. This behavior is attributed to the counter-propagating central-pump launch in conjunction with longer EDF lengths, because the LP_{11} mode ordinarily experiences greater absorption than

the LP_{01} mode at the signal input end, where the population inversion is the lowest due to the greater spatial overlap with the dopant.

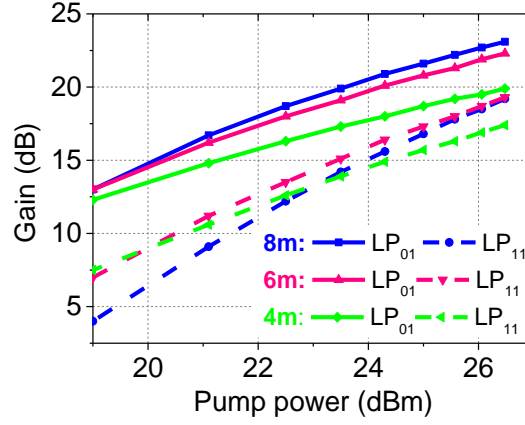


Figure 3.14. The measured modal gains as a function of input pump powers for several of EDF lengths. Data was provided by Dr Y. Jung.

Based on the experimental results that the gain for LP_{01} is about 3 dB higher than the gain for LP_{11} even under the central-pump launch condition (i.e. only circularly symmetric modes such as LP_{01} and LP_{02} were excited), we suspected that diffusion of the erbium ions from the outer ring towards the center of the core might have been taken place during the fabrication process. To test this hypothesis, I adopted an empirical mathematic formula shown below to model the erbium-doping profile as a result of the diffusion.

$$F(r) = 0.96N_{max} \cdot \left(\frac{e^{-\lambda r}}{e^{(-3.9 \times 10^{-6})\lambda}} \right) \quad 3.2$$

where r (i.e. $0 \leq r \leq 3.9 \times 10^{-6}$) is the radial position inside the inner core region, and λ determines the rate of exponential decay. In the denominator, $r = 3.9 \times 10^{-6}$ is the boundary between the inner core and the outer core of the ring-doped fiber shown in Figure 3.11. $F(r)$ provides a representation of the erbium-doping concentration distribution in the inner core of the ring-doped fiber. The erbium-doping profile is assumed to follow the FRIP in the outer core region. N_{max} is the maximum erbium-doping concentration of the ring-doped EDF, whose radial position coincides with the peak of the FRIP in the outer core region. $0.9N_{max}$ represents the erbium concentration at the inner and outer core interfaces. Given

that the measured absorption at 980 nm is 5.56 dB/m, the N_{max} can be interpreted from modeling once an assumption on the erbium-doping profile is made. Four erbium-doping profiles in the inner core region were investigated: (1) no diffusion, meaning no erbium ions in the inner core region, as shown in Figure 3.15(b); (2) slight diffusion, $F(r, \lambda = 6)$, as shown in Figure 3.16(b); (3) medium diffusion, $F(r, \lambda = 4)$, as shown in Figure 3.17(b); and (4) heavy diffusion, $F(r, \lambda = 2)$, as shown in Figure 3.18(b). Hence, the interpreted N_{max} that matches the measured absorption for the four cases are $1.46 \times 10^{25} \text{ m}^{-3}$, $1.37 \times 10^{25} \text{ m}^{-3}$, $1.22 \times 10^{25} \text{ m}^{-3}$ and $1.09 \times 10^{25} \text{ m}^{-3}$ respectively. For a simple and straight forward comparison with the experimental results, an EDF length of 6 m was chosen to perform the studies. The same input signal power per mode was used in the simulation compared to that of the experiment. From experience, the combination of LP₀₁ (i.e. 60%) and LP₀₂ (i.e. 30%) pump modes were chosen to model the central pump launch condition used in the experiment. The modal gain properties against the pump powers for the four different erbium-doping profiles are shown in Figure 3.15(a), Figure 3.16(a), Figure 3.17(a) and Figure 3.18(a) respectively.

As clearly evident by the red curves in Figure 3.15(a), the predicted gain for the LP₁₁ mode is considerably higher than the gain for the LP₀₁ mode for pump powers higher than 22 dBm, which is contrary to what was observed in the experiment. Based on this, it is strongly suggested that the diffusion of erbium dopants from the outer core towards the inner core had occurred during the fabrication process. From the following simulations presented in Figure 3.16(a), Figure 3.17(a), Figure 3.18(a), we show that the gain for LP₀₁ increases gradually as there are more erbium ions in the inner core, before finally roughly matching with the experimental results when the diffusion is modeled using Equation 3.2 with $\lambda = 2$. The doping profile shown in Figure 3.18(b) is not necessarily the real doping profile of the fiber, but it provides useful information on the amount of erbium ions that have diffused from the outer core into the inner core.

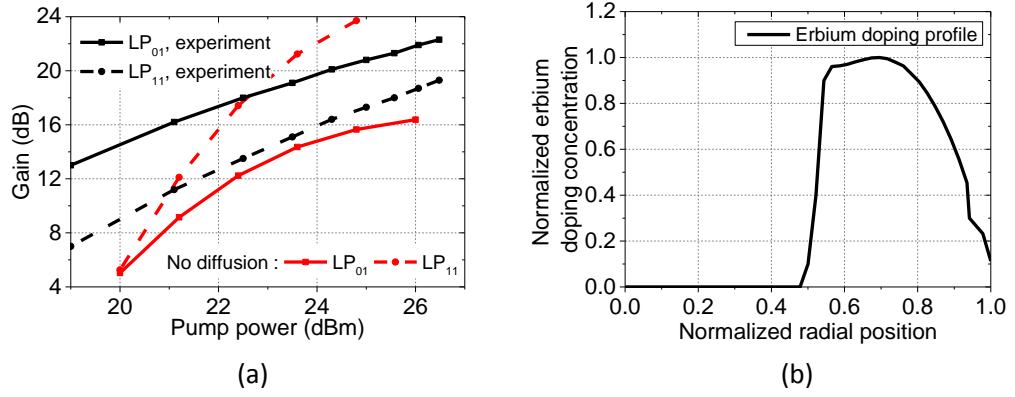


Figure 3.15. (a) Modal gain as a function of input pump powers. Black curves: experimental measurements, red curves: simulation fittings using erbium-doping profile (i.e. assuming no diffusion from outer core to inner core) shown in (b).

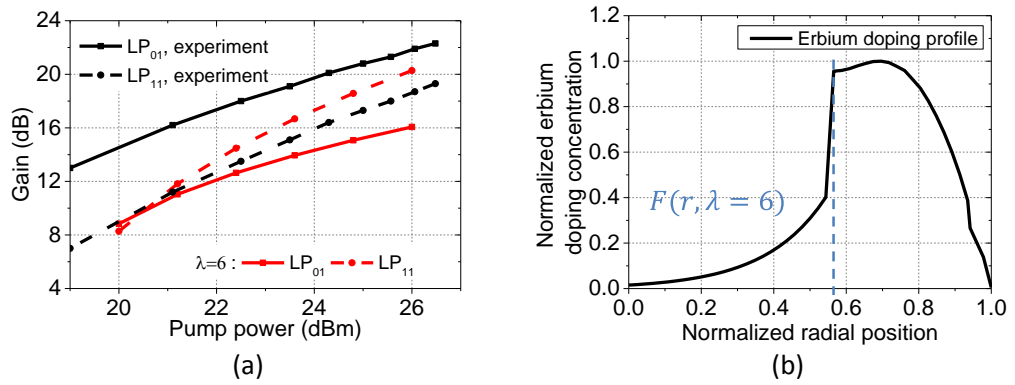


Figure 3.16. (a) Modal gain as a function of input pump powers. Black curves: experimental measurements, red curves: simulation fittings using assumed erbium-doping profile (i.e. $\lambda = 6$) shown in (b).

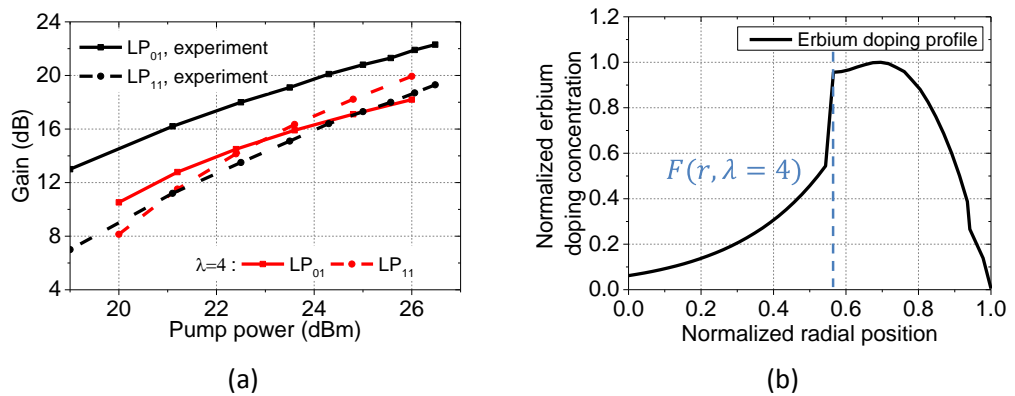


Figure 3.17. (a) The modal gain as a function of input pump powers. Black curves: experimental measurements, red curves: simulation fittings using assumed erbium-doping profile (i.e. $\lambda = 4$) shown in (b).

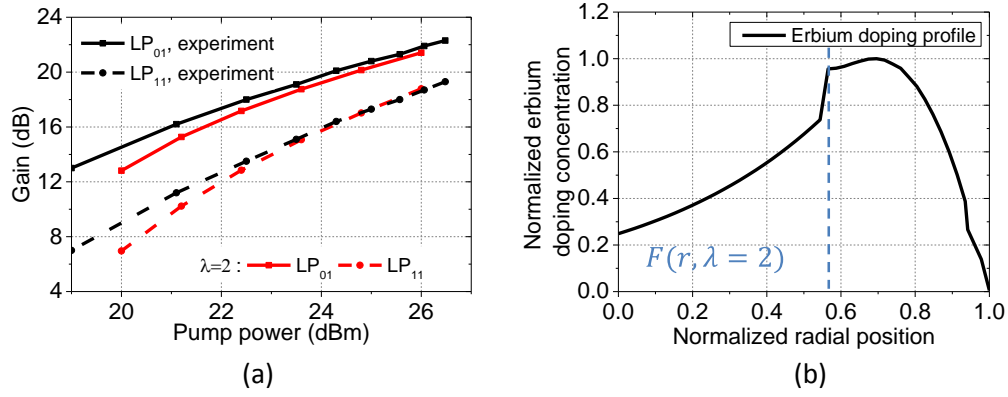


Figure 3.18. (a) Modal gain as a function of input pump powers. Black curves: experimental measurements, red curves: simulation fittings using assumed erbium-doping profile (i.e. $\lambda = 2$) shown in (b).

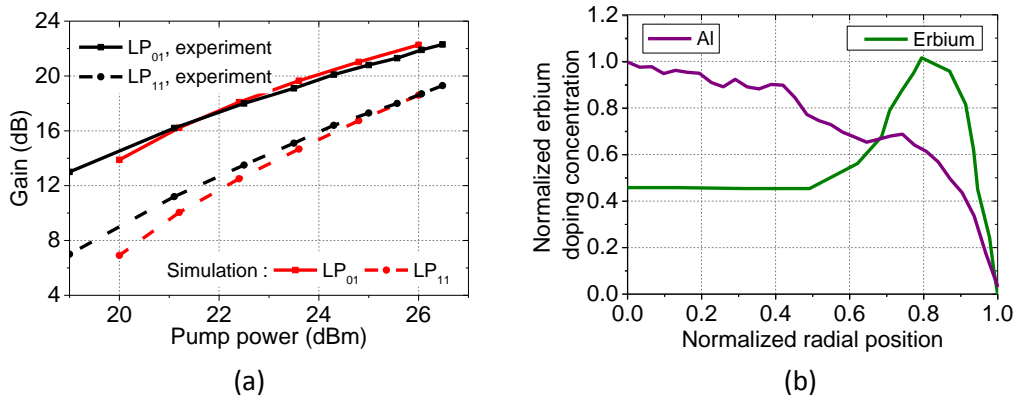


Figure 3.19. (a) The modal gain as a function of input pump powers; black curves: experimental data; red curves: simulation fittings using the measured erbium-doping profile shown in (b).

To investigate whether diffusion had occurred or not, through direct experimental verification, the dopant distribution in the fiber preform was measured by secondary ion mass spectrometry (SIMS). The normalized Al and Er dopant distributions are shown in Figure 3.19(b), where it can be seen that the RI profile closely follows the radial distribution of aluminium. However, although the erbium dopants are clearly concentrated within a distinct ring in the outer core region, undesired diffusion of Er^{3+} towards the center of the core was observed in accordance with our suspicions. The diffusion of erbium ions is to be expected to some degree during the final collapsing of the tube and/or additionally during the fiber-drawing process. The actual extent depends on several factors, including the composition of the glass host, the detailed nature of the heat treatment during the collapse, the duration of the collapse process, and

the fiber drawing temperature itself [61], [62], [66]. It may be possible to reduce this lateral dopant diffusion in future fibers by depositing a thin layer of pure SiO₂ as a diffusion barrier between the inner and outer core regions [67].

I estimated the Er doping concentration at 10×10^{24} ion/m³ according to the measured erbium profile and the 978 nm absorption value. The mode-dependent gains for central-pump launch condition with fiber lengths of 6 m are plotted as black lines in Figure 3.19(a), while the red lines denote simulations performed using the experimental parameters (e.g. measured RI and erbium profiles of the 2-mode-group EDF, signal and pump powers). The only assumption made for modeling the central-pump launch condition is that 64% of the pump power is assumed to be in the LP₀₁ mode and 36% in the LP₀₂ mode. The input signal power per channel was fixed at -2.5 dBm, and the wavelength chosen for signal modes is 1550 nm. There is a good agreement between the experimental results and simulation fittings. The differential modal gain was measured to be ~5 dB as shown Figure 3.19(a) for this choice of pump condition.

It was experimentally determined that the mode-dependent gain can be eliminated by using an offset-pump launch with a pump power of around 22-23 dBm (i.e. 6m length of EDF) as depicted by the blue lines in Figure 3.20. Again, the red lines represent simulation fittings obtained using experimental parameters. Here, the pump modal configuration is assumed to be LP₁₁ mode, as the pump profile observed by CCD camera during the experiment was found to be the LP₁₁ mode. Since the degenerate LP_{11a} and LP_{11b} pump modes can easily couple to each other, we assume that equal amount of LP_{11a} and LP_{11b} pump were excited by the offset-pump launch in this experiment. As depicted by the black lines in Figure 3.20, almost equal gain was observed for the two signal modes in the experiment and a very good agreement was reached with simulations. Both the experiments and the simulations show that the gain for the LP₁₁ signal mode becomes slightly higher than that of the LP₀₁ signal mode for high LP₁₁ pump powers.

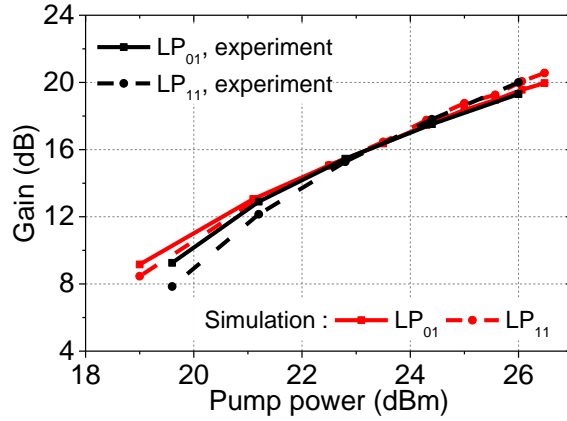


Figure 3.20. The mode-dependent gain evolution against pump powers for a 2-mode-group EDF of 6 m with the offset pump launch condition (i.e. LP₁₁ pump).

The experimental results are reasonably well matched with numerical modeling. These results demonstrate that DMG can be effectively mitigated using the author-designed ring-doped EDF in conjunction with the offset-pump launch condition (i.e. LP₁₁ pump). We ultimately expect that it will be possible to achieve zero mode-dependent gain for the simpler and more convenient case of using a central-pump launch by producing a fiber with a better-defined annular-dopant distribution illustrated in section 3.2.2.

To conclude, a 2-mode-group ring-doped EDF according to the author's design was fabricated in-house and a portable 2-mode-group EDFA with low DMG was built and tested, confirming the author's predictions. This 2-mode-group EDFA was subsequently used in joint experiments with Nokia Siemens Networks (NSN) to demonstrate a record MDM data capacity of 73.7 Tb/s over 119 km [68], [69], which was reported as a post-deadline paper at the ECOC conference in 2012. The experimental setup is shown in Figure 3.21 below. The in-line 2-mode-group EDFA was offset-core pumped and provided an almost equal gain of 18 dB per mode after the first span. In 2013, our amplifier was used in field experiments conducted by Dr V. Sleiffer, as shown in Figure 3.22 with Austrian Operator A1, providing the world-first field demonstration of the use of MDM [70]. The field experiments investigated possible single-mode transmission network upgrading scenarios, where a 2-mode-group fiber span with in-line 2-mode-group EDFA

was linked with field-deployed single-mode fibers. In early 2014, our amplifier again played a vital role in ensuring the success of a 1000 km re-circulating loop experiment based on three-spatial-mode (i.e. LP_{01} , LP_{11a} and LP_{11b}) fiber transmission, as shown in Figure 3.23 [71]. All these results generated a huge amount of technical and commercial interest. My 2-mode-group EDFA design lay at the heart of all of this success. The ORC is now commercializing the technology (i.e. core-pump 2-mode-group ring-doped EDFA) in collaboration with the company Phoenix Photonics Ltd [72].

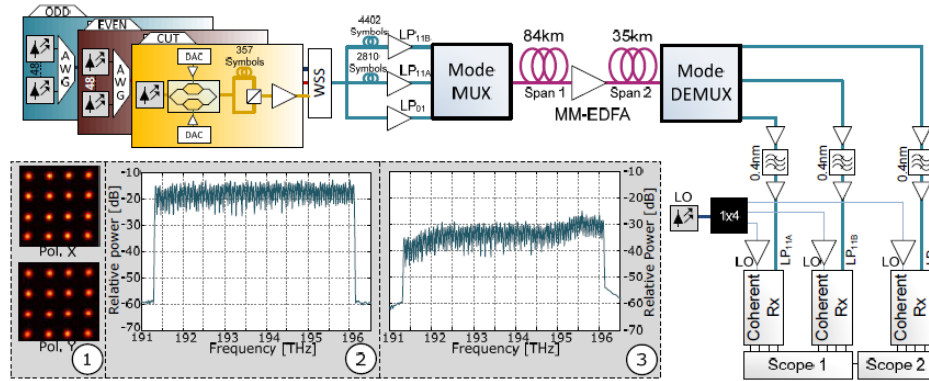


Figure 3.21. Experimental setup. 1: 256-Gb/s DP-16QAM constellations back-to-back single-mode. 2: Spectrum at the transmitter side (96 channels). 3: Spectrum after DEMUX. [27]

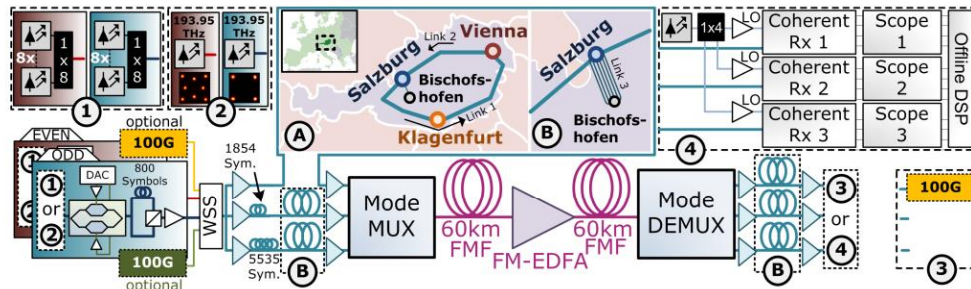


Figure 3.22. Field trial and few-mode link setup[70].

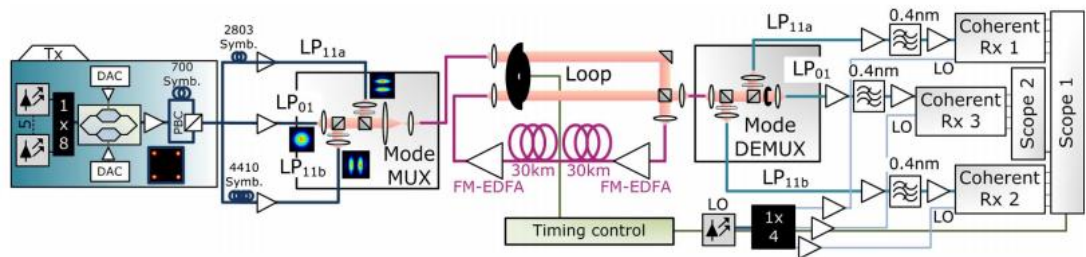


Figure 3.23. Re-circulating loop experimental setup with in-line 2-mode-group EDFAs over a total distance of over 1000 km[71].

3.4 Conclusion

This chapter started by studying the existing 2-mode-group EDFA (i.e. “batman” fiber). To evaluate the amplifier modeling tool, we conducted some simple and straight-forward experimental measurements of the “batman” 2-mode-group EDFA, of which the experimental results agreed very well with the simulation results. After obtaining confidence in the modelling, I advanced to work on new 2-mode-group EDFA designs. The most significant achievement of this chapter is the birth of the ring-doped 2-mode-group EDFA design, which underpinned all the subsequent 2-mode-group EDFA related experimental activities.

Having achieved these results, the next goal for my work was to increase the number of modes guided in a single fiber for capacity scaling. The simulation results presented in this chapter were computed by a commercial package Optisystem11.0®. However, there are several significant limitations of this commercial package:

1. The wavelength-division multiplexing (WDM) cannot be simulated simultaneously with mode-division multiplexing.
2. The maximum number of guided LP mode-group is only seven.
3. The true fiber modes, vector modes, are not supported by this commercial code.
4. It is impractical to use this packaged software to conduct numerical optimization of a large number of free design parameters.

Under these constraints, it became necessary for me to develop an in-house MM-EDFA simulator that allows for further in-depth modeling of the MM-EDFA, and to realize more sophisticated MM-EDFA designs through powerful optimization algorithms. These works are described in the following chapters.

Chapter 4: Development of the in-house MM-EDFA simulator

Due to constraints of the commercial MM-EDFA simulator summarized at the end of the previous chapter, it can be necessary to develop an in-house amplifier simulator to perform more flexible, transparent and comprehensive simulations. As we briefly discussed in chapter 2, the non-LP_{0m} modes are not real modes but linear combinations of two vector modes whose propagation constants are slightly different. So if there are no perturbations, the intensity profile of the non-LP_{0m} mode will periodically change as it propagate along the fiber, where the beat length is determined by the difference between the two vector modes that form the non-LP_{0m} mode. Whether this beating effect would make a difference and how large an impact it has on the LP mode based MM-EDFA simulation results is worth investigating. This chapter firstly introduces the step-by-step development of the in-house MM-EDFA model, starting from the simplest scalar model verified through the commercial code Optisystem 11.0®, before the development of a full-vector solution in section 4.2. Then in section 4.3, the 2-mode-group EDFA is modeled using vector modes, with different combinations of signal and pump modes to compare the difference in performance.

Next, since slight core ellipticity tends to exist in fabricated fibers, a slight core ellipticity of $\sim 0.5\%$ can transform radially, azimuthally or hybrid polarized vector modes into linearly polarized due to linear birefringence. In section 4.4, the impact of core ellipticity on the MM-EDFA is studied using our vector mode based amplifier model. In particular, the results of the vector mode based 2-mode-group EDFA with slight core ellipticity are compared to the results from the LP mode based circular-core 2-mode-group EDFA simulation.

To summarize, the main aims of this chapter are, firstly, to develop a flexible in-house MM-EDFA simulation tool (capable of modelling either LP modes or vector modes). Secondly, to investigate and compare the impact of several practical

issues (vector modes beating effects, core ellipticity) on the performance of MM-EDFA that are not considered in the LP mode based MM-EDFA simulations.

4.1 The validation of the in-house MM-EDFA simulator

The first version of the in-house MM-EDFA simulator that deals with multiple transverse modes using LP approximation was built by the author and her colleague Dr Eeleong Lim in late 2012. Our MM-EDFA simulator was written in the MATLAB language and compiled by MATLAB, based on the theories of modelling of MM-EDFA that were described in section 2.2, chapter 2. Our in-house MM-EDFA simulator was built to be capable of modeling $M \times N$ signal beams simultaneously, where M represents the number of WDM wavelengths, and N represents the number of spatial modes for MDM. There is no upper limit on the number of M and N for our MM-EDFA simulator, as long as the computer memory is sufficient. The ASE part of this in-house MM-EDFA was solely developed by the author. A shooting method was applied to solve the multimode and multi-wavelength forward and backward ASE components, as described in section 2.2.3, chapter 2.

In order to validate our in-house MM EDFA, a detailed comparison with the modeling results from the commercial code Optisystem 11.0® was conducted. Again, a weakly guiding two-mode-group EDFA (i.e. 2-mode-group EDFA) with an NA of 0.108 and core radius of 8 μm , as used in section 2.3 of chapter 2, was used to perform the simulations. The two-mode-group EDFA is fully doped with erbium ions with a concentration of $1.5 \times 10^{25} \text{ m}^{-3}$. Unlike section 2.3 of chapter 2, just two ASE components centered at 1550 nm and 1551 nm each with a 1 nm noise bandwidth, are considered in the modelling for simplicity, which is adequate for the purpose of validating the accuracy of the numerical resolution of the in-house MM-EDFA simulator. The 2-mode-group EDFA was forward pumped by a LP_{01} pump mode of 250 mW. Two signal modes, LP_{01} and LP_{11b} (i.e. defined in Table 2.2 of chapter 2) with -10 dBm per mode, were used as input signal beams. The fiber length of the 2-mode-group EDFA was chosen to be 4 m. In this very first version of the in-house MM EDFA, the so-called “shooting

method” was adopted to numerically solve the backward ASE noise. It is worth reminding the reader that the shooting method is a trial-and-error approach where in this case, the unknown backward ASE value at $z = 0$ m was initially set to zero. The system is then integrated from $z = 0$ m to $z = 4$ m. The corresponding forward ASE value at $z = 4$ m is then used as the boundary value for backward ASE at $z = 0$ m. With the updated initial value of the backward ASE from the first round, the system is integrated again from $z = 0$ m to $z = 4$ m, so that the first set of backward ASE is obtained. The backward ASE at $z = 4$ m is then compared with the desired value (i.e. ideally the backward ASE power spectrum is zero at $z = 4$ m), and the difference is used to correct the initial guess in the subsequent iterations [52]. After many integration trials, the backward ASE spectrum at $z = 4$ m should eventually vanish.

As it shown in Figure 4.1, the red dotted line represents the first set of total backward ASE data from $z = 0$ m to $z = 4$ m obtained from the in-house amplifier simulator, which reflects a good agreement with the optimal solution (i.e. shown by the solid black line given by the commercial code) from $z = 0$ m to $z = 3$ m. Here, “total” means that the power of the LP_{01} , LP_{11a} and LP_{11b} noise components is summed together. In Figure 4.1, the tail of the red dotted line near $z = 4$ m bounces back, which means that this set of backward ASE data are not the real solution yet and the values of the backward ASE at $z = 0$ m need to be slightly increased. After 10 iterations, the total backward ASE power profile, as shown by the green dotted line in Figure 4.1, vanishes at $z = 4$ m and it is in good agreement with the results given by Optisystem 11.0®. The total forward ASE power profiles obtained from the in-house amplifier simulator after 1 iteration and 10 iterations are shown by the red dotted line and green dotted line in Figure 4.2. After the 1st iteration, the forward ASE profile is in reasonable shape, but still differs slightly from the real solution given by the solid line obtained from Optisystem 11.0®. After 10 iterations, the forward ASE profile converges to the optimal profile, represented by the green dotted line and is in excellent agreement with the solid line provided by Optisystem 11.0®. The signal and pump power profiles against fiber length are illustrated in Figure 4.3 and Figure

4.4 respectively. As only two noise components are considered in the modeling, the ASE has little effect on the gain profile and pump absorption profile. The signals and pump power profiles obtained from the in-house MM-EDFA simulator were found to give an excellent agreement with the data from Optisystem 11.0®. Hence, the author's calculations are correct and the in-house MM-EDFA simulator can be reliably expanded and applied for more intensive simulations and amplifier designs.

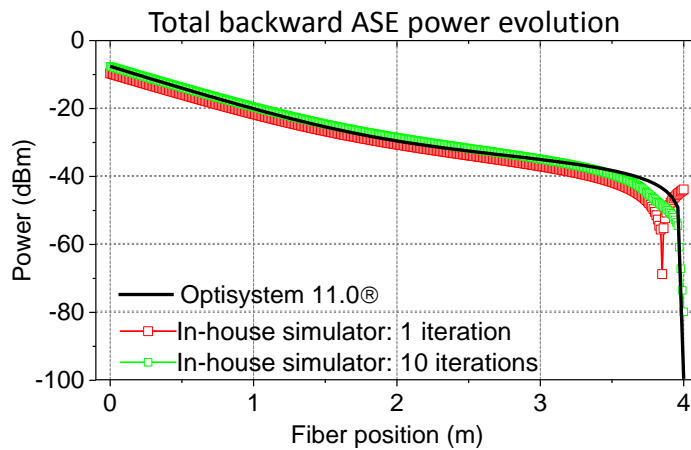


Figure 4.1. The total backward ASE power evolution against the fiber length. The solid black line represents the result obtained from Optisystem 11.0®. The red dots represent the results obtained from the in-house amplifier simulator after 1 iteration. The green dots represent the results obtained from the in-house amplifier simulator after 10 iterations.

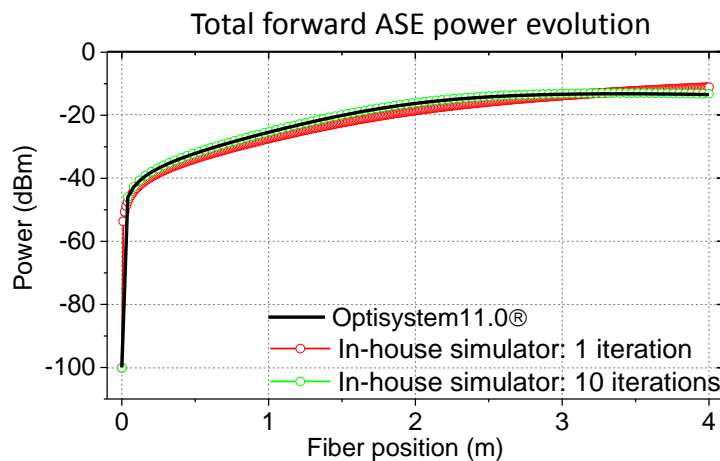


Figure 4.2. The total forward ASE power evolution against the fiber length. The solid black line represents the result obtained from Optisystem 11.0®. The red dots represent the results obtained from the in-house amplifier simulator after 1 iteration. The green dots represent the results obtained from the in-house amplifier simulator after 10 iterations.

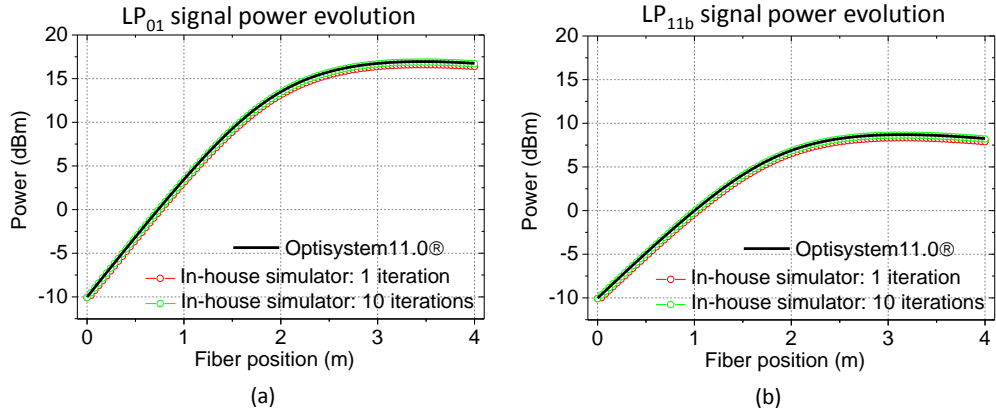


Figure 4.3. (a) The LP₀₁ signal power evolution and (b) the LP_{11b} signal power evolution against the fiber length. The solid black line represents the result obtained from Optisystem 11.0®. The red dots represent the results obtained from the in-house amplifier simulator after 1 iteration. The green dots represent the results obtained from the in-house amplifier simulator after 10 iterations.

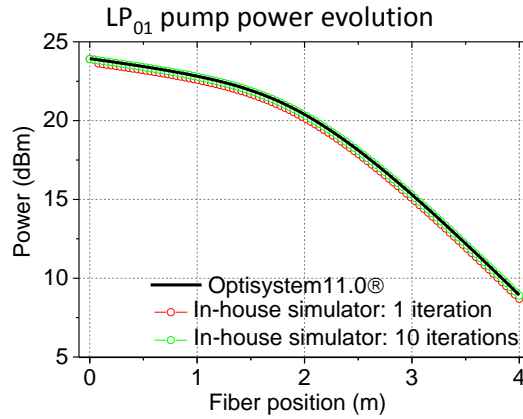


Figure 4.4. The LP₀₁ pump signal power evolutions against the fiber length. The solid black line represents the result obtained from Optisystem 11.0®. The red dots represent the results obtained from the in-house amplifier simulator after 1 iteration. The green dots represent the results obtained from the in-house amplifier simulator after 10 iterations.

4.2 Vector modes based MM-EDFA model

As discussed in section 2.1.3 of chapter 2, the LP modes (i.e. except circularly symmetric LP_{0m}) are actually composed of two vector modes that exhibit very close yet different effective RIs, and thus slightly different phase velocities. If signal modes come from a single narrow linewidth source, there will be inter-mode-beating effects, which will be discussed in section 4.3. The mode intensity profile of the LP mode formed by the constituent vector modes will evolve as it

propagates along the fiber, which is referred to as transverse-mode intensity evolution (TMIE) in [73]. For example, the LP_{11} mode is composed of TE_{01} (or TM_{01}) and HE_{21} depending on the orientation of its intensity profile. In the following section, the TMIE for LP_{11} mode in a two-mode-group SI fiber at 1550 nm is discussed.

4.2.1 Transverse mode intensity evolution in passive fibers

For the sake of consistency, a weakly guiding SI fiber with an NA of 0.108 and core radius of 8 μm is studied once more. At 1550 nm, the V number of this SI fiber is 3.50 and it guides 6 vector modes, namely $2 \times HE_{11}$, TE_{01} , TM_{01} and $2 \times HE_{21}$. Each vector mode has its corresponding propagation constant (β) and the accumulated phase shift is given by $\exp(-j\beta z)$, where z is the propagation distance. Furthermore, we define the difference in their accumulated phase shift between the two modes as the propagation phase shift (Φ_z). The propagation constants β and the electric/magnetic field distributions $E(r, \phi)$ and $H(r, \phi)$ of the vector modes are obtained from the vector mode solver in COMSOL Multiphysics 4.3®. n_{eff} of the TE_{01} mode is 1.4453339, while n_{eff} of $HE_{21(\text{odd})}$ mode is 1.4453308.

As discussed in the section 2.1.2, in the LP mode picture, the LP_{11} consists of four possible combinations of spatial orientation and polarization, commonly known as the $LP_{11a,x}$, $LP_{11a,y}$, $LP_{11b,x}$ and $LP_{11b,y}$ modes. The first subscript (e.g. a or b) indicates the spatial orientation and the second subscript (e.g. a or b) indicates the polarization orientation. When the $LP_{11b,x}$ mode, as shown in Figure 4.5 is excited at the fiber input, Φ_z between the corresponding composite vector modes TE_{01} and HE_{21} is chosen to be zero. The mode intensity profiles of TE_{01} and $HE_{21(\text{odd})}$ modes are shown in Figure 4.5 below. The combination of TE_{01} and HE_{21} results in the $LP_{11b,x}$ mode intensity profile as illustrated in Figure 4.5 at $\Phi_z = 0$. In the LP mode approximation, the propagation constant (β) is assumed to be the same for all the vector modes in the same mode group (e.g. β for TM_{01} , TE_{01} and HE_{21} in the LP_{11} mode-group). Therefore, Φ_z remains zero and the mode profile remains the same along the propagation distance. However, the β s are generally different among the vector modes within the same LP mode-group. In the SI fiber

defined above, the difference in the β of the $\text{HE}_{21(\text{odd})}$ and TE_{01} modes will result in a beat length ($L_{\text{beat},\text{signal}}$) of ~ 0.51 m at 1550 nm, according to the following equation [74]:

$$L_{\text{beat}} = \frac{2\pi}{|\beta_{\text{TE}_{01}} - \beta_{\text{HE}_{21}}|} \quad 4.1$$

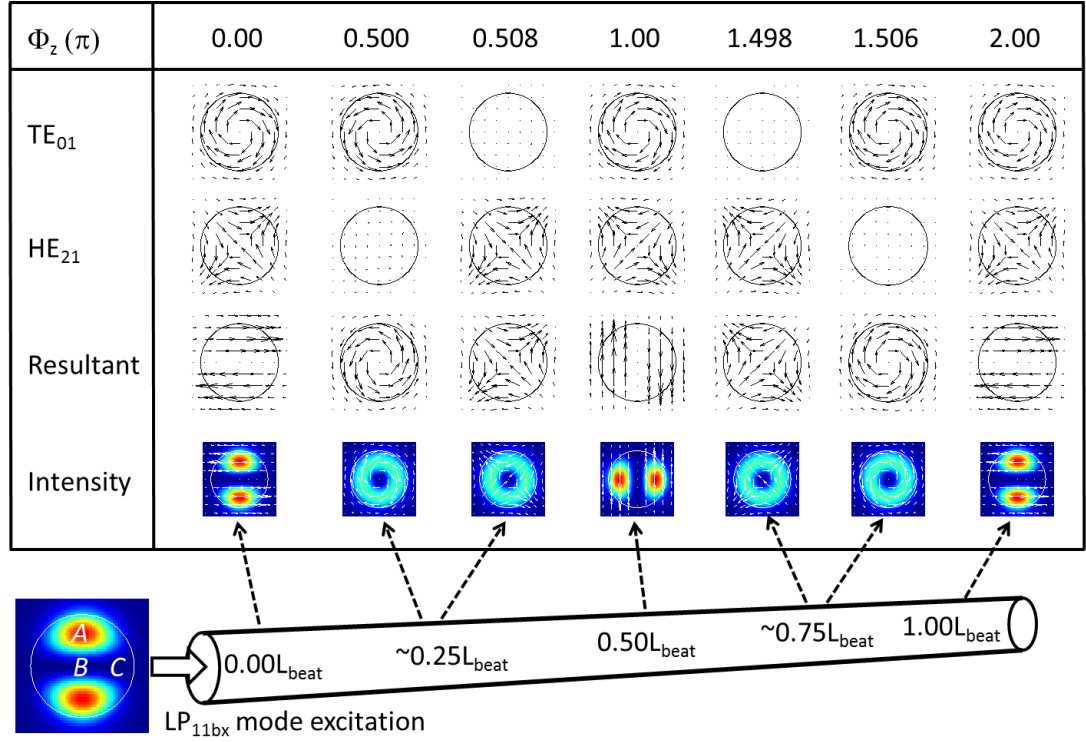


Figure 4.5. Mode intensity profile of (a) TE_{01} , and (b) $\text{HE}_{21(\text{odd})}$. The arrows indicate the electric field distribution. Location A ($0 \mu\text{m}$, $5 \mu\text{m}$), location B ($0 \mu\text{m}$, $0 \mu\text{m}$), and location C ($5 \mu\text{m}$, $0 \mu\text{m}$) are used in Figure 4.6.

The resultant mode-power density (i.e. or intensity) $I_R(r, \phi, z)$ of coherent modes is derived from the Poynting vector [75]:

$$I_R(r, \phi, z) = \frac{1}{2} \text{Re} \left(\vec{E}_R \times \vec{H}_R^* \cdot \vec{z} \right) \quad 4.2$$

Where E_R (i.e. or H_R) is the resultant electric (i.e. or magnetic) field distribution given by:

$$\begin{aligned}
E_R &= \sum \sqrt{P_k(z)} \exp(-j\beta_k z + j\theta_k) E_k \\
H_R &= \sum \sqrt{P_k(z)} \exp(-j\beta_k z + j\theta_k) H_k
\end{aligned} \tag{4.3}$$

where k is the index of the vector mode, β_k is the propagation constant, z is the propagation distance, θ_k is the initial phase, $P_k(z)$ is the power carried by the k^{th} mode and E_k (i.e. or H_k) is the normalized electric (i.e. or magnetic) field distribution of the k^{th} mode. For simplicity, the initial phase θ_k is set to zero. The resultant intensity profile $I_R(r, \phi, z)$ can also be written as:

$$I_R(r, \phi, z) = \frac{1}{2} \text{Re} \left(\begin{array}{ccc} \vec{x} & \vec{y} & \vec{z} \\ E_{Rx} & E_{Ry} & E_{Rz} \\ H_{Rx}^* & H_{Ry}^* & H_{Rz}^* \end{array} \cdot \vec{z} \right) \tag{4.4}$$

Which can be reduced to:

$$I_R(r, \phi, z) = \frac{1}{2} \text{Re} (E_{Rx} \cdot H_{Ry}^* - E_{Ry} \cdot H_{Rx}^*) \tag{4.5}$$

where E_{Rx} and E_{Ry} (i.e. or H_{Rx} and H_{Ry}) are the \vec{x} and \vec{y} components of the resultant electric (i.e. or magnetic) fields, which are calculated from the \vec{x} and \vec{y} components of the electric (i.e. or magnetic) fields of the k^{th} mode through Eq. 4.3. As the vector modes propagate along the fiber, the cumulative different phase shifts are described by the terms $\exp(-j\beta_k z)$ in Equation 4.3. Here, we define the difference in cumulated phase shift between the two modes as the propagation phase shift $\Phi_z = | \exp(-j\beta_a z) - \exp(-j\beta_b z) |$. With Equation 4.3 and Equation 4.5, the evolution of the resultant mode intensity and electric-field distributions of the two in-phase TE₀₁ and HE_{21(odd)} modes for different propagation distances are shown in Figure 4.5. At the input of the fiber, the two modes exhibit $\Phi_z = 0$ and results in LP_{11bx} mode, as shown in Figure 4.5. When $\Phi_z = \pi$ (i.e. corresponds to $0.5L_{beat,signal}$), the resultant intensity profile and electric field distributions resemble LP_{11ay}. When Φ_z equals 0.5π the resultant mode intensity is found to exhibit a doughnut-shaped intensity profile with an electric field distribution ($E_R(r, \phi, z)$) similar to that of TE₀₁ mode, as shown in Figure 4.5(d). In fact, around

$\Phi_Z = 0.5\pi$, the resultant electric field evolves rapidly between electric field distributions that resemble the TE_{01} and $HE_{21(\text{odd})}$ modes. When $\Phi_Z = \pi$ (i.e. corresponds to $0.5L_{\text{beat,signal}}$), the resultant intensity profile and electric field distributions resemble $LP_{11\text{ay}}$. Again, around $\Phi_Z = 1.5\pi$, the resultant intensity and electric field distributions again evolve rapidly between the TE_{01} and $HE_{21(\text{odd})}$ modes, i.e. similar to that at $\Phi_Z = 0.5\pi$. When the $\Phi_Z = 2\pi$ (i.e. corresponds to $L_{\text{beat,signal}}$), the resultant intensity and electric field are the same as that at the fiber input (i.e. $LP_{11\text{bx}}$). Similarly, it can be shown that when $LP_{11\text{ax}}$ is excited at the input of the fiber, it will consist of the vector modes TM_{01} and HE_{21} , and the resultant pseudo LP modes will evolve to $LP_{11\text{by}}$ when $\Phi_Z = \pi$.

This example reveals that in a weakly guiding fiber, the intensity pattern of the LP modes (i.e. except the circularly symmetric LP_{0m}) evolve periodically as they propagate along the fiber. To investigate the vectorial effects in few-mode EDFA, we have developed an MM-EDFA model based on vector modes, which will be described in the next section.

4.2.2 Vector modes based MM-EDFA model

In a vector mode (VM) based MM-EDFA, the phase as well as the mode intensity field of each signal/pump mode also needs to be considered. The terms $I_{s,k}(z)$ and $I_{p,k}(z)$ in Equations 2.46 and 2.47 of the scalar amplifier model in section 2.2.3, need to be replaced by the resultant signal/pump intensity profiles, where the mode beating effects are taken into account. Therefore, the resultant signal/pump intensity that is associated with the local erbium ions population is given by:

$$I_R(r, \phi, z) = \frac{1}{2} \text{Re} \left(E_R \times H_R^* \cdot \vec{z} \right) \quad 4.6$$

Where E_R and H_R are resultant electric and magnetic fields given by:

$$\begin{aligned} E_R &= \sum A_k \exp(-j\beta_k z + j\theta_k) E_k \\ H_R &= \sum B_k \exp(-j\beta_k z + j\theta_k) H_k \end{aligned} \quad 4.7$$

where k is the index of the vector mode, β_k is the propagation constant, z is the propagation distance, θ_k is the initial phase shift, A_k is the amplitude of the electric field corresponding to the power carried by the k^{th} mode, E_k and H_k are the normalized electric and magnetic fields of k^{th} mode. It is to be noted that, the k modes shown in Equation 4.7 are of the same wavelength and coherent to each other. Throughout this thesis, θ_k is set to 0 unless otherwise specified. The population inversion equation Equation 2.46 used for the scalar amplifier model is modified as:

$$N_1(r, \theta, z) = N_t \frac{1 + \frac{\sigma_e(\lambda_s)}{\sigma_a(\lambda_s) + \sigma_e(\lambda_s)} \frac{I_{R,s}(r, \phi, z)}{I_{sat}(\lambda_s)}}{1 + \frac{I_{R,s}(r, \phi, z)}{I_{sat}(\lambda_s)} + \frac{I_{R,p}(r, \phi, z)}{I_{sat}(\lambda_p)}} \quad 4.8$$

where $N_1(r, \phi, z)$ is the density of ions in the lower energy level, $N_t(r, \phi, z)$ is the erbium-doping profile, $\sigma_e(\lambda)$ and $\sigma_a(\lambda)$ are the emission and absorption cross-sections at a wavelength of λ , $I_{R,s}(r, \phi, z)$ and $I_{R,p}(r, \phi, z)$ are the resultant signal and pump mode intensities given by Equation 4.7, $I_{s,sat}$ and $I_{p,sat}$ are the saturation intensities at the signal and pump wavelengths respectively defined by Equation 2.38, in chapter 2. The ion density in the upper energy state level $N_2(r, \phi, z)$ is given by the difference between $N_t(r, \phi, z)$ and $N_1(r, \phi, z)$. The mode-power evolution of the signal mode is given by:

$$\frac{dP_{s,k}}{dz} = P_{s,k} \int_0^{2\pi} \int_0^{r_d} (\sigma_e(\lambda_s) N_2(r, \phi, z) - \sigma_a(\lambda_s) N_1(r, \phi, z)) I_k(r, \phi) r dr d\phi \quad 4.9$$

where $P_{s,k}$ is the mode power at the signal wavelength in the k^{th} mode, r_d is the doping radius and $I_k(r, \phi)$ is the normalized mode intensity profile. Similar equations can be formulated for the pump modes. For simplicity, we have neglected the effect of ASE when investigating the VM effects in a MM-EDFA. The

effect of TMIE on 2-mode-group EDFAs originated from the vector nature of the signal and pump mode will be discussed in the next section.

4.3 Impact of mode beating effects in 2-mode-group EDFA

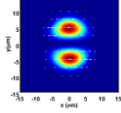
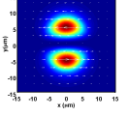
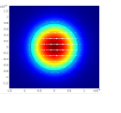
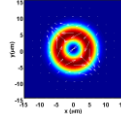
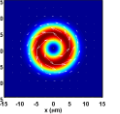
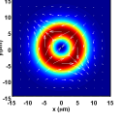
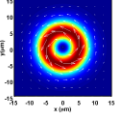
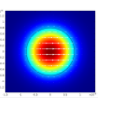
Having developed a vector amplifier model, I moved on to investigate the impact of mode beating effects in 2-mode-group EDFA. For the sake of consistency, the fiber parameters of the two-mode-group EDFA to be studied in this section are identical to the 2-mode-group EDFA analysed in section 4.1. This section is divided into 3 sub-sections according to different combinations of signal and pump modes, namely: (1) LP_{01s} and $LP_{11b,s}$ pumped by $LP_{11b,p}$; (2) LP_{01s} , $LP_{11a,s}$ and $LP_{11b,s}$ pumped by $LP_{11a,p}$ and $LP_{11b,p}$; and (3) LP_{01s} , $LP_{11a,s}$ and $LP_{11b,s}$ pumped by LP_{01p} . The signal/pump mode field profiles and their corresponding propagation constants (β) were obtained from simulation software COMSOL Multiphysics. The beat length between the $HE_{21(\text{odd})}$ and TE_{01} pump modes ($L_{beat,pump}$) is estimated to be 0.82 m at 980 nm, while the beat length ($L_{beat,signal}$) between $HE_{21(\text{odd})}$ and TE_{01} signal modes is estimated to be 0.51 m at 1550 nm. The amplifier length is chosen to be 5 m.

4.3.1 LP_{11b} pump

I investigated the case where 0.1 mW of LP_{01} / HE_{11} signal and 0.1 mW of LP_{11b} /“equivalent LP_{11b} ” signal and the EDFA is forward pumped by 250 mW of LP_{11b} /“equivalent LP_{11b} ” pump mode. The 0.1 mW of “equivalent LP_{11b} ” signal is the combination of the 0.05 mW $HE_{21(\text{odd})}$ and 0.05mW TE_{01} signals, which is equivalent to 0.1 mW of power launched into the $LP_{11b,x}$ mode at the input of the 2-mode-group EDFA and will be referred to as an “equivalent LP_{11b} signal mode” for convenience. Similar rules apply to the “equivalent LP_{11b} ” pump mode. In the LP mode model, the orientation of LP_{11b} pump mode aligned with that of the LP_{11b} signal mode along the full propagation length. Hence, the LP_{11b} signal is predicted to experience a much higher gain than the LP_{01} signal shown by the dashed lines in Figure 4.6(a). By contrast, the gain experienced by the HE_{11} mode (i.e. solid

blue) that is equivalent to the LP_{01} mode for the scalar case, is shown to be higher than the “equivalent LP_{11} signal mode” (i.e. red solid line) in the VM model.

Table 4.1. Intensity profile of the signal and pump modes used in the LP model and vector model respectively.

	Pump mode(s) intensity profile	Signal mode(s) Intensity profile
LP model	 Pump: LP_{11b}	  Signal: LP_{11b} Signal: LP_{01}
Vector model	  Pump: HE_{21odd} TE_{01}	   Signal: HE_{21odd} TE_{01} Signal: HE_{11}

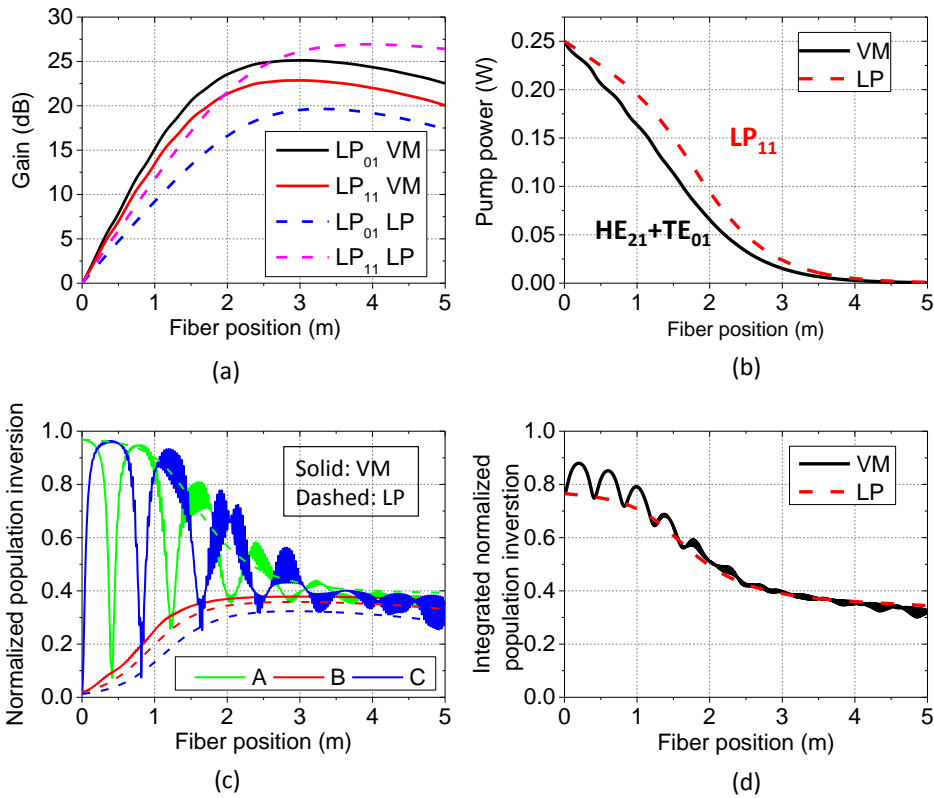


Figure 4.6. (a) Mode-power evolution of the HE_{11} signal mode (i.e. solid blue), the sum of HE_{21} and TE_{01} signal modes (i.e. dashed blue), LP_{01} signal mode (i.e. solid red) and LP_{11} signal mode (i.e. dashed red). (b) Modal pump depletion of the sum of HE_{21} and TE_{01} pump modes (i.e. solid blue) and LP_{11} pump mode (i.e. solid red) (c) The normalized population inversion along the fiber positions at 3 transverse spatial locations. Green: location A ($0 \mu\text{m}$, $5 \mu\text{m}$), red: location B ($0 \mu\text{m}$, $0 \mu\text{m}$), and blue: location C ($5 \mu\text{m}$, $0 \mu\text{m}$), as shown in

Figure 4.7 on page 69. The dashed lines are the simulated normalized population inversions based on the scalar LP model. (d) The integrated normalized population inversion against the fiber length for both the VM and the LP models.

In the vector model, the ions are pumped by the resultant intensity $I_R(r, \Phi, z)$. Therefore, there is an inversion profile that depends on $I_R(r, \Phi, z)$, which varies significantly along the fiber length. The normalized inversion profiles (N_2) shown in Figure 4.6(c) is defined as $N_2(r, \Phi, z)$ normalized to the maximum ion doping concentration. Since the population inversion exhibits a transverse spatial dependence along the FM EDFA, the evolution of N_2 at the 3 transverse positions labeled in Figure 4.5 (i.e., locations A , B and C) are plotted in Figure 4.6(c). Position A corresponds to the spatial position where the 980 nm pump intensity is maximum (i.e. at the input of the FM-EDFA, fiber position = 0 m). As shown in Figure 4.6(c), at the beginning, N_2 at A (i.e. solid green) is much higher than B (i.e. solid red) and C (i.e. solid blue). However, due to the TMIE of the pump, N_2 at A drops to a local minimum of ~ 0.08 at ~ 0.41 m (i.e., half of $L_{beat,pump}$). Thereafter, N_2 at A evolves to a local maximum of ~ 0.94 at ~ 0.82 m (i.e. at a longitudinal position corresponding to $L_{beat,pump}$). The behavior of N_2 at C exhibits the opposite trend to that of A . N_2 at C also oscillates with a high frequency component along the fiber position with a period of ~ 1.2 mm. This high frequency modulation is a result of the interference between the HE_{11} signal mode and the “equivalent LP_{11} signal mode”. Additionally, there is a further modulation due to the beating between HE_{21} (odd) and TE_{01} that results in a local minimum of N_2 at 0.7454 m and 1.4909 m (i.e. corresponding to $L_{beat,signal}$ and $2L_{beat,signal}$ respectively). N_2 at location B grows to a maximum of ~ 0.4 due to pumping of the ions by the 1550 nm HE_{11} signal as supported by the fact that maximum N_2 is close to the transparency inversion (i.e. ~ 0.42) at 1550 nm given by the expression $\sigma_a(\lambda_s)/[\sigma_e(\lambda_s) + \sigma_a(\lambda_s)]$ [76]. The inversion profiles derived from the LP mode model are shown by the dashed lines in Figure 4.6(c) for comparison. Therefore, the doughnut-shaped vector signal modes that form the LP_{11} mode at the amplifier input do not necessarily have a good spatial overlap with the inversion profile. Consequently, the “equivalent LP_{11} pump mode” does not create a higher

preferential gain for the “equivalent LP₁₁ signal mode” relative to the HE₁₁ signal mode.

The sum of the modal pump power of the HE_{21(odd)} and TE₀₁ modes is represented by the black solid line in Figure 4.6(b). The depletion of the modal pump power exhibits a degree of oscillatory behavior rather than the simple exponential-like profile of the LP-approximation model (i.e. dashed line). Furthermore, in the VM, the “equivalent LP_{11b}” pump absorption is higher because the TMIE effectively allows the pump power to be absorbed by more ions, especially when the “equivalent LP_{11b}” exhibits a donut-shaped intensity profile near Φ_z of $\sim 0.5\pi$ and 1.5π . In comparison, in the LP model the pump power is only absorbed by the ions spatially located within the LP_{11b} lobe. Hence, the pump power has the chance to interact with more ions in the VM than the LP and is therefore more strongly absorbed according to the VM.

Next, the integrated normalized population inversion $n_{int}(z)$ is defined as:

$$n_{int}(z) = \frac{\int_0^{2\pi} \int_0^{r_d} N_2(r, \phi, z) r dr d\phi}{\int_0^{2\pi} \int_0^{r_d} N_{Er}(r, \phi, z) r dr d\phi} \quad 4.10$$

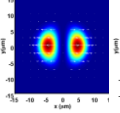
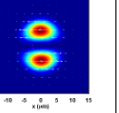
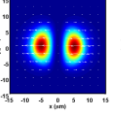
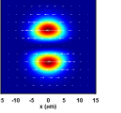
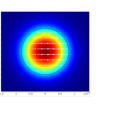
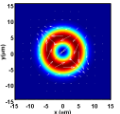
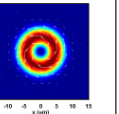
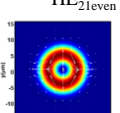
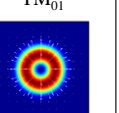
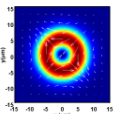
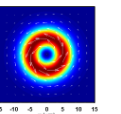
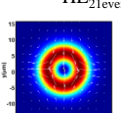
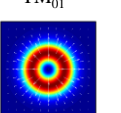
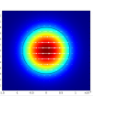
This quantity represents the portion of the ions in the excited state to the doping concentration within the transverse plane. Figure 4.6(d) shows the integrated normalized population inversion along the fiber position. The results show that the evolution of $n_{int}(z)$ for both the VM and LP are similar, except at the beginning of the fiber (i.e. fiber position < 1 m), where $n_{int}(z)$ is higher in the VM.

In summary, TMIE due to vector modes in a SI uniformly doped fiber causes the LP₁₁ signal mode to exhibit a far lower gain than the LP₀₁ signal mode when only pumped by an LP₁₁ pump mode. Moreover, the population inversion profile can exhibit strong spatial oscillations due to the TMIE associated with both pump and signal modes.

4.3.2 LP₁₁ pump

The discussion in section 4.3.1 is based on a very special case in which only LP_{11b,s} is used as a signal mode in the LP_{11s} mode-group, and only LP_{11b,p} is used as the pump mode. In this special case, the mode-beating effects is highly pronounced. Unlike this special case, in real MDM systems all spatial degeneracies (e.g. LP_{11a} and LP_{11b}) will be used as signalling channels. In this section, the investigation covers the case where 0.1 mW of LP₀₁/HE₁₁ signal and 0.1 mW of LP₁₁/“equivalent LP₁₁” signal forward pumped by 250 mW of LP₁₁/“equivalent LP₁₁” pump mode. In the LP model, the 0.1 mW of power is equally split between the LP_{11a} and LP_{11b} modes. In the VM model, the 0.1 mW of power is equally split among the HE_{21even}, HE_{21odd}, TE₀₁ and TM₀₁ modes. Unlike the case in section 4.3.1, here the LP₁₁ pump contains equal powers of LP_{11a,p} and LP_{11b,p}. Table 4.2 below gives a clear picture of the comparison between the signal and pump modes used for simulations in the LP and VM models. The simulated modal gain and pump power evolution based on the LP and VM models are shown in Figure 4.7(a) and (b) respectively.

Table 4.2. Intensity profile of the signal and pump modes used in the LP model and vector model respectively.

	Pump mode(s) intensity profile	Signal mode(s) Intensity profile
LP model	  Pump: LP _{11a} LP _{11b}	   Signal: LP _{11a} LP _{11b} Signal: LP ₀₁
Vector model	  Pump: HE _{21odd} TE ₀₁   HE _{21even} TM ₀₁	  Signal: HE _{21odd} TE ₀₁   HE _{21even} TM ₀₁  Signal: HE ₁₁

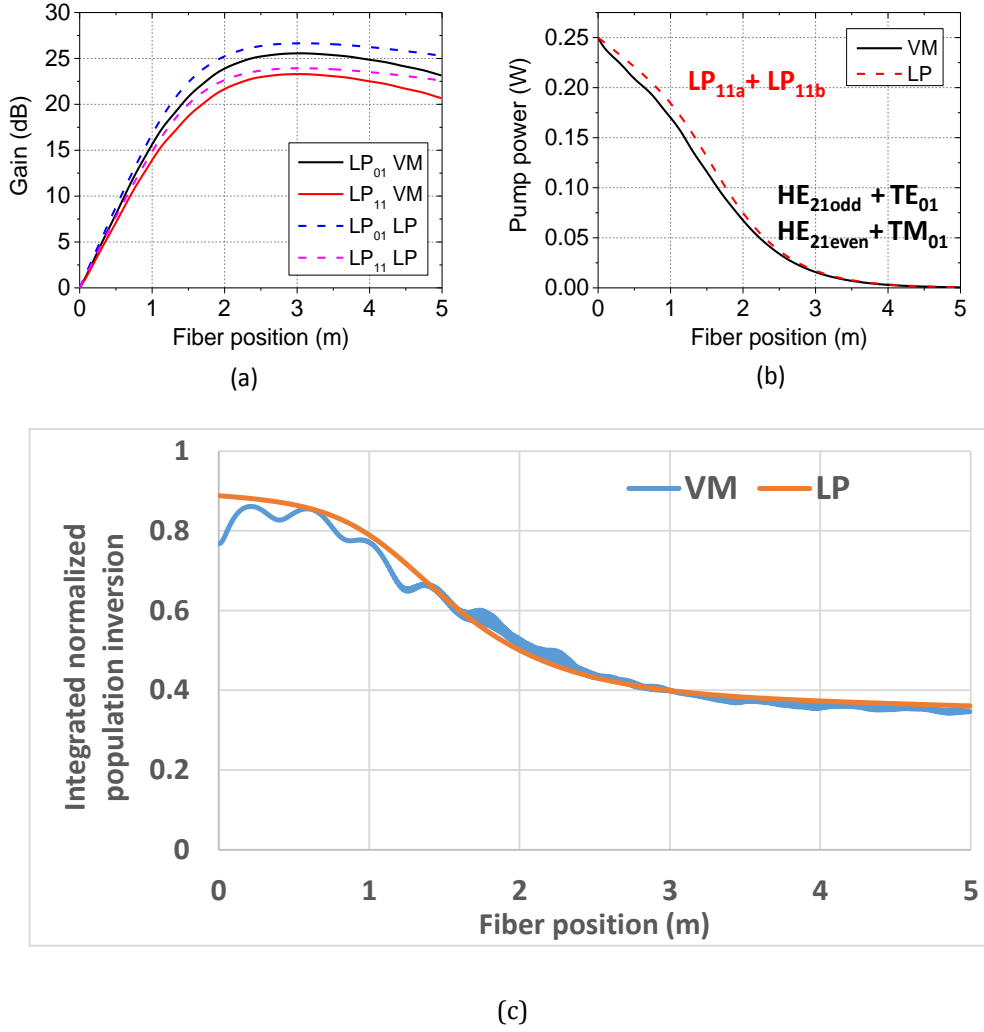


Figure 4.7. (a) Modal gain power evolution of the LP_{01} / HE_{11} signal mode (i.e. solid line) on the LP_{11} /"equivalent LP_{11} signal mode" (i.e. dashed line) pumped by LP_{11} /"equivalent LP_{11} " pump mode simulated under LP/vector 2-mode-group EDFA models. (b) The corresponding pump power evolution under 2 different models. (c) The integrated normalized population inversion against the fiber length for both the VM and LP models.

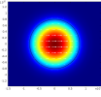
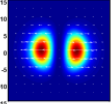
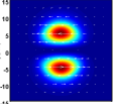
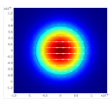
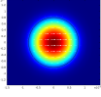
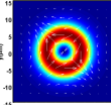
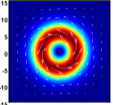

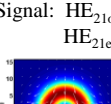
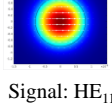
From the VM model simulation, it was confirmed as anticipated, that the four vector modes (i.e. HE_{21even} , HE_{21odd} , TE_{01} and TM_{01}) belonging to the same LP mode-group experience nearly identical gains. Hence, the modal gain for the four vector modes are represented by one red solid line shown in Figure 4.7(a). Figure 4.7(c) shows that the average population inversion at the beginning of the amplifier is slightly higher in the LP model than that in the VM model. The difference on the inversion level between the VM and LP models also resulted a

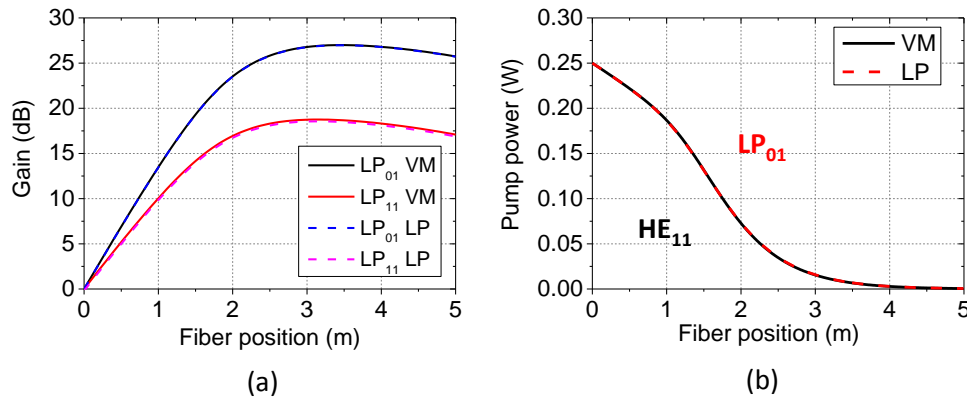
reasonable difference on the modal gains obtained from the two models. The modal gains calculated using the LP model are about 2.5 dB higher than those of the VM model. It is to be noted that in contrast to the results shown in section 4.3.1, the modal gains based on the VM model do not differ dramatically from the modal gains given by the LP model. This is because once all the spatial degeneracies are multiplexed, the overlap between the signal, pump and erbium ions becomes similar for the LP and VM models, and thus the effects of TMIE tend to be averaged out along the fiber length.

4.3.3 LP₀₁ pump

After discussions regarding the LP₁₁ pump, in this section the models are based on the circularly symmetrical pump mode, LP₀₁ pump, as shown in Table 4.3 below. The signal/pump input conditions are exactly the same as the conditions used in section 4.3.2, apart from that the LP₀₁/HE₁₁ pump mode is used rather than the LP₁₁ pump. The simulated modal gain and pump power evolutions based on the LP and VM models are shown in Figure 4.8(a) and (b) respectively. Since the LP₀₁/HE₁₁ signal exhibits a higher modal overlap with the LP₀₁/HE₁₁ pump, the LP₀₁/HE₁₁ signal experiences much a higher gain than the LP₁₁/“equivalent LP₁₁” signal mode. Furthermore, the maximum difference in the simulated signal gain among the LP and VM models is about 0.7%, which is very little. For example, the gain for LP₀₁ based on the LP model is 26.9 dB, and the gain for LP₀₁ based on the VM model is 27.1 dB at fiber position of $z = 5$ m. This is because when a circular symmetric pump mode is used, such as LP_{01p}, the overlap between signal and pump is almost the same regardless whether it is in the LP model or VM model. Figure 4.8(b) shows that there is no noticeable difference among the two cases in the pump power evolution. These results prove that the scalar model is reasonably accurate for the modeling of the amplification of the LP₀₁ and LP₁₁ signal modes pumped by the LP₀₁ pump mode [22].

Table 4.3. Intensity profile of the signal and pump modes used in the LP model and vector model respectively.

	Pump mode(s) intensity profile	Signal mode(s) Intensity profile
LP model	 Pump: LP ₀₁	   Signal: LP _{11a} LP _{11b} Signal: LP ₀₁
Vector model	 Pump: HE ₁₁	     Signal: HE _{21odd} HE _{21even} TE ₀₁ TM ₀₁ Signal: HE ₁₁

Figure 4.8(a) Modal signal power evolution of the LP₀₁/HE₁₁ signal mode (i.e. solid line) and the LP₁₁/“equivalent LP₁₁ signal mode” (i.e. dashed line) pumped by the LP₀₁/HE₁₁ pump mode simulated under LP/vector FM-EDFA models. (b) The pump power evolution under 2 different models.

4.3.4 Conclusion

To conclude, in the VM model transverse mode intensity evolution (TMIE) can create a profound impact on the modal gain performance in contrast to what is anticipated from the simpler scalar model in a 2-mode-group EDFA where the LP_{11b,s} (or LP_{11a,s}) is pumped by the LP_{11b,p} (or LP_{11a,p}) mode. The impact of the mode-beating effect on the amplifier output is very small when the full sets of the non-LP_{0m} mode group for both signal and pump modes are used in the amplifier

modeling. In particular, when the pump mode is circular symmetric LP_{0m} (i.e. LP_{01} pump), the difference on the results given by the LP model and the VM model is negligible. In weakly guiding FMF based MDM systems, it is true that all spatial degeneracies of the LP mode groups that supported in the FMF are used as signalling channels. When modeling core-pumped FM or MM-EDFA based on LP modes, it is important that the non- LP_{0m} pump mode should be treated as a combination of its two different spatial orientations, such that the pump intensity profile has no azimuthal dependence. With these precautions in mind, the LP model is sufficiently accurate to predict the gain characteristics of FM or MM-EDFAs, just like we have demonstrated in section 3.1, chapter 3.

4.4 Birefringence effects in 2-mode-group EDFAs

It has been long recognized that the core of almost all fabricated fibers, both passive and active, exhibit a finite ellipticity due to manufacturing imperfections [77], [78]. The ellipticity can result in form- and stress-induced birefringence in the optical fibers that can significantly alter their modal characteristics. For example, it will be shown in the following section that an ellipticity of $<0.5\%$ is sufficient to change the donut-shaped vector modes of a SI fiber into linearly polarized vector modes (LP VMs)[34]. In this section, we study the impact of birefringence due to core ellipticity on the characteristics of the guided modes and modal gain of 2-mode-group EDFAs.

4.4.1 The birefringence model

The form-induced birefringence in an elliptic-core fiber is due to the difference in the geometric extent of the fiber core in the x - and y -directions. However, stress-induced birefringence exists in both circular- and elliptic-core fibers and arises from the introduced stress that is imparted into the fiber during the fabrication stage. This non-uniform stress can significantly modify the RI profile of the fiber, and thus its optical characteristics. The change in the RI profile is governed by the thermo-optic and stress-optic relations. The general (i.e. tensorial) linear stress-optical relation can be written as [79]:

$$\Delta n_{ij} = -C_{ijkl} \sigma_{kl} \quad 4.11$$

where $\Delta n_{ij} = n_{ij} - n_0$, n_{ij} is the RI tensor, n_0 is the RI for a stress-free material, C_{ijkl} is the stress-optic tensor, and σ_{kl} is the stress tensor. Exploiting the symmetry and isotropic nature of the silica material system (i.e. n_{ij} and σ_{kl} are both symmetric), the stress-optic equation can be simplified to the following form [79]:

$$\begin{bmatrix} \Delta n_x \\ \Delta n_y \\ \Delta n_z \end{bmatrix} = - \begin{bmatrix} C_2 & C_1 & C_1 \\ C_1 & C_2 & C_1 \\ C_1 & C_1 & C_2 \end{bmatrix} \begin{bmatrix} \sigma_x \\ \sigma_y \\ \sigma_z \end{bmatrix} \quad 4.12$$

where $n_x = n_{11}$, $n_y = n_{22}$, $n_z = n_{33}$, $\sigma_x = \sigma_{11}$, $\sigma_y = \sigma_{22}$ and $\sigma_z = \sigma_{33}$, C_1 and C_2 are two independent parameters. Hence, Equation 4.12 can be written in the following form:

$$\begin{aligned} n_x &= n_0 - C_2 \sigma_x - C_1 (\sigma_y + \sigma_z) \\ n_y &= n_0 - C_2 \sigma_y - C_1 (\sigma_z + \sigma_x) \\ n_z &= n_0 - C_2 \sigma_z - C_1 (\sigma_x + \sigma_y) \end{aligned} \quad 4.13$$

It is assumed while using C_1 and C_2 that the non-diagonal parts of n_{ij} and σ_{kl} are negligible, implying that the shear stress corresponding to σ_{12} ($\equiv \sigma_{xy}$) can be neglected. In addition, the plane-strain approximation can be applied since the fiber is assumed to be free in the x- and y-directions and the strain in the z-direction is assumed to be zero. The plane-strain approximation implies that the shear-stress components corresponding to σ_{13} ($\equiv \sigma_{xz}$) and σ_{23} ($\equiv \sigma_{yz}$) can be neglected.

The above model was implemented through COMSOL Multiphysics 4.3® by Dr. Sonali Dasgupta. The model was used to obtain the optical mode characteristics for a fiber with an elliptic core.

4.4.2 Modes in fibers with slight core ellipticity

We quantify the fiber core ellipticity by the percentage difference between the major and the minor axes, denoted by the deviation (D). For example, the minor axis is parallel to the horizontal axis and is fixed at $8\text{ }\mu\text{m}$. Thus, a D of 0.5% corresponds to a fiber core size with minor and major axes of $8.00\text{ }\mu\text{m}$ and $8.04\text{ }\mu\text{m}$ respectively, as shown in Figure 4.9.

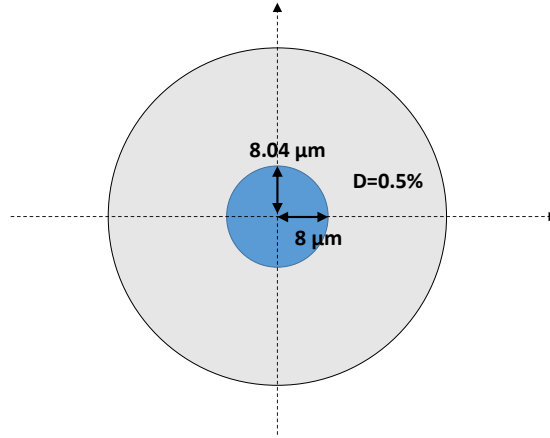


Figure 4.9. A schematic diagram to illustrate the dimensions of an elliptical core with $D = 0.5\%$.

The effects of form- and stress-induced birefringence are modeled using COMSOL Multiphysics 4.3® (i.e. elaborated in Section 4.4.1), using the following parameters for silica:

1. Thermal expansion coefficient of cladding/core: $1 \times 10^{-6} / 2 \times 10^{-6} / \text{K}$
2. Young's modulus: 78 GPa
3. Poisson's ratio: 0.42
4. Density: 110.3 kg/m^3
5. First/second stress-optic coefficient: $0.75 \times 10^{-12} / 4.2 \times 10^{-12}\text{ m}^2/\text{N}$
6. Reference temperature: 1273.2 K and operating temperature: 293.15 K .

A reference LP_{11} mode ($\text{LP}_{11,\text{ref},s}$) is first constructed from the vectorial sum of equal signal powers in the TE_{01} and HE_{21} modes of the fiber at $D = 0\%$. The mode intensity profile of $\text{LP}_{11,\text{ref},s}$ is shown as the inset in Figure 4.10. Next, this $\text{LP}_{11,\text{ref},s}$ is used as the excitation field at the fiber input. The $\text{LP}_{11,\text{ref},s}$ couples only to two guided modes with the coupling coefficient (η), defined in Equation 3.1 of chapter

3, at various values of D shown in Figure 4.10. At $D = 0.5\%$, $LP_{11,ref,s}$ effectively couples to only one of the LP VMs (i.e. $\eta \approx 1$). This mode with $\eta \approx 1$ at $D = 0.5\%$ will subsequently be denoted as LP VM (i.e. 0.5%). Due to the choice of the direction of the minor axis, the maxima of the LP VMs coincide with the maxima of $LP_{11,ref,s}$. Likewise, the HE_{21even} and TM_{01} modes in a 2-mode-group EDF with $D = 0\%$ will deform into $LP_{11a,x}$ and $LP_{11b,y}$ respectively when $D = 0.5\%$.

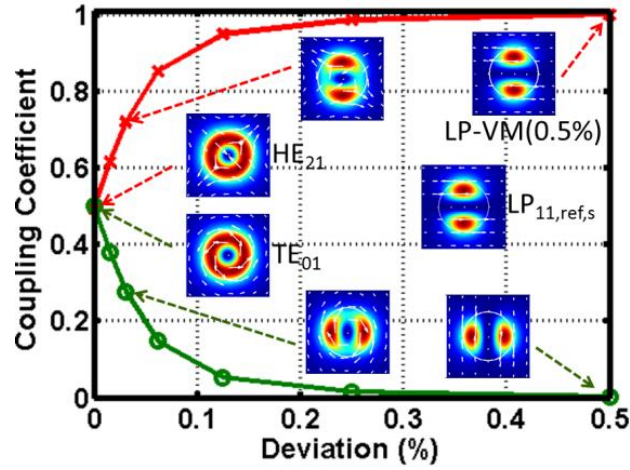


Figure 4.10 The coupling coefficient of the $LP_{11,ref,s}$ into the two vector modes at different deviations (D). The insets show the mode intensity profiles (MIPs) of the vector modes at various values of D and of the $LP_{11,ref,s}$. The white circles outline 8 mm radius circles.

4.4.3 The modal gain in two-mode erbium-doped fiber amplifiers with an elliptical core

In order to study the impact of the core ellipticity on the modal gain properties of a 2-mode-group EDFA, the modeling of the modal gain properties of a 2-mode-group EDFA with $D = 0.5\%$ and 0.1% based on the VM model is conducted. When $D = 0.5\%$, the donut-shaped vector modes (i.e. TM_{01} , TE_{01} and $2 \times HE_{21}$) evolve into LP VMs. The degenerate HE_{21even} and HE_{21odd} modes when $D = 0\%$ now become non-degenerate due to the ellipticity, which will introduce additional mode beating in the VM model compared with the $D = 0\%$ case. The modal n_{eff} of the four LP VMs (i.e. belong to the LP_{11} mode-group) at a signal wavelength of 1550 nm corresponding to a $D = 0.5\%$ obtained from COMSOL Multiphysics 4.3® are 1.4453356, 1.4453367, 1.445344 and 1.445346. The modal n_{eff} of the four LP VMs

(i.e. belong to the LP_{11} mode-group) at a pump wavelength of 980 nm are 1.4533374, 1.453338, 1.4533429 and 1.453344 respectively. The impact of this level of ellipticity (i.e. $D = 0.5\%$) on the fundamental mode HE_{11} is negligible, given that the difference on the mode intensity profile of HE_{11x} and HE_{11y} is less than 0.1%. In this section, the input signal and pump power levels are exactly the same as the conditions used in section 4.3.2, apart from that the “equivalent LP_{11} ” signal/pump is composed of the four LP VM signal/pump modes. In another words, in the VM with $D = 0.5\%$ model, the 0.1 mW power of “equivalent LP_{11} ” signal is equally split among the $LP_{11a,x}$, $LP_{11a,y}$, $LP_{11b,x}$ and $LP_{11b,y}$ signal modes, and the 250 mW power of “equivalent LP_{11} ” pump is equally split among the $LP_{11a,x}$, $LP_{11a,y}$, $LP_{11b,x}$ and $LP_{11b,y}$ pump modes. The fiber core ellipticity is assumed to be the same across the fiber length. The modal gain evolution as a function of the fiber position for the VM model with $D = 0.5\%$ are plotted as black lines (i.e. solid line for the LP_{01} mode, dashed line for the LP_{11} mode-group) shown in Figure 4.11. For comparison, the modal gain evolution against the fiber position for the VM model with $D = 0.1\%$ is shown as red lines in Figure 4.11. These results are then compared with the modal gain properties of a 2-mode-group EDFA (i.e. with $D = 0\%$) with the same input signal/pump power levels but simulated under the LP model.

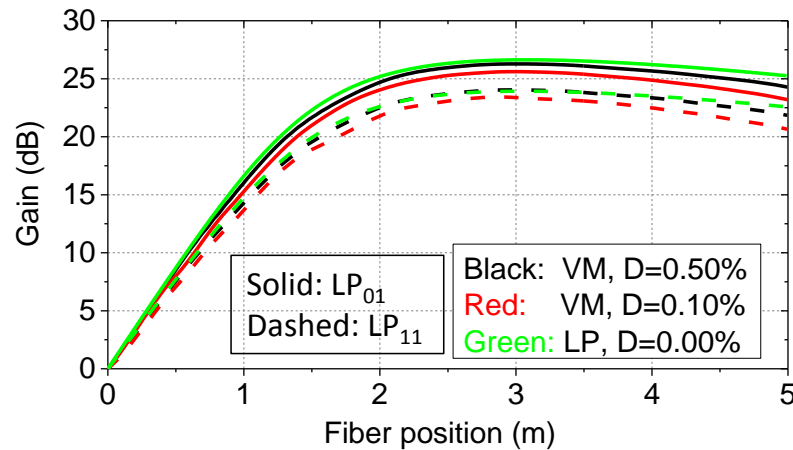


Figure 4.11. Comparison of the modal gain evolutions based on the VM model at various values of D with coherent modes, as shown by the black and red lines. The green lines represent the modal gain evolutions based on the LP model.

Although the mode intensity profile of the LP VMs (i.e. $D = 0.5\%$) look similar to the LP modes (i.e. $D = 0\%$), there is significant difference in the modeling in which the LP VMs are coherent to each other. They have similar yet different propagation constants, and thus travel at different speeds along the fiber. Therefore, mode beating is present. However, in the LP model the modes are considered incoherent to each other, so that it is mode intensity profiles that are summed together rather than the mode fields, as illustrated by Equation 2.45 in chapter 2. Therefore, mode beating is absent in the scalar amplifier model. Figure 4.11 shows that the modal gains simulated under the LP model with $D = 0\%$ are slightly higher than those simulated under the VM model with $D = 0.5\%$ and $D = 0.1\%$. It also indicates that when the fiber core is slightly elliptical, the difference in the results simulated under the LP model and VM model is reduced by a noticeable amount. As discussed in section 4.3.2, the gain difference between the LP and VM models when $D = 0\%$ is about 2.5 dB. Now with $D = 0.5\%$ the difference is reduced to ~ 0.7 dB, which is within the amplifier experimental-measurement error bar.

The core ellipticity of $D = 0.5\%$ is comparable to the typical D value of communications-grade fiber between 0.3-1.8% [77]. These results indicate that the LP model gives a fairly accurate approximation for the modeling of the amplification of LP₀₁ and LP₁₁ signal mode pumped by non-circular symmetrical pump modes (e.g. LP_{11p}) when the fiber core is slightly elliptical (e.g. $D = 0.5\%$).

4.4 Discussion of modal coherency in few-mode EDFAs

For the VM model in the previous sections, it is assumed that both the signal and pump modes are excited from one frequency source, and the multiple transverse modes at the same wavelength are fully coherent with each other. In a high bit-rate phase-modulated MDM system, there is no continuous wave (CW) power at the carrier frequency for PSK, QPSK and QAM modulation schemes. Hence, there is no interference effect due to the CW power component. Furthermore, in an MDM system, the different signal modes act as independent information channels. Hence, the digital data and phase modulation on the different signal

modes is independent. In fact, in the current MDM transmission experiments, the signal modes are intentionally symbol-delayed for de-correlation [68]. This independent phase-modulation results in a random phase variation among the signal modes. Thus, the signal modes in MDM system can be considered as incoherent modes, which applies to both circular-core EDFAs and EDFAs with slight core ellipticity.

With this concept in mind, the simulations in Figure 4.7 of section 4.4.3 were re-done, while keeping the LP VMs and all other simulation conditions the same. The beating effects were removed by modifying the mode field summation into a mode intensity summation. Figure 4.12 shows the simulated modal gain evolutions for the 2-mode-group EDFA with $D = 0.5\%$ without mode beating. As expected, nearly identical results are obtained for simulations using LP modes of 2-mode-group EDFA with $D = 0\%$ and LP VMs of the 2-mode-group EDFA with $D = 0.5\%$.

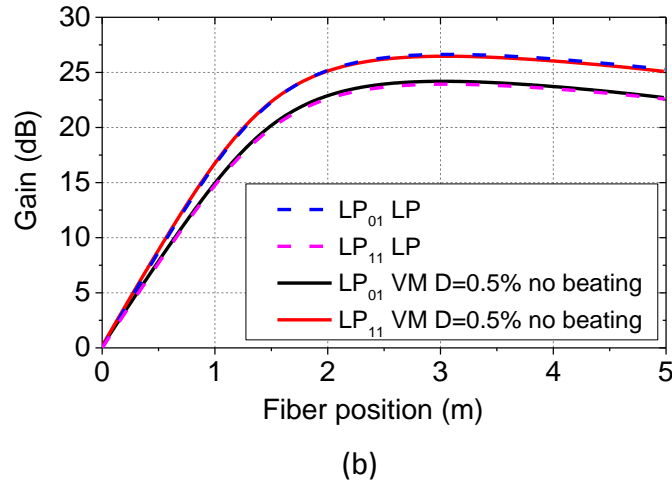


Figure 4.12. Comparison of modal gain evolutions along the fiber position for the 2-mode-group EDFA simulated using LP modes and LP VMs for $D=0.5\%$ without mode beating.

In conclusion, the results shown in Figure 4.12 that the LP and VM models are equivalent for the 2-mode-group EDFA with the conditions: (1) all the spatial degeneracies of the signal (i.e. or pump) mode-group involved are excited; (2) the fiber is weakly guiding the core is slightly elliptical for example, $D = 0.5\%$; (3)

the signal modes (i.e. the LP VMs) are incoherent. These three conditions are generally true for FM-EDFAs in real MDM systems.

4.5 Conclusion

The in-house 2-mode-group EDFA simulator based on LP modes was validated by comparing it with the results from the commercial software Optisystem 11.0®. Then, the in-house 2-mode-group EDFA model was upgraded with a full treatment of the vector modes guided in optical fibers. The subsequent analysis included the impact of the mode-beating effect and birefringence of the modal gain of FM EDFAs for MDM application.

Firstly, in an ideal circular fiber, FM-EDFA simulations based on vector modes highlighted the additional complexity of the behavior to be expected in few-mode amplifiers relative to what is to be anticipated from simpler scalar models. In particular, it was shown that the TMIE due to vector modes in a SI uniformly doped fiber causes the LP_{11b} signal mode to exhibit a far lower gain than the LP_{01} signal mode when only pumped by an LP_{11b} pump mode. Moreover, the population inversion profile can exhibit strong oscillations due to the TMIE associated with both pump and signal modes. Next, it was found that the mode-beating effect is much less pronounced when the full sets of the non-circular LP mode-group (i.e. LP_{11a} and LP_{11b}) are excited in the amplifier. In particular, when the pump mode is circularly symmetric, the difference in the results given by the LP and VM models is negligible. It was also shown that the difference in the simulated modal gains for the LP_{11p} -mode-pumped 2-mode-group EDFA model based on the LP modes and VMs become even smaller when the fiber core exhibits a slight ellipticity and all the spatial degeneracies of the LP_{11} signal and pump modes are excited. Finally, the study showed that the 2-mode-group EDFA model based on LP mode or VMs are equivalent when the guided modes are incoherent (i.e. no beating) and weakly guided when the core exhibit a slight ellipticity (i.e. $D = 0.5\%$). In a MDM system, the condition of the incoherent signal modes is valid due to the absence of the CW carrier frequency and the presence of independent phase modulation on individual signal modes.

Consequently, the conclusion is that the LP-mode-based MM-EDFA simulator is valid and reasonably accurate to predict the modal gain properties of weakly guiding MM-EDFAs in a real transmission system, given the full spatial degeneracies of the LP modes are used. Hence, it can be used for the design and optimization of weakly guiding MM-EDFAs that support more than two mode-groups.

Chapter 5: Design optimization of FM-EDFAs supporting four mode groups and beyond

Having discussed the mode-beating effects in the LP model and confirmed the validity of the LP modes based FM-EDFA simulator in the previous chapter, in this chapter, I advance the design and optimization of FM-EDFA supporting 4-mode-groups and beyond. Firstly, a core-pumped 4-mode-group EDFA is designed and simulated. Then, the simulation model is updated and re-run with the measured properties from a fabricated fiber. Next, cladding pumping is simulated as a cost-effective alternative to core pumping. A double-clad 4-mode-group EDFA was made in-house according to the cladding-pumped 4-mode-group EDFA simulations using in-house erbium-doped preforms. Again, the cladding-pumped MM-EDFA simulation model is verified from using feedback of experimental data. In order to inverse design the cladding-pumped EDFA supporting more than four modes, design optimization using the genetic algorithm is adopted. This algorithm enables many parameters to be optimized simultaneously and ensures large free-parameters spaces are searched in order to find the optimal solutions.

5.1 Design of core-pumped 4-mode-group EDFA

Having achieved great success in designing, making and demonstrating the 2-mode-group EDFA at the ORC under the MODEGAP project, I was tasked again to help our fabrication and device teams to develop a 4-mode-group EDFA. For multimode erbium-doped fiber amplifiers (MM-EDFA), low differential modal gain (DMG) is of primary importance to minimize the degradation of signal quality. Apart from our group, other 2-mode-group EDF designs for gain equalization [80] or low mode-dependent gains [81] have been reported theoretically. However, both require a sophisticated pump modal configuration, which is difficult to achieve in practice. As discussed in chapter 3, a two-mode EDF design incorporating ring doping was theoretically proposed to equalize the gain for LP_{01s} and LP_{11s} using only a LP_{01p} pump, which greatly simplifies the

pump arrangement [51]. Meanwhile, a similar ring-doping approach was applied to a four-mode-group EDF that provided equal amplification for the LP_{11s} and LP_{21s} modes has been experimentally demonstrated by G. Cocq from University Lille [82]. However, the gain for the LP_{01s} mode was seen to be considerably lower than that of the LP_{11s} mode. To address this shortcoming, an approach combining one length of ring-doped EDF and another section of uniform-doped EDF in a concatenated architecture was used to amplify all six spatial modes in a four-mode-group fiber [83]. The overall gain difference across all the modes was reported to be 4 dB. While these encouraging results were demonstrated experimentally, significant scope exists for new fiber designs providing simplified means of DMG control and improved overall gain performance.

In this section, I extend the ring-doping approach onto designing 4-mode-group EDFs. I propose a 4-mode-group EDF with reasonably good fabrication tolerance for achieving less than 1 dB gain difference across all the modes with a pump arrangement combining only LP_{01p} and LP_{41p} modes.

5.1.1 Simulation results

A SI EDF is considered with a core-cladding RI difference of 0.004 and a core radius of 10 μm , as shown in Figure 5.1(b)). It guides six distinct spatial modes within the C-band, namely LP_{01} , LP_{11a} , LP_{11b} , LP_{21a} , LP_{21b} and LP_{02} , whose intensity profiles and patterns are shown in Figure 5.1(c, e) respectively. At a pump wavelength of 980 nm, it can guide up to 7 transverse modes, whose intensity profiles are shown in Figure 5.1(d). Figure 5.1(a, b) represent the cross section of the proposed erbium-doping profile consisting of a central as well as a ring-doped area within the core. It is to be noted here that the doping concentration of the two regions is assumed to be the same. The radius of the central-doped region is assumed to be R_i , and the inner radius of the ring-doped layer is R_o , while the outer radius is equal to the core radius. The physical origin of the DMG comes from differences in the overlap of the pump modes, the signal modes and the distribution of the erbium dopant. The proposed doping structure allows control of the relative overlap of signal modes and Er-ions. From the guided pump modes,

LP_{01p} and LP_{41p} are chosen to efficiently pump the 4-mode-group EDF. This is because LP_{01p} and LP_{41p} have the largest overlap with the central- and ring-doped regions respectively, providing the greatest scope for differential gain control.

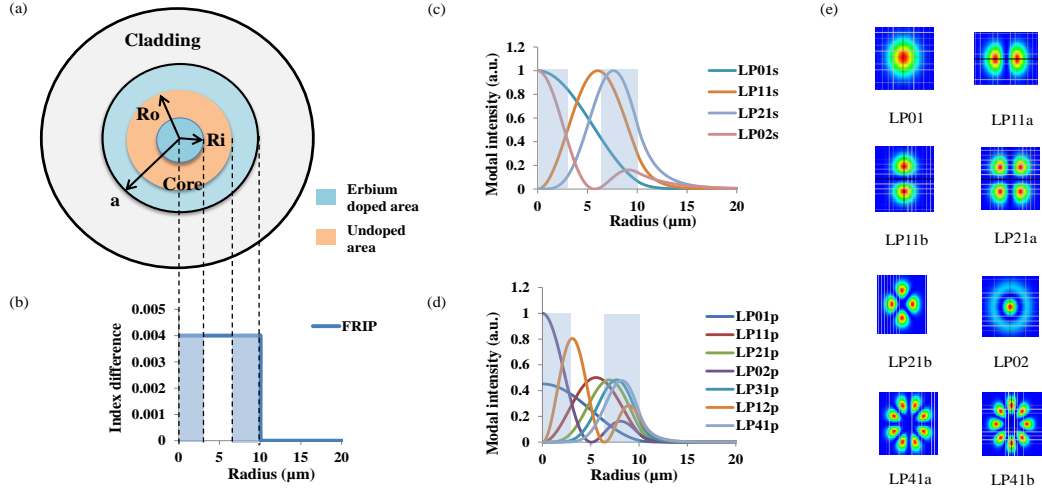


Figure 5.1. Dopant cross-sections for the four-mode-group EDF. (b) RI and doping profiles (i.e. shaded region) of the four-mode-group EDF. Mode intensity profiles of the (c) signal and (d) pump modes, where the shaded regions indicate erbium-doped regions. (e) Intensity pattern of the guided modes.

In the simulation, equal input powers were allocated to the six signal modes (as shown in Figure 5.1(e), and the average gains of LP_{11a} (LP_{21a}) and LP_{11b} (LP_{21b}) were used to plot the gain for the LP_{11} (LP_{21}) mode. Firstly, the maximum gain difference (ΔG_{max}) is plotted across the four modes based on the variations of R_i and R_o , which effectively determine the area of the central-doped region and the thickness of the ring-doped region, as shown in Figure 5.2(a). The signal power per spatial mode at 1530 nm was set to -10 dBm, and the total pump power was chosen to be 350 mW and was equally split into LP_{01p} and LP_{41p} modes. The fiber length was set to 5 m with the erbium-doping concentration chosen to be $1.2 \times 10^{25} \text{ m}^{-3}$. The dashed rectangle highlighted in Figure 5.2(a) indicates the region where very low ΔG_{max} values are possible for the chosen pump arrangement ($P_{LP01p}:P_{LP41p} = 1:1$). Attention will be focused on this region only, and the pump arrangements will be varied to explore the gain performance. For the same ΔG_{max} , any change in the power ratio between the two pump modes impacts the distribution of R_i and R_o differently, as displayed in Figure 5.2(b) for

pump arrangement $P_{LP01p}:P_{LP41p} = 6:4$ and Figure 5.2(c) for $P_{LP01p}:P_{LP41p} = 4:6$. For example, to keep the maximum gain difference within 2 dB, $2.5 \mu\text{m} < R_i < 3 \mu\text{m}$ and $6.2 \mu\text{m} < R_o < 6.8 \mu\text{m}$ are required for the pump arrangement $P_{LP01p}:P_{LP41p} = 1:1$, as shown in Figure 5.2(a). However, for $P_{LP01p}:P_{LP41p} = 6:4$, R_i needs to be smaller than $2.75 \mu\text{m}$ while R_o stays in the same range as previously indicated. For the case of $P_{LP01p}:P_{LP41p} = 4:6$, R_i can assume any value between $2.5 \mu\text{m}$ to $3.25 \mu\text{m}$ while R_o vary according to Figure 5.2(c). This can be easily understood from the physical interpretation that the effect on the gain variation caused by slight changes in the overlap between signal modes and erbium ions distribution can be compensated by carefully adjusting the pump arrangement. Basically, this indicates that large gain differences can be addressed by shaping the erbium-doping profile such that R_i and R_o fall within the ranges of $2.5 \mu\text{m} < R_i < 3.25 \mu\text{m}$ and $6 \mu\text{m} < R_o < 7 \mu\text{m}$ respectively, and small gain differences can be managed through fine tuning the power ratio between the two pump modes LP_{01p} and LP_{41p} . Thanks to the extra freedom provided by the pump arrangement, the dashed rectangle highlighted in Figure 5.2(a) indicates a reasonably good fabrication tolerance, which makes the design more practical.

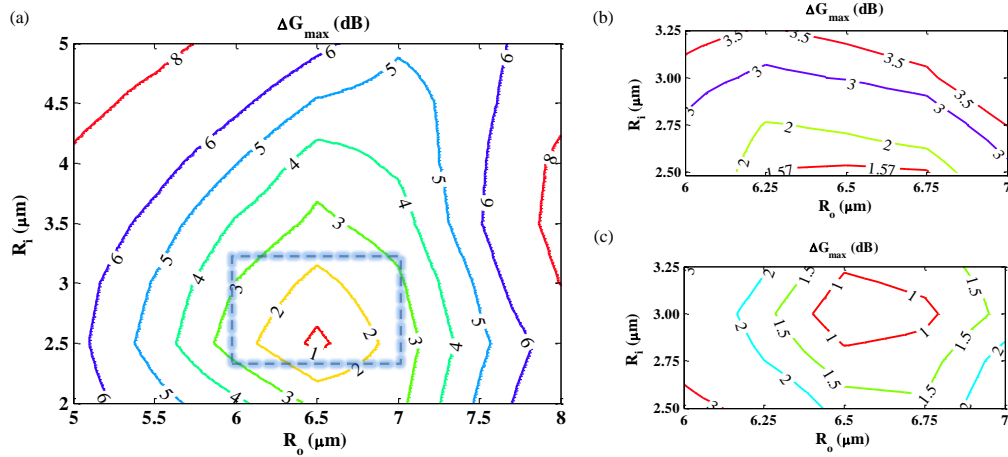


Figure 5.2. Contour plot of the maximum modal gain difference against the variation of R_o and R_i with pump arrangement of (a) $P_{LP01p}:P_{LP41p} = 1:1$, (b) $P_{LP01p}:P_{LP41p} = 6:4$, and (c) $P_{LP01p}:P_{LP41p} = 4:6$. The total pump power was set to 350 mw throughout.

A four-mode fiber with parameters $R_o = 6.5 \mu\text{m}$ and $R_i = 3 \mu\text{m}$, which gives the DMG $< 1\text{dB}$ as indicated by the Figure 5.2(c), is chosen as example to perform the

following simulations. Its modal gain properties and the root mean squared (RMS) value of the gain difference as a function of total pump power for all four signal modes are illustrated in Figure 5.3(a). The pump power was split into $LP_{01p}:LP_{41p}=4:6$. It can be seen that the overall gain excursion is well constrained to within 1 dB across all the modes for a gain of 20 dB or more. The RMS value of the gain difference for all pump powers listed in Figure 5.3(a) are below 0.3, with the lowest level reached at the total pump power of 350 mW. Figure 5.3(b) shows the modal gain against signal power per mode for a fixed total pump power of 350 mW. Again, less than 1 dB overall gain excursion across all four modes is observed for all signal power listed. The maximum gain difference emerged to be even smaller for high input signal powers.

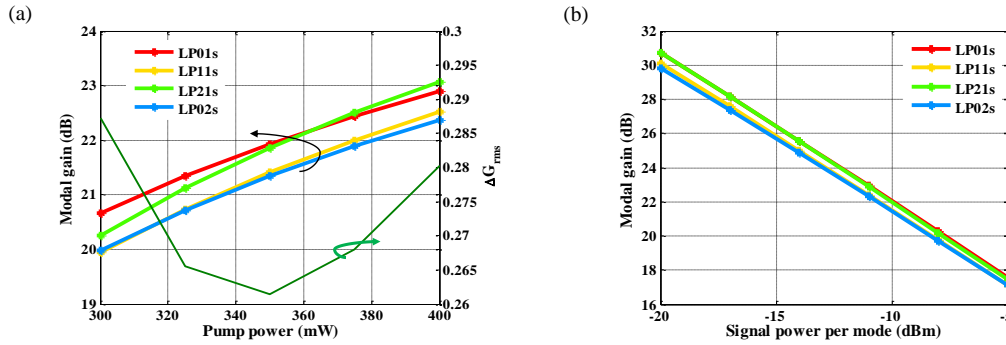


Figure 5.3. (a) The modal gain and RMS value of the gain difference across the four modes against the variation of total pump power. Signal at 1530 nm power per mode was set to -10 dBm. (b) Modal gain dependence on signal power per mode.

In conclusion, I proposed a novel fiber design incorporating two separate doped sections capable of providing low (i.e. <1 dB) gain difference in a 4-mode-group EDFA for a relatively simplified pump arrangement using only two pump modes (i.e. LP_{01p} and LP_{41p}). The extra freedom provided by this pump arrangement allows a reasonable fabrication tolerance on our fiber design, which increases the viability of the design.

5.2 Amplifier modeling based on fabricated four-mode-group EDF

Due to limited fabrication resources, it was not feasible to fabricate a new preform in the ORC based on the optimized design discussed in section 5.1. Rather we expected the possibility to use the ring-doped preform (i.e. Figure 3.10 of chapter 3) that was used to make the 2-mode-group ring-doped EDFA to fabricate a 4-mode-group EDF. Once again the experimental preform parameters were fed back into the mode solver in COMSOL Multiphysics to ascertain the required final fiber core diameter (i.e. according to the preform profile shown in Figure 3.10) to ensure that the LP_{31} mode just cuts off at 1550 nm. The best core diameter I found was $18.6\ \mu\text{m}$. Next, I used Optisystem 11.0® to do some simple preliminary simulations to check the performance of this potential 4-mode-group EDFA. The input powers of the four signal modes were set to -10 dBm per mode, where for the LP_{11} and LP_{21} modes, the -10 dBm was split equally into their two orientations, so that the intensity profiles of the LP_{11} and LP_{21} modes do not have azimuthal dependency. Considering the overlap between the signal, pump and erbium, to balance the gain among the 4 signal mode groups, it is easy to deduce that a LP_{01} pump plus a high-order pump mode are required. Consequently, I used LP_{01} and LP_{41} pump modes as the ingredients to tune the modal gain in this potential 4-mode-group EDFA. The best results I obtained was a DMG less than 1 dB among the four mode groups for a range of pump powers, as shown in Figure 5.4, where the power ratio of the LP_{01} and LP_{41} was 3:5.

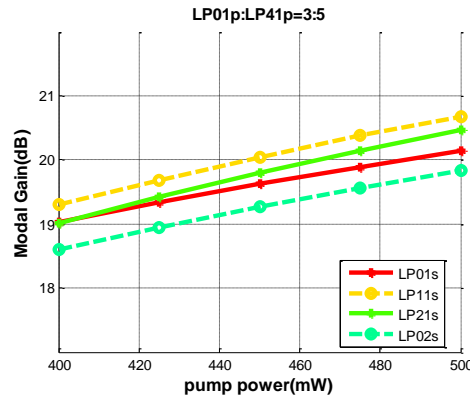


Figure 5.4. Modal gains against input pump power for the proposed ring doped 4-mode-group EDFA.

Based on the encouraging simulation results, we decided to go for the ring-doped preform. The 4-mode-group EDF was drawn from the ring-doped preform with an outer cladding diameter of 161 μm and a core diameter of 18.6 μm . The 4-mode-group EDF considered here guides up to the LP_{51} mode at 980 nm. Both experiments and simulations were undertaken to study the characteristics of this 4-mode-group EDF. The experiment was primarily carried out by the author's colleague, Dr Yongmin Jung.

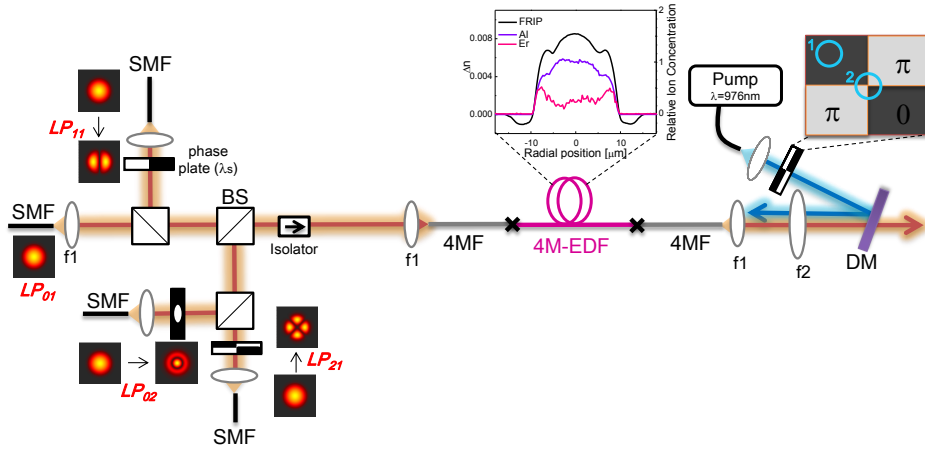


Figure 5.5. Experimental setup of the in-house 4-mode-group EDFA.

Figure 5.5 shows a schematic diagram of the 4-mode-group EDFA for simultaneous amplification of the four lowest spatial mode-groups, namely LP_{01} , LP_{11} , LP_{21} and LP_{02} . A mode multiplexer based on phase plates was first used to selectively excite the pure LP_{01} , LP_{11} , LP_{21} and LP_{02} signal modes in a passive four-mode-group fiber with four tunable external-cavity lasers. Since the current free-space mode-multiplexer scheme suffers a minimum 3 dB excess loss resulting from the use of non-polarizing beam splitters (BS) for each mode added to the system, the number of simultaneously injected spatial modes was limited to four rather than six (i.e. including spatial degeneracies, LP_{11a} and LP_{11b}) to keep the signal insertion loss within an acceptable level to allow the amplifier to be characterized over a wide range of signal input powers. Moreover, it was assumed that the spatially degenerate modes (i.e. LP_{11a} and LP_{11b}) would strongly couple into each other along the fiber due to the perturbations such as fiber

uniformity and bending. Therefore, in the simulation, I assumed that an equal amount of power is allocated to the spatially degenerate modes in the LP_{11} and LP_{21} mode-groups. The passive 4-mode-group fiber was then spliced directly to the 5 m long 4-mode-group ring-doped EDF [84], [85]. Again, the backward pumping configuration was adopted to inject the pump beam. The single-mode outputs from the 976 nm pump laser diodes were first converted to the desired pump modes using 980 nm borosilicate phase plates and then free-space coupled into the end of the passive 4-mode-group fiber. The coupling losses from free space to the passive 4-mode-group fiber depend on the particular pump mode, and were measured to be 1.1 dB and 3.5 dB for LP_{01p} , and LP_{21p} pump modes respectively. These relatively large coupling losses can ultimately be improved by using a long-period fiber-grating assisted mode converter [17, 18] written directly into the pump fiber.

Although the full de-multiplexing configuration (e.g. using phase plates) should in principle be placed for accurate characterization of the 4-mode-group EDFA, due to limited resources in the lab at the time when the experiment was conducted, an alternative method was adopted to allow a simple but effective modal gain measurement. Different wavelengths were chosen for the four different signal channels (i.e. 1546 nm for LP_{01} , 1550 nm for LP_{11} , 1554 nm for LP_{21} , and 1558 nm for LP_{02} respectively) and a tunable narrow bandpass filter (i.e. full width at half maximum of 2 nm) and a power meter were used to determine the output power and thus deduce the gain of the individual channels, similar to the setup described in [54], [65]. Splice losses of 0.6 dB for the LP_{01} , 1.0 dB for the LP_{11} , 1.2 dB for the LP_{21} , and 1.3 dB for the LP_{02} modes were measured. The variation is primarily attributed to mode mismatch between the passive 4-mode-group fiber and active 4-mode-group EDF. The signal power per mode that coupled into the active 4-mode-group EDF was ensured to be -2.5 dB after the unequal splice losses were taken into account. The theoretical coupling coefficients of the four transverse signal modes from the passive 4-mode-group fiber to the active 4-mode-group EDF were calculated using overlap integrals as shown in Equation 3.1, where the exact modal profiles of the passive 4-mode-

group fiber and the active 4-mode-group EDF were computed by COMSOL Multiphysics using the measured fiber RI profiles shown in Table 5.1. The calculated coupling coefficients are shown below:

Table 5.1. The coupling coefficients of LP_{01} , LP_{11} , LP_{21} and LP_{02} modes from the passive 4-mode-group fiber to the 4-mode-group ring-doped EDF.

At 1550nm		4-mode-group ring-doped EDF			
$in\%$		LP_{01}	LP_{11}	LP_{21}	LP_{02}
Passive 4-mode-group fiber	LP_{01}	84.2%	-	-	15.1%
	LP_{11}	-	75%		-
	LP_{21}	-	-	71%	-
	LP_{02}	13.8%	-	-	58.2%

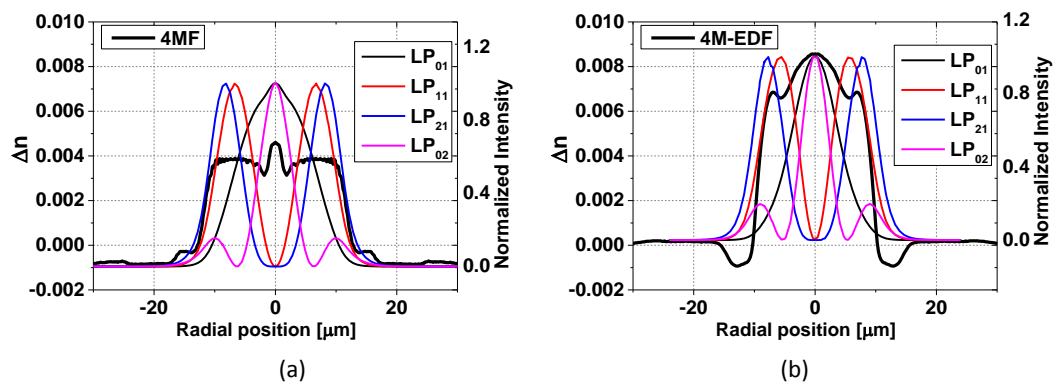


Figure 5.6. The measured RI profiles and simulated mode intensity profiles of (a) the 4-mode-group passive fiber, and (b) the 4-mode-group ring-doped EDF.

It can be seen that there is a considerable amount of power (i.e. 15%) coupling from the LP_{01s} into LP_{02s} after the splice point of the passive 4-mode-group fiber and the active 4-mode-group EDF. Likewise, about 14% of the power of LP_{02s} would couple into the LP_{01s} after the splicing point. The LP_{11s} and LP_{21s} modes would experience some coupling loss due to mode mismatch between the passive and active fibers, but no power flow into other modes. The mode mixing of LP_{01s}

and LP_{02s} will definitely have an impact on the measured modal gain properties due to the fact that the amplified power of different signal modes are separately collected based on different wavelength channels during the measurements. Figure 5.6 shows the measured modal gains against the pump powers for different pump modal configurations. For Figure 5.6 (a), though the best effort was made to align the center of the pump beam to the center of the core of the passive 4-mode-group fiber, the pump modal profile cannot achieve pure LP_{01p} . It is to be noted that the alignment for the pump beam at 980 nm is more challenging than that for the signal beam at 1550 nm, due to the metrics used to do the alignment [85]. The CCD image shown in Figure 5.7(a) confirmed that the pump was LP_{01p} dominated, and the image was taken from the output of the passive 4-mode-group fiber before it was spliced to the 4-mode-group EDF. Likewise, the CCD image shown in Figure 5.7(b) confirmed that the pump was LP_{21p} dominated. The use of a pump phase plates does help to increase the predictability of the pump modal content compared with the offset-launching method mentioned in section 3.1 of chapter 3.

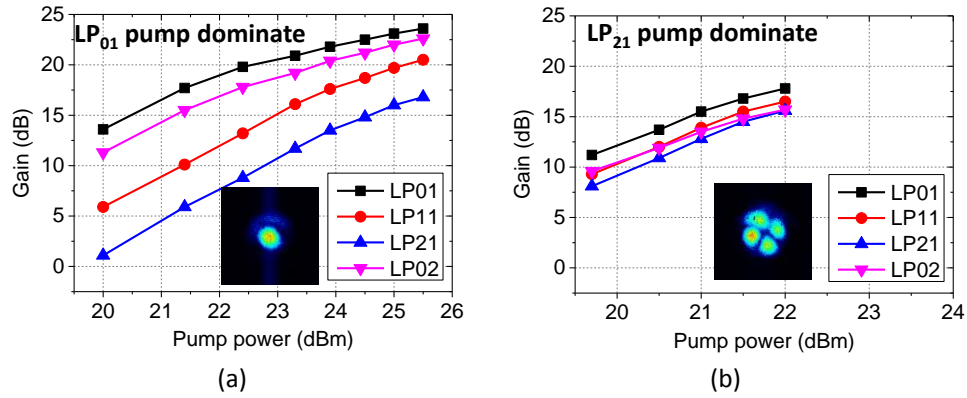


Figure 5.7. Measured mode-dependent gain as a function of launched pump power for different pump spatial modes (a) LP_{01p} , and (b) LP_{21p} with backward pumping configuration.

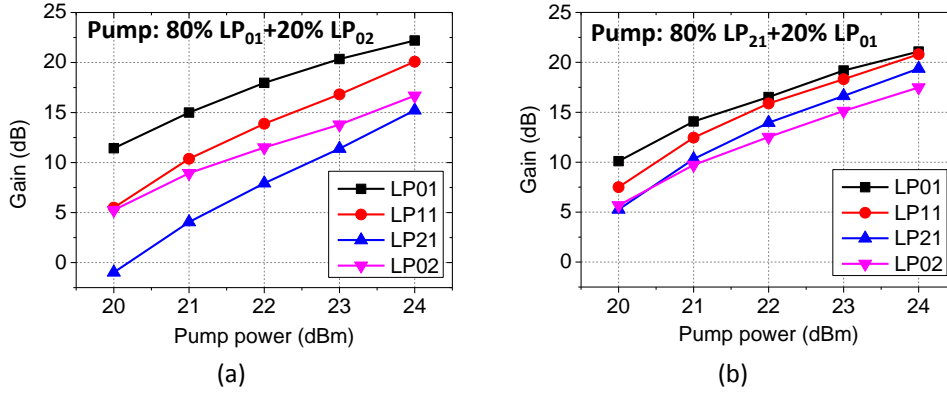


Figure 5.8. Simulation fitting of the 4-mode-group EDFA using experimental parameters for (a) LP01p dominated case, and (b) the LP21p dominated case.

The fitting of the experimental data shown in Figure 5.7 was not straight forward, as the modal gain of LP01s and LP02s are actually not accurate due to the mode mixing previously discussed. In the experiment, it was claimed that the signal power per mode was set to -2.5 dBm. However, due to the mode mixing at the splicing interface, in the simulation the input signal power per mode was modified to “at 1546 nm, LP01s: -3.2 dBm, LP02s: -10.7 dBm”, “at 1550 nm, LP11: -2.5 dBm”, “at 1554nm, LP21: -2.5 dBm”, and “at 1558 nm, LP02s: -4.8 dBm, LP01s: -11.1 dBm” respectively according to the coupling matrix in Table 5.1. The modified input signal condition is the closest approximation of the actual input signal condition in the experiment after considering multiple signal wavelengths and the mode coupling at the splicing points of the passive fiber and the amplifier in the experiment. Once the input signal condition is fixed, the next task is to estimate the pump modal content in order to reveal the true modal gain properties in the experiment. The pump modal content can be estimated through achieving the best fit of the gain curves of LP11s and LP21s. Thus for the LP01p dominated condition shown in Figure 5.7(a), it was found that the best agreement between theory and experiment for the LP11s and LP21s can be achieved by assuming that 80% of the total pump power was in LP01p mode while the remaining 20% resides in the LP02p mode. For the LP21p dominated condition shown in Figure 5.7(b), it was found that the best agreement between theory and experiment for LP11s and LP21s can be achieved by assuming that 80% of the total

pump power was in the LP_{21p} mode while the remaining 20% resides in the LP_{01p} mode. The simulated modal gain curves against the pump powers using the modified input signal condition and the best fitted pump modal configurations are shown in Figure 5.8(a) and (b). It is to be noted that the gain for the LP_{01s} shown in Figure 5.8 represents the gain for LP_{01s} at 1546nm, and the gain for the LP_{02s} represents the gain for LP_{02s} at 1558nm in the simulation. The discrepancies on the gain for LP_{01} and LP_{02} modes in Figure 5.7 (measured) and Figure 5.8 (simulated) are explained by the mode crosstalk between the LP_{01} and LP_{02} modes at two splicing points (i.e. before and after) between the passive fiber and the amplifier.

Mode crosstalk (e.g. as shown in Table 5.1) could affect the results of amplifier gain measurement, but it is not a problem for data transmission in MDM systems. In MDM systems, the mode coupling can be undone through well-established MIMO equalization technology [22], as explained in the introduction chapter of this thesis. In conclusion, we have successfully demonstrated a core-pumped 4-mode-group EDFA that can be applied into a 4 mode-group MDM transmission system. The ORC is now commercializing the technology (i.e. core pumped 4-mode-group ring-doped EDFA) in collaboration with the company Phoenix Photonics Ltd [72].

5.3 Cladding-pumped MM-EDFA model

The field of MDM is developing at a fast pace. By the end of 2014, both two and four mode-group systems had been reported, with transmission fibers [23], [68], [86]–[88] and a compatible inline few-mode erbium-doped fiber amplifier (FM EDFA) [16], [25], [54], [82], [83], [85], [87], [89]. Amongst these encouraging results, the 2-mode-group EDFAs [25], [65] and 4-mode-group EDFA [85] were demonstrated by our group under the MODEGAP project. Apart from the ORC, ring doped 2-mode-group EDFA [87] was proposed by NEC labs America and ring doped 4-mode-group EDFA [82] was proposed by University Lille, shortly after our published ring doped 2-mode-group EDFA [51]. All the FM-EDFA reported so far were core pumped. In simulation, I used a combination of selected pump

modes and sophisticated erbium-doping profiles to equalize the gain in a 4-mode-group EDFA [90]. Other theoretical works on designing core-pumped FM-EDFAs include applying numerical optimization methods (e.g. gradient descent optimization) to optimize the modal composition of the pump beam and erbium-doping profile [91], [92].

For our core-pumped ring-doped 4-mode-group EDFA discussed in the previous section, the DMG can be further minimized using higher-order pump modes, such as LP_{31} or LP_{41} . However, high-order pump modes (i.e. mode order higher than LP_{21}) are not practical because the insertion loss of generating a high-order pump mode from a single mode pump diode (i.e. through phase plate) would be very high (i.e. larger than 3.5 dB, which is the insertion loss measured for generating the LP_{21} pump beam). The maximum available pump power from a single-mode pump diode is 750 mW. Generally 26 dBm (i.e. 400 mW) pump power is required to achieve 20 dB for all signal modes (i.e. whose input power are of 10 dBm each) in a 4-mode-group EDFA. In our published ring-doped 4-mode-group paper [85], we have already used bidirectional core pumping from two single-mode pump diodes to deliver enough LP_{21} pump power in order to achieve over 20 dB modal gains. If an LP_{41} pump mode was to be used, three single-mode pump diodes might be necessary to deliver enough pump power. Clearly, as the number of modes supported in a FM-EDFA is increased, the total signal output power and required pump power needed for high-gain low-noise amplification significantly increases. This dictates the use of multiple expensive single-mode pumps. Reduction in the cost per transmitted bit is essential for SDM to be seriously considered for commercial deployment. So instead of considering the expensive core-pumped FM-EDFA approach, we decided to move our strategy onto developing cladding-pumped FM-EDFAs. Cladding-pumping using high-power multimode pump diodes provides a more practical and potentially much cheaper way in terms of \$/W to generate and deliver the pump radiation. The cladding-pumping scheme had already been demonstrated as an efficient and practical way to provide pump sharing for multiple spatial channels in multi-core EDFAs [93], [94] and few-mode multi-element EDFAs [95].

The cladding-pumping scheme can be implemented using two different technologies, namely double-clad fiber (DCF) and GTWave fiber [96]. Only the DCF is introduced and discussed in this thesis. With the DCF, the pump power from the multimode laser diodes is coupled into the inner cladding of DCF via a multi-port tapered fiber bundle [97]. Figure 5.9 shows a typical cross-section profile of a DCF with a D-shaped inner cladding. The DCF consists of a rare-earth doped core, an inner cladding and an outer cladding layer. The signal light propagating in the rare-earth doped core is guided by the RI difference between the core and inner cladding. Meanwhile, the heavily multi-moded pump light propagating in the inner cladding is guided by the RI difference between the inner and the outer claddings. The inner cladding (i.e. typical NA of ~ 0.45) has a non-circular shape (e.g. D-shape) to break the circular symmetry of the fiber. This promotes pump mode mixing, and thus increases pump absorption.

In the area of high-power lasers, the cladding-pumping scheme is usually used for brightness enhancement, as illustrated by Figure 5.10 from literature [98]. The low beam-quality pump light from a multimode laser diode at a wavelength of λ_p (i.e. green colored beam at the right-hand side) undergoes the brightness conversion process in the cladding-pump fiber to generate a high beam-quality signal light at λ_s (i.e. red colored beam at the right-hand side).

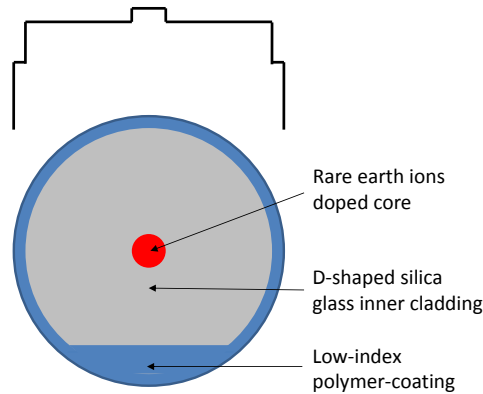


Figure 5.9. A typical cross-section of a DCF with a D-shaped inner cladding. The black solid line indicates the FRIP of the DCF.

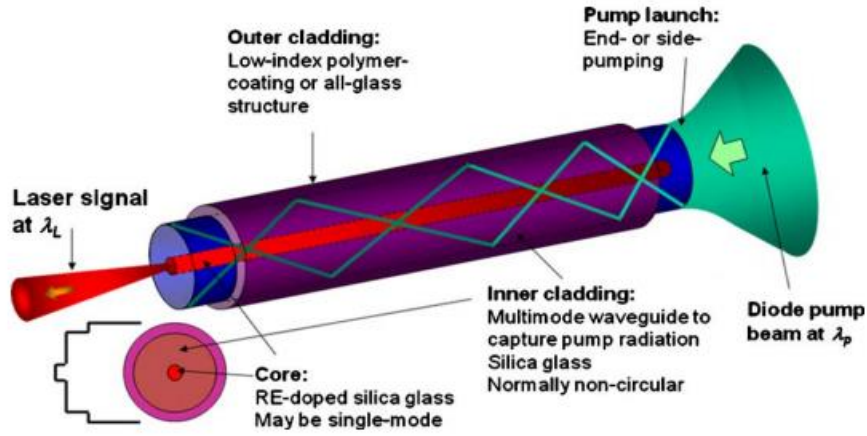


Figure 5.10. Brightness conversion in a cladding-pumped fiber [98].

In terms of the modeling of cladding-pumped MM-EDFA, the heavily multimoded pump light is assumed to be one single transverse mode with a uniform intensity distribution across the inner cladding [50], [99]. Hence, the pump intensity can be approximated by:

$$I_p = \frac{P_{pump}}{\pi r_{inner}^2} \quad 5.1$$

where r_{inner} is the radius of the inner cladding. To simulate cladding-pumped MM EDFA, the rate and propagation equations given by Equations 2.46, 2.47 and 2.50 are modified as:

$$N_1(r, \theta, z) = N_t \frac{1 + \sum_k \frac{\sigma_e(v_{s,k})}{\sigma_a(v_{s,k}) + \sigma_e(v_{s,k})} \frac{I_{s,k}(z)}{I_{sat}(v_{s,k})}}{1 + \frac{I_p(z)}{I_{sat}(v_p)} + \sum_k \frac{I_{s,k}(z)}{I_{sat}(v_{s,k})}} \quad 5.2$$

$$N_2(r, \theta, z) = N_t \frac{\frac{I_p(z)}{I_{sat}(v_p)} + \sum_k \frac{\sigma_a(v_{s,k})}{\sigma_a(v_{s,k}) + \sigma_e(v_{s,k})} \frac{I_{s,k}(z)}{I_{sat}(v_{s,k})}}{1 + \frac{I_p(z)}{I_{sat}(v_p)} + \sum_k \frac{I_{s,k}(z)}{I_{sat}(v_{s,k})}} \quad 5.3$$

$$\frac{dP_s(z)}{dz} = u_s \sigma_{e,s}(P(z) + 2h\nu_s \Delta\nu) \iint_S i_s(r, \theta) N_2(r, \theta, z) r dr d\theta \quad 5.4$$

$$- u_s \sigma_{a,s} P(z) \iint_S i_s(r, \theta) N_1(r, \theta, z) r dr d\theta - u_s \alpha_s P_s(z)$$

$$\frac{dP_p(z)}{dz} = u_p \sigma_{e,p} \iint_S I_p(r, \theta) N_2(r, \theta, z) r dr d\theta - u_p \alpha_p P_p(z) \quad 5.5$$

where the I_{sat} is the saturation intensity defined in Equation 2.38, u_s and u_p are the signal and pump propagation directions respectively, α_s and α_p are the signal and pump propagation losses respectively. Equations 5.2 to 5.5 can be numerically solved using the methods discussed in section 2.2.3 of chapter 2.

5.4 Modeling of cladding-pumped 4-mode-group EDFA using in-house erbium-doped preforms

There were two erbium-doped preforms available in the ORC back in 2013 for making a double-clad 4-mode-group EDFA. One was the ring-doped preform, as shown in Figure 3.10 of chapter 3. The other one was the so-called “batman” preform, which has been previously drawn into a 2-mode-group EDFA, as shown in Figure 3.(a) of chapter 3. The modal gain properties against input pump power for cladding-pumped four-mode “batman” EDF and four-mode ring-doped EDF are shown in Figure 5.11 with the simulation parameters in Table 5.2. The derivation of the erbium-doping concentration of the two type of EDFs were previously discussed in section 3.1 (i.e. for the “batman” EDF) and section 3.3 (i.e. for the ring-doped EDF).

Table 5.2. Simulation parameters used in the modeling of cladding-pumped 4-mode-group “batman” EDF and 4-mode-group ring-doped EDF.

	4-mode-group “batman” EDF	4-mode-group ring doped EDF
--	------------------------------	--------------------------------

Core radius	12.3 μm	9.3 μm
Erbium-doping concentration	$1.5 \times 10^{25} \text{ m}^{-3}$	$1.0 \times 10^{25} \text{ m}^{-3}$
Input signal power per mode @ 1550nm	-10 dBm	-10 dBm
Fiber length	9 m	9 m
Inner cladding diameter	100 μm	100 μm

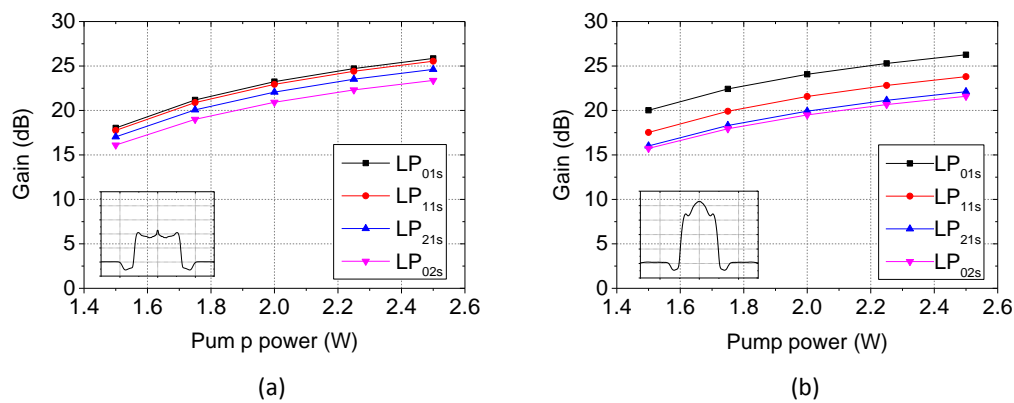


Figure 5.11. Simulated modal gain as a function of the pump power for (a) cladding-pumped 4-mode-group “batman” EDF, and (b) cladding-pumped 4-mode-group ring-doped EDF.

As shown in Figure 5.11, the differential modal gain provided by the 4-mode-group “batman” EDF is generally 2 dB lower than that of the 4-mode-group ring-doped EDF. This is due to the difference on the overlap among signals and the erbium-doping distribution. Therefore, it was clear that the “batman” erbium-doped preform is a better candidate to make a double-clad 4-mode-group EDF for cladding pumping. The “batman” erbium-doped preform is firstly etched down to a preform with an outer diameter of 5.77 mm from an original outer

diameter of 12 mm. Then, the etched preform is drawn down to 100 μm outer diameter to ensure a fiber core radius of 12.3 μm with a low-index coating.

This double-clad 4-mode-group “batman” EDF played a vital role in the MODEGAP project and brought out the world-first demonstrations of cladding-pumped few-mode EDFAs for MDM systems [100], [101]. The cladding-pumped 4-mode-group EDFA experiment, with the experimental setup shown in Figure 5.12, was mainly conducted by Dr. Yongmin Jung [101]. The measured differential modal gain across the four-mode-group is about 3 dB with average gain values around 20 dB. This agrees with the simulations shown in Figure 5.11(a). In early 2015, the side-pumped double-clad 4-mode-group EDFA was successfully applied in a heterogeneous space-division multiplexing network shown in Figure 5.13 [102], a collaborated work with Bell Laboratories (i.e. Alcatel-Lucent, US) and was presented as a post-deadline paper in the prestigious telecom conference OFC 2015.

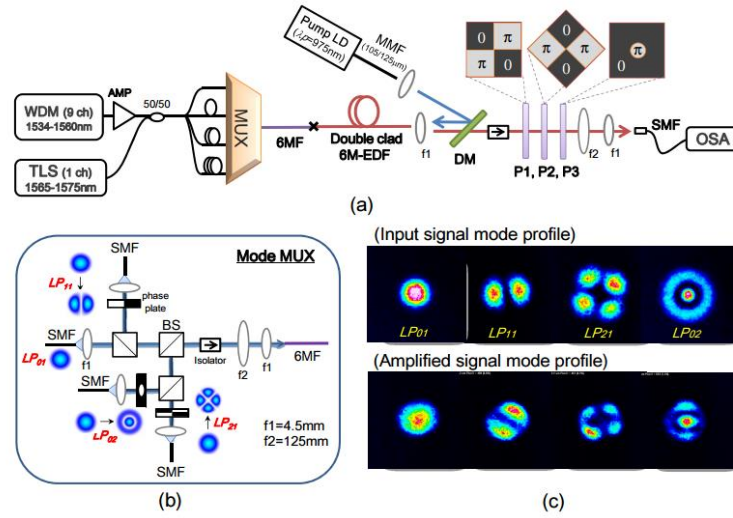


Figure 5.12. Experimental setup of the in-house cladding-pumped 4-mode-group “batman” EDF [101].

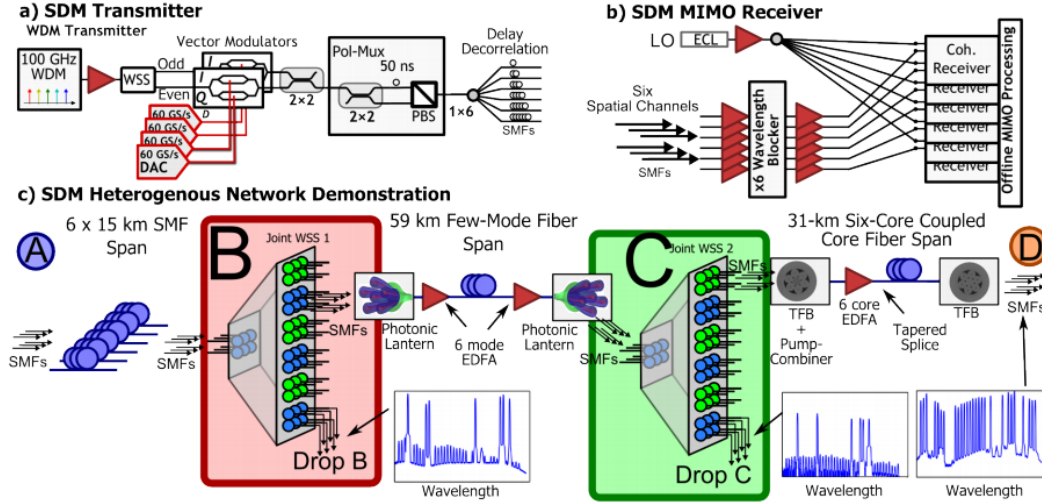


Figure 5.13. Experimental arrangement of the heterogeneous space-division multiplexing network, where a six parallel single-mode fiber span, a six-core coupled multi-core fiber span, and a six-spatial-mode fiber span (i.e. equivalent to four-mode-group fiber) are connected and integrated. The cladding-pumped 4-mode-group “batman” EDF developed at the ORC was successfully applied in the 59 km few-mode fiber span in this work [102].

5.5 Design of cladding-pumped EDFA supporting four-mode-group and beyond

This section presents the design optimization of cladding-pumped EDFAs to support four-mode-group and beyond. The mode-dependent gain is determined from a combination of the signal and pump intensity profiles and their overlap with the erbium-dopant distribution. As the pump intensity in a cladding-pumped MM EDFA can be well approximated to be uniform across the inner cladding, careful tailoring of the erbium-doping profile in an active multimode fiber is central to minimizing the DMG in cladding-pumped FM EDFAs. The FM EDFA was simulated using the simulation model described in section 5.3. For the noise calculation, the wavelength band from 1500 nm to 1600 nm was split into 40 wavelength slots of equal width (i.e. 2.5 nm). A genetic algorithm (GA) was implemented to help optimize the rare-earth doping profile of the cladding-pumped FM EDFAs. The results of the GA application will be presented followed by a discussion on the fabrication tolerances.

5.5.1 Genetic algorithm

The GA approach is a generic optimization method for optimizing multiple parameters simultaneously based on a natural selection process that mimics biological evolution. The GA works by exploring a large population in parallel. The evolution starts from a population of “individuals” with randomly generated ‘genes’ (i.e. constrained by pre-defined initial conditions). The individuals are used as “parents” to reproduce the “children” for the next generation. In each generation, the “fitness” of every “child” (i.e. and the associated set of “genes”) in the population is evaluated. “Fitness” is defined by the value of the objective function in the optimization problem being solved. Only the “fittest children” are selected to become “parents”, and over successive generations the population “evolves” toward the “fittest” individuals. Generally speaking, a GA is not guaranteed to find the optimum solution, as it may settle on a local minimum while the global minimum remains unsearched. The GA is designed with the purpose of searching efficiently large and poorly understood spaces, where a specialized technique was not available. This is the main reason why GA was chosen to tackle the inverse design of the multi-layer structured erbium-doping profile in cladding-pumped MM-EDFAs. In order to find the optimal solution rather than the quasi-solution, the initial population should be sufficiently large and the GA must be run several times to check for convergence to the same solution. The GA approach has been successfully applied to design several inverse fiber-design problems, including photonic bandgap fibers [103] and fiber gratings [104]. The basic principles of the GA were first laid down by Holland [105] and are well described in [106]. A pseudo-code, illustrating how a GA works, is shown in Figure 5.14 below.

```

BEGIN /* genetic algorithm */
  generate initial population
  compute fitness of each individual

  WHILE NOT finished DO
    BEGIN /* produce new generation */

      FOR population_size / 2 DO
        BEGIN /* reproductive cycle */
          select two individuals from old generation for mating
            /* biased in favour of the fitter ones */
          recombine the two individuals to give two offspring
          compute fitness of the two offspring
          insert offspring in new generation
        END

        IF population has converged THEN
          finished := TRUE
        END
      END
    END
  END

```

Figure 5.14. Basic process of a GA, after [107].

The GA has a parallel structure, working on multiple “individuals”, of a large population at the same time. The author has used the one of the Linux workstations (i.e. “Ruby”) of the Microstructured Fiber modelling group. The server specification of “Ruby” is: 2x 8 core Intel Xeon E7_4920, 2 GHz, 128 GB of memory. Thus using “Ruby”, 16 “individuals” can be evaluated in parallel in the GA application, which saved a lot computing time compared with using the standard office desktop. The main functional blocks of the GA used in this study were contained in a MATLAB toolbox, which allows the choice of population size, selection, and mutation functions.

In order to demonstrate the typical behaviour of a GA, a simple example is presented here to minimize the DMG across four signal mode-groups at 1550 nm in a cladding-pumped 4-mode-group EDFA. The cladding-pumped 4-mode-group EDFA studied for this case is the same as the 4-mode-group EDFA to be discussed in the next section (5.5.2). However, in the next section, the simulations were performed using WDM signals with a much more rigorous fitness function. Here, the pump power was set to 2.5 W, and the signal power was set to -10 dBm per mode. The free parameters (i.e. “gene”) of the GA are the same as the cladding-

pumped 4-mode-group EDFA problem discussed in the next section. The population size was set to 8 for this example. The results of 5 independent runs of the same GA application are shown in Figure 5.15(a). The objective value shown in Figure 5.15(a) represents the evolution of the average DMG of the whole population. Each independent simulation run has its own track, showing the random nature of the algorithm. After 50 generations, the 5 independent simulations almost converge, but into different “minimums”. This is a clear example showing the GA easily converges into a local minimum rather than giving the globe minimum. This behaviour can be minimized by increasing the population size, by selecting a more rigorous fitness function, and tweaking some probability-related parameters in the algorithm, such as the mutation rate. Figure 5.15(b) shows the evolution of the best and the mean DMG of the whole population of “simulation 4” in Figure 5.15(a). It shows that, in the first 20 generations, the GA sometimes generate worse populations than the previous generation. This is a good sign, as it allows a deeper search of the parameter space, reducing the chance of converging towards a local minimum.

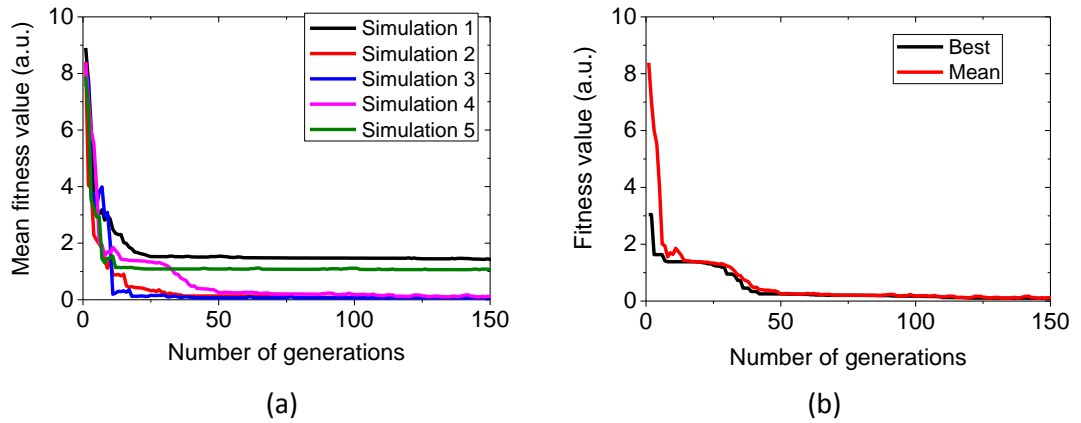


Figure 5.15. Application of a GA to minimize the DMG in a cladding-pumped 4-mode-group EDFA. (a) Evolution of the fitness value for the best individual for 5 runs of the same GA application. (b) Evolution of the best individual and the average fitness of the total population.

5.5.2 Design of a cladding-pumped four-mode-group and a six-mode-group EDFA.

In order to manipulate the erbium ion distribution, the erbium-doped core was divided into several layers while keeping the fiber refractive index profile (i.e. step-index) unchanged, so that the optimal dopant concentration in each core layer can be numerically investigated for the minimization of the DMG. For the purpose of reducing fabrication complexity, the number of erbium-doped layers should be kept to a minimum. Through initial trials, it was found that at least three-layer and four-layer doping structures shown in Figure 5.16 are required in order to achieve a DMG of less than 1 dB in the C- band (i.e. 1530-1565 nm) for the 4-mode-group EDFA and 6-mode-group EDFA respectively. Hence, for the 4-mode-group EDFA there are two structural parameters (i.e. a_1, a_2 shown in Figure 5.16(a)) determining the dimensions of the three-core layers and three doping concentration parameters (i.e. ρ_1, ρ_2, ρ_3) describing the erbium ion concentration of each core layer to be optimized. Similarly, there are three structural parameters (i.e. a_1, a_2, a_3 shown in Figure 5.16(b)) and four doping concentration parameters (i.e. $\rho_1, \rho_2, \rho_3, \rho_4$) to be optimized for the 6-mode-group EDFA. In addition, the fiber length is another key parameter that can be used as a free parameter to optimize the performance of the amplifier. Owing to the involvement of more than 5 free parameters, a GA was implemented to establish the optimum choice of the dopant concentration and the dimension of each core layer for the minimization of the DMG. In the GA implemented here, the fitness function (F) that I used to evaluate the quality of a given structure and to be minimized by the algorithm, is defined as:

$$F = \sum_{\lambda_i=1530nm}^{1565nm} \frac{DMG(\lambda_i)}{G_{ave}(\lambda_i)} \quad 5.6$$

where $DMG(\lambda_i)$ is the differential modal gain calculated at a wavelength of λ_i , and $G_{ave}(\lambda_i)$ is the average gain over the distinct special modes wavelength of λ_i . The sum of the ratio is performed over 15 WDM signals (i.e. uniformly spaced in the C-band from 1530 nm to 1565 nm). The free parameters (i.e. or the “genes” of the

algorithm) are the structural parameters (i.e. a_1, a_2, \dots), the doping concentration parameters (i.e. ρ_1, ρ_2, \dots) of the i^{th} core layer and the fiber length of the amplifier. It is to be noted that other fitness functions can easily be chosen and incorporated within the GA depending on the end design objectives. The current choice shown in Equation 5.6 is reasonable for minimizing the overall DMG and maximizing the average gain over the C-band. For all modeling work in this paper the WDM signals are assumed to have an input signal power of -20 dBm per spatial mode per wavelength and co-propagating with a multimode pump at 980 nm with an input power of 2.5 W. Note that for the non- LP_{0m} mode-groups (e.g. LP_{11}), an equal power of -20 dBm was assigned to the two degenerate modes (e.g. LP_{11a} and LP_{11b} modes), so that the sum of the two LP modes has no azimuthal dependence. The gain for the two degenerate modes (e.g. LP_{11a} and LP_{11b} modes) of the non- LP_{0m} mode-group is identical under the weakly guided approximation and the uniform pump intensity approximation in the case of cladding pumping. This pump power level was chosen based on past experience with the goal of ensuring more than 20 dB gain over the C-band for a WDM signal power of -20 dBm per channel. In the GA loop, the ASE calculation is ignored to reduce computing time. The tolerance threshold of F was set to 1×10^{-5} , which is close to zero and the maximum iteration number is set to 200. The algorithm terminates either when there is can be no further minimization of F after 20 successive generations or the maximum iteration number is reached. In general, it requires 50 to 70 generations for the GA to converge. Owing to the nature of GA techniques for a given set of starting conditions, the algorithm might only converge to a locally rather than globally optimum solution. To mitigate this risk, a relatively large population number (i.e. 32) was used for each generation in the GA. Also, the optimization tool was ran several times (i.e. typically 5) to robustly identify the “fittest” solution. Next, the robustness of the design to variation in each design parameter for the “optimal” fiber design in each instance was investigated.

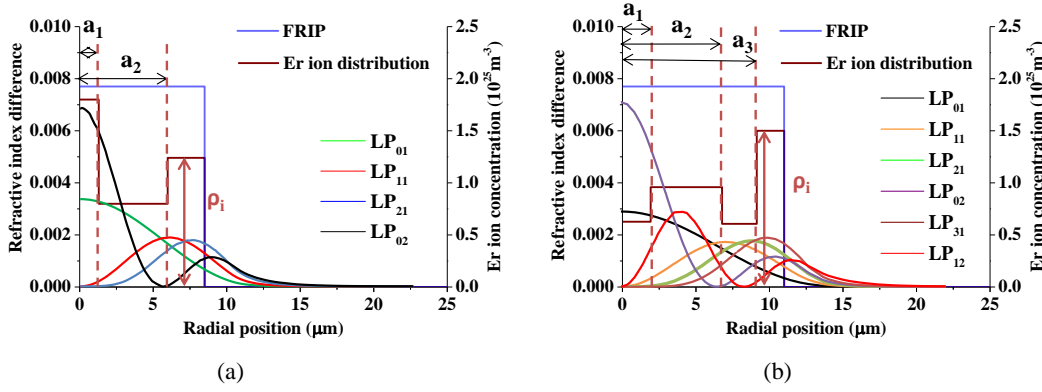


Figure 5.16. The fiber RI profile, the signal mode intensity distributions, and the doping profile of (a) 4-mode-group EDFA, denoted as “F1”, and (b) 6-mode-group EDFA, denoted as “F2”, to be optimized through the GA. ρ_i (m^{-3}) is the doping concentration of the i^{th} core layer.

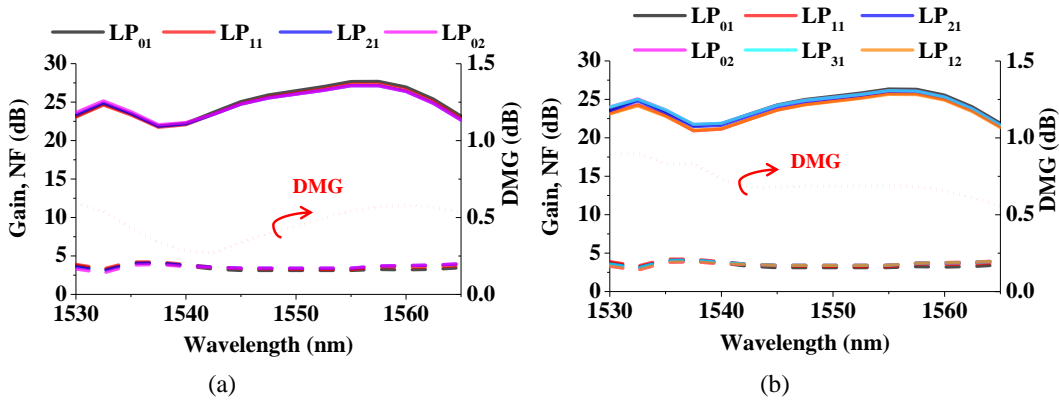


Figure 5.17. Modal gain (i.e. solid line), noise figure (i.e. dashed line) and DMG (i.e. red dotted line) characteristics of the best (a) four-mode-group EDFA, and (b) six-mode-group EDFA calculated by the GA.

(1) Four-mode-group EDFA

On the basis of our amplifier and fiber fabrication experience, a double-clad SI erbium EDF was studied with a core-to-inner clad NA of 0.15 and a core diameter of $17\text{ }\mu\text{m}$. It is assumed that the fiber is weakly guiding and supports the lowest-order four transverse mode-groups between 1530 nm to 1565 nm, whose mode intensity profiles are shown in Figure 5.16. The fiber diameter was chosen such that the LP₀₂ mode is strongly guided while the LP₃₁ mode is extremely leaky when the fiber is bent to a radius of 10 cm. The bend loss of the guided modes were calculated by using the imaginary part of the effective mode indices (i.e. computed using the COMSOL Multiphysics software). The diameter of the inner-

cladding was chosen to be 70 μm , compatible with the preferred choice of pigtailed pump diode, which creates a uniform pump intensity of $6.5 \times 10^8 \text{ W/m}^2$ at the input end of the fiber. The optimum fiber length selected by the GA was 6.2 m. The best fiber design (i.e. $a_1 = 1.3 \text{ }\mu\text{m}$, $a_2 = 6.0 \text{ }\mu\text{m}$, $\rho_1 = 1.8 \times 10^{25} \text{ m}^{-3}$, $\rho_2 = 8.0 \times 10^{24} \text{ m}^{-3}$, $\rho_3 = 1.2 \times 10^{25} \text{ m}^{-3}$) obtained through the GA is shown in Figure 5.16 (a), here denoted as “F1”. This W-shaped erbium-dopant distribution provides a similar amount of overlap between the dopants and the signal modes. The gain and noise characteristics of the best fiber design are plotted in Figure 5.17(a). The multimode ASEs were calculated at 15 wavelengths uniformly spaced from 1530 nm to 1565 nm. The input signal/ pump conditions are same as used in the GA. As can be seen from the red dotted curve in Figure 5.17(a), the DMG is controlled to better than 0.6 dB from 1530 nm to 1565 nm, with a minimum of 0.3 dB at 1542.5 nm and maximum of 0.6 dB at 1530 nm. The modal gains are found to be more than 20 dB with an average gain of 24.8 dB. The NFs shown in Figure 5.17(a) are found to be between 3.2 and 5.3 dB and are comparable with those of the cladding-pumped multi-core EDFA proposed in [93].

From more extensive simulations, it was also found that changes up to $\pm 10\%$ in length or pump power of the amplifiers based on F1 only results in a very small variation in the DMGs (i.e. still less than 1.0 dB over the C-band).

(2) Six-mode-group EDFA

In this instance the core diameter of the EDF was scaled up to 22 μm in order to support six mode-groups while keeping the NA exactly the same as that of the previous case. The fiber diameter was chosen such that the LP_{12} mode is well-guided and the LP_{41} mode becomes very leaky when the fiber is bent to a radius of 10 cm. The FRIP and signal intensity profiles of the 6-mode-group EDFA (i.e. denoted as “F2”) and its optimal erbium-dopant profile (i.e. $a_1 = 1.9 \text{ }\mu\text{m}$, $a_2 = 6.8 \text{ }\mu\text{m}$, $a_3 = 9.1 \text{ }\mu\text{m}$, $\rho_1 = 6.3 \times 10^{24} \text{ m}^{-3}$, $\rho_2 = 9.6 \times 10^{24} \text{ m}^{-3}$, $\rho_3 = 6.1 \times 10^{24} \text{ m}^{-3}$, $\rho_4 = 1.5 \times 10^{25} \text{ m}^{-3}$) obtained from the GA are shown in Figure 5.16(b). The corresponding optimum fiber length found by the GA was 5.9 m. The gain and NF characteristic of the optimum 6-mode-group EDFA are shown in Figure 5.17(b).

As shown in Figure 5.17(b), the DMG (i.e. red dotted line) was found to be below 1 dB with the minimum value of 0.554 dB at 1565 nm and the highest value of 0.901 dB at 1530 nm. The gain and noise characteristics of F2 are similar to those of F1. The modal gains are well above 20 dB with an average gain of 24.0 dB. The NFs shown in Figure 5.17(b) are found to be between 3.4 dB and 5.2 dB.

Again, it was found that changes up to $\pm 20\%$ in length or pump power of the amplifiers based on fiber F2 only result in a small variation in the DMGs (i.e. still less than 1.5 dB over the C-band).

(3) Fabrication tolerance discussion

Having demonstrated that very low DMG in both 4-mode-group and 6-mode-group cladding-pumped EDFAs can be theoretically realized, the next step is to investigate how the inevitable imperfections introduced during the EDF fabrication process can affect the EDFA performance. Firstly, a tolerance check on the doping concentration of each erbium-doped layer is studied in this section to assess the fabrication challenge in achieving the predicted levels of amplifier performance. A set of simulations was ran on both F1 and F2, in which the doping concentration of each core layer (i.e. $\rho_1, \rho_2 \dots$) was modified by $\pm 5\%$ and $\pm 10\%$ from the optimum value. Results for F1 and F2 are presented in Figure 5.18 and Figure 5.19 respectively. Note that in the tolerance studies, the fiber length for both F1 and F2 was fixed at the optimum lengths selected by the GA.

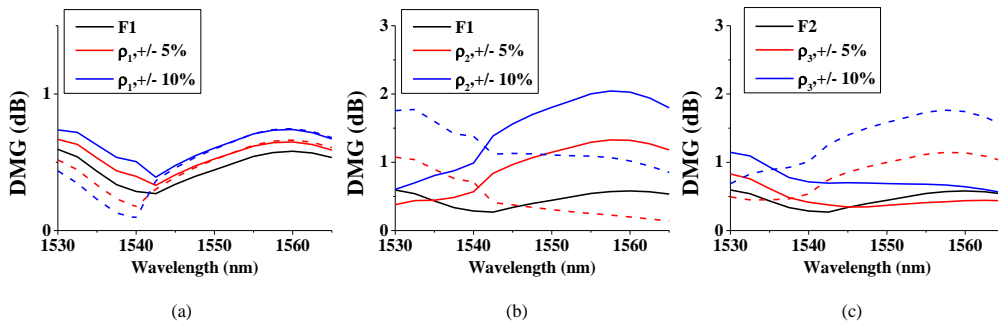


Figure 5.18. Variation of the DMG vs. signal wavelength as the doping concentration of (a) the 1st, (b) the 2nd, and (c) the 3rd core layer is changed for fiber F1. Solid lines represent “+” variations, while dashed lines represent “-” variations.

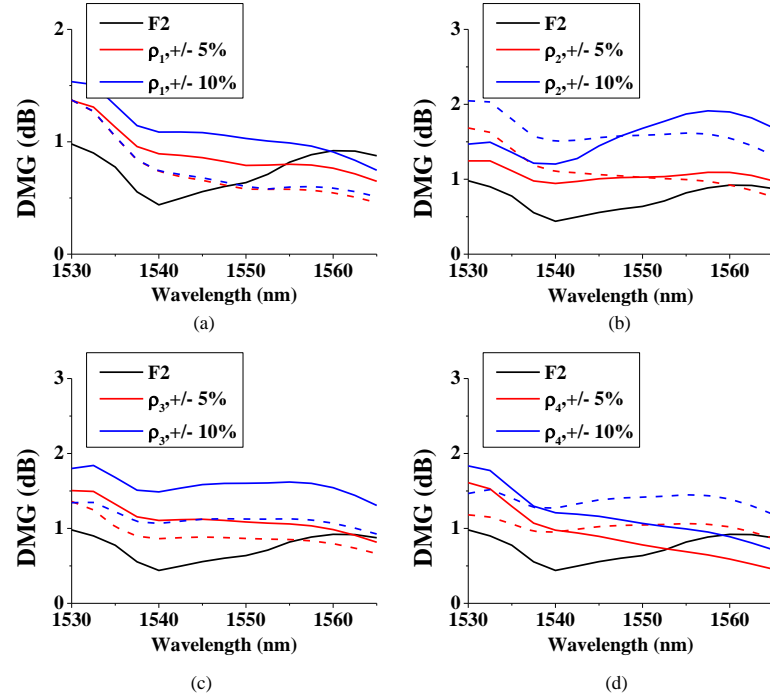


Figure 5.19. Variation of the DMG vs. signal wavelength as the doping concentration of (a) the 1st, (b) the 2nd, (c) the 3rd and (d) the 4th core layer is changed for the fiber F2. Solid lines represent “+” variations, while dashed lines represent “-” variations.

From Figure 5.18(a), it is evident that less than 1 dB DMG can be achieved over the full C-band with up to $\pm 10\%$ variation in the doping concentration of the 1st layer of F1. Decreasing the doping concentration of the 2nd layer of F1 by 5% brings about a rise in the DMG at shorter wavelengths while the DMG values at longer wavelengths are even smaller than for the optimum fiber. On the contrary, increasing the doping concentration of the 2nd layer of F1 results in a large increase in the DMG over the entire C-band. For the 3rd layer of F1, increasing the doping concentration (ρ_3) up to 10% results in an increase in DMG at shorter wavelengths, but the DMG is still below 1.2 dB over the entire C-band. In particular, when ρ_3 is increased by 5% (i.e. red solid line in Figure 5.18(c)), the DMG of the design is about 0.2 dB higher than that of F1 at 1530 nm, but at 1565 nm the DMG is about 0.1 dB lower than the optimum design. This means that “ $\rho_3 + 5\%$ ” is as good as F1. However, F1 is still the best solution providing the lowest DMGs over the whole C-band. Decreasing ρ_3 results in an increase in gain for the LP₀₁ mode relative to the other signal modes at longer wavelengths, and thus

increasing the DMG as shown by the dashed lines in Figure 5.18(c). In general, the performance of F1 is robust for up to -5% change in erbium concentration of the 2nd core layer and up to +10% change for the 3rd core layer.

Figure 5.19(a, b) show that the performance of F2 is acceptable (i.e. with DMG lower than 1.5 dB over the C-band) for up to $\pm 10\%$ change in the doping concentration of the first layer (ρ_1), and up to +5% change in ρ_2 . However, even a small decrease in the doping concentration of the 2nd layer (ρ_2) from its optimum value results in an increase of the DMG to nearly 2 dB at the short wavelength edge of the C-band. For the doping concentration of the 3rd layer of F2 indicated by Figure 5.19(c), decreasing ρ_3 by 10% results in an increase in DMG but still below 1.5 dB over the C-band. The 4th layer presents a slightly more complicated relationship, as shown in Figure 5.19(d). Up to -5% change of ρ_4 is acceptable. At wavelengths longer than 1535 nm, the DMG is lower than 1.5 dB when ρ_4 changes by up to +10%. However, the DMGs are considerably increased at shorter wavelengths when ρ_3 is increased by more than +5%. For example, if ρ_3 increases by +10% from its optimum position while the simulation conditions and other parameters of F2 are kept unchanged, the gain of the LP₀₁ mode slightly decreases and the gain of the LP₃₁ mode increases. This results in a larger DMG (i.e. 2 dB).

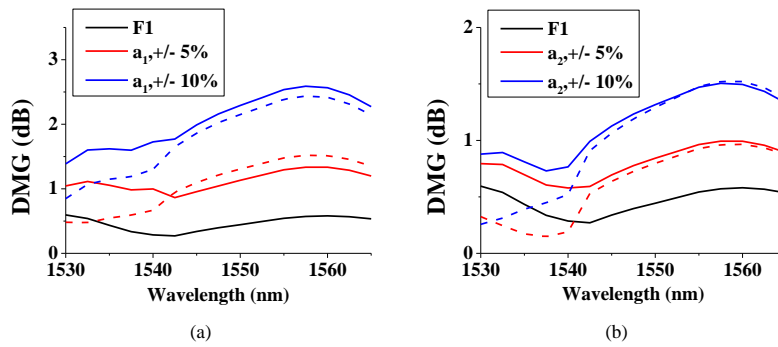


Figure 5.20. Variation of the DMG against signal wavelength as the structural parameter (a) x_1 , and (b) x_2 is changed for the fiber F1. Solid lines represent “+” variations, while dashed lines represent “-” variations.

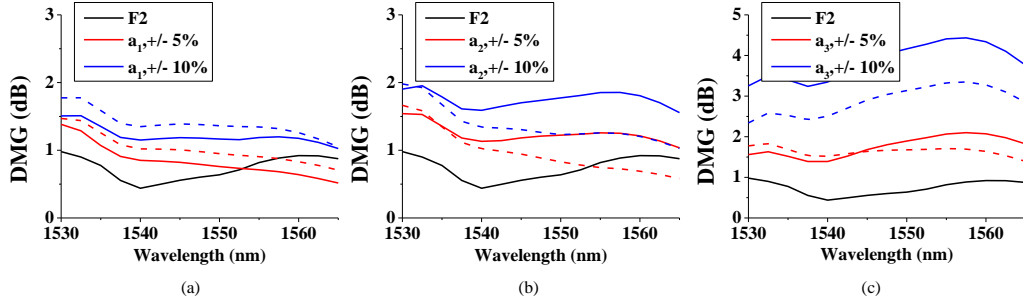


Figure 5.21. Variation of the DMG vs. signal wavelength as the structural parameter (a) a_1 , (b) a_2 , and (c) a_3 is changed for the fiber F2. Solid lines represent a "+" variations, while dashed lines represent "-" variations.

A tolerance check of the structural parameters (i.e. $a_1, a_2 \dots$) of both F1 and F2 was also undertaken. Once again a set of simulations were ran on both F1 and F2, in which the structural parameters (i.e. $a_1, a_2 \dots$) were modified by $\pm 5\%$ and $\pm 10\%$ from the optimum value. Results for F1 and F2 are presented in Figure 5.20 and Figure 5.21 respectively. Again note that in the tolerance studies, the fiber lengths for both F1 and F2 were fixed at the optimum lengths selected by the GA.

From Figure 5.20(a), it can be seen that increasing a_1 of F1 by +10% or decreasing a_1 by 10% results in a large rise (i.e. $>1.5\text{dB}$) in the DMG across the C-band (i.e. 1545 nm to 1565 nm). If a performance of $\text{DMG} < 1.5\text{ dB}$ for the full C-band is required, the variation of a_1 in F1 should be kept to $\pm 5\%$. However, from Figure 5.20(b), it is evident that the DMG values for the full C-band are below the upper limit (i.e. 1.5 dB) with up to $\pm 10\%$ variation in a_2 for F1.

Figure 5.21(a, b) show that the performance of F2 is acceptable for changes from -5% to +10% in the a_1 , and -5% to +5% variation in a_2 if a $\text{DMG} < 1.5\text{ dB}$ across the C-band. a_3 determines the thickness of the 3rd and the 4th core layers of F2, such that any changes in a_3 mainly affect the overlap between the erbium dopants, LP_{31} and LP_{12} modes. Simulations show that the gain for the LP_{12} and LP_{01} modes become the largest among all the modes when a_3 is increased, while the gain for the LP_{31} mode becomes highest when a_3 is decreased. Overall, the results in Figure 5.21(c) show that a_3 is the most critical parameter of all. Only small variations in a_3 are tolerable and particular care must be applied to try and match the optimum value in order to maintain a low DMG.

Such complex fibers (e.g. F1 and F2) with multi-layer cores are likely to be challenging to realize using conventional MCVD/solution-doping preform manufacturing techniques, though they are by no means impossible. However, alternative approaches offering improved spatial dopant control exist, and could be preferable in practice. For example, by using microstructured fibers [89] or chelate-based vapour-phase technology [108].

In conclusion, I have applied a Genetic Algorithm to minimize the differential modal gain in cladding-pumped EDFAs supporting four and six-mode-groups. The optimum 4-mode-group EDFA and 6-mode-group EDFA designs, exhibiting three-layer and four-layer core structures (denoted as 'F1' and 'F2') respectively, provide less than 1 dB DMG across the C-band. Over 20 dB gain across the C-band is obtained for both F1 and F2 using a forward pump power of 2.5W and EDF lengths of 6.2 m and 5.9 m respectively. I have also studied the impact of variation in doping concentration and physical dimension of each core layer of F1 and F2 on DMG. For both F1 and F2, the sensitivity to the changes in concentration is the least (up to $\pm 10\%$ of its optimal value) for the inner most layer. The dimension of the inner-most layer (i.e. a_1) of both F1 and F2 are tolerant to changes from -5% to $+5\%$ variation of its optimal value. Simulations show that the a_3 of F2 is the most critical, and the optimum value should be targeted if a low DMG profile is required.

5.6 Conclusion

This chapter summaries the designs and theoretical supports for FM-EDFAs supporting four and six mode groups during my PhD, within the frame work of the MODEGAP project. Initially, I performed the systematic design of the core-pumped 4-mode-group EDFA using a multi-ring structure. Due to then limited fabrication resources, we decided to make a 4-mode-group EDFA using our existing ring-doped preform, as simulations showed it would also give a reasonably good performance when pumped by high-order modes. We experimentally characterised the ring-doped 4-mode-group EDFA using a LP₂₁ pump mode configuration. There were discrepancies between the simulation

fittings and the measured modal gain properties, but the discrepancies can be explained by the mode coupling due to the mode mismatch between the passive fiber and the 4-mode-group EDFA. In real MDM systems, mode crosstalk will not be a problem, as the independent signal channels can be recovered through MIMO processing.

Considering the reduction of both the pump power costs and the pump modal profile complexity, we moved on to investigate cladding-pumped FM-EDFAs. I upgraded my core-pumped MM-EDFA simulator to make it compatible with cladding pumping. Next, I performed the initial simulations to assess our existing erbium-doped preforms to see whether we can use an existing preform to make a good performance cladding-pumped 4-mode-group EDFA. Subsequently, a double-clad 4-mode-group EDFA was made in-house according to my simulations. Our cladding-pumped 4-mode-group EDFA was successfully demonstrated and has been applied in a 6-spatial-mode heterogeneous SDM network in collaboration with Bell Labs US. Lastly, I upgraded my MM-EDFA simulator in conjunction with a powerful GA optimization tool. Based on my GA tool, I advanced the theoretical works in the design and optimization of the cladding-pumped 4-mode-group and 6-mode-group EDFAs.

The amplifier activities summarized in this chapter are the final deliverables on the amplifier aspect of the MODEGAP project. Yet, a significant scope of scaling the number of modes of a single fiber still exists. Our ongoing 9-mode-group EDFA activity will be briefly discussed in the “conclusion and future work chapter” of this thesis.

Chapter 6: Modeling of active fibers with ring-index profile

In the ideal situation, orthogonal modes in a few-mode fiber do not exchange power among each other. In another words, they do not couple. However, in practice, the modes will couple into each other during the propagation due to fiber imperfections, bending and twisting. MIMO digital signal processing [22] is usually required at the receiver end to equalize the cross talk. The complexity of MIMO scales linearly with the differential modal group delay, number of modes and the symbol rate [109]. Mode-division multiplexing for capacity-scaling technology has been primarily demonstrated over few-mode fibers whose RI profiles are graded-index [26], [68], [70], [86], [88], [110], where the technology relied on intense MIMO digital processing. As the number of modes (i.e. information channels) increases, the complexity of MIMO processing increases significantly for the multimode step-index or graded-index fibers. However, if mode coupling can be minimized, the use of MIMO processing can be avoided or simplified. Hence, the complexity of MDM systems can be reduced and scaled up.

This chapter illustrates the amplifier modeling based on two types of ring fibers. The first type is ring-core fibers (RCFs) that support LP modes, which can be used for MDM systems with the benefits of reducing MIMO complexity due to their unique modal properties [111], [112]. The modeling of the multimode ring-core EDFA under various conditions is discussed in section 6.1. The second type is ring-index fibers with an air hole in the center that supports orbital angular momentum (OAM) modes. The OAM modes are also eigenmodes of the fiber that use different basis sets compared with the vector modes discussed in section 2.1.1 of chapter 2. OAM modes offer another degree of freedom for information multiplexing and due to the large vector-splitting nature of the OAM modes, MIMO free transmission can potentially be achieved [30], [31]. Section 6.2 presents the modeling of the amplification of such OAM modes and the design optimization of the OAM EDFA.

6.1 Modeling of erbium-doped ring-core fibers

Ring-core multimode fibers were studied as early as the 1970s [113], [114]. At the time, only fiber modal guidance properties [114] and fiber impulse responses [113] were studied. In 1982, the mode-multiplexing principle was implemented for the first time on a highly multimode graded-index ring-core fiber using spatial filtering techniques [18]. However, shortly afterwards the interest in fiber communication shifted to single-mode fibers, while the discussion of multimode ring-core fibers for MDM was paused for almost 30 years. In 2013, researchers from the University of Oxford theoretically proposed that the MM RCFs supporting 1st radial modes have great potential for improving the capacity of MDM systems, due to their low digital signal processing complexity. This is because the effective RI difference (Δn_{eff}) between two adjacent LP mode-groups significantly increases with increasing azimuthal number of LP modes [112]. Δn_{eff} is inversely proportional to the mode coupling coefficient [115]. Therefore, in the ring-core fiber based MDM system, MIMO is only needed to recover signals from the low-order LP modes which have strong mode coupling. The high-order LP modes with negligible mode coupling can be transmitted MIMO-free. Another feature of RCFs is that the intensity profile of the spatial modes are similar to each other, confined by the not-so-thick ring core. This feature can potentially result in a low differential modal gain (DMG) among all the spatial modes, which will be investigated in the following sections.

This work is a part of the EPSRC-funded project “COMIMO”, which aims to demonstrate high-capacity MDM transmission networks based on novel RCFs. The author’s role in this project is to design and model the RC EDFAs that match the state-of-the-art transmission RCFs designed by project partners from the University of Oxford. The RCF is designed to create a large effective RI difference (Δn_{eff}) between the adjacent LP mode-groups, in order to suppress bend-induced mode coupling. Unlike the SI RC MMF reported in [112], the fiber to be studied in this section has a graded-index ring profile that allows larger fabrication tolerance over the ring thickness [111]. A graded-index RC MM EDFA is designed

to match the passive GI RCF given in [111]. This RC MM EDFA effectively guides LP_{01} , LP_{11} , LP_{21} , LP_{31} , LP_{41} and LP_{51} mode-groups within the C-band (i.e. 1530 nm to 1565 nm). The modal gain performance of this RC EDFA is simulated under both core- and cladding-pumped conditions with special consideration to macro-bending.

6.1.1 Modeling of bent ring-core multimode erbium-doped fiber amplifier

A simple picture shown in Figure 6.1 describes bend distortion in terms of the fiber RI (i.e. ring-core fiber), and the equivalent index n_{eq} (i.e. dashed, slanted RI profile) defining our bent-fiber model [116], [117]. This basic model says that a bend of radius R_{bend} shifts n_{eq} in proportion to the position x along the bend: $n_{eq} = n(1 + \frac{x}{1.40R_{bend}})$, where 1.40 is a coefficient with the photoelastic effect taken into account [118].

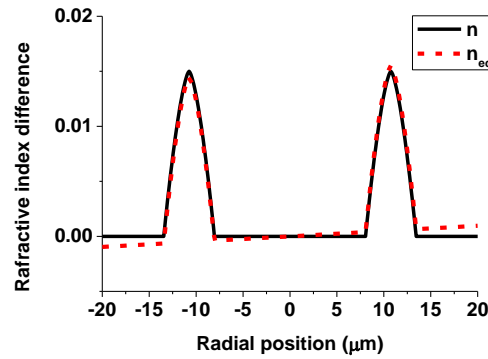
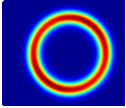
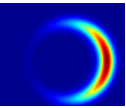
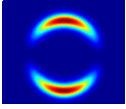
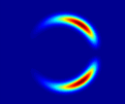
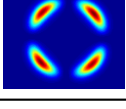
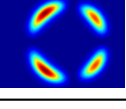
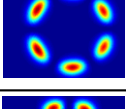
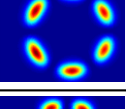
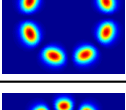
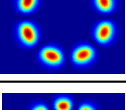
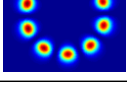
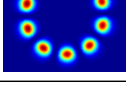


Figure 6.1. RI of the RC EDFA when it is straight (i.e. black line) and with a bend radius of 5 cm.

The simulation finds that this RC EDFA can be bent to a radius of 5 cm with negligible propagation loss for all the modes guided at 1550 nm. The bend loss of the guided modes were calculated by using the imaginary parts of the effective RI computed by the COMSOL Multiphysics 4.3® software. The mode intensity profiles of the guided modes at 1550 nm for both straight and bent fibers (i.e. $R_{bend} = 5$ cm) are shown in Table 6.1. The fiber RI profile is lifted at the side opposing the bending center, yielding a shift of intensity of guided modes to that side. This is due to the better modal guidance, as shown by the LP_{01} , LP_{11} and LP_{21} modes in Table 6.1. However, the higher order modes (i.e. LP_{31} , LP_{41} and LP_{51})

preserve their intensity profile. As long as the effective RI of the higher-order modes are higher than the surrounding cladding RI (i.e. also lifted as a result of bending), the higher-order modes are well guided in the fiber core. The detailed physical explanation of the bend-distortion immunity of higher-order modes can be found in [119].

Table 6.1. Modal properties of the RC EDFA.

Signal Mode	Mode intensity profile (Straight)	Overlap integral with Er^{3+} (Straight)	Mode intensity profile ($R_{\text{bend}}=5\text{cm}$)	Overlap integral with Er^{3+} ($R_{\text{bend}}=5\text{cm}$)
LP01		0.9800		0.5286
LP11 odd		0.9822		0.6334
LP21 odd		0.9848		0.9214
LP31 odd		0.9867		0.9820
LP41 odd		0.9672		0.9658
LP51 odd		0.9795		0.9719

6.1.2 Modeling of core-pumped ring-core multimode erbium-doped fiber amplifier

The core-pumped RC MM EDFA was simulated using the simulation model described in section 2.2.3. Here, the ASE has been neglected for simplicity. The erbium-doping profile is assumed to follow the RI profile. The calculated overlap integrals of the normalized signal-mode profiles and the erbium-dopant distribution with and without bending are shown in Table 6.1. It was found that

the overlap between signal and rare-earth dopants are almost equal for each mode group. Firstly, the performance of RC MM EDFA was analysed under the core-pumping condition by using a pure LP_{01} pump and a pure LP_{41} pump at 980 nm. For each investigation, a co-propagating pump power of 350 mW and an input signal power of -10 dBm per mode group were used. The modal gain evolution of each signal mode-group against the fiber position along the z-axis for a pure LP_{01} pump and a pure LP_{41} pump without bending the fiber is illustrated in Figure 6.2(a). Under the same simulation parameters but with a bending radius of 5 cm was also considered. The other pair of gain curves are plotted in Figure 6.2(b).

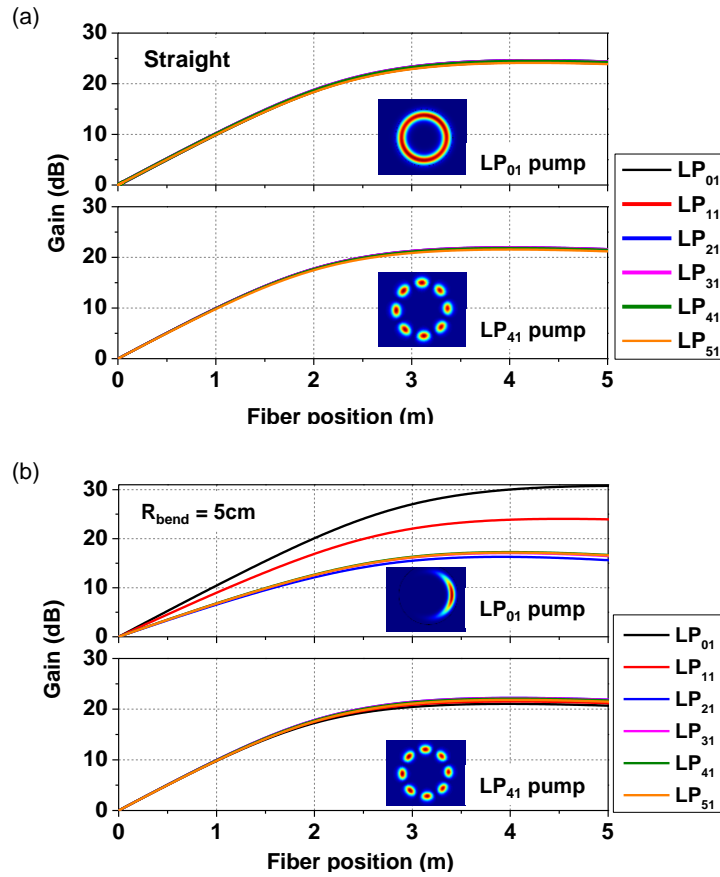


Figure 6.2. Modal gain evolution against fiber position for LP_{01} pump and LP_{41} pump in a (a) straight, and (b) bent fiber.

As it shown in Figure 6.2(a), for both pump modes, the signal gains are nearly identical to each other, which can be explained by the almost equal overlap integrals between signal modes and the rare-earth dopants shown in the third

column of Table 6.1. However, when the RC EDFA is bent with a radius of 5 cm, large gain differences among the signal modes (i.e. particularly between the LP_{01} mode and higher-order modes) were observed due to the bend-induced distortion on low-order modes (i.e. especially the LP_{01} mode). In this case, the LP_{01} pump mode is unsuitable for core pumping due to its high sensitivity to bending. The simulations also found that the LP_{41} pump mode guided in the RC EDFA is robust to bending down to a radius of 3 cm. Combined with the simulation results shown in Figure 6.2, it can be concluded that the LP_{41} mode is the best pump mode for reliable amplifier performance of the core-pumped configuration.

6.1.3 Modeling of cladding-pumped ring-core multimode erbium-doped fiber amplifier

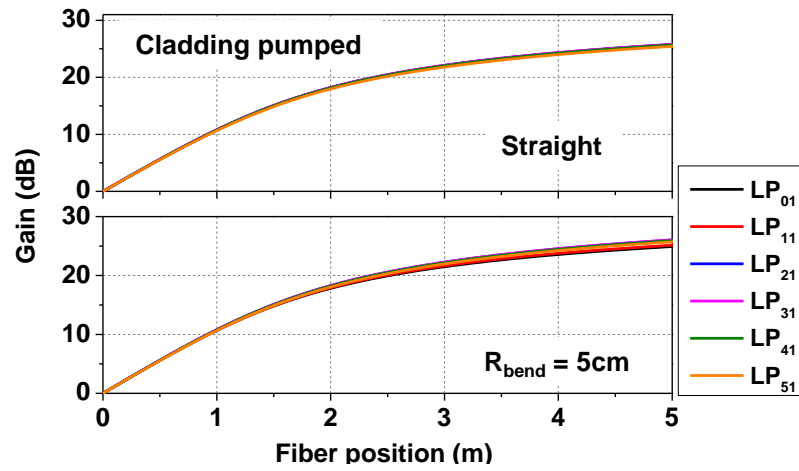


Figure 6.3. Modal gain evolution against fiber position for cladding pumping in straight, and bent RC EDFA.

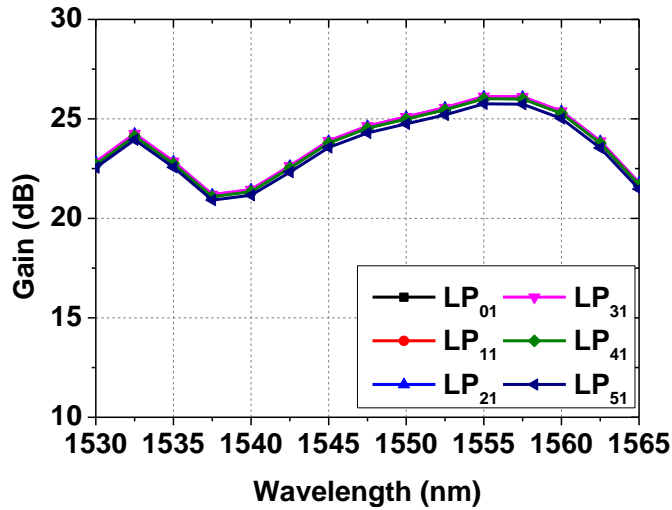


Figure 6.4. WDM signal gain spectrum of the cladding-pumped RC EDFA.

The cladding-pumped RC MM EDFA was simulated using the simulation model described in section 5.3, where the ASE is neglected for simplicity. In the simulation, a 70 μm inner cladding diameter (i.e. chosen with practical fabrication and power coupling considerations in mind) was selected and 2 W co-propagating input multimode pump power (i.e. at 980 nm), which creates pump intensity of $5.2 \times 10^8/\text{m}^2$ at the input end of the fiber. Figure 6.3 shows the simulated modal gain evolutions against fiber position for all the signal modes with an input power of -10 dBm per mode at 1550 nm for the cladding-pumped RC EDFA with and without bending. In Figure 6.3, at fiber position of 5 m, the maximum gain difference among the six mode-groups is 0.6 dB for the straight fiber, and 1.5 dB for the fiber with R_{bend} of 5 cm. In conclusion, more than 20 dB gain for all the signal modes at 1550 nm can be achieved after 5 m length of the amplifier without much compromise to the extent of bending.

Finally, the WDM plus multimode signal gain for the RC EDFA was simulated. 15 wavelengths spaced equally from 1530 nm to 1565 nm and 6 spatial modes at each wavelength with power of -20 dBm per mode per wavelength were used as the input signals. The input multimode pump power was set to be 2 W, and the fiber length was chosen to be 5 m in order to balance the gain in between the short wavelengths (i.e. 1530 nm to 1535 nm) and longer wavelengths (i.e. 1550

nm to 1565 nm). The WDM plus multimode signal gain spectrum is shown in Figure 6.4. It can be seen from Figure 6.4 that the gain curves arise from the overlap of different spatial modes at all the wavelengths within the C-band. The total gain difference across the whole band is about 5 dB. The WDM plus multimode gain is relatively immune to bending down to R_{bend} of 5 cm.

6.1.4 Conclusion

Simulations show that under the core-pumping condition, the RC EDFA can provide impressive equal modal gain with little required control on the pump modal content when the fiber is straight. When the fiber is bent to a radius of 5 cm, the LP_{01} pump mode will create a significant gain preference on the LP_{01} signal mode relative to the other signal modes due to the bend-induced modal distortion. However, if a high-order mode pump (i.e. LP_{41}) is used, then small modal gain differences can still be achieved. Lastly, the RC EDFA under the cladding-pumped condition is presented. Not only was very small gain differences across all the signal modes found, but the DMG was also relatively immune to macro-bending down to radius of 5 cm.

The proposed design has the potential to be scaled up to guide many more spatial modes. A cladding-pumped ring-core EDFA based on this design will be produced in the near future (as one of the deliverables of the COMIMO project). The cladding-pumping scheme will be the ultimate choice for heavily multimoded RC EDFA not only to reduce costs but also to provide robust amplifier performance.

6.2 Amplification of twelve orbital-angular-momentum modes in an air-core erbium-doped fiber

It is well known that photons can carry orbital angular-momentum (OAM), characterized by a helical phase front, $\exp(iL\phi)$, where L is the topological charge [120]. Recently, the use of OAM states as orthogonal signal channels in communication systems has gained considerable interest [30], [121]–[124]. In particular, 1km length MIMO free transmission of the two first order OAM modes was successfully demonstrated using a vortex fiber by Boston University in 2013

[30]. To date, two classes of fibers have demonstrated stable propagation OAM modes over km length. The first class is based on solid-core fiber designs (e.g. vortex fiber [30], [125], high-index-contrast ring-core fiber [123]), transmission of low-order OAM states has been achieved. However, solid-core fibers are typically incapable of transmitting higher-order OAM states, either because the effective V-number is not sufficient, or the vector splitting of the higher-order OAM states becomes small. The second class features an air core and an annular raised-index region which guides light [31], [126]. The high index-contrast of the air-glass interface enables a large effective RI splitting among the vector (HE/EH) modes of the same $|L|$ family, even for high orders of L [125]. This significantly reduces modal crosstalk and allows stable transmission of the high-order OAM states. Higher-order OAM states have also been theoretically postulated to exhibit better tolerance to fiber ellipticity, birefringence [123] and experimentally demonstrated to resist bend perturbations [31]. Hence, they appear more suitable for long distance transmission. The development of in-line OAM mode amplifiers is essential for serious considerations of OAM modes based fiber communication network. Similar to few-mode erbium-doped fiber amplifiers (FM EDFAs) used in few-mode transmission, the differential modal gain (DMG) for independent OAM modes will be a key characteristic of OAM EDFAs, and thus must be minimized to optimize system performance.

6.2.1 Orbital angular-momentum modes in fibers

Prior to the amplifier discussion, a brief review of OAM modes in fibers is presented here, while a comprehensive review of fiber OAM modes can be found in [125].

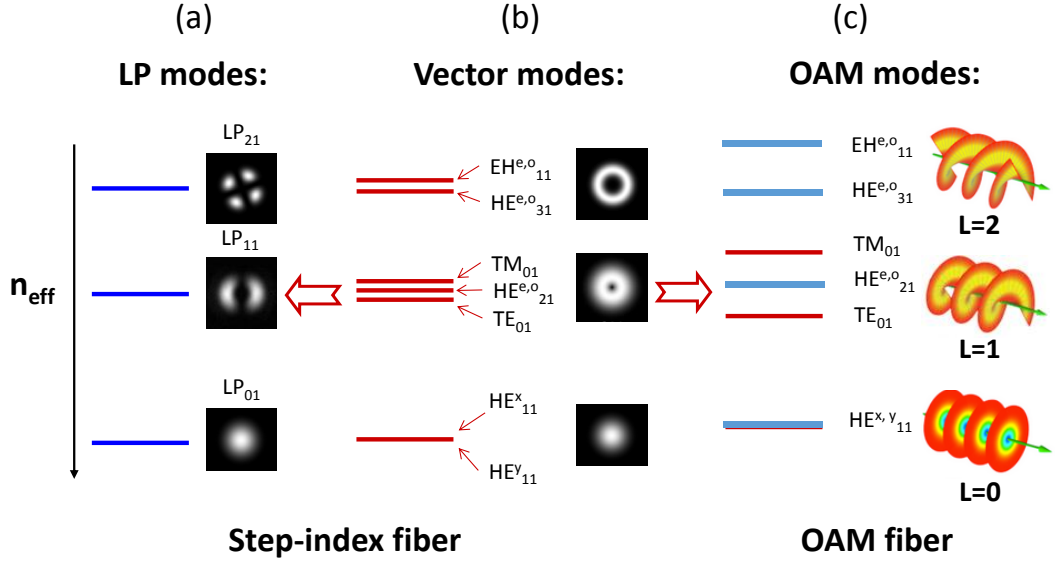


Figure 6.5. Modes of a SI fiber under the (a) scalar approximation, and (b) full-vector solutions. (c) Large modal effective RI splitting between the vectors modes in an OAM fiber.

Figure 6.5 gives a schematic diagram of the modes in a step-index fiber (i.e. under the scalar approximation and the full-vector solutions) and an OAM fiber. As discussed in chapter 2, the LP modes are scalar representations of vector modes. In weakly guiding fibers, the effective RI of the vector modes that belongs to the same LP mode-group become very similar. As shown in Figure 6.5(b), the red lines that represent TM₀₁, HE₂₁ and TE₀₁ sit closely next to each other. The LP modes can be represented as linear combinations of the non-degenerate vector modes, assuming their propagation constants are the same, as summarized in Table 2.1. Unlike weakly guiding fibers, in an OAM fiber the effective RI of the vector modes are pushed far apart from each other, usually larger than 1×10^{-4} . Mathematically, the fiber OAM modes can be represented by combinations of half- π phase-shifted degenerate vector modes, with a few exceptions in some special fibers [127], which are not discussed in this thesis:

$$OAM_{(l,m)} = \begin{Bmatrix} HE_{l+1,m}^e \pm iHE_{l+1,m}^o \\ EH_{l-1,m}^e \pm iEH_{l-1,m}^o \end{Bmatrix} = F_{l,m}(r) \begin{Bmatrix} \hat{\sigma}^{\pm} \exp(\pm il\phi) \\ \hat{\sigma}^{\mp} \exp(\pm il\phi) \end{Bmatrix} \quad 6.1$$

where $\hat{\sigma}^{\pm} = \hat{x} \pm i\hat{y}$ represents left- or right-hand circular polarization, also denoted by $S = \pm 1$. The term $\exp(\pm il\phi)$ represents the helical phase, and l (i.e. or

$|L|$) denotes the OAM-mode order. The OAM modes are the true modes in the fiber, as they are combinations of only degenerate vector modes that have identical propagation constants. The OAM modes formed from HE modes have their spins aligned with the sign of L . The OAM modes constructed by EH modes have their spins anti-aligned with the sign of L . TE_{0m} and TM_{0m} modes have different propagation constants, so that they cannot be used to create OAM modes.

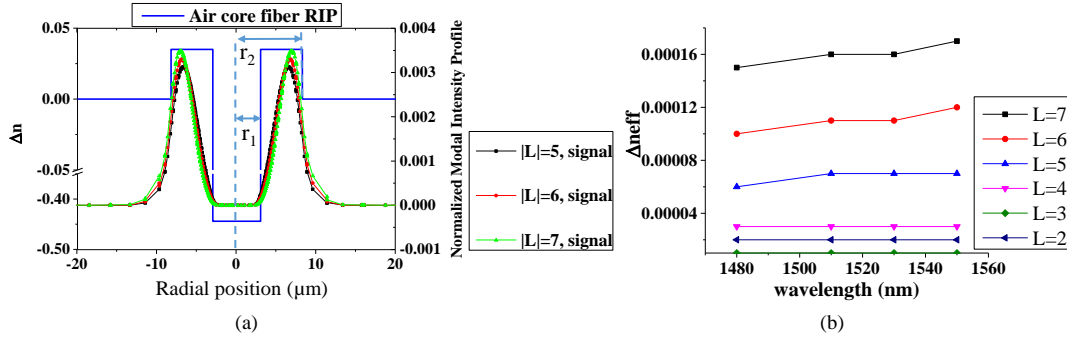


Figure 6.6. (a) RIP of the air-core fiber overlaid with the normalized signal intensity profile of the OAM states $|L|=5, 6, 7$. (b) The effective RI difference (Δn_{eff}) between the vector modes within the same $|L|$ family as a function of wavelength, for a radial order of $m=1$.

Figure 6.6(a) shows the RI profile (RIP) of the state-of-art OAM transmission air-core fiber from our collaborators in University of Boston [31]. The inner radius (r_1) of the air core is 3 μm , the outer radius (r_2) is 8.25 μm and the RI difference between the annular guiding region and the silica cladding is 0.035. The air-core fiber is designed to guide up to the $|L|=7$ OAM family. Here, the OAM modes are identified as $\text{OAM}_{(L,m)}$, where L is the OAM mode order, and m is the number of concentric rings in the intensity profile of the mode. The mode intensity profiles of $\text{OAM}_{(L,1)}$ with $|L|=5, 6$ and 7 modes are shown in Figure 6.6(a). Figure 6.6(b) shows the effective RI difference between the vector modes (i.e. HE/EH modes) from the same $|L|$ family (i.e. $m=1$) as a function of wavelength. Figure 6.6(b) shows that a large effective RI splitting is observed among the high-order OAM families (i.e. $|L|=5, 6$ and 7), which makes these OAM modes more resilient to perturbations as they propagate along the fiber. The low-order $\text{OAM}_{(L,1)}$ modes (i.e. $|L|=1-4$) are not considered in this work due to insufficient vector splitting. The double-ring modes (i.e. $\text{OAM}_{(0,2)} - \text{OAM}_{(3,2)}$) can also be guided in the air-core

fiber at 1550 nm in principle. However, these modes are not considered in this work for two reasons. Firstly, if the double-ring modes become degenerate in some wavelength regime with the high-order ring modes, phase-matched cross-coupling is possible. Second, passive fiber coupling and transmission of such states has not yet been demonstrated.

The core-pumped OAM mode amplifier was simulated using the full-vector mode FM-EDFA simulator described in section 4.2 of chapter 4. The vector fields of signal and pump modes were computed using the COMSOL Multiphysics 4.3® software. In the cladding-pumped case, the heavily multimoded pump is treated as a single transverse mode with a uniform intensity across the inner cladding and annular guiding regions [50]. Co-propagating pumps are used for all models presented in this chapter in order to speed up computation, and thus facilitate the exploration of a wider range of pump modes and design parameters.

6.2.2 Core-pumped orbital angular-momentum erbium-doped fiber amplifiers

A schematic diagram of the refractive profile and dopant distribution of the OAM EDFA is shown in Figure 6.7(a). The erbium-doping profile is assumed to be uniform within the annular guiding region with a doping concentration of $1.5 \times 10^{25} \text{ m}^{-3}$. The noise calculation is ignored in the core-pumped OAM EDFA. Firstly, the fundamental pump mode LP_{01} (i.e. also known as $\text{OAM}_{(0,1)}$) is used to assess the amplifier performance of the OAM EDFA. The pump power was set to 400 mW. 8 wavelength channels spaced equally from 1530 nm to 1565 nm and 12 OAM modes at each wavelength with the power of -20 dBm per mode per wavelength were used as the input signals. The amplifier length was set to 5 m. The WDM gain profile of the $|L|=5, 6, 7$ OAM modes pumped by the fundamental pump mode is shown in Figure 6.7(b). It is found that the LP_{01} pump mode and a uniform doping profile would result in a 3.5 dB gain difference among the three OAM mode-groups. The DMG can be further minimized through either pump modal control or doping-profile manipulation.

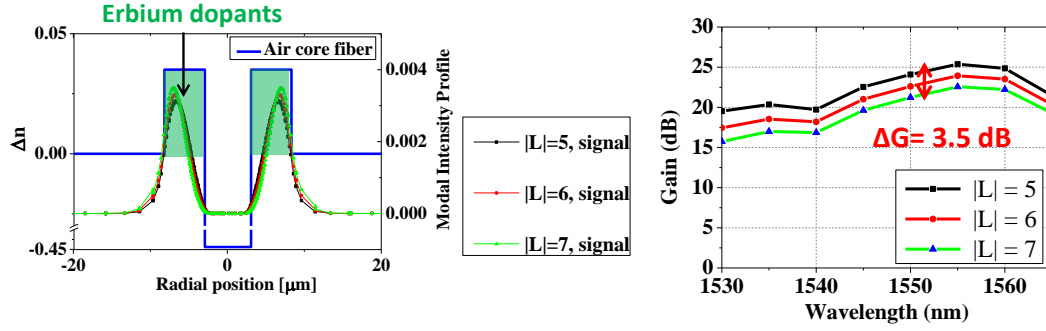


Figure 6.7. (a) RIP of the air-core fiber overlaid with the normalized signal intensity profile of the OAM states with $|L|= 5, 6, 7$. The green shaded areas indicate fully doped cores. (b) WDM performance of the air-core fiber pumped by the fundamental mode LP_{01} (i.e. or $OAM_{(0,1)}$).

At 980 nm, this fiber guides 110 vector modes (i.e. including degeneracies), which can be grouped into 29 (L, m) OAM families and $TM_{0,m}$, $TE_{0,m}$ (i.e. $m=1, 2, 3$) modes. Each $OAM_{(|L|, m)}$ ($|L|=0, 1$) family has two OAM modes, while each $OAM_{(|L|, m)}$ ($|L|\neq 0, 1$) family has four OAM modes. In order to completely describe how each pump mode impacts the DMG among the $|L|=5, 6$, and 7 signal modes, I assessed the 110 pump modes individually. In each simulation run, only one pump mode was launched into the OAM amplifier. The pump power was set to 200 mW and the input signal power at 1550 nm was set to -20 dBm per OAM mode. I chose the amplifier length (i.e. around 5 m with small variations depending on the pump mode) at which the amplified signal power reaches its maximum. The erbium doping profile is assumed to be uniform within the annular guiding region with a doping concentration of $1.5 \times 10^{25} \text{ m}^{-3}$. Due to the circular symmetry of the air-core fiber, the simulated DMGs denoted by ΔG in Fig. 2 using different pump modes that belong to the same $OAM_{(L, m)}$ family (e.g. the $OAM_{2,1}^+$ and $OAM_{-2,1}^+$ modes of the $OAM_{(2, 1)}$ family) are nearly identical. The calculated DMGs using the $TM_{(0,m)}$ and $TE_{(0,m)}$ modes resemble those using $OAM_{(1,m)}$ families, due to similar modal intensity profiles. Similarly, the gains for different signal modes that belong to the same OAM family (e.g. $OAM_{5,1}^+$ and $OAM_{-5,1}^+$) are nearly identical. I summarized the 29 possible pump OAM families and their corresponding DMGs into three groups, according to their radial mode orders (i.e. $m=1, 2, 3$), as shown in Figure 6.8.

The physical origin of the DMG results from differences in the overlap of the pump modes, signal modes and the distribution of the rare-earth dopant. The observed variation of DMGs for different pump modes is expected, as the pump mode intensity varies according to the mode order. As shown by the pink highlighted region in Figure 6.8, the best pump family that provides the lowest DMGs (i.e. ~ 0.25 dB) is $\text{OAM}_{(8,1)}$. In comparison, the calculated DMG is about 3.1 dB when pumped by $\text{OAM}_{(0,1)}$, because the $\text{OAM}_{(0,1)}$ pump has a much better overlap with the $\text{OAM}_{(5,1)}$ signal mode over the $\text{OAM}_{(7,1)}$ signal mode. Although very low DMG can theoretically be achieved with the $\text{OAM}_{(8,1)}$ mode, in practice the excitation of a pure $\text{OAM}_{(8,1)}$ pump may be challenging. It is also possible that significant power will couple into other pump modes (for example, $\text{OAM}_{(8,2)}$) and compromise amplifier performance. In addition, the insertion loss can potentially be quite high to excite high-order pump modes, such as $\text{OAM}_{(8,1)}$ from a single-mode pump diode without the use of high precision or custom components, which makes the OAM EDFA very expensive and less practical.

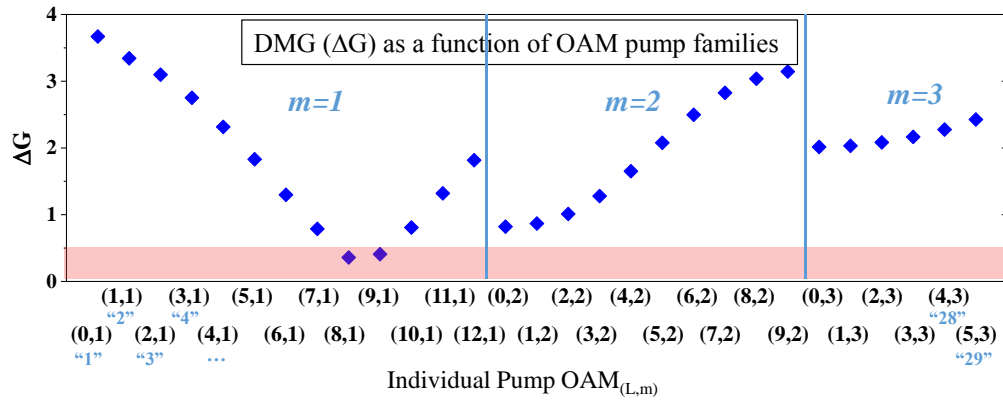


Figure 6.8. The distribution of DMGs and their corresponding pump $\text{OAM}_{(L,m)}$, plotted in order of decreasing mode effective index that of the same "m" group, where "m" denotes the radial mode order. The blue numbers (e.g. "1", "2") under the mode labels corresponds to the mode number shown in Figure 6.9.

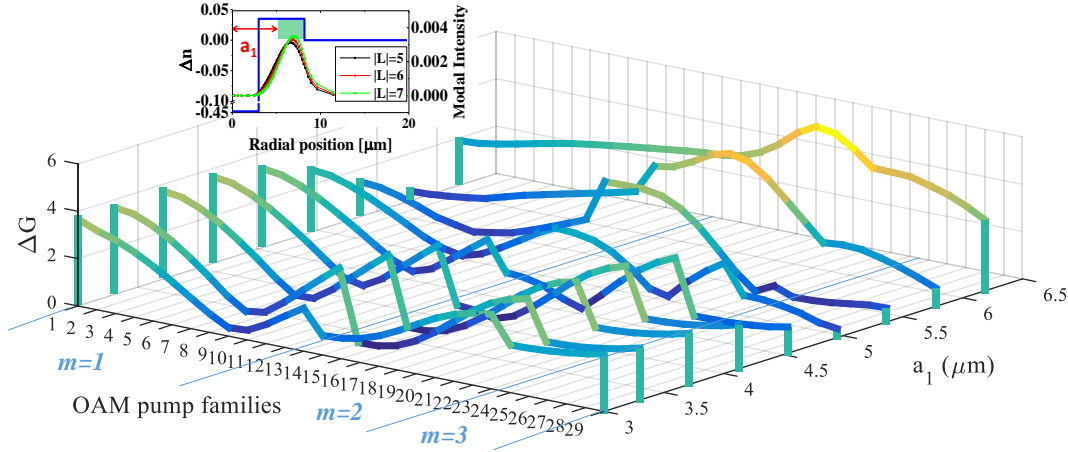


Figure 6.9. The waterfall plots of the DMGs (ΔG) against to the 29 pump OAM_(L,m) families (correspond to the pump modes listed in Figure 6.8) and the variation of a_1 . The insert on the upper left hand side corner shows the confined doping structure determined by parameter a_1 in the air core OAM amplifier.

In the following discussion, we investigate whether using a confined doping profile can reduce the strong modal gain dependence on pump families observed in the fully doped case discussed above. The parameter a_1 is introduced to determine the dimension of the confined doping distribution inside the annular guiding region, as shown in the insert of Figure 6.9. The waterfall plots shown in Figure 6.9 presents the DMG (ΔG) as a function of the OAM pump families and the variation of a_1 . The same input signal and pump power levels are used for Figure 6.9 compared with Figure 6.8. The fiber length was set to 5 m. a_1 was tuned from 3 μm (i.e. the fully doped case) to 6.2 μm (i.e. for $a_1 > 6.2 \mu\text{m}$, the overlap between the erbium and the signals reduces significantly). As shown in Figure 6.9, generally the DMGs still exhibit a strong dependence on the OAM pump families when the confined doping profiles are considered. As different pump modes overlap differently with the erbium ions, in this OAM EDFA a certain doping profile would only favour specific pump modes to ensure low ΔG among the 12 OAM signal modes. However, using this approach of tuning a_1 , we find that for $a_1 = 5 \mu\text{m}$, $\Delta G < 1 \text{ dB}$ can be achieved using any pump modes ranging from (1) OAM_(7,1) to OAM_(11,3) from the $m=1$ group, (2) OAM_(5,2) to OAM_(7,2) from the $m=2$ group, (3) all the modes from the $m=3$ group. Consequently, tailoring the erbium doping profile (i.e. confined doping) is likely give a larger tolerance on the pump mode excitation for this core-pumped OAM EDFA to deliver high gain and low ΔG .

Alternatively, complete removal of the pump mode dependency would be beneficial, and, as we demonstrate in the following section, this is achievable with cladding pumping.

6.2.3 Cladding-pumped orbital angular-momentum erbium-doped fiber amplifiers

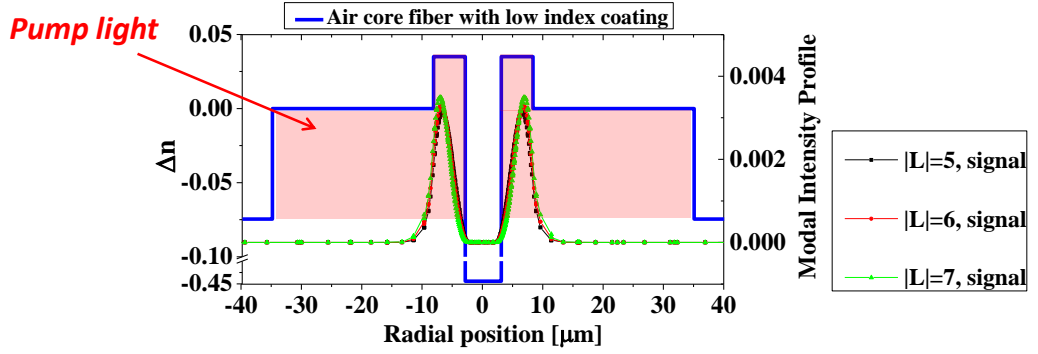


Figure 6.10. Schematic diagram showing the RI profile of a double-clad OAM EDFA, and the overlap between the pump light and signal intensity distributions.

Cladding pumping has the advantages of very high pump powers (i.e. $>10\text{W}$) available from multimode pump diodes and a much lower cost compared with the single-mode pump diode in term of $\$/\text{W}$. A schematic diagram showing the RI profile of the double-clad OAM EDFA is given in Figure 6.10.

Initially, the erbium-doping profile is assumed to be the same (i.e. uniformly doped) as in the previous section. The inner cladding is assumed to be $70\text{ }\mu\text{m}$ in diameter and the pump power is set to 2.5 W , which creates a uniform pump intensity of $6.5 \times 10^8\text{ W/m}^2$ at the input end of the fiber. The input signal power at 1550 nm is set to -10 dBm per OAM mode (e.g. $\text{HE}_{6,1}^{\text{even}} \pm i\text{HE}_{6,1}^{\text{odd}}$). The amplifier length is chosen to be 4 m where the amplified signal powers are around their maximum.

The maximum simulated DMG (i.e. ΔG in Figure 6.11) was found to be 2.5 dB , which needs to be further minimized for practical applications. In order to do so, a design parameter (a_1) is introduced that defines the dimension of the confined erbium-doped layer inside the annular guiding region as shown in Figure 6.11(a).

The DMG dependence on the value of a_1 was investigated, which varied from 3 μm (i.e. uniformly doped core) to 5.75 μm . For the purpose of exploring the optimal doping profile for cladding-pumping operation, the noise calculation was ignored for the simulations shown in Figure 6.11(b) for simplicity. As shown in Figure 6.11(b), the DMG reduces to 0.25 dB as a_1 increases from 3 μm to 5.25 μm , and increases again when a_1 becomes larger than 5.25 μm .

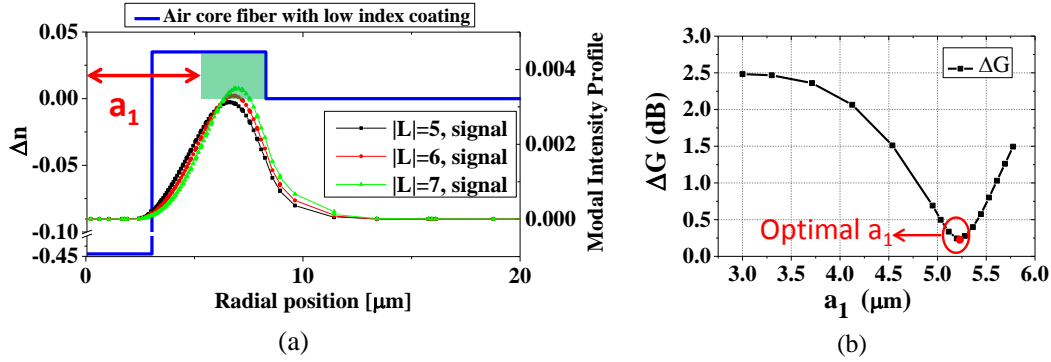


Figure 6.11. (a) RIP of the air-core fiber with labelled design parameter (a_1). (b) DMG as a function of a_1 for cladding-pumping operation.

Finally, the WDM gain profiles of the cladding-pumped OAM amplifier using the optimal value of a_1 was examined. 8 wavelength channels spaced equally from 1530 nm to 1565 nm and 12 OAM modes at each wavelength with the power of -20 dBm per mode per wavelength were used as the input signals. The fiber length was chosen to be 4 m in order to balance the gain between short (i.e. 1530 nm to 1535 nm) and long (i.e. 1550 nm to 1565 nm) wavelengths. The WDM gain profiles and the NF for OAM modes with $|L|=5, 6$, and 7 are shown in Figure 6.12. The noise wavelengths were set to be exactly the same as the WDM signals, thus giving a noise bandwidth of 5 nm each. Since the OAM EDFA guides OAM modes (and also TE_{0m} , TM_{0m} modes) up to the order of $|L|=7$ in the 1.5 μm wavelength range, the ASE will be generated among all these guided modes. With so many ASE components to handle simultaneously, it was found that the “shooting method” became very inefficient to resolve the OAM EDFA. This is because the backward ASEs do not converge even after 200 iterations. The “relaxation method” was used instead to numerically resolve the heavily multimode ASEs. The convergence of the total power of the backward ASEs (i.e. vanish at $L = 4$ m)

is shown in Figure 6.13. The total power of the backward ASEs at the beginning of the OAM EDFA is shown to be 11 dBm, and the total power of the forward ASEs at the output end of the OAM EDFA is shown to be 6 dBm. Figure 6.14 presents the normalized population inversion along the fiber length, which shows that the backward and forward ASEs play profound roles at the beginning and the end of the OAM EDFA respectively. Although the full vector treatment was applied in the simulation, the modal-beating effect is not significantly pronounced in the inversion profiles along the fiber length (i.e. see Figure 6.14). This is because the beating effect among the high-order modes (i.e. $|L|=5, 6, 7$) does not create a significant difference on the overall overlap between the signal intensity and erbium ions compared with the case of LP_{11} signal mode-group studied in section 4.3 of chapter 4. It can be seen that the gain curves for different spatial modes overlap with each other at all wavelengths within the C-band to within 0.25 dB, illustrating excellent modal performance. The NFs are generally found to be between 4 dB to 5.2 dB.

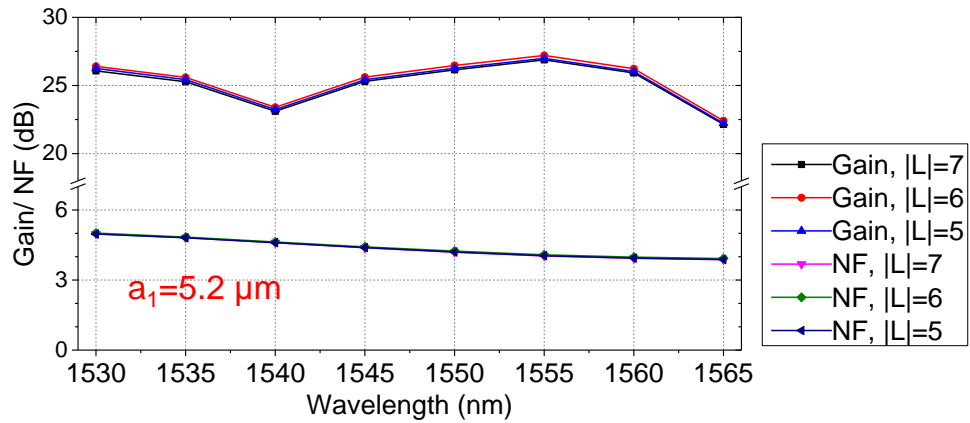


Figure 6.12. WDM performance of the cladding-pumped OAM amplifier.

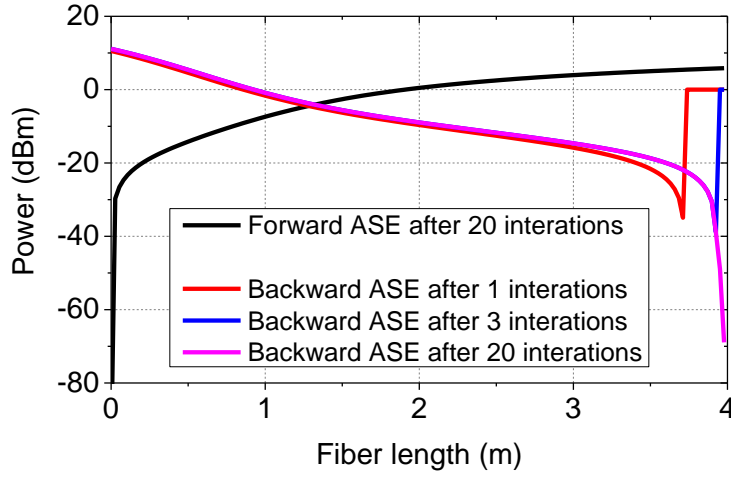


Figure 6.13. Forward and backward ASEs of the cladding-pumped OAM amplifier.

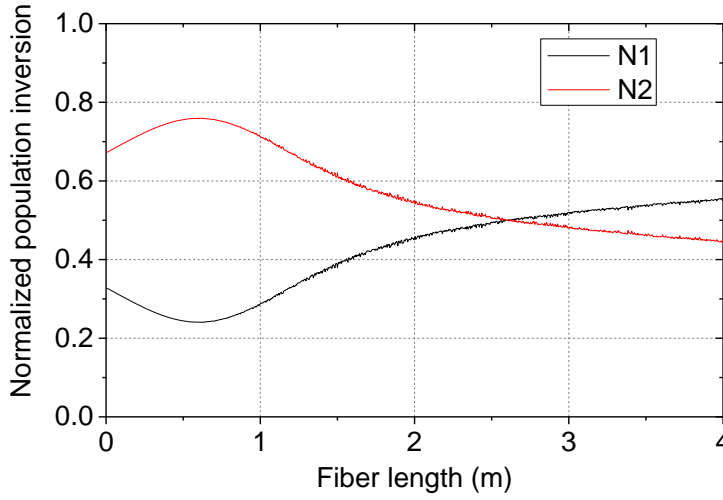


Figure 6.14. Normalized population inversion of the cladding-pumped OAM amplifier.

In conclusion, modeling results on the amplification of 12 OAM modes (i.e. $|L|=5, 6, 7$ for all combinations of L and S , with S representing spin) over the C-band in an air-core fiber using either core- or cladding-pumping at 980 nm were presented. Under the core-pumping condition, it was found that pumping using the OAM mode with $|L|=8$ provides the lowest DMG of 0.25 dB among the signal modes with $|L|=5, 6$ and 7. Most other choices of pump modes would create a $\text{DMG} > 1$ dB. Using the optimized confined-doping profile for the $\text{OAM}_{(0,1)}$ pump condition, a DMG of 0.5 dB can be achieved among $|L|=5, 6$ and 7 modes. However, the DMG dependence on the pump modes is still very strong, and thus pump-

mode excitation must be precise to ensure the best amplifier performance. Under the more desirable and practical case of cladding-pumped operation, there is a ~ 2.5 dB gain difference between the signal modes when the annular ring core is fully doped. With an optimized erbium-doping profile, exceptionally well-equalized modal gain (i.e. $\text{DMG} \leq 0.25$ dB) can be achieved for all 12 OAM modes.

We are currently considering the possibility of manufacturing an OAM amplifier although it is to be appreciated that the cost would potentially be significant given the complexity of the structure (e.g. air hole, confined doping).

6.3 Conclusions

This chapter presents the modeling results based on special MM-EDFAs that exhibit a ring-index profile. The first type is a ring-core fiber (RCF) that supports LP modes, which can be used for MDM systems with the benefits of reducing MIMO complexity due to their unique modal properties. A double-clad ring-core EDFA according to my design shown in section 6.1.3, will be produced in the near future, supported by the COMIMO project.

The second type is a ring-index fiber with an air hole in the center that supports orbital angular momentum (OAM) modes. The OAM modes are also eigenmodes of the fiber and uses different basis sets compared with the vector modes discussed in section 2.1.1 of chapter 2. OAM modes offer another degree of freedom for information multiplexing and due to the large vector-splitting nature of the OAM modes, MIMO-free transmission can be potentially achieved. Section 6.2 preforms the detailed discussions of the simulations of OAM amplifiers under both core- and cladding-pumped operation. Our conclusion is that, cladding-pumped operation is more practical in terms of cost and also benefits from the removal of the pump mode dependence that tends to exist in the core-pumped operation.

Chapter 7: Conclusion and Future work

7.1 Conclusion

As the capacity of optical systems based on single-mode single-core fibers is approaching its fundamental limit, further capacity growth requires breakthroughs in the existing network technology. Time-division multiplexing (TDM) and wavelength-division multiplexing (WDM) are examples of parallel transmission in time/frequency domains which have been fully exploited in single-mode single-core fiber systems. To further increase the number of parallel channels, the spatial dimensions may be exploited. SDM is believed to be the most promising technology as a solution to the predicted capacity crunch. It can be implemented through multi-core fibers or multi-mode fibers in the form of MDM transmission system. The MM-EDFA is critical to the commercial viability of MDM, providing the key capability of amplifying all signal modes simultaneously, thereby providing a higher efficiency and lower cost per bit compared with the use of N -parallel single-mode EDFAs. Careful engineering of the mode-dependent gain in a MM-EDFA is of paramount importance to obtain reliable system operation and to prevent system outages.

In chapter 3, my modelling work was initiated using commercial software (Optisystem11.0®) to model a MM-EDFA supporting 2 mode groups (or 3 spatial modes). As the doped fiber design was not fully optimized, a complex pump modal configuration (i.e. high-order pump modes) had to be employed in order to reduce the DMG. Based on this initial work I proposed a 2-mode-group EDF design incorporating ring doping that allows accurate modal gain control amongst the two-mode groups using a LP_{01} pump mode. Subsequently a 2-mode-group ring-doped EDF according to my design was successfully fabricated in-house and a portable 2-mode-group EDFA with low DMG was built and tested, confirming my predictions. This 2-mode-group EDFA was subsequently used in joint experiments with Nokia Siemens Networks to demonstrate a record MDM data capacity of 73.7 Tb/s over 119 km. The amplifier was then used in field

experiments with Austrian Operator A1, providing the first field demonstration of the use of MDM. All these results generated a huge amount of technical and commercial interest. My 2-mode-group EDFA design lay at the heart of all of this success. The ORC is now commercializing the 2-mode-group EDFAs in collaboration with the company Phoenix Photonics Ltd.

The commercial software Optisystem11.0® computes using LP modes. However, the LP amplifier model becomes inaccurate when the pump intensity profile exhibits azimuthal dependence. To address the problem, in chapter 4, we developed and verified our own amplifier simulation code and used it to analyse the impact of mode beating and core ellipticity, that are absent in the LP model, on FM-EDFAs using full vector solutions. In conclusion, the LP amplifier model is valid and accurate enough to predict amplifier performances given pump intensity profile is circularly symmetrical.

Chapter 5 summarizes the designs and theoretical support for FM-EDFAs supporting four- and six-mode groups during my PhD, within the framework of the MODEGAP project. I proposed a core-pumped multi-ring-doped 4-mode-group EDFA design that offered a DMG of less than 1 dB using a combination of LP_{01} and LP_{41} pump modes. A core-pumped 4-mode-group EDFA was made in-house, confirming my predictions. As the number of guided modes increases, cladding pumping becomes attractive for two main reasons: (1) it is much cheaper in terms of \$/W compared with single-mode pump diodes; and (2) the heavily multi-moded pump guided in the inner cladding can be treated as a single pump mode with a uniform intensity profile. Consequently, the pump mode dependency is removed. Next, I performed the inverse design of cladding-pumped 4- and 6-mode-group EDFAs using my upgraded cladding-pumped MM-EDFA simulator incorporating the genetic algorithm. My design and modelling work paved the way for the first experimental demonstration of a cladding-pumped 4-mode-group EDFA and the subsequent high-profile 4-mode-group fiber based transmission experiments listed in chapter 5.

Chapter 6 summaries my theoretical works on a solid-core ring-core amplifier and an air-core OAM amplifier. Passive ring-core fibers have been proposed as a promising candidate for MDM applications [111], [112], with the benefit of reduced MIMO complexity due to their unique modal properties. I proposed a 6-mode-group ring-core multimode erbium-doped fiber amplifier (RC-MM-EDFA) capable of providing almost identical gain among the six mode-groups within the C-band using either core- or cladding-pumped implementations. A double-clad ring-core EDFA according to my design will be produced in the near future, supported by the COMIMO project. Lastly, we proposed the amplification of 12 OAM modes ($|L|=5, 6$ and 7) in an air-core OAM-EDF over the C-band. Under the core pumping condition based on a fully doped core, the performance of all the supported pump modes (110 in total) were individually assessed. The DMG varies significantly depending on the pump mode used, and the lowest DMG was found to be 0.25 dB provided by the $\text{OAM}_{(8,1)}$ pump mode. Under the more practical case of cladding-pumped operation, where the pump modal dependency is almost removed, a DMG of 0.25 dB and a small signal gain of >20 dB can be achieved for the 12 OAM modes across the full C-band.

7.2 Future work

During my PhD, I have developed a flexible and powerful MM-EDFA simulation tool incorporating the genetic algorithm, which will not only enable us to investigate new EDFA designs directly, but also can be transformed into other rare-earth element-doped fiber amplifier/laser simulation tool. In short, there are two aspects that we can work on as natural extensions of this thesis: (1) design and modeling of EDFAs for SDM applications; and (2) design of special rare-earth doped fibers.

7.2.1 Erbium doped fiber amplifiers for SDM applications

(1) MM-EDFA

The highest mode count in FMFs reported in this thesis is 6-mode groups, which contains 10 spatial modes. Having been pushed by the fast development of MDM

technology, MM-EDFAs that support more than 6-mode groups is one of the apparent next steps. However, scaling up the number of modes in FMF based MDM systems are faced by many challenges, which would ultimately limit the maximum number of modes can be used in FMF-based MDM system. Some of the biggest issues are: (1) the crosstalk between the modes cannot be avoided after long distances (e.g. 100 km), so that very complex MIMO-DSP must be employed at the receiver to recover the independent signal streams carried by each mode; and (2) the mode-dependent loss caused by MUX/DEMUX devices, splicing; as the number of modes increases, to make sure all the modes survive is also a very difficult task. With all these challenges in front, FMF-based MDM system supporting more than 10 spatial modes (i.e. 20×20 MIMO chips required to undo the cross talk) will be very expensive, hence non-practical. Although the possibility of commercial deployment of more than 10 spatial modes based MDM system is likely to be slim, research interests towards the scalability of MDM technology do not stop. Very recently, Bell Labs US demonstrated the state-of-the-art 30×30 MIMO transmission of over 15 spatial modes [110]. The 15 spatial modes guided in passive fibers are actually grouped into 5 mode groups, because the effective indexes of the modes within the same mode group are nearly identical. Consequently, the modes from the same mode group strongly couple to each other. At the ORC, we are collaborating with Bell Labs US by having committed to make a 15-spatial-mode EDFA. We need to carefully design the 15-spatial-mode EDFA so that it can compensate the mode dependent loss across the effective 5-mode groups experienced in transmission. Lastly, what about more than 15 spatial modes? Only time will tell the how far the MDM technology can take us.

(2) Multi-core EDFAs and few-mode multi-core EDFAs

As I briefly reviewed in the introduction of this thesis. SDM technology based on multi-core fibers has attracted immense interests in the optical communication community and so far has made significant progress. Recently, the ORC has succeeded to get a large scale research project named SAFARI (i.e. jointly funded

by EU and Japan government), aiming to demonstrate the next-generation ultra-dense multicore fibers for SDM applications. At the ORC, our task is to design and make high performance ultra-dense multicore EDFAs that match the passive multicore fibers provided by Japan. The multi-core fiber technology can be integrated into my multimode amplifier simulation tool to facilitate the design and modeling of multi-core EDFAs, including single-mode multicore EDF and few-mode multi-core EDF, as shown in Figure 7.1. For uncoupled multi-core fibers, the fiber design is crucial to ensure minimal cross talks between the adjacent cores. Thus core-to-core crosstalk calculation must be developed as well as the multi-core EDFA simulator.

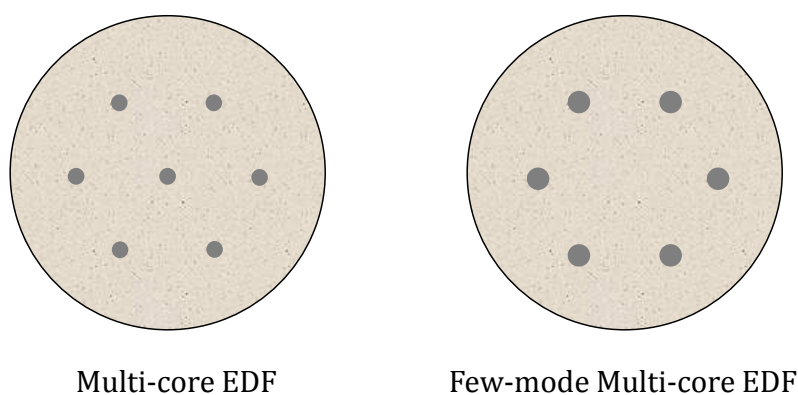


Figure 7.1. Two types of uncoupled Multicore EDFs.

7.2.2 Design of special rare-earth-doped fibers

Regardless of whether the lasing medium is erbium, ytterbium or thulium, they are generally governed by the same mathematical rules. The MM-EDFA simulation tool I developed can be transformed into other rare-earth-doped amplifier or laser simulation tools, to conduct fiber designs and provide theoretical support to experimental activities. For example, the ORC has recently succeeded in an EPSRC-funded project known as “Spatiotemporally pulse shaped high power fibre lasers for energy resilient manufacturing”. In this project, the ORC is tasked to make a robust Yb-doped fiber laser that delivers radially polarized beams, which is the TM_{01} mode. Careful fiber design is needed to minimize the mode coupling between the TM_{01} mode and other vector modes in the active fiber to ensure a clean TM_{01} output.

References

- [1] W. K. Johnston, "The birth of fiberoptics from 'light guiding'," *J. Endourol.*, vol. 18, no. 5, pp. 425–426, 2004.
- [2] Y. Koike, *Fundamentals of plastic optical fibers*. Wiley-VCH, 2004.
- [3] M. Fransman, *Japan's Computer and Communications Industry*. Oxford University Press, 1995.
- [4] D. J. Richardson, J. M. Fini, and L. E. Nelson, "Space-division multiplexing in optical fibres," *Nat. Photonics*, vol. 7, no. April, pp. 354–362, 2013.
- [5] R. J. Mears, L. Reekie, I. M. Jauncey, and D. N. Payne, "Low-noise erbium-doped fibre amplifier operating at 1.54 μ m," vol. 23, no. 19, pp. 1026–1028, 1987.
- [6] E. Desurvire, J. R. Simpson, and P. C. Becker, "High-gain erbium-doped traveling-wave fiber amplifier," *Opt. Lett.*, vol. 12, no. 11, pp. 888–890, 1987.
- [7] R. H. Stolen, E. P. Ippen, and a. R. Tynes, "Raman oscillation in glass optical waveguide," *Appl. Phys. Lett.*, vol. 20, no. 2, pp. 62–64, 1972.
- [8] R. H. Stolen and E. P. Ippen, "Raman gain in glass optical waveguides," *Appl. Phys. Lett.*, vol. 22, no. 6, pp. 276–278, 1973.
- [9] J. Bromage, "Raman Amplification for Fiber Communications Systems," *Lightwave*, vol. 22, no. 1, pp. 79–93, 2004.
- [10] S. Namiki and Y. Emori, "Ultrabroad-band Raman amplifiers pumped and gain-equalized by wavelength-division-multiplexed high-power laser diodes," *IEEE J. Sel. Top. Quantum Electron.*, vol. 7, no. 1, pp. 3–16, 2001.
- [11] D. J. Richardson, "Filling the Light Pipe," *Science (80-.)*, vol. 330, no. 6002, pp. 327–328, 2010.
- [12] A. D. Ellis, J. Zhao, and D. Cotter, "Approaching the Non-Linear Shannon Limit," *J. Light. Technol.*, vol. 28, no. 4, pp. 423–433, 2010.
- [13] C. E. Shannon, "A mathematical theory of communication," *Bell Syst. Technol. J.*, vol. 27, pp. 379–423, 623–656, 1948.
- [14] R.-J. Essiambre, G. Kramer, P. J. Winzer, G. J. Foschini, and B. Goebel, "Capacity Limits of Optical Fiber Networks," *J. Light. Technol.*, vol. 28, no. 4, pp. 662–701, 2010.
- [15] T. Hayashi, T. Taru, O. Shimakawa, T. Sasaki, and E. Sasaoka, "Design and fabrication of ultra-low crosstalk and low-loss multi-core fiber," *Opt. Express*, vol. 19, no. 17, p. 16576, 2011.

References

- [16] R. Ryf, a. Sierra, R.-J. Essiambre, S. Randel, a. H. Gnauck, C. Bolle, M. Esmaeelpour, P. J. Winzer, R. Delbue, P. Pupalakise, a. Sureka, D. W. Peckham, a. McCurdy, and R. Lingle, "Mode-equalized distributed Raman amplification in 137-km few-mode fiber," *ECOC*, 2011.
- [17] R. G. H. van Uden, R. A. Correa, E. A. Lopez, F. M. Huijskens, C. Xia, G. Li, a. Schülzgen, H. de Waardt, a. M. J. Koonen, and C. M. Okonkwo, "Ultra-high-density spatial division multiplexing with a few-mode multicore fibre," *Nat. Photonics*, vol. 8, no. 11, pp. 865–870, 2014.
- [18] S. Berdagué and P. Facq, "Mode division multiplexing in optical fibers.," *Appl. Opt.*, vol. 21, no. 11, pp. 1950–1955, 1982.
- [19] H. M. P. G. Nykolak, S. A. Kramer, J. R. Simpson, D. J. DiGiovanni, C. R. Giles, "An Erbium-Doped Multimode Optical Fiber," vol. 3, no. 12, pp. 79–81, 1991.
- [20] N. W. Spellmeyer, "Communications Performance of a Multimode EDFA," *IEEE Photonics Technol. Lett.*, vol. 12, no. 10, pp. 1337–1339, 2000.
- [21] M. Gong, Y. Yuan, C. Li, P. Yan, H. Zhang, and S. Liao, "Numerical modeling of transverse mode competition in strongly pumped multimode fiber lasers and amplifiers.," *Opt. Express*, vol. 15, no. 6, pp. 3236–3246, 2007.
- [22] G. J. Foschini, "Layered space-time architecture for wireless communication in a fading environment when using multi-element antennas," *Bell Labs Tech. J.*, vol. 1, no. 2, pp. 41–59, 1996.
- [23] R. Ryf, S. Randel, a. H. Gnauck, C. Bolle, R.-J. Essiambre, P. J. Winzer, D. W. Peckham, A. McCurdy, and R. Lingle, "Space-division multiplexing over 10 km of three-mode fiber using coherent 6x6 MIMO processing," *2011 Opt. Fiber Commun. Conf. Expo. Natl. Fiber Opt. Eng. Conf.*, p. PDPB10, 2011.
- [24] N. Bai, E. Ip, T. Wang, and G. Li, "Multimode fiber amplifier with tunable modal gain using a reconfigurable multimode pump," *IEEE Photonic Soc. 24th Annu. Meet. PHO 2011*, vol. 19, no. 17, pp. 589–590, 2011.
- [25] Y. Yung, S. Alam, Z. Li, A. Dhar, D. Giles, I. Giles, J. Sahu, L. Gruner-Nielsen, F. Poletti, and D. J. Richardson, "First demonstration of multimode amplifier for spatial division multiplexed transmission systems," *37th Eur. Conf. Exhib. Opt. Commun.*, p. Th.13.K.4, 2011.
- [26] E. Ip, N. Bai, Y. Huang, E. Mateo, F. Yaman, M. Li, and S. Bickham, "88 × 3 × 112-Gb / s WDM Transmission over 50 km of Three- Mode Fiber with Inline Few-Mode Fiber Amplifier," *ECOC*, paper Th.13.C, 2011.
- [27] Y. Amma, Y. Sasaki, K. Takenaga, S. Matsuo, J. Tu, K. Saitoh, and M. Koshiba, "High-density Multicore Fiber with Heterogeneous Core Arrangement," vol. 2, no. c, pp. 8–10, 2015.

References

- [28] J. Sakaguchi, W. Klaus, J. D. Mendinueta, B. J. Puttnam, R. S. Luis, Y. Awaji, N. Wada, T. Hayashi, T. Nakanishi, T. Watanabe, Y. Kokubun, T. Takahata, and T. Kobayashi, "Realizing a 36-core , 3-mode Fiber with 108 Spatial Channels," *Opt. Fiber Commun. Conf.*, paper Th5C.2, 2015.
- [29] J. Sakaguchi, W. Klaus, B. J. Puttnam, J. M. D. Mendinueta, Y. Awaji, N. Wada, Y. Tsuchida, K. Maeda, M. Tadakuma, K. Imamura, R. Sugizaki, T. Kobayashi, Y. Tottori, M. Watanabe, and R. V Jensen, "19-core MCF transmission system using EDFA with shared core pumping coupled via free-space optics.," *Opt. Express*, vol. 22, no. 1, pp. 90–5, 2014.
- [30] N. Bozinovic, Y. Yue, Y. Ren, M. Tur, P. Kristensen, H. Huang, A. E. Willner, and S. Ramachandran, "Terabit-scale Orbital Angular Momentum Mode Division Multiplexing in Fibers," *Science*, vol. 340, pp. 1545–1548, 2013.
- [31] P. Gregg, P. Kristensen, and S. Ramachandran, "Conservation of orbital angular momentum in air-core optical fibers," *Optica*, vol. 2, no. 3, pp. 267–270, 2015.
- [32] J. Bures, "Guided Optics," in *Guided Optics*, Wiley-VCH, 2009, p. 117.
- [33] J. Bures, "Guided Optics," in *Guided Optics*, Wiley-VCH, 2009, p. 71.
- [34] J. D. L. A.W. Snyder, "Optical Waveguide Theory," in *Optical Waveguide Theory*, Chapman and Hall, 1983, p. 590.
- [35] R. B. Adler, "Waves on Inhomogeneous Cylindrical Structures," *Proc. IRE*, vol. 40, no. 3, 1952.
- [36] D. Gloge, "Dispersion in weakly guiding fibers.," *Appl. Opt.*, vol. 10, no. 11, pp. 2442–2445, 1971.
- [37] J. Bures, "Guided Optics," in *Guided Optics*, Wiley-VCH, 2009, p. 123.
- [38] J. Bures, "Guided Optics," Wiley-VCH, 2009, p. 155.
- [39] <http://www.comsol.com>.
- [40] R. Billington, "Effective Area of Optical Fibres Definition and Measurement Techniques," *Cent. Opt. Environ. Metrol.*, 1999.
- [41] "Optical fibers, cables and systems," *Telecommunication standardization sector of ITU*. [Online]. Available: <https://www.itu.int/pub/T-HDB-OUT.10-2009-1>.
- [42] R. J. Mears, L. Reekie, I. M. Jauncey, and D. N. Payne, "Low-noise erbium-doped fibre amplifier operating at 1.54 μ m," *Electron. Lett.*, vol. 23, pp. 1026–1028, 1987.
- [43] E. Desurvire, *Erbium-doped Fiber Amplifiers-Principles and Applications*. Wiley-Interscience, 1994.

References

- [44] M. J. Yadlowsky, "Independent control of EDFA gain shape and magnitude using excited-state trapping," *IEEE Photonics Technol. Lett.*, vol. 11, no. 5, pp. 539–541, 1999.
- [45] A. Yariv, *Quantum Electronics*, Second edi. New York: John Weley, 1975.
- [46] W. L. Barnes, R. I. Laming, E. J. Tarbox, and P. R. Morkel, "Absorption and emission cross section of Er³⁺ doped silica fibers," *IEEE J. Quantum Electron.*, vol. 27, no. 4, pp. 1004–1010, 1991.
- [47] E. Desurvire, J. W. Sulhoff, J. L. Zyskind, and J. R. Simpson, "Study of spectral dependence of gain saturation and effect of inhomogeneous broadening in erbium-doped aluminosilicate fiber amplifiers," *IEEE Photonics Technol. Lett.*, vol. 2, no. 9, pp. 653–655, 1990.
- [48] R. Peretti, B. Jacquier, D. Boivin, E. Burov, and A. M. Jurdyc, "Inhomogeneous gain saturation in EDF: Experiment and modeling," *J. Light. Technol.*, vol. 29, no. 10, pp. 1445–1452, 2011.
- [49] K. Morishita, "Numerical Analysis of Pulse Broadening in Graded Index Optical Fibers," *Microw. Theory Tech.*, vol. 29, no. 4, pp. 348–352, 1981.
- [50] Z. Jiang and J. R. Marciante, "Impact of transverse spatial-hole burning on beam quality in large-mode-area Yb-doped fibers," *Journal of the Optical Society of America B*, vol. 25, no. 2, p. 247, 2008.
- [51] Q. Kang, E.-L. Lim, Y. Jung, J. K. Sahu, F. Poletti, C. Baskiotis, S. Alam, and D. J. Richardson, "Accurate modal gain control in a multimode erbium doped fiber amplifier incorporating ring doping and a simple LP₀₁ pump configuration," *Opt. Express*, vol. 20, no. 19, pp. 20835–20843, 2012.
- [52] W. H. Press, S. a Teukolsky, W. T. Vetterling, and B. P. Flannery, *Numerical recipes in C (2nd ed.): the art of scientific computing*, vol. 29, no. 4. 1992.
- [53] H. Heffner, "The Fundamental Noise Limit of Linear Amplifiers," *Proc. IRE*, vol. 50, no. 7, 1962.
- [54] Y. Jung, S. Alam, Z. Li, a. Dhar, D. Giles, I. P. Giles, J. K. Sahu, F. Poletti, L. Grüner-Nielsen, and D. J. Richardson, "First demonstration and detailed characterization of a multimode amplifier for space division multiplexed transmission systems," vol. 19, no. 26, pp. 952–957, 2011.
- [55] N. Bai, E. Ip, Y.-K. Huang, E. Mateo, F. Yaman, M.-J. Li, S. Bickham, S. Ten, J. Liñares, C. Montero, V. Moreno, X. Prieto, V. Tse, K. Man Chung, A. P. T. Lau, H.-Y. Tam, C. Lu, Y. Luo, G.-D. Peng, G. Li, and T. Wang, "Mode-division multiplexed transmission with inline few-mode fiber amplifier," *Opt. Express*, vol. 20, no. 3, p. 2668, 2012.
- [56] E. Ip, N. Bai, Y.-K. Huang, E. Mateo, F. Yaman, M.-J. Li, S. Bickham, S. Ten, Y. Luo, G.-D. Peng, G. Li, T. Wang, J. Linares, C. Montero, and V. Moreno, "6x6 MIMO Transmission over 50+25+10 km Heterogeneous Spans of Few-Mode Fiber with

References

- Inline Erbium-Doped Fiber Amplifier - OSA Technical Digest," in *Optical Fiber Communication Conference*, 2012, p. OTu2C.4.
- [57] K. J. Garcia, "Calculating component coupling coefficients," *WDM Solut. Suppl. Laser Focus World (Chatsworth, CA Pen Well Corp.)*, 2000.
- [58] J. Nilsson, J. D. Minelly, R. Paschotta, a C. Tropper, and D. C. Hanna, "Ring-doped cladding-pumped single-mode three-level fiber laser," *Opt. Lett.*, vol. 23, no. 5, pp. 355–357, 1998.
- [59] R. S. Quimby, T. F. Morse, R. L. Shubochkin, and S. Ramachandran, "Yb³⁺ ring doping in high-order-mode fiber for high-power 977-nm lasers and amplifiers," *IEEE J. Sel. Top. Quantum Electron.*, vol. 15, no. 1, pp. 12–19, 2009.
- [60] D. Marcuse, "Influence of curvature on the losses of doubly clad fibers," *Appl. Opt.*, vol. 21, no. 23, pp. 4208–4213, 1982.
- [61] J. E. Townsend, S. B. Poole, and D. N. Payne, "Solution-doping technique for fabrication of rare-earth-doped optical fibres," *Electronic Letters*, Vol 23, No. 7, pp. 329–331, 1987.
- [62] K. Lyytikainen, S. Huntington, A. Carter, P. McNamara, S. Fleming, J. Abramczyk, I. Kaplin, and G. Schötz, "Dopant diffusion during optical fibre drawing," *Opt. Express*, vol. 12, no. 6, pp. 972–977, 2004.
- [63] W. Sellmeier, "No Title," *Ann. Phys. Chem.*, vol. 143, p. 271, 1871.
- [64] I. H. Malitson, "Interspecimen Comparison of the Refractive Index of Fused Silica," *J. Opt. Soc. Am.*, vol. 55, no. 10, p. 1205, 1965.
- [65] Y. Jung, Q. Kang, V. a J. M. Sleiffer, B. Inan, M. Kushnerov, V. Veljanovski, B. Corbett, R. Winfield, Z. Li, P. S. Teh, a Dhar, J. Sahu, F. Poletti, S. Alam, and D. J. Richardson, "Three mode Er³⁺ + ring-doped fiber amplifier for mode-division multiplexed transmission," *Opt. Express*, vol. 21, no. 8, pp. 10383–10392, 2013.
- [66] F. Z. Tang, P. McNamara, G. W. Barton, and S. P. Ringer, "Multiple solution-doping in optical fibre fabrication II - Rare-earth and aluminium co-doping," *J. Non. Cryst. Solids*, vol. 354, no. 15–16, pp. 1582–1590, 2008.
- [67] S. I. N. Shukunami, "Doped optical fiber having core and clad structure for increasing the amplification band of an optical amplifier using the optical fiber," 778, 1998.
- [68] V. a J. M. Sleiffer, Y. Jung, V. Veljanovski, R. G. H. van Uden, M. Kushnerov, H. Chen, B. Inan, L. G. Nielsen, Y. Sun, D. J. Richardson, S. U. Alam, F. Poletti, J. K. Sahu, A. Dhar, A. M. J. Koonen, B. Corbett, R. Winfield, A. D. Ellis, and H. de Waardt, "737 Tb/s (96 x 3 x 256-Gb/s) mode-division-multiplexed DP-16QAM transmission with inline MM-EDFA," *Opt. Express*, vol. 20, no. 26, p. B428, 2012.

References

- [69] V. a J. M. Sleiffer, Y. Jung, V. Veljanovski, R. G. H. Van Uden, M. Kuschnerov, Q. Kang, L. Gruner-Nielsen, Y. Sun, D. J. Richardson, A. S., F. Poletti, J. K. Sahu, A. Dhar, H. Chen, B. Inan, a. M. J. Koonen, B. Corbett, R. Winfield, A. D. Ellis, and H. Waardt, "73.7 Tb/s (96X3x256-Gb/s) mode-division-multiplexed DP-16QAM transmission with inline MM-EDFA," *Proc ECOC, Th.3.C.4*, no. 1, pp. 7–9, 2012.
- [70] V. a J. M. Sleiffer, H. Chen, Y. Jung, P. Leoni, M. Kuschnerov, a. Simperler, H. Fabian, H. Schuh, F. Kub, D. J. Richardson, S. U. Alam, L. Grüner-Nielsen, Y. Sun, a. M. J. Koonen, and H. de Waardt, "Field demonstration of mode-division multiplexing upgrade scenarios on commercial networks," *Opt. Express*, vol. 21, no. 25, p. 31036, 2013.
- [71] V. a J. M. Sleiffer, Y. Jung, M. Kuschnerov, S. U. Alam, D. J. Richardson, L. Grüner-Nielsen, Y. Sun, and H. de Waardt, "Optical chopper-based re-circulating loop for few-mode fiber transmission," *Opt. Lett.*, vol. 39, no. 5, p. 1181, 2014.
- [72] http://www.phoenixphotonics.com/website/products/Few_Mode_EDFA.htm.
- [73] S. A. and D. J. R. E.L. Lim, Q. Kang, M. Gecevicius, F. Poletti, "Vector Mode effects in Few Moded Erbium Doped Fiber Amplifiers," in *OFC*, 2013, p. OTu3G.2.
- [74] A. W. Snyder and W. R. Young, "Modes of optical waveguides," *Journal of the Optical Society of America*, vol. 68, no. 3. p. 297, 1978.
- [75] J. Bures, "Guided Optics," in *Guided Optics*, Wiley-VCH, 2009, p. 29.
- [76] E.-L. Lim, S. Alam, and D. J. Richardson, "Optimizing the pumping configuration for the power scaling of in-band pumped erbium doped fiber amplifiers," vol. 20, no. 13, pp. 1540–1543, 2012.
- [77] W. L. M. Ashish M. Vengsarkar, A. H. Moesle, L. G. Cohen, "Polarization mode dispersion in dispersion-shifted fibers: an exact analysis," *Opt. Lett.*, vol. 18, no. 17, pp. 1412–1414, 1993.
- [78] R. E. Schuh, "Characterisation of birefringence in optical fibres," University of Essex, 1997.
- [79] R. M. Anwar and M. S. Alam, "Thermal stress effects on higher order modes in highly elliptical core optical fibers," in *Proceedings of ICECE 2008 - 5th International Conference on Electrical and Computer Engineering*, 2008, pp. 561–565.
- [80] E. Ip, "Gain equalization for few-mode fiber amplifiers beyond two propagating mode groups," *IEEE Photonics Technol. Lett.*, vol. 24, no. 21, pp. 1933–1936, 2012.
- [81] D. Askarov and J. M. Kahn, "Design of transmission fibers and doped fiber amplifiers for mode-division multiplexing," *IEEE Photonics Technol. Lett.*, vol. 24, no. 21, pp. 1945–1948, 2012.

References

- [82] G. Le Cocq, L. Bigot, A. Le Rouge, M. Bigot-Astruc, P. Sillard, C. Koebele, M. Salsi, and Y. Quiquempois, "Modeling and characterization of a few-mode EDFA supporting four mode groups for mode division multiplexing," *Opt. Express*, vol. 20, no. 24, pp. 27051–61, 2012.
- [83] M. Salsi, D. Peyrot, G. Charlet, S. Bigo, R. Ryf, N. K. Fontaine, M. a. Mestre, S. Randel, X. Palou, C. Bolle, B. Guan, G. Le Cocq, L. Bigot, and Y. Quiquempois, "A Six-Mode Erbium-Doped Fiber Amplifier," *Eur. Conf. Exhib. Opt. Commun.*, no. 2, p. Th.3.A.6, 2012.
- [84] Y. Jung, Q. Kang, J. K. Sahu, B. Corbett, F. Poletti, R. Winfield, S. U. Alam, and D. J. Richardson, "Few-mode EDFA Supporting 5 Spatial Modes with Reconfigurable Differential Modal Gain Control," *39th Eur. Conf. Exhib. Opt. Commun. (ECOC 2013)*, p. We.4.A.2, 2013.
- [85] Y. Jung, Q. Kang, J. K. Sahu, B. Corbett, J. O'Callaghan, F. Poletti, S. U. Alam, and D. J. Richardson, "Reconfigurable modal gain control of a few-mode EDFA supporting six spatial modes," *IEEE Photonics Technol. Lett.*, vol. 26, no. 11, pp. 1100–1103, 2014.
- [86] and R. L. Roland Ryf, Nicolas K. Fontaine, Miquel A. Mestre, Sebastian Randel, Xavi Palou, Cristian Bolle, Alan H. Gnauck, Sethumadhavan Chandrasekhar, Xiang Liu, Binbin Guan, René-Jean Essiambre, Peter J. Winzer, Sergio Leon-Saval, Joss Bland-Hawthorn, Roger Delbu, "12 x 12 MIMO Transmission over 130-km Few-Mode Fiber," in *Frontiers in Optics 2012*, 2012, p. FW6C.4.
- [87] E. Ip, M. Li, Y. Huang, and A. Tanaka, "146λx6x19-Gbaud Wavelength-and Mode-Division Multiplexed Transmission over 10x50-km Spans of Few-Mode Fiber with a Gain-Equalized Few-Mode EDFA," *Opt. Fib. Commun. Conf.*, p. PDP5A.2, 2013.
- [88] A. Lobato, Y. Chen, Y. Jung, H. Chen, B. Inan, M. Kuschnerov, N. K. Fontaine, R. Ryf, B. Spinnler, and B. Lankl, "12-mode OFDM transmission using reduced-complexity maximum likelihood detection," *Opt. Lett.*, vol. 40, no. 3, pp. 328–331, 2015.
- [89] G. Le Cocq, Y. Quiquempois, A. Le Rouge, G. Bouwmans, H. El Hamzaoui, K. Delplace, M. Bouazaoui, and L. Bigot, "Few mode Er³⁺-doped fiber with micro-structured core for mode division multiplexing in the C-band," *Opt. Express*, vol. 21, no. 25, p. 31646, 2013.
- [90] Q. Kang, E. L. Lim, Y. Jung, F. Poletti, S. Alam, and D. J. Richardson, "Design of Four-Mode Erbium Doped Fiber Amplifier with Low Differential Modal Gain for Modal Division Multiplexed Transmissions," *Opt. Fiber Commun. Conf. Fiber Opt. Eng. Conf. 2013*, p. OTu3G.3, 2013.
- [91] L. E. Cocq, G. Bigot, and L. Quiquempois, "Gradient Descent Optimization for Few-Mode Er³⁺ + Doped Fiber Amplifier with Micro- structured core," no. july, pp. 1–71, 2014.

References

- [92] G. Le Cocq, Y. Quiquempois, and L. Bigot, "Optimization Algorithm Applied to the Design of Few-Mode Erbium Doped Fiber Amplifier for Modal and Spectral Gain Equalization," *J. Light. Technol.*, vol. 33, no. 1, pp. 100–108, 2015.
- [93] K. S. Abedin, T. F. Taunay, M. Fishteyn, D. J. DiGiovanni, V. R. Supradeepa, J. M. Fini, M. F. Yan, B. Zhu, E. M. Monberg, and F. V. Dimarcello, "Cladding-pumped erbium-doped multicore fiber amplifier," *Optics Express*, vol. 20, no. 18, p. 20191, 2012.
- [94] K. S. Abedin, J. M. Fini, T. F. Thierry, B. Zhu, M. F. Yan, L. Bansal, F. V. Dimarcello, E. M. Monberg, and D. J. DiGiovanni, "Seven-core erbium-doped double-clad fiber amplifier pumped simultaneously by side-coupled multimode fiber," *Opt. Lett.*, vol. 39, no. 4, pp. 993–996, 2014.
- [95] S. Jain, Y. Jung, T. C. May-Smith, S. U. Alam, J. K. Sahu, and D. J. Richardson, "Few-mode multi-element fiber amplifier for mode division multiplexing," *Opt. Express*, vol. 22, no. 23, p. 29031, 2014.
- [96] M. N. Zervas, A. Marshall, and J. Kim, "Effective absorption in cladding-pumped fibers," *Proc. SPIE*, vol. 7914, p. 79141T, 2011.
- [97] G. G. H. Injeyan, G. D. Goodno, *High Power Laser Handbook*. McGraw-Hill, 2011.
- [98] D. J. Richardson, J. Nilsson, and W. A. Clarkson, "High power fiber lasers: current status and future perspectives [Invited]," *Journal of the Optical Society of America B*, vol. 27, no. 11, p. B63, 2010.
- [99] A. Hardy and R. Oron, "Signal amplification in strongly pumped fiber amplifiers," *IEEE J. Quantum Electron.*, vol. 33, no. 3, pp. 307–313, 1997.
- [100] E. L. Lim, Y. Jung, Q. Kang, T. C. May-Smith, N. H. L. Wong, R. Standish, F. Poletti, J. K. Sahu, S. Alam, and D. J. Richardson, "First Demonstration of Cladding Pumped Few-moded EDFA for Mode Division Multiplexed Transmission," *Opt. Fiber Commun. Conf.*, p. M2J.2, 2014.
- [101] Y. Jung, E. L. Lim, Q. Kang, T. C. May-Smith, N. H. L. Wong, R. Standish, F. Poletti, J. K. Sahu, S. U. Alam, and D. J. Richardson, "Cladding pumped few-mode EDFA for mode division multiplexed transmission," *Opt. Express*, vol. 22, no. 23, p. 29008, 2014.
- [102] N. K. Fontaine, T. Haramaty, R. Ryf, H. Chen, L. Miron, L. Pascar, and M. Blau, "Heterogeneous Space-Division Multiplexing and Joint Wavelength Switching Demonstration," *Opt. Fiber Commun. Conf. Exhib.*, paper Th5C.5, 2015.
- [103] F. Poletti, V. Finazzi, T. M. Monro, N. G. R. Broderick, V. Tse, and D. J. Richardson, "Inverse design and fabrication tolerances of ultra-flattened dispersion holey fibers," *Opt. Express*, vol. 13, no. 10, pp. 3728–3736, 2005.
- [104] J. Skaar and K. M. Risvik, "A genetic algorithm for the inverse problem in synthesis of fiber gratings," *J. Light. Technol.*, vol. 16, no. 10, pp. 1928–1932, 1998.

References

- [105] J. H. Holland, *Adaptation in natural and artificial systems: an introductory analysis*. University of Michigan Press, 1975.
- [106] D. E. Goldberg, *Genetic algorithms in search, optimization and machine learning*. New York: Addison-Wesley, 1989.
- [107] D. Beasley, D. R. Bull, and R. R. Martin, "An Overview of Genetic Algorithms : Part 1, Fundamentals," *Univ. Comput.*, vol. 2, no. 15, pp. 1–16, 1993.
- [108] C. Jin, B. Ung, Y. Messaddeq, and S. LaRochelle, "Tailored modal gain in a multi-mode erbium-doped fiber amplifier based on engineered ring doping profiles," vol. 8915, p. 89150A, 2013.
- [109] C. X. Guifang Li, Neng Bai, Ningbo Zhao, "Space-division multiplexing: the next frontier in optical communication," *Adv. Opt. Photonics*, vol. 6, pp. 413–487, 2014.
- [110] N. K. Fontaine, R. Ryf, H. Chen, A. V. Benitez, J. E. A. Lopez, R. A. Correa, B. Guan, B. Ercan, Y. Sun, R. J. Lingle, R. P. Scott, S. J. Ben Yoo, and L. Gr, "30 × 30 MIMO Transmission over 15 Spatial Modes," no. Mdl, pp. 20–22, 2015.
- [111] X. Q. Jin, A. Gomez, D. C. O. Brien, and F. P. Payne, "Influence of Refractive Index Profile of Ring-Core Fibres for Space Division Multiplexing Systems," *Summer Topicals Meeting Series*, 2014, pp. 178–179, 2014
- [112] X. Q. Jin, R. Li, D. C. O'Brien, and F. P. Payne, "Linearly polarized mode division multiplexed transmission over ring-index multimode fibres," *2013 IEEE Photonics Soc. Summer Top. Meet. Ser. PSSTMS 2013*, vol. 3, pp. 113–114, 2013.
- [113] E. A. J. M. D. Gloge, "Impulse Response of Fibers with Ring-Shaped Parabolic Index Distribution," *Bell Syst. Tech. J.*, vol. 52, no. 7, pp. 1161–1168, 1973.
- [114] R. H. Stolen, "Modes in fiber optical waveguides with ring index profiles.," *Appl. Opt.*, vol. 14, no. 7, pp. 1533–1537, 1975.
- [115] R. Olshansky, "Mode Coupling Effects in Graded-index Optical Fibers.," *Appl. Opt.*, vol. 14, no. 4, pp. 935–945, 1975.
- [116] R. T. Schermer and J. H. Cole, "Improved bend loss formula verified for optical fiber by simulation and experiment," *IEEE J. Quantum Electron.*, vol. 43, no. 10, pp. 899–909, 2007.
- [117] R. T. Schermer, "Mode scalability in bent optical fibers," *Opt. Express*, vol. 15, no. 24, pp. 15674–15701, 2007.
- [118] K. Nagano, S. Kawakami, and S. Nishida, "Change of the refractive index in an optical fiber due to external forces," *Appl. Opt.*, vol. 17, no. 13, pp. 2080–2085, 1978.
- [119] J. M. Fini and S. Ramachandran, "Natural bend-distortion immunity of higher-order-mode large-mode-area fibers.," *Opt. Lett.*, vol. 32, no. 7, pp. 748–750, 2007.

References

- [120] L. Allen, M. W. Beijersbergen, R. J. C. Spreeuw, and J. P. Woerdman, "Orbital angular momentum of light and the transformation of Laguerre-Gaussian laser modes," *Phys. Rev. A*, vol. 45, no. 11, pp. 8185–8189, 1992.
- [121] C. Brunet, P. Vaity, and L. a Rusch, "Design , fabrication and validation of an OAM fiber supporting 36 modes," *Opt. Express*, vol. 536, no. 2013, pp. 4919–4922, 2014.
- [122] C. Brunet, B. Ung, P.-A. Bélanger, S. Larochelle, and L. A. Rusch, "Vector Mode Analysis of Ring-Core Fibers: Design Tools for Spatial Division Multiplexing," *J. Light. Technol.*, vol. 32, no. 23, pp. 4046–4057, 2014.
- [123] S. Li and J. Wang, "A compact trench-assisted multi-orbital-angular-momentum multi-ring fiber for ultrahigh-density space-division multiplexing (19 rings \times 22 modes),," *Sci. Rep.*, vol. 4, p. 3853, 2014.
- [124] Y. Yue, Y. Yan, N. Ahmed, J. Y. Yang, L. Zhang, Y. Ren, H. Huang, K. M. Birnbaum, B. I. Erkmen, S. Dolinar, M. Tur, and A. E. Willner, "Mode properties and propagation effects of optical orbital angular momentum (OAM) modes in a ring fiber," *IEEE Photonics J.*, vol. 4, no. 2, pp. 535–543, 2012.
- [125] S. Ramachandran and P. Kristensen, "Optical vortices in fiber," *Nanophotonics*, vol. 2, no. 5–6, pp. 455–474, 2013.
- [126] P. Gregg, P. Kristensen, S. Golowich, J. Olsen, P. Steinvurzel, and S. Ramachandran, "Stable Transmission of 12 OAM States in Air-Core Fiber," *Cleo 2013*, vol. 1, no. c, p. CTu2K.2, 2013.
- [127] S. Ramachandran, P. Gregg, P. Kristensen, and S. E. Golowich, "On the scalability of ring fiber designs for OAM multiplexing," *Opt. Express*, vol. 23, no. 3, p. 3721, 2015.

Appendix: List of publications

Journal Publications

Q. Kang, P. Gregg, Y. Jung, E. L. Lim, S.U. Alam, S. Ramachandran, D.J. Richardson, "Amplification of 12 OAM States in an Air-core Erbium Doped Fiber", *Optics Express* 2015 (Accepted).

Y.Jung, E.L.Lim, **Q.Kang**, T.C.May-Smith, N.H.L.Wong, R.Standish, F.Poletti, J.K.Sahu, S.U.Alam, D.J.Richardson, "Cladding pumped few-mode EDFA for mode division multiplexed transmission", *Optics Express* Vol.22(23) pp.29008-29013 (2014).

G.S.D.Gordon, F.Feng, **Q.Kang**, Y.Jung, J.K.Sahu, T.Wilkinson, "Coherent, focus-corrected imaging of optical fiber facets using a single-pixel detector", *Optics Letters* Vol.39(20) pp.6034-6037 (2014).

Q. Kang, E. L. Lim, F. Poletti, Y. Jung, C. Baskiotis, S-U. Alam, D. J. Richardson, "Minimizing differential modal gain in cladding-pumped EDFAs supporting four and six mode groups", *Optics Express* Vol.22(18) pp.21499-21507 (2014).

Y. Jung, **Q. Kang**, J. K. Sahu, B. Corbett, J. O'Callaghan, F. Poletti, S. U. Alam, D. J. Richardson, "Reconfigurable modal gain control of a few-mode EDFA supporting 6 spatial modes", *IEEE Photonics Technology Letters* Vol.26(11) pp.1100-1103 (2014).

Y. Jung, **Q. Kang**, V. A. J. M. Sleiffer, B. Inan, M. Kushnerov, V. Veljanovski, B. Corbett, R. Winfield, Z. Li, P. S. Teh, A. Dhar, J. Sahu, F. Poletti, S. -U. Alam, and D. J. Richardson, "Three mode Er^{3+} ring-doped fiber amplifier for mode-division multiplexed transmission", *Optics Express* **21**(8), pp.10383-10392 (2013).

Q. Kang, E.L. Lim, Y. Jung, J.K. Sahu, F. Poletti, S. Alam and D. J. Richardson, "Accurate modal gain control in a multimode erbium doped fiber amplifier incorporating ring

doping and a simple LP01 pump configuration.”, *Optics Express* **20** (19), pp. 20835-20843(2012).

Conference Publications

N.K.Fontaine, T.Haramaty, R.Ryf, H.Chen, L.Miron, L.Pascar, M.Blau, B.Frenkel, L.Wang, Y.Messaddeq, S.LaRochelle, R.Essiambre, Y.Jung, **Q.Kang**, J.K.Sahu, S.U.Alam, D.J.Richardson, D.M.Marom, “Heterogeneous space-division multiplexing and joint wavelength switching demonstration”, *OFC’15 Los Angeles* 22-26 Mar 2015 Th5C.5 (Postdeadline)

F.Feng, G.S.Gordon, X.Q.Jin, D.C.O’Brien, F.P.Payne, Y.Jung, **Q.Kang**, J.K.Sahu, S.U.Alam, D.J.Richardson, T.D.Wilkinson, “Experimental characterization of a graded-index ring-core fiber supporting 7 LP mode groups”, *OFC’15 Los Angeles* 22-26 Mar 2015 Tu2D.3

S.U.Alam, Y.Jung, **Q.Kang**, F.Poletti, J.K.Sahu, D.J.Richardson, “Recent progress in the development of few mode fiber amplifier”, *OFC’15 Los Angeles* 22-26 Mar 2015 Tu3C.1 (Invited)

Q. Kang, P. Gregg, Y. Jung, E. L. Lim, S.U. Alam, S. Ramachandran, D.J. Richardson, “Amplification of 12 OAM States in an Air-core EDF”, *OFC Los Angeles*, 22-27 March 2015 Tu3C.2.

Q. Kang, E. Lim, Y. Jung, X. Jin, F. P. Payne, S. Alam, D. J. Richardson, “Gain Equalization of a Six-Mode-Group Ring Core Multimode EDFA”, *European Conference on Optical Communications (ECOC)* Cannes 21–25 Sep 2014 P1.14.

Q. Kang, E. L. Lim, F. Poletti, Y. Jung, S-U. Alam, D. J. Richardson, “Minimizing differential modal gain in cladding pumped MM-EDFAs for mode division multiplexing in C and L Bands”, *OSA topical Meeting-Fiber-Based Technologies and Applications (part of the International Photonics and Optoelectronics Meetings, POEM)* Wuhan, China 19 Jun 2014

Appendix: List of publications

E. L. Lim, Y. Jung, **Q. Kang**, T. C. May-Smith, N. H. L. Wong, R. Standish, F. Poletti, J. K. Sahu, S. U. Alam, D. J. Richardson, "First demonstration of cladding pumped few-moded EDFA for mode division multiplexed transmission", *OFC'14* San Francisco, USA 9-13 Mar 2014 M2J.2.

Y. Jung, **Q. Kang**, J. K. Sahu, B. Corbett, R. Winfield, F. Poletti, S. U. Alam, D. J. Richardson, "Few-mode EDFA Supporting 5 Spatial Modes with Reconfigurable Differential Modal Gain Control", ECOC 2013 London, We.4.A.2.

Y. Jung, V. Sleiffer, B. Inan, M. Kushnerov, V. Veljanovski, B. Corbett, R. Winfield, **Q. Kang**, A. Dhar, J. K. Sahu, F. Poletti, S. Alam, D. J. Richardson, "Multimode EDFA performance in mode-division multiplexed transmission systems", OFC 2013, JW2A.24.

E.L. Lim, **Q. Kang**, M. Gecevicius, F. Poletti, S. Alam and D. J. Richardson, "Vector Mode effects in Few Moded Erbium Doped Fiber Amplifiers", OFC 2013, OTu3G.2.

Q. Kang, E.L. Lim, Y. Jung, F. Poletti, S.-U Alam and D. J. Richardson, "Design of Four-Mode Erbium Doped Fiber Amplifier with Low Differential Modal Gain for Modal Division Multiplexed Transmissions", OFC 2013, OTu3G.3.

S. Alam, Y. Jung, **Q. Kang**, J.K. Sahu, F. Poletti, D.J. Richardson, "MM amplifier – Enabling the next generation spatial division multiplexed transmission system" ICP 2012 (Invited).

V.A.J.M. Sleiffer, Y. Jung, V. Veljanovski, R.G.H. van Uden, M. Kushnerov, **Q. Kang**, L. Grüner-Nielsen, Y. Sun, D.J. Richardson, S. Alam, F. Poletti, J.K. Sahu, A. Dhar, H. Chen, B. Inan, A.M.J. Koonen, B. Corbett, R. Winfield, A.D. Ellis, and H. de Waardt, "73.7 Tb/s (96X3x256-Gb/s) mode-division-multiplexed DP-16QAM transmission with inline MM-EDFA", ECOC 2012, Th.3.C.4 (Postdeadline).

Q. Kang, E.L. Lim, Y. Jung, J.K. Sahu, F. Poletti, S. Alam and D. J. Richardson, "Modal Gain Control in a Multimode Erbium Doped Fiber Amplifier Incorporating Ring Doping", ECOC 2012, P1.05.